TESTING EXTENSIONS TO THE STANDARD MODEL OF COSMOLOGY WITH THE GROWTH OF STRUCTURE

Sam Stafford

A thesis submitted in partial fulfilment of the requirements of
Liverpool John Moores University
for the degree of
Doctor of Philosophy.
November 2021

Declaration

The work presented in this thesis was carried out at the Astrophysics Research Institute, Liverpool John Moores University. Unless otherwise stated, it is the original work of the author.

While registered as a candidate for the degree of Doctor of Philosophy, for which submission is now made, the author has not been registered as a candidate for any other award. This thesis has not been submitted in whole, or in part, for any other degree.

Sam Stafford
Astrophysics Research Institute
Liverpool John Moores University
IC2, Liverpool Science Park
146 Brownlow Hill
Liverpool
L3 5RF
UK

JANUARY 7, 2022

Abstract

The past century has seen cosmologists piece together a working theory for the origin and evolution of structure in the Universe which has been hugely successful at describing a wide range of observations. This theoretical paradigm is called the ΛCDM model, which describes the two main constituents of our Universe: Λ, representing dark energy which drives the late time accelerated expansion of space and CDM, representing cold dark matter, the main matter constituent of our Universe. Despite this, this thesis lays out some of the current tensions which have arisen with the current concordance model of cosmology and uses these to motivate exploring extensions to ΛCDM. The thesis is comprised of three main parts; in the first part I explore one of the predictions of inflation, which is a non-zero running of the scalar spectral index – usually set to be zero in the ΛCDM model – and its effects on the formation and evolution of large-scale structure. In particular I examine its effects on the abundance (through the halo mass function), distribution (through the two point auto-correlation function) and internal properties (through total matter density profiles) of dark matter haloes, finding effects of the order 10% in all of these quantities when comparing to a ΛCDM simulation. I also show that these effects due to cosmology are separable from the effects present due to galaxy formation physics to typically better than 1% accuracy. In the second part of this thesis, I focus on the effects warm dark matter, self-interacting dark matter and a running scalar spectral index have on galaxy scales, with particular focus on Milky Way mass haloes. In this part of the thesis I explore the degeneracies present between the effects of these different cosmological models on the abundance and distribution of substructure, as well as the distribution of matter inside host haloes in dark matter-only simulation. In general these models all show strong

degeneracies in their effects, but in detail differences can be discerned. This part of the thesis also illustrates the degeneracy between the effects from baryons and galaxy formation physics and cosmological effects. In the third and final part of this thesis I explore whether future stage-IV weak lensing surveys will be able to place independent and competitive constraints on the parameters associated with the aforementioned extensions ($M_{\rm WDM}$, σ/m, α_s). This is done using the non-linear matter power spectrum extracted from dark matter-only simulations to compute the cosmic shear power spectrum. I then compute a realistic set of error bars associated with the cosmic shear power spectrum which are representative of future upcoming surveys, taking into account the expected sky coverage, number density of source galaxies, and associated shape noise. I find that weak lensing should be able to place useful, independent, constraints on each of these cosmological parameters, supporting current observational efforts in doing so.

Publications

In the course of completing the work presented in this thesis, the following papers have been accepted for publication in a refereed journal:

First author publications:

Stafford, Sam G.; McCarthy, Ian G.; Kwan, Juliana; Brown, Shaun T.; Font, Andreea S.; Robertson, Andrew. Testing extensions to ΛCDM on small scales with forthcoming cosmic shear surveys. *MNRAS, 508(1):2537-2555*, Dec 2021, doi: 10.1093/mnras/stab2787.

Stafford, Sam G., Brown, Shaun T., McCarthy, Ian G., Font, Andreea S., Robertson, Andrew, Poole-McKenzie, Robert. Exploring extensions to the standard cosmological model and the impact of baryons on small scales. *MNRAS, 497(1):3809-3829*, Sep 2020, doi: 10.1093/mnras/staa2059

Stafford, Sam G., McCarthy, Ian G., Crain, Robert A., Salcido, Jaime, Schaye, Joop, Font, Andreea S., Kwan, Juliana, Pfeifer, Simon. The BAHAMAS project: effects of a running scalar spectral index on large-scale structure. *MNRAS, 493(1):676-697*, Mar 2020, doi: 10.1093/mnras/staa129

Acknowledgements

To begin, I offer my gratitude to Ian McCarthy. Over the past five years, you have gone from helping me with undergraduate questions on Cosmology to supervising me as I undertake a PhD in the same subject. Much of my personal and academic development is due, in no small part, to all of the help and advice you have given over these years. Your keenness about science along with your insight has been a genuine pleasure to be around and, whether intentional or not, was a significant motivating factor for me. I would also like to make a particular mention of the lockdown period, during which time I experienced the most difficult part of my PhD, and your unwavering help and encouragement were invaluable. For these reasons and many more, I thank you.

I would also like to extend thanks to my other PhD supervisors, Andreea Font and Rob Crain, both of whom have helped in my academic development either through advice or feedback. The work I have done during this time has undoubtedly been enriched through your help, and I appreciate all of it.

Next, I would like to thank the entire BAHAMAS team, all of whom have been a genuine pleasure to know and work with. Throughout my PhD, I think all of you have given me help or advice at some point, but in addition to this, my PhD has been a genuinely enjoyable time through our general conversations, either about work or not. I would like to go slightly further and offer a special thank you (and potential apologies) to Juliana Kwan, Simon Pfeifer and Shaun Brown. All three of you have answered more of my silly questions than I care to count (my apologies), and I thank you for your patience and unwavering readiness to help with any question I had.

I would like to thank my family for all of the support they have given through the years.

In particular, my Mother and Father, thank you for everything.

Lastly, and chiefly, Elli. I can say with certainty that any success I have in life is as much yours as it is mine and this is especially true for the PhD. Your constant love, encouragement, and understanding through the past few years have been instrumental in my ability to achieve this. Thank you.

Actual last thing, shout out to Penny.

"You miss 100% of the shots you don't take. -Wayne Gretzky"

- Michael Scott

"The Road goes ever on and on
Down from the door where it began.
Now far ahead the Road has gone,
And I must follow, if I can,
Pursuing it with eager feet,
Until it joins some larger way
Where many paths and errands meet.
And whither then? I cannot say."

- J.R.R. Tolkein, The Fellowship of the Ring

Contents

List of Tables

List of Figures

Chapter 1

General Introduction

Over the past century, the field of cosmology has undergone drastic and rapid development. From its humble beginnings of philosophy and mythology, cosmology has cemented itself as a scientific discipline, leading to the development of a quantitative cosmological model which has stood firm to many observational tests in its description of the formation and evolution of our Universe.

Our theories regarding the Universe, in their earliest forms, were expressed through mythology and religion. One of the earliest examples of this is the Rigveda of Hinduism containing hymns about the creation of the Universe at around 1500 BCE. Following this, our understanding of the Universe, and our place in it has seen several notable revisions. At around 400 BCE ancient Greek philosophers such as Aristotle placed the Earth firmly at the centre of a spatially finite, temporally infinite Universe. This anthropocentric view of the Universe was developed further by Ptolemy, who placed the Earth at the centre of the solar system and posited that the Sun, Moon and the visible planets revolved around it. From here, the next notable development comes from Nicolaus Copernicus[1], who overthrows this anthropocentric view of the Universe and replaces it with his heliocentric view, which places the Sun stationary at the centre of the solar system (and Universe), with the Earth and other planets orbiting around

[1] Although a similar heliocentric view was first presented by the ancient Greek astronomer Aristarchus around the same time as the anthropocentric view was being pushed.

it. The next notable revision was developed by William Herschel who placed the solar system at the centre of a wider collection of stars which we know as the Milky Way. This view was eventually overthrown by Harlow Shapley who placed the galactic centre far away from the sun.

This series of drastic re-writings of our understanding of the Universe serves to elucidate the significant development the field of cosmology has undergone throughout its long history and brings us up to the 20th century. It is from this time onwards where our current understanding of the Universe, its origins and evolution, really gets into gear. The 20th century saw, for the first time in human history, cosmology coming into its own as a precise, testable scientific field; as such this past century has seen the development of the so-called "standard model of cosmology". However, as a victim of its success, this standard model has been put under intense scrutiny, leading to questions being asked about its very foundations.

1.1 The development of a concordance model

The currently accepted cosmological paradigm has various parts to it, which in combination, have been incredibly successful at describing the Universe that we live in. One of the cornerstones of the current cosmological model is that gravitational interactions in the Universe are assumed to be described by Einstein's theory of General Relativity (GR) published in 1915, improving upon the previous description of gravity given by Isaac Newton. However, one of the most notable developments in modern cosmological theory started in 1915 with Vesto Slipher who measured the Doppler shifts of spiral nebulae (Slipher, 1915). This redshifting of spectral lines was later used by Edwin Hubble (Hubble, 1929; Hubble and Humason, 1931) to detect the expansion of the Universe. A natural conclusion of this detection was that at some point in the past everything in the Universe was much closer together. This was the first hint for the "Big Bang", the epoch of formation of our Universe and everything in it, another cornerstone of our current standard model of cosmology.

The detection of an expanding Universe, although an important contribution, was not the smoking gun needed to cement the Big Bang model as the accepted paradigm. The Big Bang was proposed as a cosmological method for generating the abundance of elements (Gamow, 1946; Alpher et al., 1948) and it was realised that in such a scenario there should be a relic background radiation with temperature of a few K left over from this initial hot dense beginning (Alpher and Herman, 1948, 1949). This relic radiation, termed the cosmic microwave background (CMB), was indeed later discovered by Penzias and Wilson (1965), and was found to be isotropic and free from seasonal variation, firmly placing the Hot Big Bang model as the accepted description of the beginning of the Universe.

The next key part of the standard model of cosmology is an era of rapid expansion during the very early Universe. This epoch, termed inflation, was proposed in the early 1980s (Guth, 1981; Linde, 1981) to naturally solve some of the problems that had been highlighted in the intervening years with the Hot Big Bang model. Two of the most notable are the flatness problem and the horizon problem (although more do exist, such as the magnetic monopole problem, which inflation is also able to solve). In the case of the flatness problem, it was identified early on (Dic, 1970) that for the Universe to appear approximately flat today the total energy density of the Universe, when expressed in units of the critical density[2], had to be almost exactly one at early times. As there is no a priori physical motivation for a flat Universe, the fact that this appeared to be the case presented a fine-tuning problem with the Hot Big Bang Model. The second problem mentioned, the horizon problem, addresses the fact that the CMB appeared to be isotropic when observed, including from regions of the sky that are causally disconnected. Furthermore, inflation also gives rise to the structure that we see in the Universe today from quantum fluctuations in the scalar field responsible for the rapid expansion of space. These fluctuations are blown up to cosmological scales during inflation. These subtle perturbations in the matter density of the Universe are able to grow over time into the cosmic structure we see today. One of the predictions of inflation is that these initial density perturbations should be nearly Gaussian dis-

[2]The density required to halt the expansion of the Universe after an infinite amount of time.

tributed, and their power spectrum should be close to scale-invariant. The search for primordial non-Gaussianity is an area of active research (see e.g. Renaux-Petel 2015; Shirasaki et al. 2021; Viljoen et al. 2021) and the spectral index has been confirmed, with recent CMB experiments, to have a value almost equal to – but slightly less than – one (Planck Collaboration et al., 2020).

The next components of the standard model are related to what makes up the Universe and are also what gives the model its common reference. These components are dark matter and dark energy. Starting with dark matter, its place in the current cosmological paradigm as the main matter constituent of the Universe came from observations of the Coma cluster by Fritz Zwicky. Zwicky noted that if one measured the mass of the Coma cluster using the velocity dispersion of constituent galaxies, this mass was far larger than the mass inferred from the luminous component of the cluster (Zwicky, 1933, 1937). For the galaxies to have such a large velocity dispersion, Zwicky realised that the Coma cluster must in fact possess more mass than what was present in luminous matter, i.e. there must be "dark matter" holding the galaxies in the cluster. The presence of dark matter in and around galaxies was further supported by observations of flat rotation curves (Babcock, 1939; Rubin and Ford, 1970), indicating that galaxies had a linearly increasing mass profile in the outskirts, which did not agree with the stellar profile of galaxies.

Finally, one more, and potentially the most conclusive, piece of evidence for a non-baryonic component of the total matter content of the Universe comes from detailed measurements of the CMB. These measurements were pioneered by the $COBE$ satellite which detected tiny fluctuations in the temperature of photons originating from the CMB. $COBE$ was later succeeded by the increasingly sensitive $WMAP$ and $Planck$ satellites. The angular power spectrum of these anisotropies in the CMB is a very powerful probe of cosmology. Of interest here are the acoustic peaks present in the power spectrum. The position of the first acoustic peak in the angular power spectrum of temperature anisotropies of the CMB tells us the sound horizon at recombination. This physical scale is then projected onto the sky at recombination as an angular scale that depends on the geometry of the Universe. As such, this parameter is robustly measured

independently of the cosmological model. This allows one to fix the sound horizon in order to measure the matter densities using the CMB. Firstly, the total matter density, $\Omega_{\rm m}$, can be constrained using the amount of small-scale power, with larger values for $\Omega_{\rm m}$ seeing a reduction, for example. Secondly, one can constrain the baryon density, $\Omega_{\rm b}$, from its effect on the relative heights of even and odd acoustic peaks. Using this constraining power, most recently, the $Planck$ satellite mission has confirmed that baryons only account for approximately 16% of the matter content of the Universe, with a dark component making up the other 84% (Planck Collaboration et al., 2020).

Following the discovery that there was some unseen constituent making up the matter content of the Universe, a debate broke out over its nature. Cosmologists were split into two camps, each relating to the nature of the dark matter, and in particular the mass of the theorized dark matter particle. In the first case you had hot dark matter (HDM) which would be a light particle with a mass of the order of a few tens of eV, and as such would have a large thermal velocity at early times. In the second case, you had the opposite, a heavy particle of the order of GeV, which would have a negligible thermal velocity at early times and as such was termed cold dark matter (CDM). These different models had distinct differences in their predictions for structure formation, in the case of the former HDM model, due to their large thermal velocities at early times, density perturbations on scales smaller than the free-streaming scale of the dark matter particle are smoothed out. In the case of HDM, this scale corresponds to dark matter haloes with mass $\approx 10^{15}$ $\mathrm{M}_{\odot}$, i.e. corresponding to cluster scales. Therefore, in a universe dominated by HDM, structure formation proceeds in a top-down manner, with the largest structures in the universe forming first which then fragment into smaller objects. Conversely, for the case of the heavier CDM model, structure formed in a bottom-up scenario, with the smallest objects forming first which then grow through mergers and accretion into the largest objects seen in the universe. It was this latter model, the CDM model, which prevailed out of the two as the currently accepted dominant matter constituent of the Universe. This was primarily driven by the stark differences in the predicted clustering of galaxies in a HDM universe to the observed clustering in galaxy redshift surveys (White et al., 1983).

The final component to be introduced for the standard model of cosmology is dark energy. Dark energy was discovered through observations of supernovae (Riess et al., 1998; Perlmutter et al., 1999) who noted that not only was the Universe expanding, but the speed at which the Universe was expanding appeared to be increasing. In the standard model of cosmology, this accelerated expansion is being driven by what we call dark energy, a repulsive force, which is represented by the cosmological constant Λ and is assumed to be constant with space and time. Together, we believe CDM and Λ combine to form the majority of the energy budget of our Universe ($\approx 95\%$ Planck Collaboration et al. 2020) at late times as well as forming the commonly accepted name for the above described concordance model of cosmology, the ΛCDM model.

1.2 An incomplete model

The ΛCDM model has been hugely successful at predicting and reproducing observations made of our Universe. For example, the polarisation of the CMB (Kovac et al., 2002), the presence of baryon acoustic oscillations (BAO) in the clustering of galaxies (Eisenstein et al., 2005; Cole et al., 2005), the statistics of weak gravitational lensing (see e.g. DES Collaboration et al. 2021), redshift space distortions (see e.g. Ruggeri et al. 2019), the clustering of galaxies (see e.g. Alam et al. 2017) and the properties of the CMB (Planck Collaboration et al. 2020). However, with the wealth and quality of observations being made of our Universe today, such as those already outlined here, hints have appeared that the current standard model might be missing something. I have split the current "tensions" with the ΛCDM model up into large-scale tensions, which are primarily related to constraints on cosmological parameters, and small-scale tensions, which relate to observations of galactic and sub-galactic scales.

1.2.1 Large-scale structure tensions

One of the most highlighted tensions with the ΛCDM model is that relating to the Hubble constant, H_0, which stems from different methods of placing constraints on

this parameter. On the one hand, you can use observations of the "early Universe", i.e. by using observations of the CMB, to place constraints on the parameter value for H_0. Existing constraints which have used this method include observations from the $WMAP$ satellite mission (H_0 = 69.7 $\pm$ 2.4 km s^{-1} Mpc^{-1}, Hinshaw et al. 2013), the $Planck$ satellite mission (H_0 = 67.36 $\pm$ 0.54 km s^{-1} Mpc^{-1}, Planck Collaboration et al. 2020), the Atacama Cosmology Telescope (H_0 = 67.9 $\pm$ 1.5 km s^{-1} Mpc^{-1}, Aiola et al. 2020) and the South Pole Telescope (H_0 = 68.8 $\pm$ 1.5 km s^{-1} Mpc^{-1}, Dutcher et al. 2021). On the other hand, one can place constraints on H_0 using observations of the "late Universe" with most notable measurements coming from observations of type Ia supernovae by the $SH0ES$ team (H_0 = 73.2 $\pm$ 1.3 km s^{-1} Mpc^{-1}, Riess et al. 2021), and observations of lensed quasars made by the $H0LiCOW$ team (H_0 = 73.3$^{+1.7}_{-1.8}$ km s^{-1} Mpc^{-1}, Wong et al. 2020). Therefore, this discrepancy (see also Verde et al. 2019 for a recent review of the H_0 tension) between early Universe constraints, which all systematically prefer a lower value for H_0, and late Universe constraints now stands at $> 4\sigma$ and poses a potentially significant problem with the standard ΛCDM model.

The second tension related to cosmological parameters is an emerging tension on the parameter combination $S_8 = \sigma_8(\Omega_{\rm m}/0.3)^{0.5}$, where σ_8 is the amplitude of mass fluctuations on scales of 8 Mpc h^{-1} and $\Omega_{\rm m}$ is the matter density in units of the critical density. Here, again constraints using the primary CMB prefer a different value than what is preferred using measurements of large-scale structure. In the case of the CMB, $Planck$ places the constraint S_8 = 0.832 $\pm$ 0.013 (Planck Collaboration et al., 2020), and ACT gives S_8 = 0.830 $\pm$ 0.043 (Aiola et al., 2020). Whereas, if one uses weak gravitational lensing to constrain this parameter, it seems to prefer a lower value. For example, three recent large cosmic shear surveys all consistently find lower values than that preferred by $Planck$, the Subaru Hyper Suprime-Cam (HSC) gives $S_8 = 0.780^{+0.030}_{-0.033}$ (Hikage et al., 2019), the Kilo-Degree Survey (KiDS)-1000 gives $S_8 = 0.766^{+0.0203}_{-0.014}$ (Heymans et al., 2021), the Dark Energy Survey (DES) Year 3 3x2pt function analysis gives $S_8 = 0.776^{+0.017}_{-0.017}$ (DES Collaboration et al., 2021). In this case, the primary CMB seems to prefer higher values than that preferred by large-scale structure observations,

[3]Note, this constraint comes from the KiDS-1000 3x2pt function analysis which includes the data sets of cosmic shear, galaxy-galaxy lensing and galaxy-galaxy correlation functions together.

which translates to the primary CMB preferring a more "lumpy" Universe than what we seem to observe. Together, this tension and the H_0 tension perhaps hint that the ΛCDM model is incomplete and there may be some discrepancy between early and late time evolution of the Universe that has not been included in the model.

These creeping tensions with the ΛCDM model are the motivation I use for exploring a minimal extension to the standard model in Chapter 2. In this first part of my thesis, I seek to explore the effects a running scalar spectral index has on large-scale structure, and whether or not it can go some way in alleviating the above tensions. A running spectral index works to alter the amount of power present on both large and small scales. Physically this means a running scalar spectral index can either enhance (or suppress) large- and small-scale density perturbations, which as a result, should effect the resultant structure which forms on these scales. The motivation for choosing this extension to study is two-fold. Firstly, as already detailed in this introduction, the ΛCDM model is an incredible success of modern cosmology, and if it is wrong, at this point it is only subtly wrong, at least in its mathematical description of our Universe. Therefore, any extension that is made to the standard model has to keep the broad strokes of the resultant universe the same as what we observe, and a running scalar spectral index is capable of doing this. Furthermore, some level of "running" is expected from inflationary theory, even for the currently accepted slow-roll inflation model (Kosowsky and Turner, 1995). However, currently, one of the assumptions of the ΛCDM model is that the "running" is equal to zero, and so the spectral index has no scale dependence. The second motivation for studying this extension to the standard model comes from current observations. This is detailed more thoroughly in Chapter 2, but in short, there seems to be mounting evidence that the value for the running of the spectral index is mildly negative (Planck Collaboration et al., 2020; Palanque-Delabrouille et al., 2020). Therefore, anticipating the effects of a non-zero running of the spectral index on large-scale structure will be important for upcoming surveys.

1.2.2 Small-scale structure tensions

In the previous section, I detailed a couple of the tensions that have been highlighted with the ΛCDM model, both of which were focused on parameter constraints from large-scale structure observations. However, these are not the only problems that have been raised regarding the standard model of cosmology. If one turns their attention to smaller scales, in particular, focusing on galaxy scales, several problems have been raised with the ΛCDM model. A comprehensive review of the identified small-scale problems with ΛCDM can be found in Bullock and Boylan-Kolchin (2017), however, I will introduce here three of the most relevant, and widely shared, problems which I explore further in Chapter 3.

To start with there is the 'missing satellites' problem (Klypin et al., 1999; Moore et al., 1999) which describes the apparent under-abundance of low-mass galaxies in the Local Group as well as, in particular, around the Milky Way (MW). Secondly, there is the 'cusp-core problem' (Flores and Primack, 1994), which refers to the fact that measurements of the rotation curves of dark matter-dominated galaxies appear to have a cored (have a shallow, almost flat) inner density profile. In comparison, haloes from a numerical simulation of a ΛCDM cosmology appear to have a cuspy (increasingly dense) inner density profile (Navarro et al., 1996). Lastly, there is the 'too-big-to-fail' problem (Boylan-Kolchin et al., 2011), which describes the fact that satellites of the MW appear to have central masses which are too low in comparison with their counterparts from numerical simulations. Together, these so-called 'small-scale problems' with ΛCDM highlighted here appear to point towards a common sign, the ΛCDM model predicts more structure on small-scales than is observed in the real Universe.

One of the results found from Chapter 2 is that, because a running spectral index affects the power spectrum on small-scales, either through an enhancement or suppression, it also has an increasingly large effect on haloes of decreasing mass. For a cosmology with a negatively running scalar spectral index, this was particularly interesting, as this leads to a suppression of small-scale density perturbations which in turn leads to a decrease in structure formation on small-scales. Therefore, this result, along with the

above problems highlighted with the ΛCDM model on small-scales was the motivation for the work presented in Chapter 3. However, alongside a running scalar spectral index, there are other extensions to the ΛCDM model which are not beyond current observational constraints which work to suppress small-scale structure and therefore go some way in alleviating the above tensions. These extensions are different to running, in that they alter the nature of dark matter (DM) somewhat, whereas a running spectral index alters the initial conditions for structure formation. Firstly, there is warm dark matter (WDM), which lies somewhere between the DM models mentioned previously of HDM and CDM. Here, the DM particles have enough thermal velocity at early times to smooth out density perturbations on dwarf galaxy scales (compared with the cluster scales associated with HDM). This suppression in small-scale power leads to a reduction in the number of low-mass haloes which form in these cosmologies while retaining the large-scale structure necessary to explain the clustering of galaxies. Secondly, there is self-interacting dark matter (SIDM), which allows the DM particles to have significant self-interactions and momentum exchange and again works to suppress small-scale density perturbations, being particularly successful at decreasing the inner density profile of galaxies. Due to the similarity in the effects on small-scale structure between these two additional extensions to the standard model of cosmology, I include these cosmological models in my analysis in Chapter 3. Here I explore the degeneracies which exist between the models and compare how well each does in turn in alleviating the previously highlighted small-scale problems with ΛCDM.

One of the results of Chapter 3 is that these three cosmological models, as expected, have significant degeneracies in their effects on small-scale structure, for example, all of the models can reduce the number of satellite galaxies of MW analogues. This has significant consequences when it comes to placing constraints on these additional parameters as they all have very similar effects on the usual observables. As such, I explore in Chapter 4 whether or not competitive constraints can be placed on these additional cosmological parameters using the effects that they have on the non-linear matter power spectrum. I do this by exploring the effects these parameters have on the cosmic shear power spectrum, and whether or not future stage-IV weak lensing

surveys will be sensitive enough to constrain these additional parameters.

1.3 Modifications due to baryons

One caveat to the small-scale problems discussed previously is that they are present when comparing dark matter-only numerical simulations to the real Universe. However, the real Universe does not just consist of DM. Despite only accounting for $\approx 16\%$ of the mass budget of the Universe, baryons have a non-negligible impact on the structure in the Universe. For example, past studies which account for the effects of baryonic processes either through semi-analytic models (e.g. Bullock et al. 2000; Benson et al. 2002) or state-of-the-art hydrodynamic simulations, which incorporate baryonic particles as well as subgrid recipes for galaxy formation physics, have shown that this is sufficient enough to solve the aforementioned tensions with the ΛCDM model (see e.g. Navarro et al. 1996; Kravtsov et al. 2004; Mashchenko et al. 2008; Governato et al. 2012; Brooks and Zolotov 2014; Oñorbe et al. 2015; Sawala et al. 2016). Furthermore, previous studies have shown that the effects of baryonic physics are not contained to galactic scales, with hydrodynamic simulations showing that galaxy formation physics can have measurable effects on the masses of haloes (Velliscig et al., 2014), the clustering of haloes (van Daalen et al., 2014) and the non-linear matter power spectrum (van Daalen et al., 2011, 2020).

Therefore, given the importance of baryons and their effects on structure in the Universe, I also explore in Chapter 2, whether or not the effects due to a running scalar spectral index are separable from those due to baryonic physics, which will be important for future surveys which aim to measure the matter power spectrum to percent level accuracy. I also explore in Chapter 3 the degeneracies that exist between the different cosmological models already mentioned and simulations which incorporate a realistic treatment of baryons in their effects on the satellite population of haloes as well as the internal properties of haloes.

1.4 Simulating the Universe

The results in this thesis rely completely on numerical simulations which have become invaluable in modern cosmology allowing us to go beyond linear theory and perturbation theory to study the deep non-linear regime of structure formation. Typically this is done by simulating N collisionless particles, which only interact gravitationally, inside a periodic box with a side length equal to some relevant comoving scale. As computers and numerical techniques have improved, so has the scale of numerical simulations, with for example a recent study by Euclid Collaboration et al. (2019) finding that to have a converged non-linear matter power spectrum to $k-$scales of 5.48 Mpc^{-1} h one requires a simulation with side length equal to 1250 Mpc h^{-1} and 2048^3 particles. This is one giant leap beyond the first N-body simulation by Holmberg (1941) who used 37 light bulbs as gravitational particles to study the tidal interactions of two stellar systems. Similarly, this is a giant leap beyond even the first numerical N-body simulations that were run on computers (von Hoerner, 1960; Aarseth, 1963; Peebles, 1970) which used between 25 and 300 particles in their simulations, illustrating how far the field of numerical cosmology has come. I will provide a qualitative description of simulations below but provide a quantitative description of key aspects (for example, resolution and box size, etc.) in Chapters 2 & 3 (an extensive review on cosmological simulations can also be found in Vogelsberger et al. 2020).

1.4.1 Generating initial conditions

Numerical simulations start at some desired redshift – e.g. z = 127 for the works in this thesis – where an initial particle distribution is defined and then evolved through to the present day (or desired final redshift). The initial particle distribution is called the Initial Conditions (ICs), and they are generated such that the initial particle load match some desired input power spectrum. To start with, however, the initial particle load will typically be in a grid configuration, i.e. homogeneously distributed, and then the positions of the particles will be perturbed such that they reproduce the desired power

spectrum, as well as being given an initial velocity[4]. This process can be done using methods such as the Zel'dovich approximation (Zel'dovich, 1970). This only works, however, provided that the density perturbations to be generated in the ICs are linear, which is why the simulations typically start at higher redshifts.

The generation of the ICs is particularly relevant for this thesis as two of the cosmological extensions examined here, a running of the spectral index and WDM, are modelled primarily through their effect on the ICs of the simulations. Both of these extensions affect the supplied input linear theory matter power spectrum by affecting either the amount of small-scale power or both the amount of small- and large-scale power. The resultant structure formation, and any differences therein, from these modified ICs, is purely due to these initial differences from ΛCDM. This is discussed in more detail in Chapter 3.

1.4.2 N-body simulations

Following the generation of the ICs, the particle distribution needs to be evolved through to the present day, which requires an N-body solver. These N-body codes solve the equations of motion, computing the acceleration each particle experiences due to all other particles in the simulation at each time step, and updates the position and velocity of each particle accordingly. These effects are then integrated over many time steps through to the present day. The results I present in this thesis have relied extensively on the `Gadget3` (Springel, 2005) N-body code which uses a hybrid technique for computing the gravitational forces acting on each simulation particle. For short-range separations between particles `GADGET3` uses an oct-tree, whilst for large separations, it uses a particle mesh. These hybrid techniques are used to significantly speed up the calculation of the gravitational forces acting on each particle[5].

[4]Note, in the case of a hydrodynamical simulation, as well as an initial position and velocity, the baryonic particles also need to be given an initial density, velocity and temperature, which is often initialised to the redshift-dependent CMB temperature.

[5]To calculate the gravitational force acting on each particle due to every other particle in the simulation scales as $\mathcal{O}(N^2)$. However, by employing the hybrid techniques outlined here this cost can be reduced to $\mathcal{O}(N \log(N))$.

1.4.3 Hydrodynamic simulations

As described above, as the quality of numerical simulations has improved over the years, so has their complexity. Modern simulations are now able to capture hydrodynamical effects through, typically, modelling the gaseous component as an ideal fluid, going beyond the usual collisionless gravity-only simulations. A popular method for simulating baryons in hydrodynamical simulations is using a Lagrangian method which evolve the gas particles using smoothed particle hydrodynamics (SPH), where the fluid is equally discretised in mass, with quantities being attached to particles and smoothed over a spherically symmetric kernel function. These simulations, therefore, start with two particle species, a collisionless dark matter particle, which is only subject to the forces of gravity, and a gas particle. It is this method which `Gadget3` uses in its hydrodynamic calculations[6].

Although SPH allows numerical simulations to model a baryonic fluid component as well as a dark matter component, this still neglects a host of astrophysical processes important for structure formation. These processes are typically associated with scales much smaller than the resolution limit of the simulations and so they have to be captured with "subgrid" routines. Modern hydrodynamic simulations include subgrid prescriptions for radiative cooling, photoionizing heating, an ionizing background radiation which models the reionization of the universe, star formation, stellar feedback, supermassive black holes and feedback from active galactic nuclei. These are all very important aspects of galaxy formation and have non-negligible effects on the structure which forms in the Universe. The work in this thesis makes use of the `BAHAMAS` (McCarthy et al., 2017, 2018) and `EAGLE` (Schaye et al., 2015; Crain et al., 2015) hydrodynamic simulations to compare cosmological effects to a realistic treatment of baryonic physics. A discussion on the modelling of the subgrid physics included in these simulations, as well as its calibration, is included in Chapters 2 & 3.

[6]Note, however, that this is not the only method available for modelling hydrodynamical effects in numerical simulations. Other techniques include Eulerian methods which focus on specific points in space, and the flow of hydrodynamic quantities across their boundaries. Alongside this there is also Lagrangian-Eulerian methods, which use techniques such as Voronoi tessellation which allow the underlying mesh to adapt and move. A more detailed description of these other methods, and associated references, can be found in Vogelsberger et al. (2020).

1.5 Thesis Outline

This thesis is organised as follows:

In Chapter 2 I explore the differences present in the large-scale structure which forms in cosmological models which have been chosen to have a non-zero value for the running of the scalar spectral index when comparing to the ΛCDM counterpart. I do this using statistics such as the halo mass function, the non-linear matter power spectrum and the two-point autocorrelation function of haloes. I also explore the effects on the internal properties of haloes by looking at the concentration-mass relation and the total matter density profiles of haloes. Furthermore, as this work is part of the BAHAMAS project (McCarthy et al. 2017), I examine how separable the effects on the aforementioned statistics due to a non-zero running scalar spectral index are from the effects due to galaxy formation physics.

In Chapter 3 the attention turns to smaller physical scales. Here I introduce a new suite of simulations that includes cosmological models with a non-zero value for the running of the scalar spectral index, warm dark matter and self-interacting dark matter. I focus on the effects these non-standard cosmologies have on the abundance and distribution of satellite haloes, pitching the results in the context of the small-scale problems associated with the ΛCDM model. I also examine the effects on the dark matter distribution in host haloes, examining again the concentration-mass relation, the total matter density profiles as well as the circular velocity profiles. Simultaneously I self-consistently measure the same statistics in state-of-the-art hydrodynamical simulations, in particular the EAGLE−RECAL simulation and the ARTEMIS (Font et al., 2020) simulation, commenting on the degeneracy between the effects due to galaxy formation physics and different cosmological models.

In Chapter 4 I use the simulations, with some additional runs included, introduced in Chapter 3 to explore the effects of the different cosmological models examined in this thesis on the cosmic shear power spectrum. This chapter starts off by introducing the effects on the non-linear matter power spectrum. I then motivate how I construct a total matter power spectrum spanning a large range of $k-$scales. Following this,

I detail how I calculate the cosmic shear power spectrum, as well as how I evaluate realistic error bars for future stage-IV weak lensing surveys. I also introduce in this chapter a new analytic form for the error associated with the cross-correlation power spectrum incorporating a residual Poisson error term.

Finally, in Chapter 5 I summarise the results of this thesis and discuss future work relating to jointly modelling baryons and extensions to ΛCDM.

Chapter 2

The BAHAMAS project: Effects of a running scalar spectral index on large-scale structure

The following chapter appeared in Stafford et al. (2020a). The appendices for this work are included in Appendix A.

Recent analyses of the cosmic microwave background (CMB) and the Lyman-α forest indicate a mild preference for a deviation from a power-law primordial matter power spectrum (a so-called 'running'). In the following chapter, I introduce an extension to the BAHAMAS suite of simulations designed to explore the effects that a running scalar spectral index has on large-scale structure (LSS), using $Planck$ CMB constraints to initialize the simulations. I do this by making use of the $Planck$ Markov chains which include the running of the scalar spectral index as a free parameter. These chains allow me to choose values for all of the necessary cosmological parameters, for a given value of the running, while assuring the resultant cosmology is consistent with current CMB constraints. In this chapter I focus on 5 key statistics: i) the non-linear matter power spectrum ii) the halo mass function; iii) the halo two-point autocorrelation function; iv) total mass halo density profiles, and v) the halo concentration-mass relation. I find that the matter power spectrum in a $Planck$-constrained running cosmology is affected on

all $k-$scales examined in this study. These effects on the matter power spectrum should be detectable with upcoming surveys such as LSST and EUCLID. A positive running cosmology leads to an increase in the mass of galaxy groups and clusters, with the favoured negative running leading to a decrease in mass of lower-mass ($M \lesssim 10^{13}\mathrm{M}_{\odot}$) haloes, but an increase for the most massive ($M \gtrsim 10^{13}\mathrm{M}_{\odot}$) haloes. Changes in the mass are generally confined to 5-10% which, while not insignificant, cannot by itself reconcile the claimed tension between the primary CMB and cluster number counts. I also demonstrate that the observed effects on LSS due to a running scalar spectral index are separable from those of baryonic effects to typically a few percent precision. Finally, one key result I find in this chapter is that the effects of a running scalar spectral index become more pronounced when looking at lower mass objects, or by looking at its effects on smaller scales. I explore these effects further with an additional complementary suite of simulations which are at a higher resolution. These simulations are introduced in Chapters 3 & 4, where I exploit the increased resolution to investigate these enhanced small-scale effects and compare them to the effects from other popular extensions to the ΛCDM model.

2.1 Introduction

The standard model of cosmology is remarkably successful at describing how structure in the Universe formed and, with the recent $Planck$ mission, the model has been validated and constrained to an unprecedented precision (see Planck Collaboration XIII 2016). One of the remarkable aspects of this model, termed the ΛCDM model, is that it can be described in full by just 6 independent adjustable parameters. However, with the wealth of observational data available today, being taken with ever more precise instruments, a few interesting tensions have arisen with some of the derived parameters of this model. For example, there is the well-known tension in the Hubble constant (H_0) with local measurements (e.g. Bonvin et al., 2017; Riess et al., 2018), preferring a higher value for H_0 than the value obtained via the analysis of the primary Cosmic Microwave Background (CMB) and Baryon Acoustic Oscillations (BAO) (e.g.

Planck Collaboration XIII 2016). There also exists a mild tension when comparing various large-scale structure (LSS) joint constraints on the matter density $\Omega_{\rm m}$ and σ_8 (the linearly evolved amplitude of density perturbations on 8 Mpc h^{-1} scales) to the constraints on these quantities from $Planck$ measurements of the CMB. In particular, there are a number of LSS data sets which appear to favour relatively low values for $\Omega_{\rm m}$ and/or σ_8 (see e.g. Heymans et al., 2013; Planck Collaboration, 2016; Hildebrandt et al., 2017; Joudaki et al., 2018; McCarthy et al., 2018; Abbott et al., 2019). In addition to these tensions with low-redshift probes, a number of studies have demonstrated that there are a few mild internal tensions in the $Planck$ data/modelling itself (see e.g. Addison et al., 2016; Planck Collaboration et al., 2017). Together, these tensions, if they are not just statistical fluctuations or unaccounted for systematic errors in the analyses, could be signs of interesting new physics.

There are many possible ways to extend the standard model of cosmology that could potentially reconcile some of the above tensions, including (non-minimal) massive neutrino cosmologies (e.g. Battye and Moss, 2014; Beutler et al., 2014; Wyman et al., 2014; McCarthy et al., 2018), dynamical dark energy models (e.g. Di Valentino et al., 2017; Yang et al., 2019), and deviations from general relativity ('modified gravity') (e.g. De Felice and Tsujikawa, 2010; Li et al., 2012; Nunes, 2018) to name just a few. One of the possible extensions that is perhaps less commonly discussed is a running of the scalar spectral index of the primordial power spectrum. The primordial spectral index, n_s, of scalar perturbations is most often assumed to be independent of scale (i.e., that the primordial power spectrum is a pure power-law). However, virtually all models of inflation predict at least some small level of scale dependence in n_s. For example, the simplest models of inflation (e.g., single-field, slow-roll inflation) predict a running of n_s of order $\mathcal{O}(1 - n_s)^2$ (Kosowsky and Turner 1995) (this would be $\sim$ 0.001 for $Planck$ CMB constraints on n_s), where the scale dependence of the spectral index is given by $n_s(k) = n_s(k_0) + \alpha_s \ln(k/k_0)$, with α_s being the 'running' of the scalar spectral index and k_0 the pivot scale.

Using the $Planck$ 2015 full mission temperature data, α_s is constrained to have a central value of: $\alpha_s = -0.00841^{+0.0082}_{-0.0082}$ (68% CL $PlanckTT+lowTEB$). That is, there is

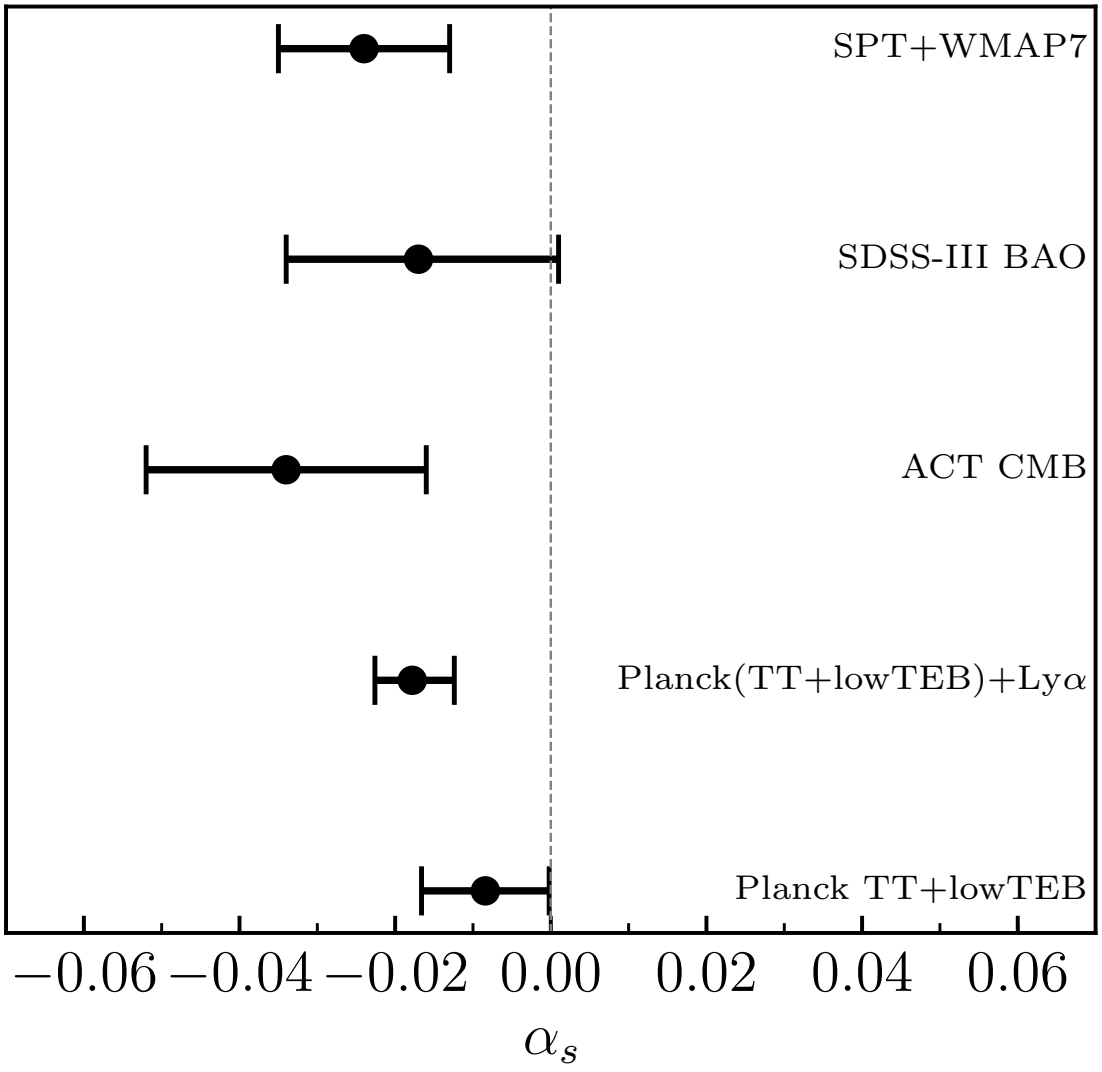

Figure 2.1: Summary of the observational constraints discussed in the introduction to this study. The vertical dashed line indicates no running. There is currently a mild preference for a negative value for α_s.

a very mild preference for a negative running from the $Planck$ CMB data. Palanque-Delabrouille et al. (2015) combine their measurements of the Lyman-alpha forest with the $Planck$ 2015 full mission temperature data and low multipole polarisation data to find a much stronger preference for a negative running: $\alpha_s = -0.0178^{+0.0054}_{-0.0048}$ (68% CL $Planck(TT + lowTEB) + Ly\alpha$). They do note, however, that this result may be due to unaccounted for systematics in their measurements. In addition to this, there have been other independent measurements (i.e., measurements which have not used $Planck$ CMB data) of a running scalar spectral index, at varying levels of significance e.g.: $\alpha_s = -0.034^{+0.018}_{-0.018}$ ($ACT\ CMB$) (Dunkley et al. 2011); $\alpha_s = -0.017^{+0.018}_{-0.017}$ ($SDSS - III\ BAO$)(Zhao et al. 2013); $\alpha_s = -0.024^{+0.011}_{-0.011}$ ($SPT + WMAP7$)(Hou et al. 2014). A visual summary of the current empirical constrains on the running is shown in Fig. 2.1.

Note that, since different models of inflation predict different scale dependencies, measurements of α_s and its running (i.e., running of the running) can be used to constrain, or possibly rule out, models of inflation (see Escudero et al. 2016 for a discussion on the impact on inflationary models in the light of the $Planck$ results).

Given these results, and the possible tensions which currently exist, it is interesting to see what effects a running spectral index that is within observational constraints would have on the LSS that we see in the Universe today. This is the aim of this present study. I use direct numerical simulations which allow us to accurately model the non-linear growth of structure for cosmologies with a running spectral index imprinted into the initial conditions (ICs) to explore the differences which arise compared to the standard ΛCDM model. I do this using a new extension to the `BAHAMAS` suite of cosmological hydrodynamic simulations (McCarthy et al., 2017, 2018), which is described below. In this study, I will explore 5 main statistics to investigate the effects due to a $\Lambda\alpha_s$CDM model. These statistics are: the non-linear total matter power spectrum, the halo mass function (HMF), the halo two-point autocorrelation function, total halo mass density profiles, and the halo concentration-mass relation. I will also examine how separable the effects of a running scalar spectral index are from the effects due to baryonic physics, to assess if they can be treated as two separate multiplicative corrections to

the standard model.

This chapter is organized as follows: in Section 2.2 I present a brief summary of the simulations used, as well as my parameter selection method. In Section 2.3 I examine the effects of a running scalar spectral index on the LSS present in the simulations, including the HMF, the two-point autocorrelation function, and the total matter power spectrum. In Section 2.4 I show the effects a running scalar spectral index has on certain internal halo properties, such as the total mass density profiles, and the concentration-mass relation. In Section 2.5 I present a separability test of the effects due to a running scalar spectral index, and baryonic physics, to assess if these two processes can be treated independently. In Section 2.6 I summarise and discuss my findings.

2.2 Simulations

2.2.1 BAHAMAS

This study extends the current BAHAMAS suite of cosmological hydrodynamic simulations. In this extension, a running scalar spectral index is incorporated into the initial conditions.

The BAHAMAS suite of cosmological simulations described in McCarthy et al. (2017) (see also McCarthy et al. 2018) consists of 400 comoving Mpc h^{-1} on a side, periodic box, smooth particle hydrodynamics (SPH) simulations containing 2×1024^3 particles. The present study adds to the pre-existing suite of BAHAMAS simulations with a new subset, whose initial conditions are based on the *Planck* maximum-likelihood cosmological parameters derived from the *Planck* 2015 data release (Planck Collaboration XIII, 2016). The cosmological parameters of each run were varied, including values for the running of the scalar spectral index α_s (the method for how the cosmologies were chosen is discussed in detail in Section 2.2.4). The Boltzmann code CAMB[1]

[1] http://camb.info/

(Lewis et al. 2000, August 2018 version) was used to compute the transfer functions, and a modified version of N-GenIC was to used to create the initial conditions for the simulations, which start at a redshift of $z = 127$. N-GenIC has been modified to include second-order Lagrangian Perturbation Theory corrections alongside support for massive neutrinos[2]. Note that when producing the initial conditions, I use the separate transfer functions computed by `CAMB` for each individual component (i.e., baryons, neutrinos, and CDM) for the hydrodynamical simulations. Note also that, when producing the initial conditions for each of the simulations, the same random phases are used for each, implying that any comparisons made between the different runs are not subject to cosmic variance complications.

The simulations were carried out using a modified version of the Lagrangian TreePM-SPH code `GADGET3` (last described in Springel 2005). This is a Lagrangian code used to calculate the gravitational and hydrodynamic forces on a system of particles. It was modified to include new subgrid physics as part of the OWLS project (see section 3 of Schaye et al. 2010). The gravitational softening is fixed to 4 kpc h^{-1} (in physical coordinates for $z \leq 3$ and in comoving coordinates at higher redshifts) and the SPH smoothing is done using the nearest 48 neighbours. The `BAHAMAS` run used here for a $Planck$ maximum-likelihood cosmology (with no running of the scalar spectral index) has dark matter and (initial) baryon particle mass of $\approx 4.36 \times 10^9$ $\mathrm{M}_\odot$ h^{-1} and $\approx 8.11 \times 10^8$ $\mathrm{M}_\odot$ h^{-1} respectively. The particle masses for the other cosmologies in this suite do not differ much from these values but can be found in Table A.1 (note that these slight differences in particle mass are due to the slight differences in Ω_m and h).

This suite of `BAHAMAS` simulations also uses a massive neutrino extension, described in McCarthy et al. (2018). Here the simulations incorporate the *minimum* summed neutrino mass equal to $\Sigma M_\nu = 0.06$ eV implied by the results of atmospheric and solar oscillation experiments when adopting a normal hierarchy of masses (Lesgourges and Pastor, 2006). I adopt the minimum neutrino mass for consistency, as this was what was adopted in the $Planck$ analysis when constraining the running of the scalar spectral index. To model the effects of massive neutrinos on both the background expan-

[2]https://github.com/sbird/S-GenIC

sion rate and the growth of density fluctuations, the semi-linear algorithm developed by Ali-Haïmoud and Bird (2013) (see also Bond et al., 1980; Ma and Bertschinger, 1995; Brandbyge et al., 2008; Brandbyge and Hannestad, 2009; Bird et al., 2012) was implemented in the GADGET3 code. This algorithm computes neutrino perturbations on the fly at each time step (see McCarthy et al. 2018 for further details). A study into the combined and separate effects of neutrino free-streaming and baryonic physics on collapsed haloes within BAHAMAS can be found in Mummery et al. (2017). In addition to neutrinos, all of the BAHAMAS runs (with or without massive neutrinos, or a running scalar spectral index) also include the effects of radiation when computing the background expansion rate.

Note that for each hydro simulation, I also produce a corresponding 'dark matter-only' simulation, where the collisionless particles follow the same total transfer function as used in the hydro simulations[3]. These have the same cosmologies and initial phases as the hydro runs, but a dark matter particle mass of $\approx 5.17 \times 10^9\ \mathrm{M}_\odot h^{-1}$ (a complete list of dark matter particle masses for these simulations can also be found in Table A.1).

2.2.2 Baryonic physics

As in the original BAHAMAS suite of simulations, this extension also includes prescriptions for various 'subgrid' processes, including: metal-dependent radiative cooling (Wiersma et al. 2009a); star formation (Schaye and Dalla Vecchia 2008) and stellar evolution; mass loss and chemical enrichment from Type II and Ia supernovae, Asymptotic Giant Branch (AGB) and massive stars (Wiersma et al. 2009b). Furthermore, the simulations include prescriptions for stellar feedback (Dalla Vecchia and Schaye 2008) and supermassive black hole growth and AGN feedback (Booth and Schaye 2009, which is a modified version of the model originally developed by Springel et al. 2005).

[3]As shown in van Daalen et al. (2020) (see also Valkenburg and Villaescusa-Navarro 2017), this setup leads to a small $\sim 1\%$ offset in the amplitude of the $z = 0$ matter power spectrum of the hydro simulations with respect to the dark matter only counterpart. This offset can be removed by instead using a dark matter-only simulation with two separate fluids (one with the CDM transfer function and the other with the baryon transfer function). This is unnecessary for the purposes of the present study, as I am only interested in the *relative* effects of different values of the running on LSS.

As explained by McCarthy et al. (2017) and discussed in Section 2.5, BAHAMAS is calibrated to reproduce the present-day galaxy stellar mass function for $M_* > 10^{10} M_\odot$ and the amplitude of the gas mass fraction-halo mass relation of groups and clusters, as inferred from high-resolution X-ray observations (note that synthetic X-ray observations of the original simulations were used to make a like-with-like comparison). The latter is particularly important for large-scale structure, since hot gas dominates the baryon budget of galaxy groups and clusters. To match these observables, the feedback parameters which control the efficiencies of the stellar and AGN feedback were adjusted. I have verified that the changes in cosmology explored here do not affect the calibration of the simulations, as such I have left these parameters at their calibrated values from McCarthy et al. (2017) for the present study.

2.2.3 Running of the scalar spectral index

As mentioned in the introduction, this study looks into an extension to the standard model of cosmology in the form of adding a scale dependence to the spectral index n_s of the primordial matter power spectrum. This results in a modification to the equation for the primordial matter power spectrum.

$$P_s(k) = A_s(k_0) \left(\frac{k}{k_0} \right)^{n_s(k_0)+\alpha_s'(k)}, \tag{2.1}$$

where $\alpha_s'(k) \equiv (\alpha_s/2)\ln(k/k_0)$, α_s is the running of the scalar spectral index, which is defined as dn_s/d$\ln(k)$. The pivot scale k_0 is the scale at which the amplitude of the power spectrum (A_s) and the spectral index (n_s) are defined. In this study I adopt the same pivot scale as was used for the cosmological parameter estimation of Planck Collaboration XIII (2016): k_0 = 0.05 Mpc^{-1} .

The effect that the addition of this parameter has on the linear matter power spectrum can be computed using CAMB and the result is shown in Fig. 2.2. This plot shows directly how large the effects can be on both small and large scales, with the negative (positive) running cosmologies showing a suppression (enhancement) of power on

these scales. In terms of overdensities, this can be thought of as a smoothing out (amplification) of these overdensities for a negative (positive) running. There is, however, an interesting region near the pivot scale, where these effects are actually reversed, and a negative running leads to an amplification of power and a positive running leads to a suppression. This behaviour is due to how the other cosmological parameter values are chosen, as described in Section 2.2.4.

Note that α_s is not the only additional parameter predicted by inflation. There is also the so-called running of the running, β. This parameter adds a second-order scale-dependence to the spectral index in the form of: $\beta_s \equiv d^2 n_s / d\ln(k)^2$, and leads to a power spectrum of the form:

$$P_s(k) = A_s(k_0) \left(\frac{k}{k_0} \right)^{n_s(k_0)+\alpha_s'(k)+\beta_s'(k)}, \tag{2.2}$$

where $\beta_s' \equiv (\beta_s/6)(\ln(k/k_0))^2$ and all other terms are as previously defined. Similarly to α_s, analysis of the $Planck$ 2015 data indicates a mild preference for a non-zero running of the running, with $\beta_s = 0.029^{+0.015}_{-0.016}$ (68% CL $PlanckTT + lowTEB$) (Planck Collaboration XX 2016). In the present study I focus just on the first-order effect and leave an exploration of running of the running on large-scale structure for future work.

2.2.4 Cosmological parameter selection

To generate a set of cosmological parameters for the simulations, this study makes use of the publicly-available set of Planck Collaboration XIII (2016) Markov chains, in particular those which include α_s as a free parameter. The parameter chains were produced using CosmoMC[4] using a fast-slow dragging algorithm (Neal 2005) and have already had burn-in removed.

The parameter chains that are used are based on the $Planck$ temperature power spectrum measurements, alongside low multipole measurements of the polarisation power spectrum (*TT+lowTEB*). From these, the one-dimensional posterior distribution for α_s

[4]https://cosmologist.info/cosmomc/

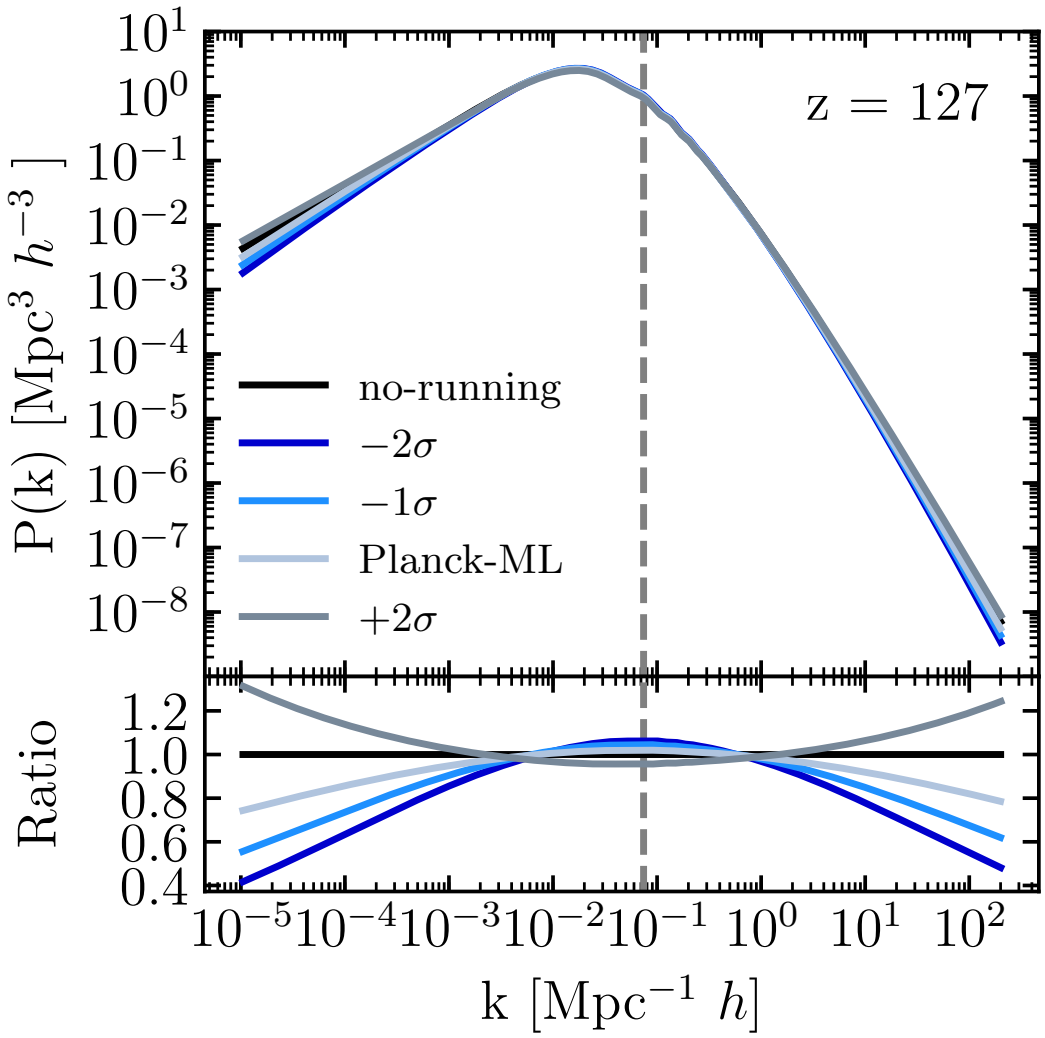

Figure 2.2: Linear matter power spectrum at z = 127, as computed by CAMB for the 5 models presented in Table 2.1. The lines here are coloured by the adopted value of α_s. The vertical dashed grey line indicates the pivot scale k_0. As expected, the largest effect on the power spectrum is on the largest and smallest scales. At these scales, a negative running leads to less power compared with a no-running cosmology, whereas the positive running cosmology predicts more power on these scales.

was obtained, which can be seen in the top panel of Fig. 2.3. From this distribution I choose a sample of values for α_s that probe as much of the available parameter space as possible. These values were the maximum likelihood of the distribution, alongside $\pm 1, 2\sigma$ of this value. With these adopted values, all chain sets which had a value of the running within $\frac{\sigma}{200}$ of the target value were selected[5]. From them, the weighted means of the other important cosmological parameters were taken using the weights of each parameter chain provided. By selecting the values of the other parameters in this way, the predicted angular power spectrum of CMB fluctuations should retain a good match to the $Planck$ data. In other words, I only select 'running' cosmologies which are consistent with the observed primary CMB.

That procedure is followed for each chosen value of α_s. Note, normally one would also simulate a reference $Planck$ cosmology, with α_s fixed to zero, to be able to quantify the differences between $\Lambda\alpha_s$CDM and ΛCDM itself. However, due to the closeness of the $+1\sigma$ value to 0 ($\alpha_s = -0.00025$), this cosmology will be treated as the base $Planck$ no-running cosmology throughout, and will be referred to as the "no-running" model. Fig. 2.4 shows the 2D marginalized constraints on n_s and α_s, with points coloured by the value for the joint constraint on the parameter $S_8 \equiv \sigma_8\sqrt{\frac{\Omega_\mathrm{m}}{0.3}}$. The resultant cosmologies that were selected can be found in Table 2.1 and are indicated by the black triangles in Fig. 2.4.

As a test, I have verified that when selecting the parameters in this way the resultant predicted CMB TT angular power spectrum (as computed by `CAMB`) for each of these different cosmologies is consistent with the $Planck$ 2015 angular power spectrum, which they are (see Fig. A.1). Choosing the parameters in this way, however, has a non-negligible effect on the matter power spectrum (seen in Fig. 2.2), particularly on the largest and smallest scales, the latter of which are not probed by the $Planck$ data. By forcing the model to match the CMB angular power spectrum over a range of scales, the amplitude of the matter power spectrum at the pivot scale is forced to vary between the models. The result of which is a negative running that has a larger

[5]This value was chosen so that when the weighted mean of α_s was calculated, it recovered the target value, but still had more than 50 chain sets available for a weighted average of the other important parameters.

Table 2.1: The cosmological parameter values for the suite of simulations are presented here. The columns are as follows: (1) The labels for the different cosmologies simulated, that are used throughout the chapter. (2) Running of the spectral index, (3) Hubble's constant, (4) present-day baryon density, (5) present-day dark matter density, (6) spectral index, (7) Amplitude of the initial matter power spectrum at a CAMB pivot scale of 0.05 Mpc^{-1}, (8) present-day amplitude of the matter power spectrum on scales of 8 Mpc/h in linear theory (note that when computing the initial conditions for the simulations, A_s is used, meaning that the ICs are 'CMB normalised'). (9) $S_8 \equiv \sigma_8 \sqrt{\Omega_\mathrm{m}/0.3}$.

(1)	(2)	(3)	(4)	(5)	(6)	(7)	(8)	(9)
Label	α_s	H_0 (km/s/Mpc)	Ω_b	Ω_CDM	n_s	A_s (10^{-9})	σ_8	S_8
-2σ	-0.02473	67.53	0.04959	0.26380	0.96201	2.34880	0.85147	0.87286
-1σ	-0.01657	67.72	0.04905	0.26018	0.96491	2.28466	0.83939	0.85468
Planck ML	-0.00841	67.54	0.04990	0.26186	0.96519	2.24159	0.83442	0.85167
no-running	-0.00025	67.39	0.04901	0.26360	0.96535	2.21052	0.83156	0.85119
+2σ	0.00791	66.95	0.04915	0.26843	0.96478	2.14737	0.82140	0.85013

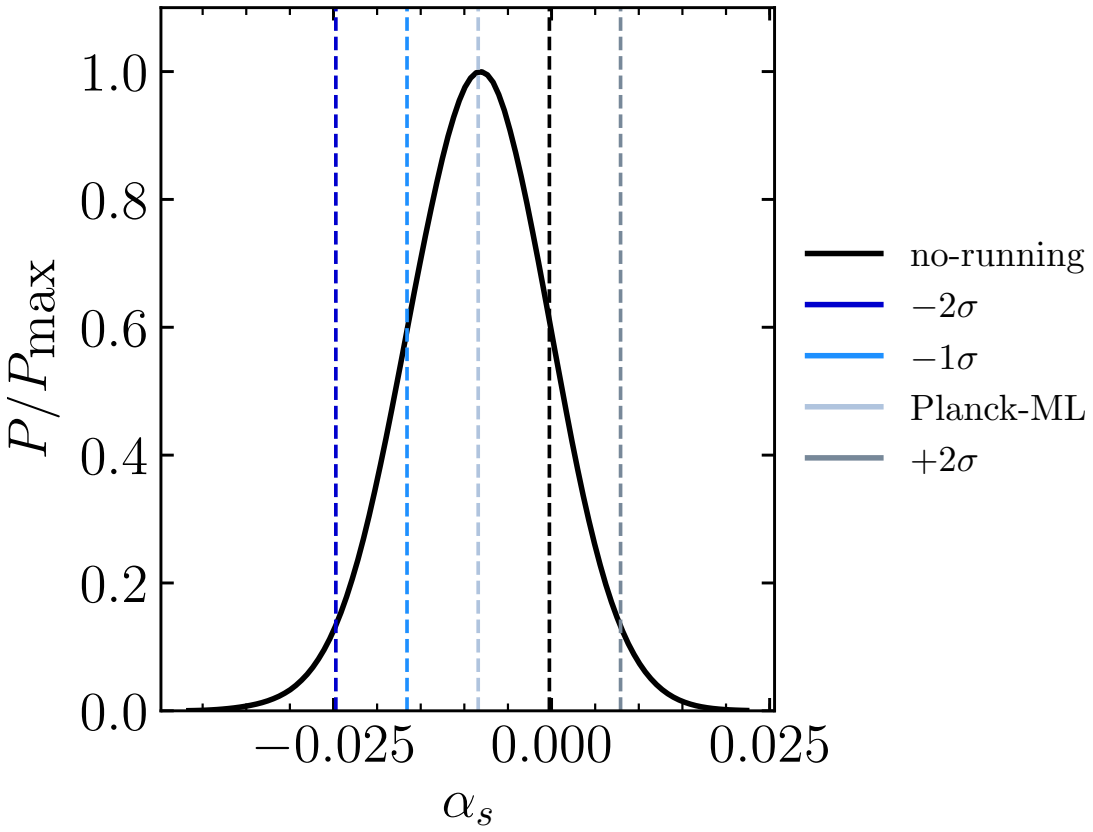

Figure 2.3: Marginalized posterior distribution for the running of the primordial spectral index when included in the *Planck* MCMC analysis as a free parameter. The vertical coloured lines represent the regions of the α_s distribution function chosen to calculate weighted means for the other important cosmological parameters.

amplitude (A_s), and a positive running that has a lower amplitude, compared with the standard no-running model. Therefore, it can be expected from the matter power spectrum alone that the inclusion of α_s in the standard model should have measurable effects on the LSS seen in the simulations, with the magnitude and sign of the effect dependent on what range of modes is sampled within the simulated volume.

As briefly discussed in the introduction, a small number of mild 'internal' tensions in the $Planck$ CMB analysis have previously been noted (e.g., Addison et al. 2016; Planck Collaboration et al. 2017) and these could have some bearing on cosmological parameter selection. Of particular relevance for LSS is the apparent asymmetry in the cosmological parameter constraints when derived from low and high multipole ranges (Addison et al., 2016). In particular, the high-ℓ peaks and troughs in the observed angular power spectrum appear smoother than that predicted by the best-fit ΛCDM model. This is qualitatively similar to the effect of lensing of the CMB by LSS, hence when the CMB lensing amplitude, $A_{\rm lens}$, is allowed to float (rather than fixing to the natural value of unity), the CMB TT power spectrum prefers $A_{\rm lens} > 1$. Allowing the lensing amplitude to float results in cosmological parameter constraints that are insensitive to the range of multipoles analysed, but does result in a few sizeable shifts (1-2 sigma) of parameters important for LSS, including σ_8 and Ω_m (Addison et al., 2016; McCarthy et al., 2018).

The $Planck$ team did not explore the potential impact of allowing $A_{\rm lens}$ to float on the constraints on the running of the scalar spectral index. In Appendix A.1 I examine the constraints on the running while marginalizing over $A_{\rm lens}$. I show that the constraints on the running are virtually unaffected by marginalizing over $A_{\rm lens}$. I therefore adopt the publicly-available $Planck$ 2015 chains with $A_{\rm lens} = 1$ for my analyses.

Lastly, it is worth noting that the effects on the statistics examined in this study should not be solely attributed to a running of the scalar spectral index. This is because as I vary the running, the other cosmological parameters change in order to retain consistency with the primary CMB constraints from $Planck$. Of particular relevance for this study is the amplitude of the initial matter power spectrum, A_s, which I discuss further in Section 2.3.1. As such, when discussing the results from the simulations, I will re-

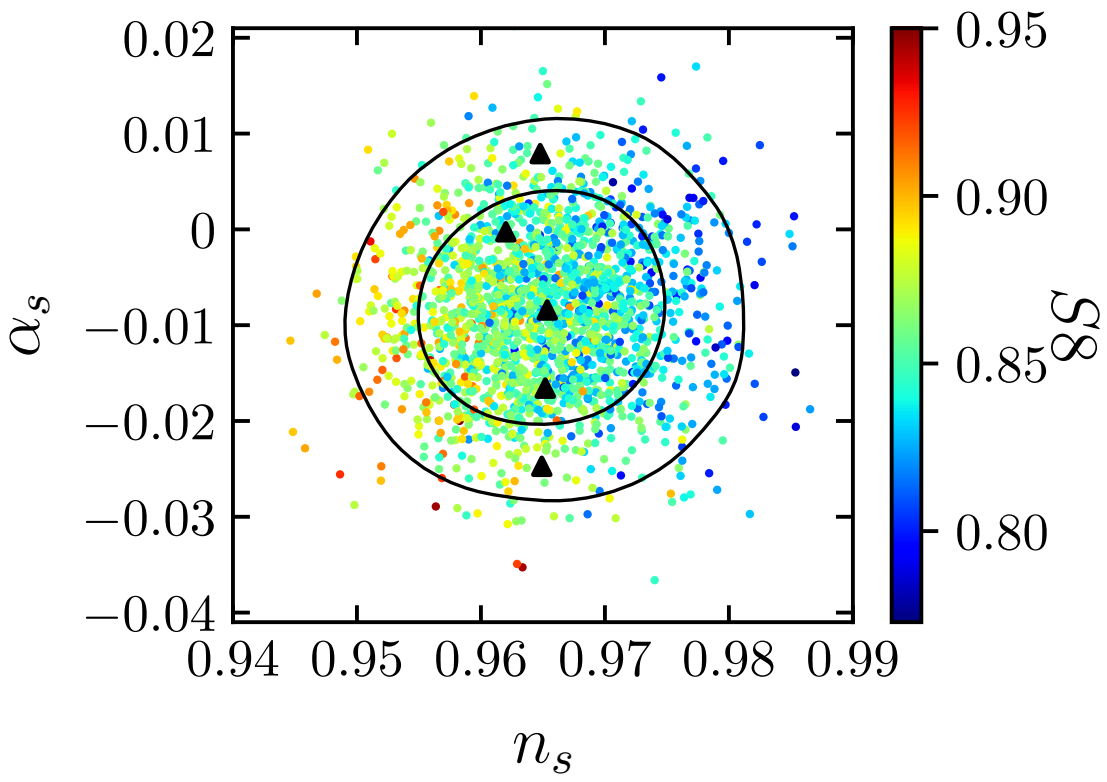

Figure 2.4: Marginalized constraints at 68% and 95% CL in the $(n_s - \alpha_s)$ plane. Here, points are coloured by that chains' value for the S_8 parameter. The black triangles indicate values for $(n_s - \alpha_s)$ that were chosen to be simulated.

fer to the changes seen as being a result of a *Planck*-constrained running cosmology, abbreviated as a $\Lambda\alpha_s$CDM cosmology, rather than due to the running parameter alone.

2.3 Effects on large-scale structure

Here I present my predictions for the effects that a $\Lambda\alpha_s$CDM cosmology has on LSS. Note that the results shown in this section and Section 2.4 are derived from the suite of dark matter only simulations. The effects due to the inclusion of baryonic physics are explored in Section 2.5.

Furthermore, as part of the BAHAMAS project, we are exploring the effects that massive neutrinos (Mummery et al., 2017; McCarthy et al., 2018) and dynamical dark energy (Pfeifer et al., 2020) have on LSS. I will comment throughout on the similarities and differences between these extensions to ΛCDM.

2.3.1 Non-linear matter power spectrum

I first look at what effect a cosmology with a free-running spectral index has on the recovered non-linear matter power spectrum extracted from the simulations for redshifts ≤ 2. To compute this, I make use of the publicly-available code `GenPK`[6] which computes the 3D matter power spectrum for each particle species in the simulation. The calculated total matter power spectrum is shown in Fig. 2.5 for $z = 0, 1, 2$. The power spectra are plotted up to a maximum k-mode equal to the Nyquist frequency of the simulation: $k_{nyq} \equiv \pi(N/L)$, where N is the cube root of the total number of particles in the simulation, and L, the side length of the box. This means that the simulations are able to probe the power spectrum into the linear and non-linear regimes ($k > 0.1$ Mpc^{-1}h), allowing us to see the effect a running spectral index has on these scales. The bottom panel(s) of this plot shows the matter power spectra of the separate cosmologies, at the three different redshifts, normalised with respect to the no-running case at the corresponding redshift. It can be seen that, although there is a large amount of scatter at large scales in the un-normalised power spectra (which arises due to the fact that the simulations do not sample many independent modes on these scales), this scatter largely divides out in the ratios. This is because the ICs of the simulations, as mentioned, have the same random phases (i.e., there is no cosmic variance between the different volumes).

The result shown in the bottom panel(s) is similar to that seen in the linear matter power spectrum (see Fig. 2.2), in that a $\Lambda\alpha_s$CDM cosmology which has a negative value for the running produces an excess of power in this $k-$range, and one which has a positive value leads to a suppression of power. It is worth noting, however, that these effects (the enhancement of power in the negative running cosmology for example) extend to higher k-modes compared with what was seen in the linear matter power spectrum. The reason for this is that there is a transfer of power from large scales down to small scales during non-linear growth. As expected, the inclusion of running affects all scales in the simulations, with the maximum effect being seen at $k-$scales around 0.1-1.0 Mpc^{-1}h, of $\approx$ 5-10$\%$ increase in power on these scales in the most negative running cosmology,

[6] https://github.com/sbird/GenPK/

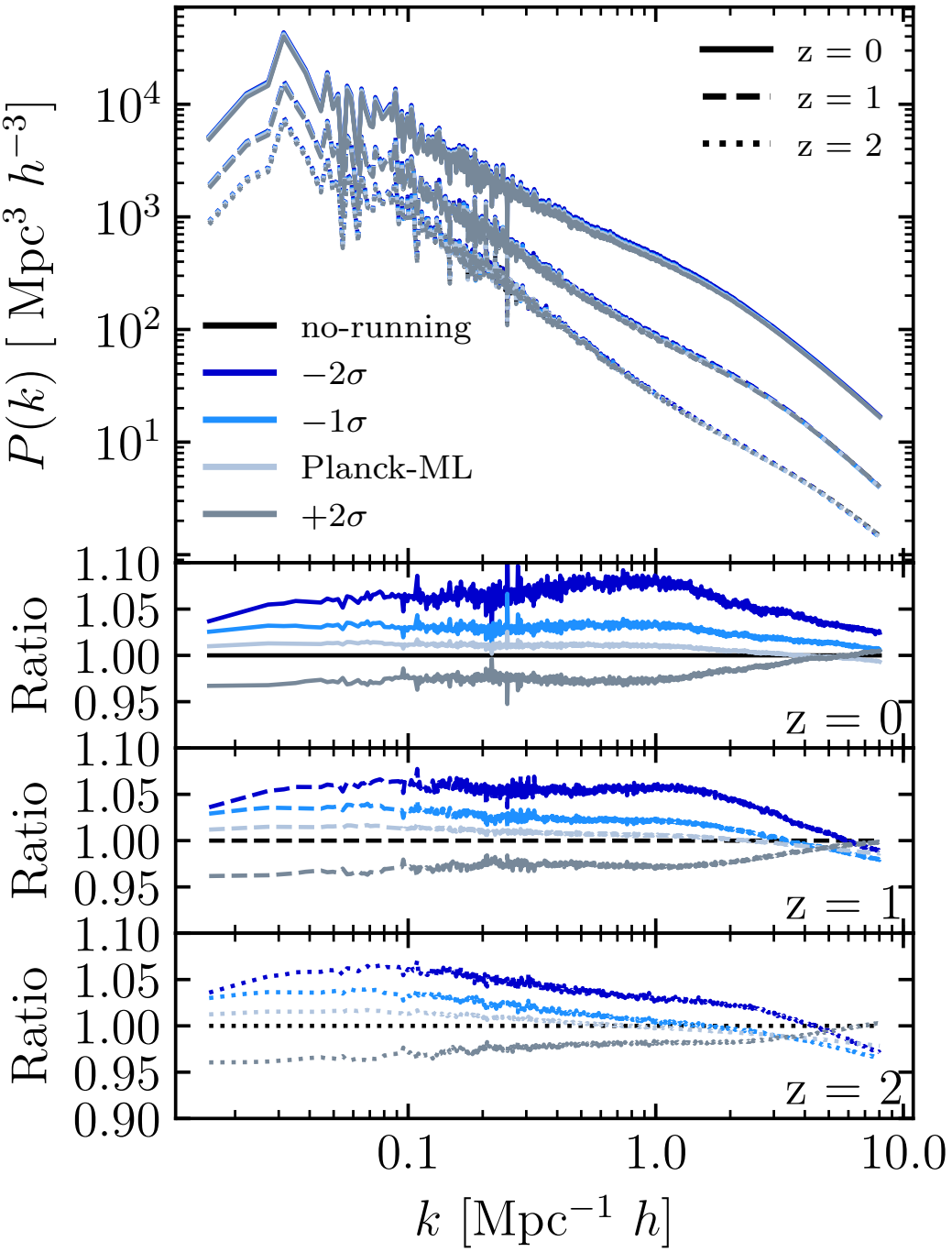

Figure 2.5: Top: the 3D total matter power spectrum for all 5 cosmologies. The different linestyles indicate the matter power spectra measured from the simulations at redshifts 0, 1 and 2 (solid, dashed and dotted respectively). Bottom: the matter power spectra of the different runs normalised to the no-running model result at a given redshift. A negative running cosmology can lead to an amplification of power on large scales by up to 5-10% compared to a standard ΛCDM cosmology, and a positive running cosmology can lead to a $\sim 5\%$ reduction in power.

and $\approx 5\%$ suppression in power on these scales in the positive running cosmology. To put this into perspective, both LSST (LSST Dark Energy Science Collaboration, 2012) and EUCLID (Amendola et al., 2013) are aiming to measure the matter power spectrum (via weak gravitational lensing and galaxy clustering) to a precision of better than 1% on scales (larger than, and) probed by this volume (see also Huterer 2002; Huterer and Takada 2005; Hearin et al. 2012). If this precision can be achieved, measurements from LSST and EUCLID should be able to distinguish between the (CMB-constrained) cosmologies I have explored here.

Note that there is a slight redshift dependence in the differences between the different cosmologies, with the largest amount of evolution apparent in the -2σ cosmology. This redshift evolution highlights the transfer of power from large scales to small scales. For example, in the most negative running cosmology, the k-scale where there is a transition from an enhancement of power to a suppression, moves to larger k-scales (i.e., smaller physical scales) with increasing redshift.

It is interesting that this cosmological volume size samples the region of the power spectrum which sees a negative running produce an amplification, and a positive running produce a suppression. The reason for this being that the $Planck$ pivot scale, and so the scale at which A_s is defined, corresponds to cluster scales, i.e., scales for which the dominant contribution to the matter power spectrum comes from groups and clusters (van Daalen and Schaye, 2015). These are also the scales BAHAMAS is designed to sample. Thus, because introducing a negative (positive) running into the standard model of cosmology leads to an increase (decrease) in A_s (see Section 2.2.4), I see this effect in the power spectrum of the simulations. It can be expected from Fig. 2.2 that if the resolution of the simulations were significantly increased or, alternatively, significantly larger volumes were simulated, the effects one might naively associate with a negative, or positive running, i.e. a suppression and amplification of power on these larger and smaller scales respectively, would be more apparent.

I note that the effects on the power spectrum shown here are of a similar magnitude as those that are seen through the inclusion of (CMB-constrained) dynamical dark energy in the standard model (Pfeifer et al., 2020). The results seen in the dynamical dark

energy extension also display an almost scale independent (over the $k-$range sampled in these studies, at least) suppression/amplification of the power spectrum (depending on the values for w_0 and w_a), with a maximum magnitude of around 10%. By constrast, the inclusion of massive neutrinos always leads to a suppression of the matter power spectrum. For example, Mummery et al. (2017) showed that for $\Sigma M_\nu = 0.24$ (0.48) eV, the matter power spectrum is suppressed by nearly 15% (30%) on non-linear scales. (See McCarthy et al. 2018 for a discussion of current constraints on the summed mass of neutrinos.)

In Fig. 2.6 I show the ratio of the non-linear matter power spectrum from the simulations to the linear prediction result from `CAMB` (top) and the non-linear prediction from `HALOFIT` (Smith et al., 2003; Takahashi et al., 2012) (bottom). The top panel isolates the non-linear growth of structure. I note here that the most negative running case shows the strongest non-linear growth, most likely because this model has an enhancement of power on large scales (due to the increase in A_s), which is transferred to small scales during non-linear evolution. The bottom panel tests the accuracy of the `HALOFIT` prescription for the non-linear matter power spectrum in running cosmologies. It can be seen that up to $k \approx 4$ Mpc^{-1}h, it can reproduce the power spectrum relatively well (to within 5%). However, on scales smaller than this, it appears that `HALOFIT` does not accurately model the impact that a running scalar spectral index has on the non-linear matter power spectrum.

However, a recent study into modelling the non-linear effects of a running scalar spectral index on the matter power spectrum was performed by Smith and Angulo (2019). This was done using a suite of high-resolution N-body simulations, with an extended cosmological parameter space, with values for these parameters centered on the best-fit $Planck$ 2015 standard model. Smith and Angulo (2019) produced a modification to `HALOFIT` to try to better model the non-linear effects of non-standard cosmologies. I have used the publicly-available software developed by Smith and Angulo (2019) `NGENHALOFIT`[7] to generate a non-linear matter power spectrum at $z = 0$ for the 5 separate cosmologies explored here. These are also plotted in Fig. 2.6, shown in the

[7] https://bitbucket.org/ngenhalofitteam/

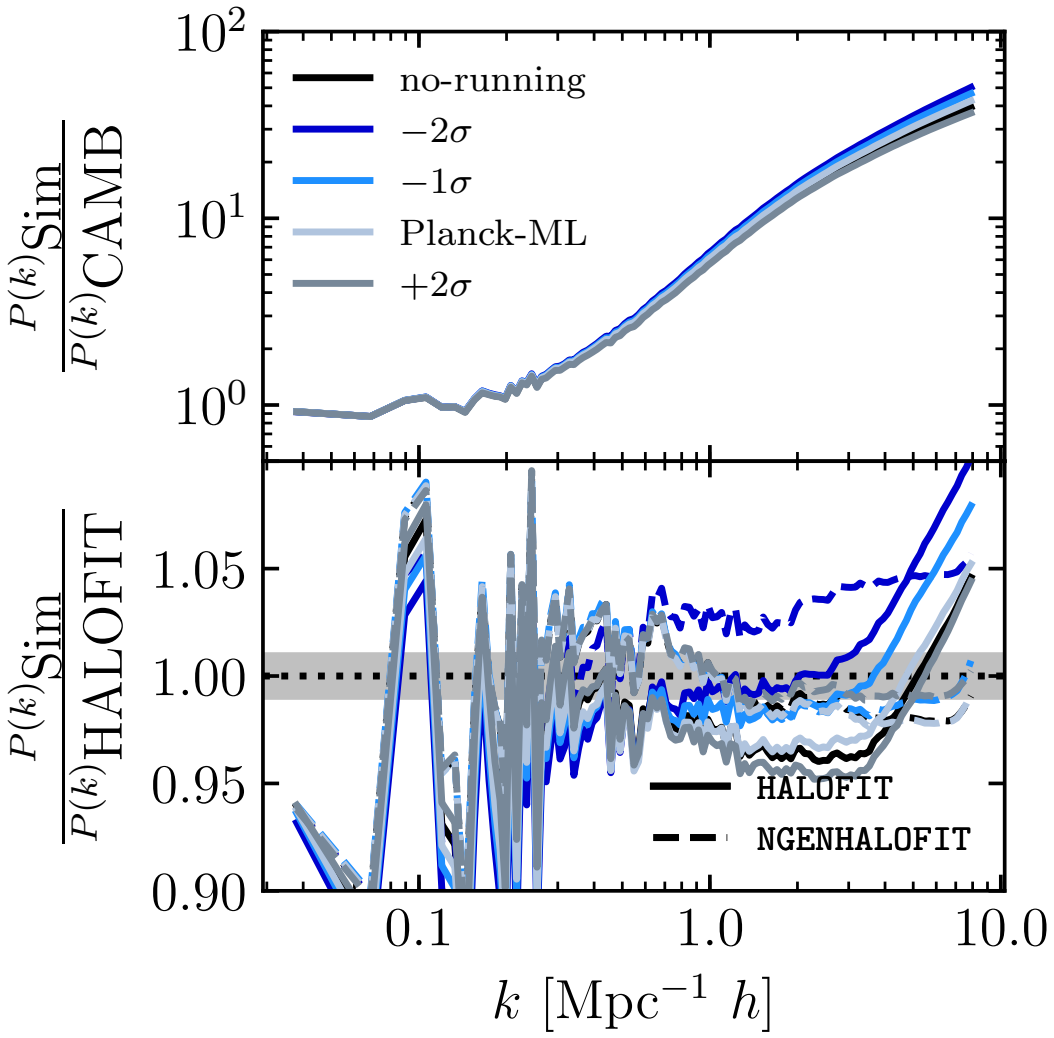

Figure 2.6: Top: the power spectrum output from the simulation at $z = 0$, normalised with respect to the CAMB result at this redshift. This demonstrates the non-linear growth of structure, which linear theory is not able to predict. Bottom: the power spectrum output from the simulation, normalised with respect to the HALOFIT non-linear prediction. A prominent feature present in both panels is the large fluctuations at low k which arise because the simulated volume does not sample these $k-$modes well, leading to increased numerical noise. Also shown is the non-linear power spectrum prediction from NGENHALOFIT (dashed line), which models the non-linear effects of a running scalar spectral index much better, except for the -2σ cosmology. This is highlighted by the shaded region centred on unity which represents a 1% accuracy region. It can be seen that almost all models lie within or just outside this shaded region up to $k \sim 5$ Mpc^{-1}h.

bottom plot as dashed lines. It can be seen that for 3 out of 4 of the different running models NGENHALOFIT does indeed do better at reproducing the non-linear matter power spectrum. There is still an offset for the -2σ cosmology, which may be due to this cosmology being more extreme compared to the running cosmologies sampled in Smith and Angulo (2019) ($\alpha_s = -0.01, 0.01$). Note, as mentioned in Section 2.2, all of the BAHAMAS simulations include a prescription for massive neutrinos. However, the power spectrum computed by GenPK in the collisionless simulations corresponds to the dark matter + baryons power spectrum (i.e. it does not have a massive neutrino component). As such, when taking the ratio, the corresponding statistic is used in the approximate result (i.e. the power spectra computed by HALOFIT/NGENHALOFIT).

2.3.2 Halo counts

Halo mass function

I now examine the effects of a $\Lambda\alpha_s$CDM cosmology on the HMF. The HMF is defined here as the number of haloes of mass, $M_{200,\mathrm{crit}}$, that exist per cubic comoving Mpc, per logarithmic mass interval: $\phi \equiv dn/d\log_{10}(M_{200,\mathrm{crit}})$. The masses of haloes used in this study, unless otherwise stated, represent the mass that is contained within a spherical overdensity whose radius encloses a mean density of 200 times that of the critical density of the Universe at that redshift. Note also that all distances used in this study are comoving, unless otherwise stated.

Haloes in this study are identified using the SUBFIND algorithm (Springel et al., 2001; Dolag et al., 2009) which first runs a standard friends-of-friends (FoF) algorithm on the dark matter distribution, linking all particles which have a separation less than 0.2 $\times$ the mean interparticle separation (Davis et al., 1985). This is used to return the spherical overdensity mass $M_{200,\mathrm{crit}}$. It then goes through FoF groups and identifies locally bound sub-structure within each group. The FoF group is centered on the position of the particle in the central subhalo that has the minimum gravitational potential.

The measured HMF for the various running simulations can be seen in Fig. 2.7. The

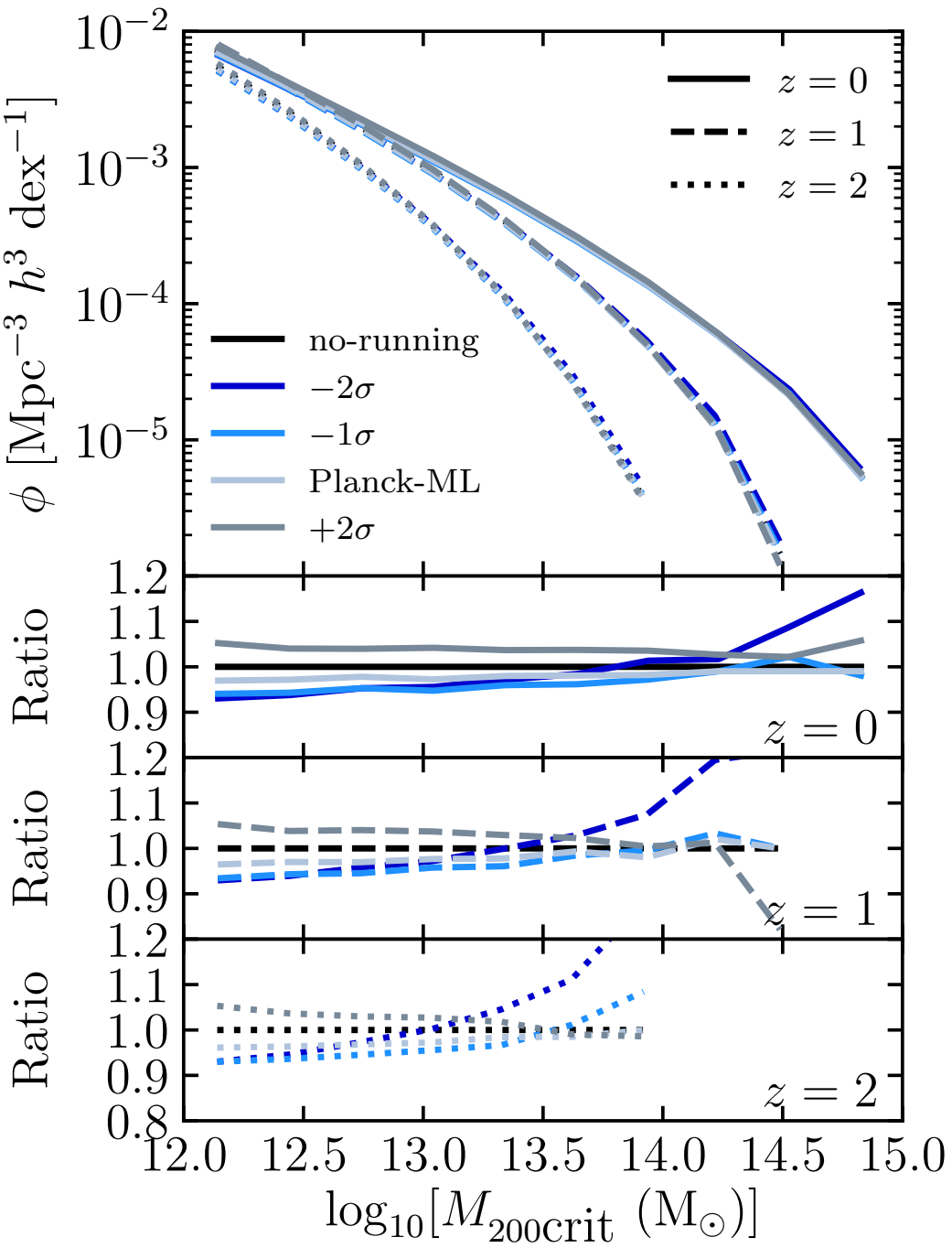

Figure 2.7: Top: Halo mass function (HMF) measured for the 5 separate running cosmologies. The colours here represent the different values for α_s, with the linestyles representing the measured HMF at a particular redshift. Bottom: The HMFs normalised with respect to the HMF measured in the no-running simulation. Here the effect due to a change in cosmology and the inclusion of running is evident. A cosmology with a negative running in general leads to fewer low-mass haloes, whereas a cosmology with a positive running leads to more low-mass haloes, with the magnitude of this effect being insensitive to redshift. However, a negative running cosmology predicts more high-mass haloes (at least in the case of the most negative running case), with this effect amplified at earlier redshifts.

inclusion of running in the simulation has a measureable effect, which is most obvious when looking at the bottom panel of Fig. 2.7. Here the HMF is normalised with respect to the measured HMF in the no-running simulation, and it can be seen that there is an almost 10% decrease (increase) for the most negative (positive) running cosmology in the number of lower mass haloes that exist in the simulation (10^{12} - 10^{13} $M_{\odot}$). A similar effect on the HMF in an N-body simulation was found by Garrison-Kimmel et al. (2014), who showed that the inclusion of a negative running reduced the number of haloes in their simulation at fixed low-mass. The effect on the HMF due to running depends strongly on the adopted value for α_s as expected, with a more negative value leading to the largest effect on the HMF. An interesting feature is the fact that the most negative running cosmology appears to predict more haloes that are of a higher mass (10^{14} - 10^{15} $M_{\odot}$), with this effect being stronger at earlier redshifts. This is likely because these mass scales correspond to the regions of the matter power spectrum where a negative running cosmology leads to an excess of power compared with the no-running model (see Fig. 2.2). Therefore, if the initial seed fluctuations which will grow into these massive haloes are amplified, these haloes will form earlier and will therefore be present at earlier times, compared with the no-running model.

To try to understand this a little better, it is more intuitive to look at the mass of a halo at fixed number density. The reason for this being that it is the halo masses that change, not their number density (i.e. it is a shift along the x-axis, not the y-axis), which leads to the changes seen in the HMF. For example, a halo which evolves from a peak in the density field to a $10^{15}M_{\odot}$ halo will have this density peak either diminished, or enhanced, depending on the value for α_s, and thus its final mass is sensitive to this effect.

To look at this, a matched set of haloes needs to be constructed. To match haloes one first needs a reference, and so all haloes in the no-running ($\alpha_s = 0$) dark matter only simulation are chosen as the reference haloes. For each halo in the reference simulation, a matched halo is found in the simulations with a non-zero value for α_s. Haloes are matched using the unique particle IDs of the dark matter particles assigned to them. Thus, for each dark matter particle assigned to a halo in the reference simulation, the

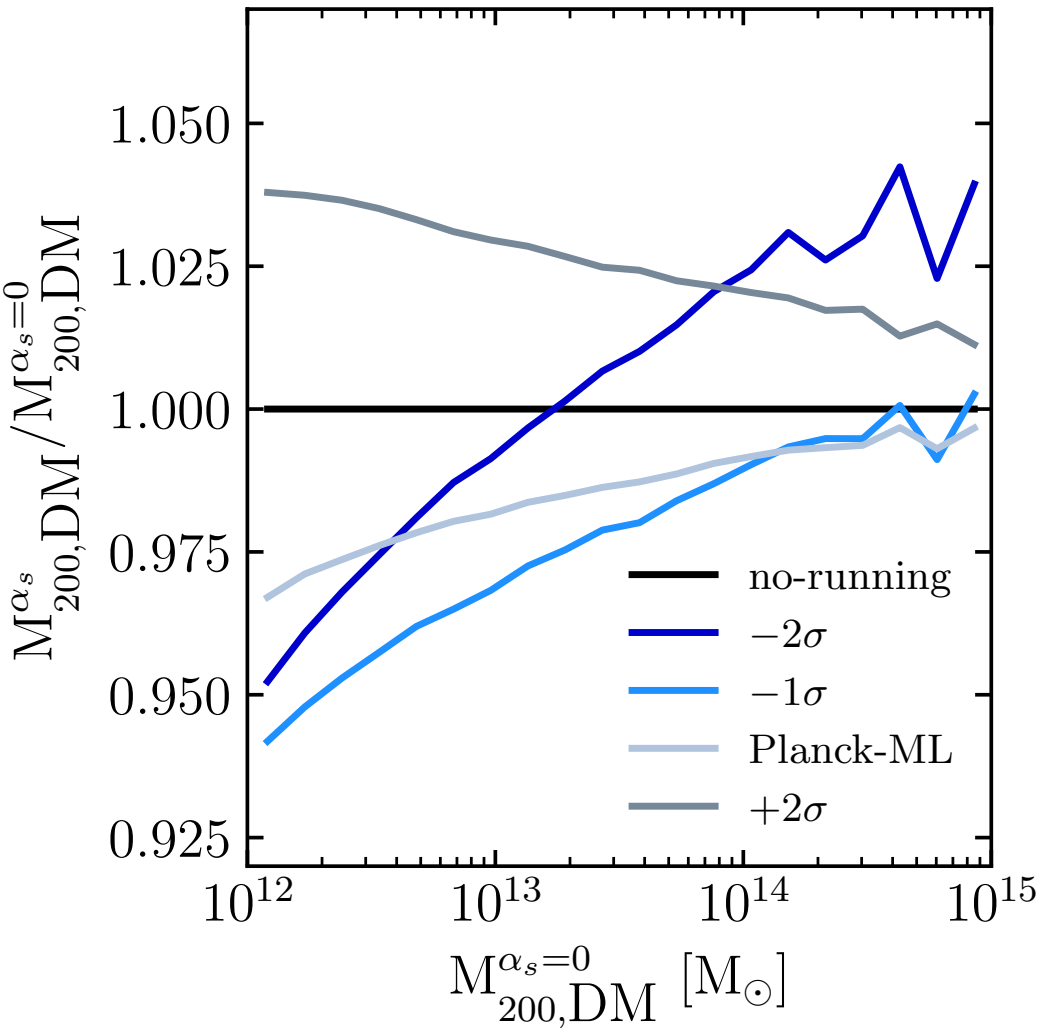

Figure 2.8: The fractional change in halo mass for a matched set of haloes across the 5 different cosmologies, indicated by colour. This plot illustrates the effect a running scalar spectral index has on a halo by halo basis. Here, a halo in a standard ΛCDM cosmology, would be more massive, if it were instead in a positive running cosmology. Likewise, if it were instead in a negative running cosmology, it could be either less massive or more massive, depending on the magnitude of the running, and the size of the halo. It is this effect on halo mass which drives the differences seen in the HMF.

particle with the matching ID in the other simulations is identified, along with what halo they belong to. The halo in each case which contained the largest fraction of identified particles[8] is selected as the matching halo in that simulation. Any halo for which a match could not be found across all 5 of the simulations was discarded from the analysis. Overall $> 99\%$ of all haloes in the mass range $10^{12} - 10^{15}\mathrm{M}_{\odot}$ in the dark matter-only reference simulation were matched across all other simulations.

The resultant fractional change in halo mass for the matched set of haloes as a function of halo mass in the dark matter only-reference simulation is shown in Fig. 2.8. The result is almost identical to the effect that is seen in the HMF. A cosmology with a positive running leads to more massive haloes across the entire mass range compared with the reference simulation. A cosmology with a negative running generally leads to a decrease in matched halo mass. This is however a mass-dependent effect, with the more massive haloes not being affected as much in the cosmologies with a negative running. In fact, for the most negative running cosmology the most massive haloes are somewhat more massive than their no-running counterparts. This is what leads to the excess of these haloes in the HMF compared with the standard cosmology. This plot is for haloes at redshift 0, however, I also looked into the fractional change in halo mass at redshifts 1 and 2. It was found that the effects present in the HMF are echoed here, in that at earlier redshifts, the effect on halo mass in the two most extreme cosmologies in this study is amplified (Fig. A.3).

Going forward, when using a matched set of haloes, I use the values of $M_{200,\mathrm{c}}$ and $R_{200,\mathrm{c}}$ for the matching halo in the reference no-running dark matter only simulation.

When comparing the effects on the HMF due to running, and those due to dynamical dark energy (Pfeifer et al., 2020), and massive neutrinos (Mummery et al., 2017), it is found that massive neutrinos have the largest effect. For example, for $\Sigma M_{\nu} = 0.24$ (0.48) eV, the number of massive haloes at fixed mass can be suppressed by nearly 20% (40%) at the present day. This is in comparison to allowing the running to be free but constrained by the CMB, which predicts either no suppression of the most massive

[8]Note: a minimum matching threshold is also set, so that a halo must contain at least 51% of the particles from the reference simulation's halo for it to be classified as the matching halo.

objects, or conversely an increase in their numbers. Dynamical dark energy behaves similarly to a running scalar spectral index, leading to an increase in the number of massive objects at fixed mass (although certain models can lead to a suppression by up to 20%). The effects from massive neutrinos also have the largest redshift dependence, with the effects due to running not varying much with redshift, and those due to dynamical dark energy having a slight redshift dependence, but not to the same extent.

Comoving halo number density

The HMF provides a measure of the number density of objects of a certain mass at a certain redshift. Another, similar quantity is the comoving halo number density $n(M, z)$ which is the integral of the HMF above a certain mass threshold, at a certain redshift. This is a useful quantity to look at, as it is closer to what is actually measured through observations. The effects that a $\Lambda\alpha_s$CDM cosmology on this quantity are shown in Fig. 2.9 for three separate mass thresholds of $10^{12}M_\odot$, $10^{13}M_\odot$ and $10^{14}M_\odot$. Due to the steep, negative slope of the HMF, the majority of counts which make up $n(> M)$ come from haloes closest to the mass cut. The bottom panel of Fig. 2.9 shows the measured halo number density normalised to the no-running result. It can be seen here that the effects of running are mass dependent, with a negative running cosmology predicting more massive objects at later redshifts compared with the reference cosmology, and a positive running cosmology predicting fewer of these massive haloes at later redshifts compared to the negative running and the no-running cosmology. This result can be understood again in terms of the effect running has on the overdensities in the initial conditions. As seen, although a negative running suppresses overdensities on small and large scales, there is a region of the power spectrum which is enhanced in a best-fit cosmology, with a negative running of the spectral index (due to the simultaneous increase in A_s). Thus, these enhanced density perturbations are larger at earlier times than in the reference cosmology, or in a positive running cosmology (which has density perturbations smoothed out on these scales and sees a reduction in power). As a result, more of these high-mass systems form at earlier times, and because one is looking at rarer systems as the mass threshold is increased,

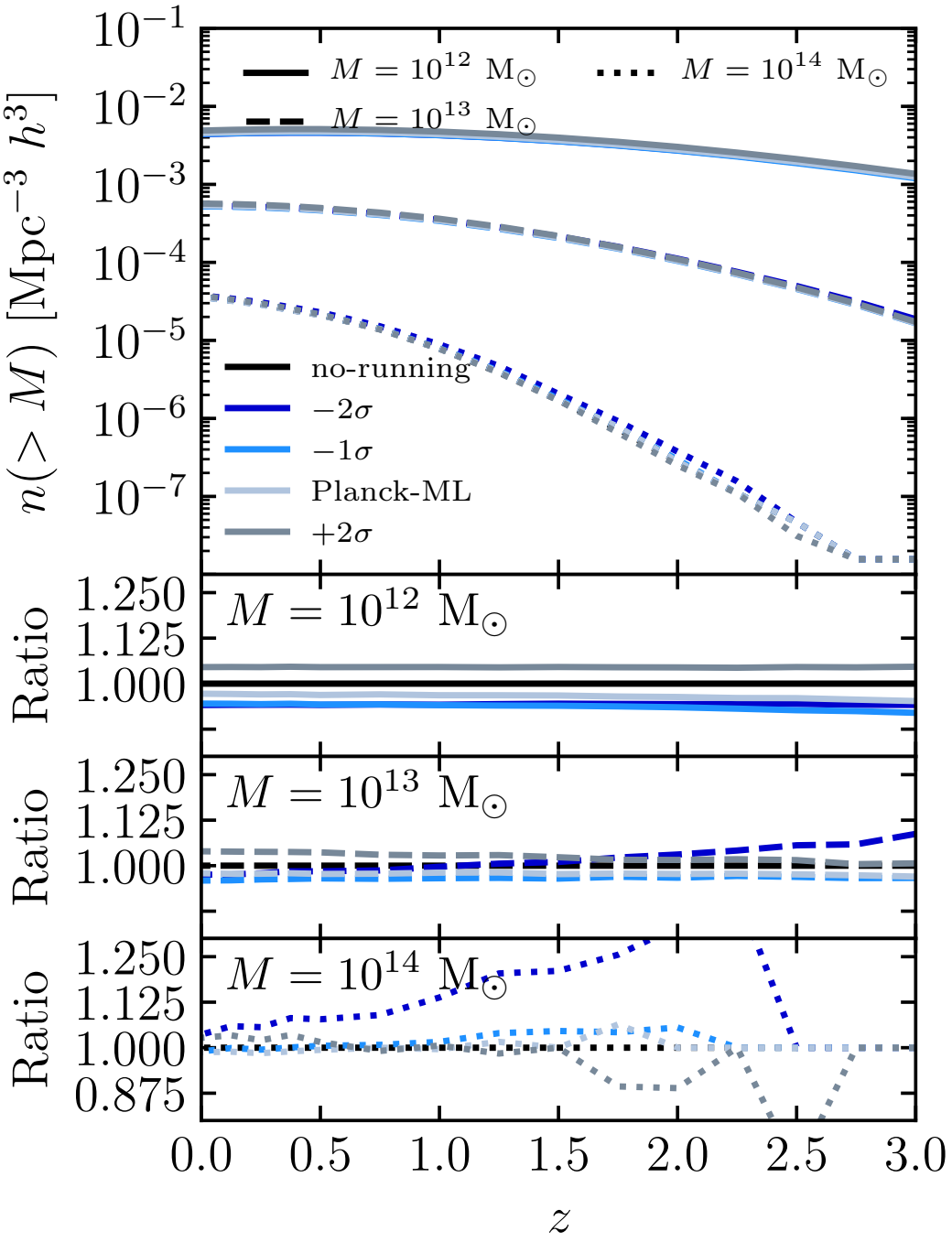

Figure 2.9: Top: redshift evolution of the comoving halo number density, for haloes above three separate mass thresholds. The different linestyles in this plot correspond to the different mass thresholds investigated in this study. Bottom: the comoving halo number density normalised with respect to the no-running model. The effect that a $\Lambda\alpha_s$CDM cosmology has on this quantity is mass and redshift dependent, with for example, the most negative running cosmology having fewer haloes above $10^{12}M_\odot$ at all redshifts, but more haloes above $10^{14}M_\odot$. This result is amplified with increasing redshift. The opposite holds for the positive running cosmology: more haloes above $10^{12}M_\odot$ but fewer below $10^{14}M_\odot$.

the overall number of objects that exist at early times is small so the relative increase can be quite large.

2.3.3 Clustering of haloes

Having looked at the effects that including α_s in the cosmological model has on the mass of dark matter haloes, it is interesting to see how it affects the haloes' spatial distribution. In particular, I look at how running affects the 3D two-point autocorrelation function (Davis and Peebles 1983) of haloes.

The correlation function of matter is related to the power spectrum through the Fourier transform, and dark matter haloes are related to the clustering of matter via a prescription for the halo bias (see Desjacques et al., 2018, for a recent review). Thus, it can be expected based on the analysis of the matter power spectrum that a $\Lambda\alpha_s$CDM cosmology should have some effect on the spatial distribution of haloes. In this study I compute the autocorrelation function $\xi(r)$ of FoF groups as the excess probability, compared with a random distribution, of finding another FoF group at some particular comoving distance r:

$$\xi(r) = \frac{DD(r)}{RR(r)} - 1, \tag{2.3}$$

where $DD(r)$ and $RR(r)$ are the number of pairs of haloes found at a radial distance r in the simulation and the number of haloes expected for a random distribution, respectively. $RR(r)$ is computed analytically, by assuming that haloes are distributed homogeneously throughout the simulation volume with a density equal to the mean number density of haloes. Furthermore, I compute the correlation function for haloes in specific mass bins, so the mean density of haloes is taken to be the mean density of haloes in a particular mass range. To compute $\xi(r)$, I use 20 logarithmically spaced radial bins between 0.1 and 100 comoving Mpc h^{-1}.

The effect that a $\Lambda\alpha_s$CDM cosmology has on the calculated two-point autocorrelation function of haloes in the three separate mass bins is shown in Fig. 2.10. It can be seen

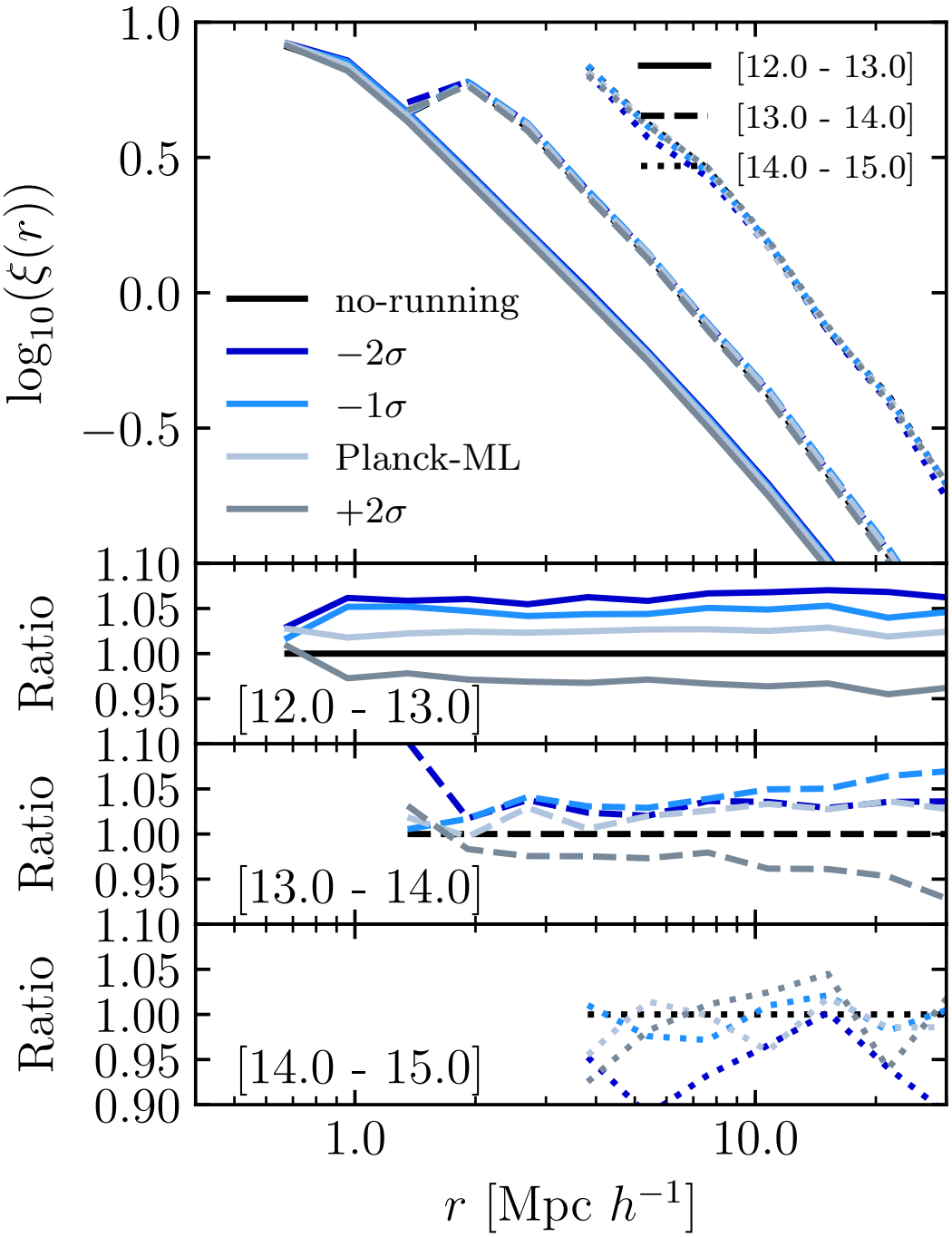

Figure 2.10: Top: the effect a $\Lambda\alpha_s$CDM cosmology has on the 3D two-point halo autocorrelation function, $\xi(r)$. The clustering signal is measured in 3 separate halo mass bins which are indicated by the different line styles. The mass range is shown in the bottom panel and is quoted in units of $\log_{10}(M/\mathrm{M}_\odot)$. Bottom: the correlation function for the different running cosmologies normalised with respect to the no-running model. The introduction of running has a measureable effect on the clustering signal of haloes in the simulation, with the effect depending strongly on mass. For example, the -2σ cosmology results in a near 10% increase in the clustering signal of haloes in the mass range $10^{12} - 10^{13}\mathrm{M}_\odot$, but a near 5% decrease for haloes in the mass range $10^{14} - 10^{15}\mathrm{M}_\odot$.

that the effect depends on halo mass, with the effects most clearly represented in the bottom panel(s) where the measured correlation functions are normalised to the no-running cosmology. Looking at the most negative running cosmology as an example (as this shows the largest effects), for the lowest mass bin of $10^{12} - 10^{13}$ $M_{\odot}$ there is an overall increase in the amplitude of the correlation function, with the most negative running cosmology predicting an increase of $\approx 10\%$. Whereas for the largest mass bin ($10^{14} - 10^{15}$ $M_{\odot}$) the most negative running cosmology leads to a very mild decrease in the clustering amplitude, with this being around a 5% decrease. This makes sense when looking at the HMF, or the comoving halo space density, which showed that a negative running cosmology led to an increase in the number of haloes in this higher mass bin, and therefore one can expect them to be a less biased tracer of the underlying matter distribution, which as a result will lead to a lower clustering signal compared to the no-running cosmology's result. This result agrees with that predicted by Fedeli et al. (2010), who showed that in a negative running cosmology dark matter haloes in the cluster regime are less biased compared with the standard model (see figure 10 in Fedeli et al. 2010). The other two negative running cosmologies see a similar trend, but not to the same level. Conversely, the positive running cosmology shows the inverse effect, with the clustering amplitude being lower for the lowest mass bin, but slightly increasing as the mass range is increased (although it is still lower, or at the same level, as the no-running model). This again makes sense as the number of objects in the higher mass ranges tends towards the no-running simulation's result (see Fig. 2.7).

Another feature which is present in Fig. 2.10 is the downturn in the clustering signal, which occurs at around 0.7, 2, and 4 Mpc h^{-1} for haloes in the mass range: $10^{12} - 10^{13}$ $M_{\odot}$; $10^{13} - 10^{14}$ $M_{\odot}$; $10^{14} - 10^{15}$ $M_{\odot}$ respectively. This downturn is present as these scales correspond to the radius of the FoF haloes in the respective mass bins. On scales smaller than this, FoF haloes overlap and would not be distinguished as separate haloes and so one cannot measure a clustering signal.

So far I examined the clustering signal measured with haloes being placed in mass bins depending on their self-consistent masses, i.e. the mass they have in their own simulation. However, since running changes the mass of a halo (Fig. 2.8), it is inter-

esting to look at the effect it has on the distribution of matched haloes, i.e. for haloes of a constant number density. The reason being that the clustering signal is bound to be different simply because one is looking at a different set of haloes. This is done by putting haloes in mass bins based on their no-running cosmology counterpart. The result on the clustering signal when binning haloes this way is qualitatively the same as that shown in Fig. 2.10. Again, in this case a negative running cosmology leads to an increase in the clustering signal of low mass haloes, and a positive running cosmology leads to a decrease, with this effect being mass dependent. The magnitude of this effect also does not change much, with the effect being slightly less in the highest mass bin for the -2σ cosmology, but otherwise almost unchanged for the different running models in each mass bin. For brevity I do not show this here.

As a final comparison with the other extensions to ΛCDM examined in the BAHAMAS project, Mummery et al. (2017) found that the most massive summed neutrino mass cosmology leads to a suppression of the large-scale clustering signal of around 10%, with all non-zero neutrino masses investigated leading to some level of suppression of the clustering signal. Conversely, and similar to what is found in the present study, dynamical dark energy can lead to both a suppression and amplification of the clustering signal, depending on the model. It is also found when comparing the three separate studies that the clustering signal of the largest haloes in the simulations are much less sensitive to the cosmology than the lower-mass haloes.

2.4 Internal Structure of Haloes

Having investigated the effect a running spectral index has on the LSS in the universe, including the abundance of haloes and how they are distributed, I now turn my focus to the internal structure of the haloes themselves. To look into this I use two statistics in particular: the spherically-averaged density profiles of haloes, alongside the halo concentration-mass relation.

2.4.1 Total mass density profiles

To start, I look at the effect on the spherically-averaged total mass density profiles, shown in Fig. 2.11. Each panel shows the median density profile of all haloes in that mass bin (indicated in the top right hand corner of the plot), with the mass bins ranging from $12.0 \leq \log_{10}(M_{200,\mathrm{c}}/\mathrm{M}_{\odot}) \leq 15.0$, each with a width of 0.5 dex. In order to reduce the dynamic range of the plot, I scale the mass density by r^2, i.e., so that an isothermal distribution would be a horizontal line. I plot the density profiles in dimensionless units. The bottom plot for each panel shows the density profiles normalised to the median density profile of that mass bin, as measured in the reference no-running simulation.

As mentioned when looking at the two-point autocorrelation function in bins of halo mass, if the haloes are binned according to their self-consistent masses, i.e., the mass they have in their own simulation, this will result in looking at a slightly different population of haloes in each bin across the different simulations. Instead, the panels in Fig. 2.11 show the median density profile of matched haloes in mass bins corresponding to the masses of haloes in the reference, no-running simulation. Similarly, the values of $R_{200,\mathrm{c}}$ used in this statistic are those corresponding to the haloes in the reference simulations. This is done as I want to isolate the effects a running scalar spectral index has on a given set of haloes.

It can be seen from Fig. 2.11 that the qualitative effect on the density profiles of haloes in a $\Lambda\alpha_s$CDM cosmology is to either raise or lower the overall amplitude of the density profile, depending on the sign of the running and the mass of the object. For example, haloes in the lowest mass bin have the amplitude of their density profile decreased in a cosmology which has a negative running and increased in one which as a positive running. Whereas for haloes in the highest mass bin, almost all cosmologies, regardless of the sign of the running, see an increase in the amplitude of the density profiles. There is also a hint that a running in this mass range leads to a change in the shape of the density profile, with the central regions being more dense in a cosmology that has a running spectral index. This trend of a change in amplitude makes sense when

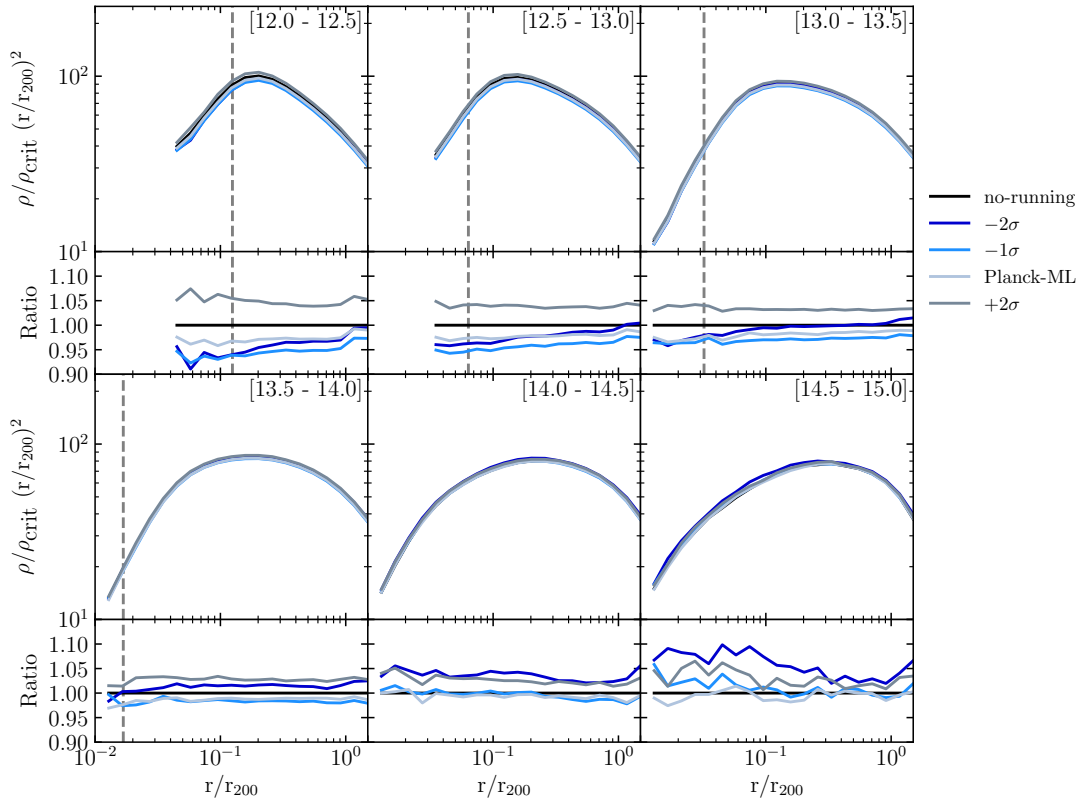

Figure 2.11: Median total mass density profiles of all haloes in each simulation, split into 6 separate mass bins, as indicated in the top right corner of each panel. Haloes are binned according to their mass in the reference no-running cosmology. The halo density profiles are plotted in dimensionless units, normalised by the critical density, and re-scaled so that an isothermal distribution would be a horizontal line. Note, that the profiles are plotted as a function of r/r_{200} also, where r_{200} in this case is taken from the reference simulation. The bottom part of each panel corresponds to the density profiles normalised to that measured in the reference simulation. The vertical dashed line shows the convergence radius (discussed in Section 2.4.2), and shows the point beyond which the density profiles are converged. The overall effect that a $\Lambda\alpha_s$CDM cosmology has on the density profile of a halo is to either raise or lower its amplitude, without much of an effect on the shape of the profile, although this depends both on mass and on the sign of the running.

looking at Fig. 2.8, which showed that for a matched set of haloes a negative running cosmology leads to a decrease in mass for lower-mass haloes but an increase in mass (dependent on the magnitude of α_s) for larger-mass haloes. Conversely, a positive running cosmology led to an increase in mass for all mass ranges. Also plotted in Fig. 2.11, shown by the grey-dashed line, is the maximum convergence radius of haloes in each respective mass bin (the convergence radius is discussed in Section 2.4.2).

2.4.2 Concentration-mass relation

It has been shown through cosmological simulations that the internal structure of dark matter haloes retain a memory of the conditions of the Universe at the time they were formed, with the formation time of a halo being typically defined as the time when the halo obtains some fraction of its final mass. For example, Navarro et al. (1996) showed that lower-mass haloes have a higher central concentration than high-mass ones, which they note is as expected given that lower-mass haloes tend to collapse at a higher redshift when the mean density of the Universe was higher. This is a result which has now been confirmed through many N-body simulations, in many different ways (see for example Child et al., 2018, and references therein), with many now relating this result to the mass accretion history (MAH) of a halo (e.g. Zhao et al., 2003; Correa et al., 2015a; Ludlow et al., 2016; Child et al., 2018). The MAH represents the increase in mass of the main progenitor of a halo, with lower mass systems accreting more of their mass at earlier times, while larger haloes assemble most of their mass at later times, when the mean density of the Universe has decreased.

During their hierarchical growth, dark matter haloes have been found to acquire an approximately universal shape described by the Navarro, Frenk & White density profile (NFW) (Navarro et al. 1996), which takes the form of:

$$\rho(r) = \frac{\delta_c \rho_c}{\frac{r}{r_s}\left[1 + \frac{r}{r_s}\right]^2}, \tag{2.4}$$

where r is the radius, δ_c is an overdensity parameter, ρ_c is the critical density of the

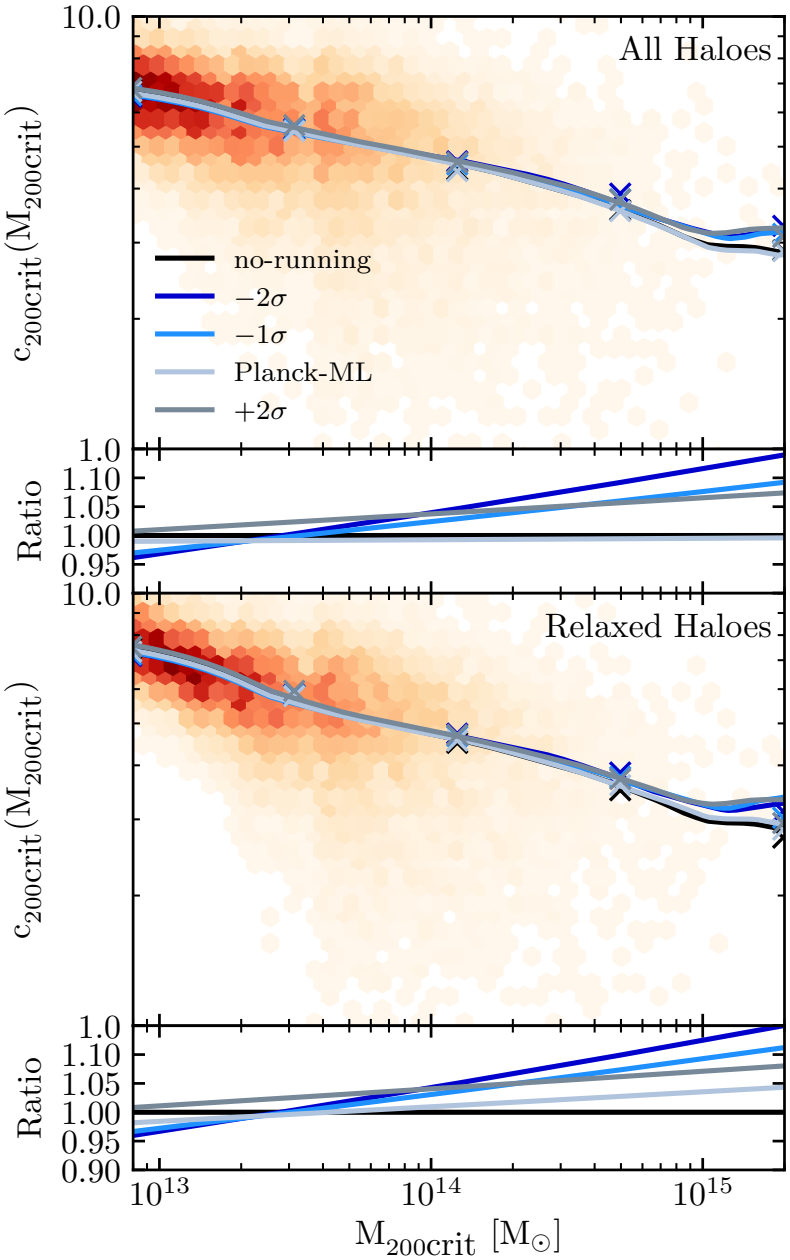

Figure 2.12: The best-fit c-M relation for all 5 cosmologies simulated. The solid curves represent the running median of the concentrations measured in the 5 separate cosmologies, coloured by their values for α_s. The shaded regions represent the scatter that is present in the reference simulation, with the intensity of the colour indicating the number density of haloes in this region. The crosses represent the best fit to the data assuming a power-law relationship. The top half of this plot shows the median c-M relation for all haloes in the simulation above the threshold mass of $10^{12.8} M_\odot$, with the lower subplot showing the Equation 2.5 fit normalised with respect to the result obtained in the standard model case. The bottom half of the plot shows the same when only relaxed haloes are included. The inclusion of a running spectral index as a an additional free parameter in the standard model tends to lower the concentration of low-mass haloes, but increase the concentration of high-mass haloes. Making a cut on relaxed haloes reduces the scatter in concentration at fixed mass, however the general result due to a $\Lambda\alpha_s$CDM cosmology is maintained.

Universe and r_s is the scale radius, corresponding to the radius at which the logarithmic slope of the density profile is -2 (i.e., equal to that of an isothermal distribution). This profile can equivalently be parameterized with the halo mass M and the halo concentration c, which is defined as the ratio of the radius enclosing a spherical overdensity Δ times the critical density, which in this study I take as 200 times the critical density of the universe, and the scale radius: $c_{200,\mathrm{c}} \equiv R_{200,\mathrm{c}}/R_s$. A result of this is that, if one has a prescription for the concentration-mass (c-M) relation, one can fully specify the internal structure of a DM halo at a fixed mass.

In order to measure the concentration of a halo, I derive an estimate for the scale radius by fitting an NFW profile to each halo in the sample. However, haloes are dynamically evolving objects, meaning that when taking these measurements there is the potential that some haloes are not in virial equilibrium and not well described by an NFW profile. It has been shown in previous studies that haloes which are not in dynamic equilibrium tend to have lower central densities compared with relaxed haloes (e.g. see Tormen et al., 1997; Macciò et al., 2007; Romano-Díaz et al., 2007). Thus, in order to limit this effect, a simple relaxation test was implemented as proposed by Neto et al. (2007). This deems any halo whose barycentre is offset from the centre of potential by more than $0.07R_{200,\mathrm{c}}$ to be unrelaxed and excluded from the relaxed halo sample. Note that Neto et al. (2007) proposed two further checks on if a halo is relaxed or not, however the test implemented in this current study was shown by Neto et al. (2007) to remove the vast majority of unrelaxed haloes, as such, similar to what was done in Duffy et al. (2008) I only use this criterion to remove unrelaxed haloes. The centre of mass of a halo is calculated using all of the particles inside $R_{200,\mathrm{c}}$ of the halo, and is calculated using the iterative shrinking spheres algorithm (Power et al. 2003). Another selection criterion I apply to the halo sample is that they must have a minimum of 5000 particles inside $R_{200,\mathrm{c}}$. However, due to the relatively low resolution of these simulations, I extend the mass range of the halo samples by stacking haloes that have between $800 \leq N_{200,\mathrm{c}} < 5000$ particles, so that the stacked halo has the minimum number of particles required. This allows us to plot the c-M relation down to haloes of mass $10^{12.8} M_{\odot}$. One final cut on haloes is performed after the NFW profile is fit

to the haloes, which sees any halo which has an inferred convergence radius (defined below) < 6 times the gravitational softening length ϵ removed from the halo sample. This is quite a conservative cut and follows Diemer and Kravtsov (2015), who note it was shown that halo density profiles are converged at radii beyond 4-5 $\times$ ϵ (Klypin et al., 2000).

When fitting an NFW profile to haloes, the radial range used is between $0.1 \leq r/R_{200,\mathrm{c}} \leq 1.0$ and is divided into 20 logarithmically spaced bins. However, as a result this can lead to the innermost bins being dominated by numerical noise, and two-body scattering effects, due to poor particle sampling of these innermost radial bins. This is studied in detail in Power et al. (2003). In this study they showed that there is a critical radius below which the density profile of a halo measured in an N-body simulation is not converged (their equation 20, which is satisfied when the collisional relaxation time is roughly the age of the Universe). Thus, when it comes to fitting an NFW profile to a halo in this study, I only fit to radial bins which lie above the convergence radius. Note that I fit to the quantity: ρr^2 as done in several previous studies (e.g. see Neto et al. 2007). Note also that, most recently Ludlow et al. (2019) conducted a convergence study on numerical results from an N-body simulation (such as the shapes of haloes) using haloes simulated inside a cosmological volume, in contrast to the Power et al. (2003) study where they only simulated the convergence of results for a single halo. Ludlow et al. (2019) also provide a convergence criterion, which I tested to see if this resulted in any differences in the computed c-M relation, which it did not. As such, I use the Power et al. (2003) convergence radius when calculating the c-M relation.

The resultant effect a running spectral index has on the c-M relation is shown in Fig. 2.12. Here the solid line represents the running median of the concentration, which I calculate using the locally-weighted scatterplot smoothing-method (LOWESS; see Cleveland 1979). The top panel shows the recovered c-M relation for all haloes in the sample, the bottom panel shows the recovered relation when only using relaxed haloes.

Previous studies have shown that the c-M relation for dark matter only haloes at $z = 0$

is well fitted with a simple power-law (e.g. Bullock et al. 2001) of the form:

$$c_{\Delta} = A \left(\frac{M_{\Delta}}{M_{\rm Fiducial}} \right)^{B}, \tag{2.5}$$

where I adopt $M_{\rm Fiducial} = 10^{14}{\rm M}_{\odot}$. Equation 2.5 is fit to the data, and shown in Fig. 2.12 as crosses. Overall, a power-law form is able to describe the c-M relation well. The bottom panel shown below each main plot shows the result of this fit normalised with respect to the no-running simulation. Also shown by the shaded regions is the overall scatter of the c-M relation at fixed mass, shown just for the no-running cosmology. As expected, the scatter is reduced at fixed mass when making a cut on relaxed haloes. Looking at the bottom panels it can be seen that there is an overall trend for a $\Lambda\alpha_s$CDM cosmology to produce lower concentrations in low-mass haloes ($M \leq 2\times10^{13}{\rm M}_{\odot}$), and larger concentrations in high-mass haloes ($M \geq 2\times10^{13}{\rm M}_{\odot}$), although the effect is not as large at low masses as it is at high masses.

A qualitatively similar result was found by Fedeli et al. (2010), who showed using semi-analytic methods that the concentration of low-mass haloes in a negative running cosmology is lower than in the standard ΛCDM model. They also showed that to a small extent this effect was reversed at the high-mass end, with these objects being slightly more concentrated. The reason for this may be attributable to formation time. As mentioned, it has been shown that haloes which formed at earlier times have higher concentrations. It has also been shown through the effect on the matter power spectrum that the original overdensities of these high-mass haloes are amplified in cosmologies which have a negative running spectral index. As a result, these haloes will have formed earlier on, and thus formed when the universe had a larger mean density, and so compared to the no-running cosmology these objects are centrally denser. The fact that the differences seen in concentration at low-masses in the different cosmologies is not as large, compared with that seen at higher masses ($M \approx 10^{15}{\rm M}_{\odot}$), may reflect the fact that because these objects form at even earlier times, their concentrations are less sensitive to their relative formation times.

2.5 Separability of Baryonic Effects

I now turn my attention to how separable the effects of allowing the running to be free are from the inclusion of baryonic physics in the simulations. That is, I explore whether the effects of baryons on LSS are dependent on the choice of running cosmology (and vice-versa).

The BAHAMAS suite of hydrodynamic simulations are a first attempt at explicitly calibrating the feedback in large-volume cosmological hydrodynamic simulations aiming to quantify the impact of baryon physics on cosmological studies using LSS. It is important, however, to check to what extent this calibration is dependent on the cosmology adopted in the simulation. The reason being that, if the calibration of the simulations depended significantly upon cosmology, one would have to re-adjust the feedback parameters for each cosmological model simulated. Thus, for this reason, the baryonic processes in BAHAMAS were calibrated on internal halo properties (specifically the stellar and baryon fraction of haloes), as opposed to the abundance of haloes or the power spectrum of density fluctuations (for more details see McCarthy et al. 2017 for the calibration method). The benefit of this being that the internal properties of haloes ought to be less sensitive to cosmology.

With this in mind, I explicitly verified that the stellar and gaseous properties of haloes in the simulations (particularly the galaxy stellar mass function and the gas fractions of groups and clusters) are insensitive to the variations in cosmology presented here. Thus, no aspect of the subgrid physics, feedback or otherwise, was changed from that presented in McCarthy et al. (2017).

Previous simulation work has shown that the various physical processes which are involved in galaxy formation and included in modern hydrodynamic simulations as subgrid physics, are capable of affecting the underlying distribution of dark matter. For example, it has been shown that the total matter power spectrum (e.g. van Daalen et al. 2011; Schneider and Teyssier 2015) and the halo mass function (e.g. Sawala et al. 2013; Cui et al. 2014; Velliscig et al. 2014; Cusworth et al. 2014; Schaller et al. 2015) along with the binding energies of haloes (Davies et al., 2019), can be affected

by a non-negligible amount compared with a dark matter only simulation, through the inclusion of feedback mechanisms. In addition, this study demonstrates that allowing the running to be free can also have a near 10% level effect on the total matter power spectrum at $z = 0$ and the halo mass function. Hence, an interesting and important question is: how separable are these effects? Can they be treated independently of one another, or do they work to amplify or perhaps suppress certain effects.

To answer this question, we separate the effects into two multiplicative factors: an effect due to the change in cosmology (free-running) and an effect due to baryonic physics. This results in the simple ansatz shown below, which is employed when trying to reproduce an observed quantity measured in the full hydrodynamic simulation:

$$\psi_{\text{mult}} = \psi^{\text{DM}}_{\alpha_s=0} \left(\frac{\psi^{\text{DM}}_{\alpha_s}}{\psi^{\text{DM}}_{\alpha_s=0}} \right) \left(\frac{\psi^{\text{H}}_{\alpha_s=0}}{\psi^{\text{DM}}_{\alpha_s=0}} \right), \tag{2.6}$$

where ψ represents the quantity that is being measured, for example the halo mass function or the matter power spectrum, with ψ_{mult} being the multiplicative prediction made from treating the two effects separately; ψ^{DM} and ψ^{H} represent the quantity measured in the dark matter only, or the full hydrodynamic simulation respectively; $\psi_{\alpha_s=0}$ and ψ_{α_s} represent the values measured in the simulation which has zero running and a running equal to α_s, respectively. This equation can be split up into two main parts: one which accounts for the effects due to the change in cosmology (free-running), accounted for by the first bracketed quantity in Equation 2.6; and one which accounts for effects due to baryonic physics, such as AGN feedback, accounted for by the second bracketed term.

All of the statistics examined in previous sections for the dark matter only simulation were treated with this simple ansatz, to see if the result obtained in the full hydrodynamic simulation could be recovered. However for brevity, I focus my attention on 4 main statistics: the total matter power spectrum, the halo mass function, the two-point halo autocorrelation function, and the density profiles of haloes.

2.5.1 Matter power spectrum

To begin, I go back to the total matter power spectrum of the simulations. As described previously (Section 2.3.1), the power spectrum is computed using the algorithm `GenPK` which computes the power spectrum of a simulation snapshot for each individual particle species. As a result, one first needs to combine the individual matter power components of each particle species to compute a total matter power spectrum. The resulting total matter power spectrum for the hydrodynamic simulations can be seen in the top panel of Fig. 2.13. Here the lines represent the total matter power spectrum measured for 3 different redshifts: $z = 0, 1, 2$. The crosses indicate the recovered result when using Equation 2.6 (note, here $\psi = P(k)$) to try to reproduce the result from simultaneously simulating baryonic physics and a running scalar spectral index by treating the effects separately. The bottom panel(s) of this figure show that over the entire $k-$range examined here, the total matter power spectrum for redshifts out to at least $z = 2$ can be reproduced to $< 2\%$ by treating these effects separately. On $k-$scales below 3.0 Mpc^{-1}h, the result is even more accurate, with the matter power spectrum being reproduced to sub-percent accuracy. This is better than the accuracy required for the likes of LSST (e.g. Huterer and Takada, 2005; Hearin et al., 2012).

2.5.2 Halo mass function

Next, I look at the HMF, which is shown in Fig. 2.14. The HMF as measured for the 5 separate cosmologies in the full hydro simulation is shown by the different lines and is plotted for redshifts: $z = 0, 1, 2$. I use Equation 2.6 (where $\psi \equiv \phi$ in this case) to test how separable the effects on the HMF due to the inclusion of baryonic physics and a running scalar spectral index are. The resultant multiplicative prediction is shown as crosses in Fig. 2.14. The bottom panel(s) of this figure shows the ratio for each cosmology of the measured result from the hydro simulation, i.e. treating both a running scalar spectral index and baryonic physics at the same time, to the predicted result from the multiplicative prescription treating each effect separately. It can be seen that for all redshifts examined here, the HMF can be reproduced with this simple

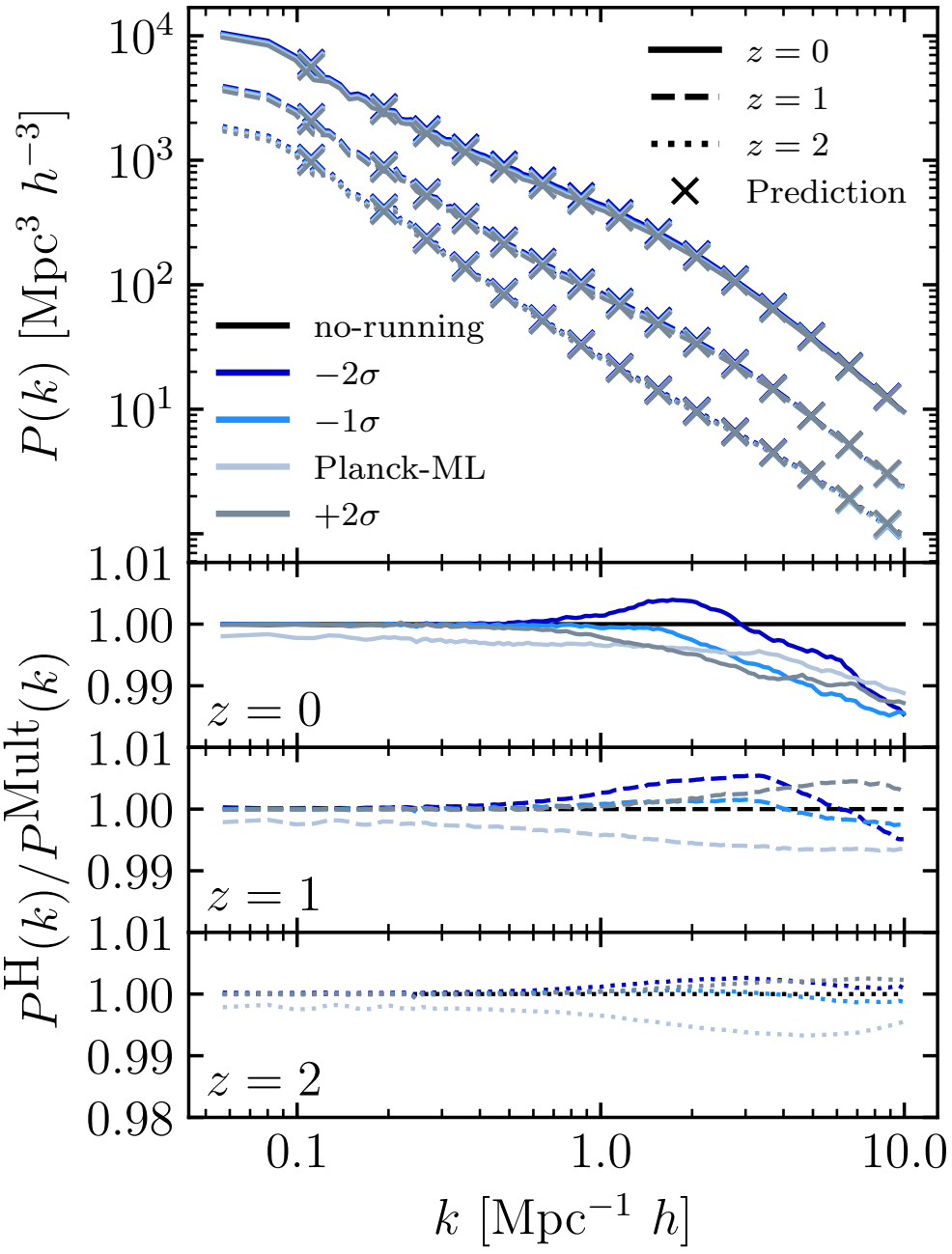

Figure 2.13: Test of the separability of the effects that a running scalar spectral index and baryonic physics have on the total matter power spectrum. Top: The total matter power spectrum for the 5 cosmologies. Here lines represent the result obtained from the simulations, with linestyle representing the different redshifts at which the total matter power spectrum was measured. The crosses represent the result obtained from treating the effects due to a running spectral index and the effects due to baryonic physics on the total matter power spectrum separately. Bottom: the ratio of the self-consistent result measured from the hydro simulation and the result obtained from treating the effects separately. Treating each effect as a simple multiplicative correction, reproduces the total matter power spectrum on all $k-$scales examined here to better than 2%.

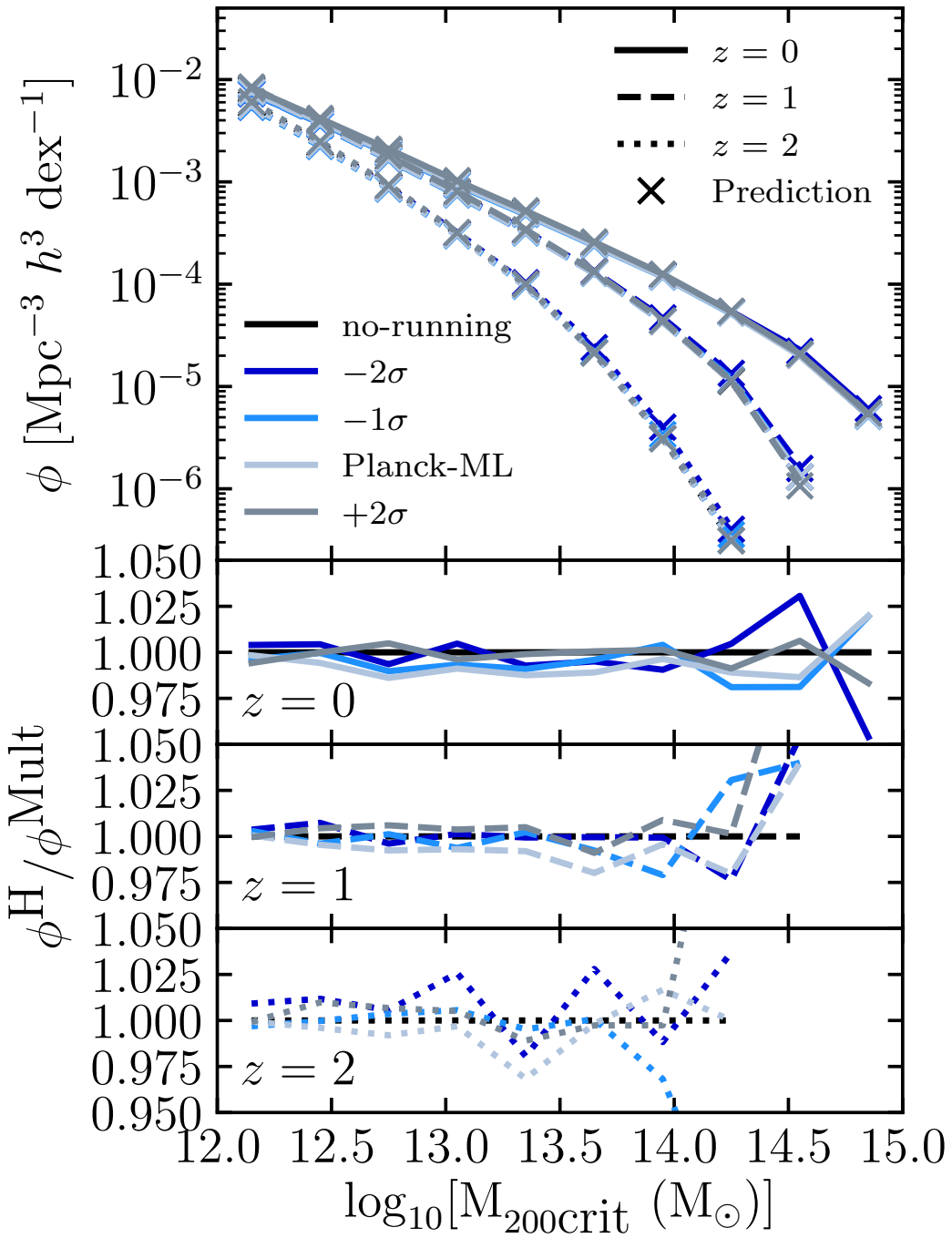

Figure 2.14: Test of the separability of the effects of inclusion of baryonic physics and a running scalar spectral index on the halo mass function measured in a full hydrodynamic simulation. Top: the HMFs measured when simulating both a running spectral index and baryonic physics, with the different linestyles indicating the HMFs measured at different redshifts. The crosses represent the HMF recovered when treating the effects separately. Bottom: the ratio of the measured HMF from the simulation to that predicted using the multiplicative prescription (Equation 2.6). Treating each effect as a multiplicative correction is able to reproduce the measured HMF to better than $\approx 3\%$ up to $z = 2$.

ansatz to within better than $\approx 3\%$ over the full range of halo masses examined in this study, up to $z = 2$, with an even better accuracy for lower redshifts.

As a separate test, I look at how separable these effects are on the mass of a halo, with baryonic physics known to reduce the mass of a dark matter halo in the mass range examined in this study (e.g. Sawala et al., 2013; Cui et al., 2014; Velliscig et al., 2014; Schaller et al., 2015), and having seen here that a running spectral index can also have a significant effect on halo mass.

The result is shown in Fig. 2.15. The top panel shows the effect baryonic physics has on halo mass, for different values of the running scalar spectral index, i.e. it shows, for a fixed value of α_s, the ratio of masses of a matched set of haloes in the hydrodynamic and dark matter only simulations. The result shown is the median ratio in bins of halo mass. This shows that, to an accuracy of $\approx 1\%$, the effect on halo mass due to baryonic physics is independent of the change in cosmology. Also shown in the bottom panel of this figure, is the effect that a running scalar spectral index has on halo mass in the BAHAMAS calibrated feedback model normalised to the corresponding result from the dark matter only simulations. This allows us to test how sensitive the effect a running scalar spectral index has on halo mass is to different physics models. It can be seen again here, for almost the entire range in mass, the effect due to a running scalar spectral index is nearly independent of the baryonic physics. Poor statistics are likely responsible for the larger deviations at high masses, whereas the small deviation at the lowest masses is likely a resolution effect (note that the different cosmologies have slightly different particle masses, due to the different values of $\Omega_{\rm m}$ and H_0).

2.5.3 Clustering of haloes

The separability of the effects due to baryonic physics and allowing the scalar spectral index to be free on the two-point autocorrelation function are shown in Fig. 2.16. Here haloes are binned using their self-consistent masses, and not the masses of their matched reference counterparts. The lines represent the measured two-point autocorrelation function obtained from simulating baryonic physics and a running spectral

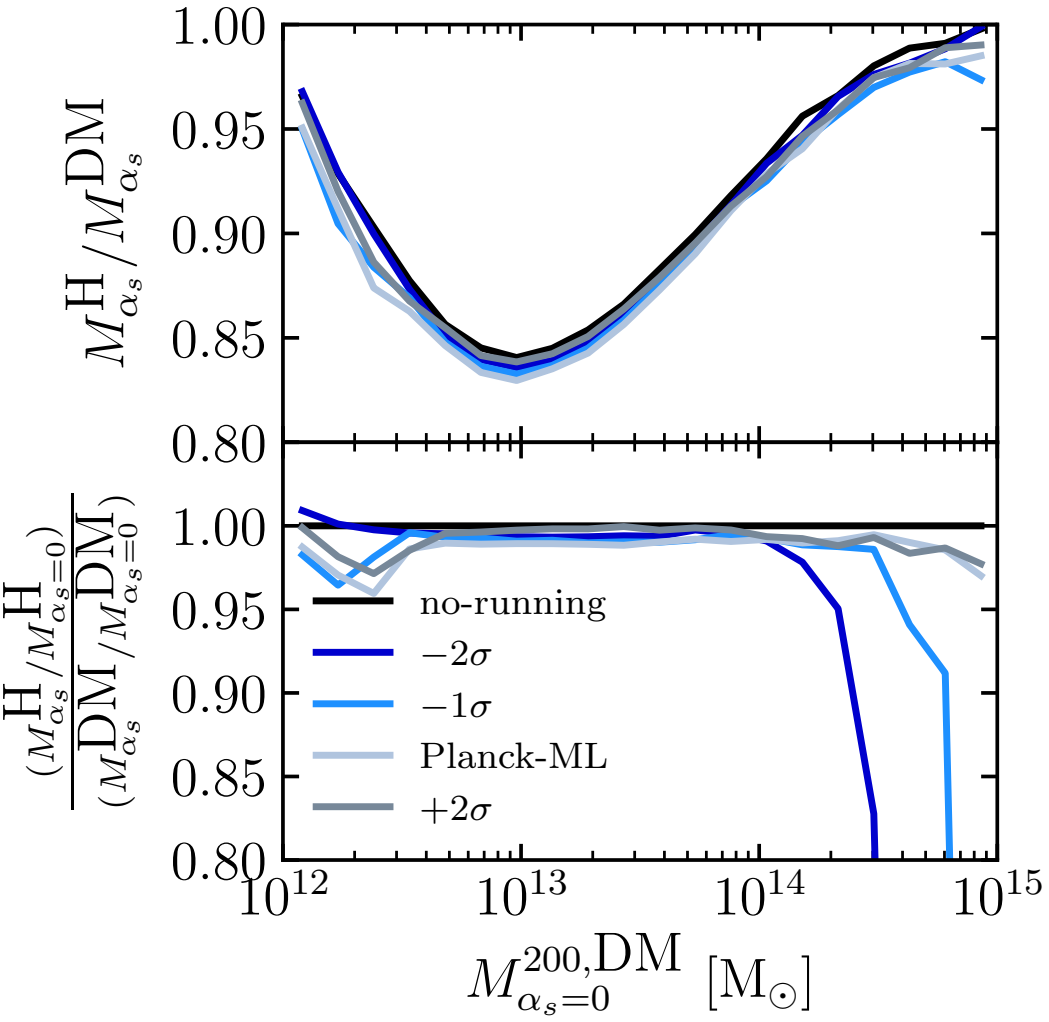

Figure 2.15: Test of the separability of the effect of baryonic physics and a running scalar spectral index on the mass of haloes. Top: the reduction in halo mass of a matched set of haloes due the inclusion of baryonic physics. Bottom: the effect a running scalar spectral index has on halo mass in the full BAHAMAS hydrodynamic simulations, normalised to the collisionless case. This shows that for most of the mass range sampled here the effect on halo mass due to a running spectral index is insensitive to the implemented baryonic physics.

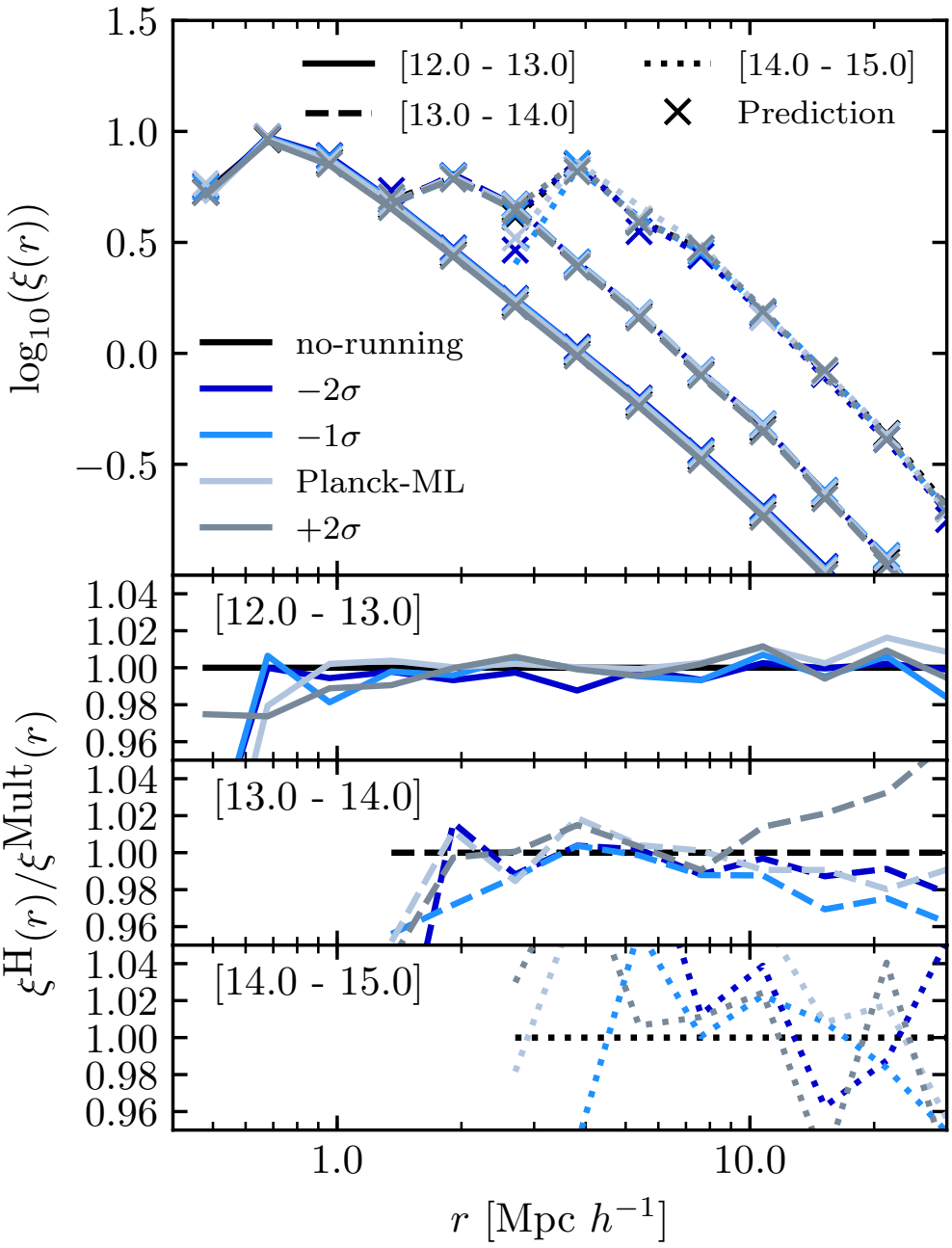

Figure 2.16: Test of the separability of the effects of baryonic physics and a running scalar spectral index on the clustering of haloes in bins of halo mass. Top: clustering signal when simultaneously simulating a running scalar spectral index and baryonic physics. The different linestyles represent the measured clustering between objects in different mass ranges, note that here haloes are binned according to the self-consistent masses of each simulation. The crosses represent the recovered result when treating the effects as separate multiplicative corrections (Equation 2.6). Bottom: the measured clustering signal from simultaneously simulating both effects, normalised with respect to the corresponding multiplicative prediction. For almost all of the radial range examined here, and for all mass bins, the clustering signal is reproduced to better than $\approx 4\%$ by treating these two effects separately.

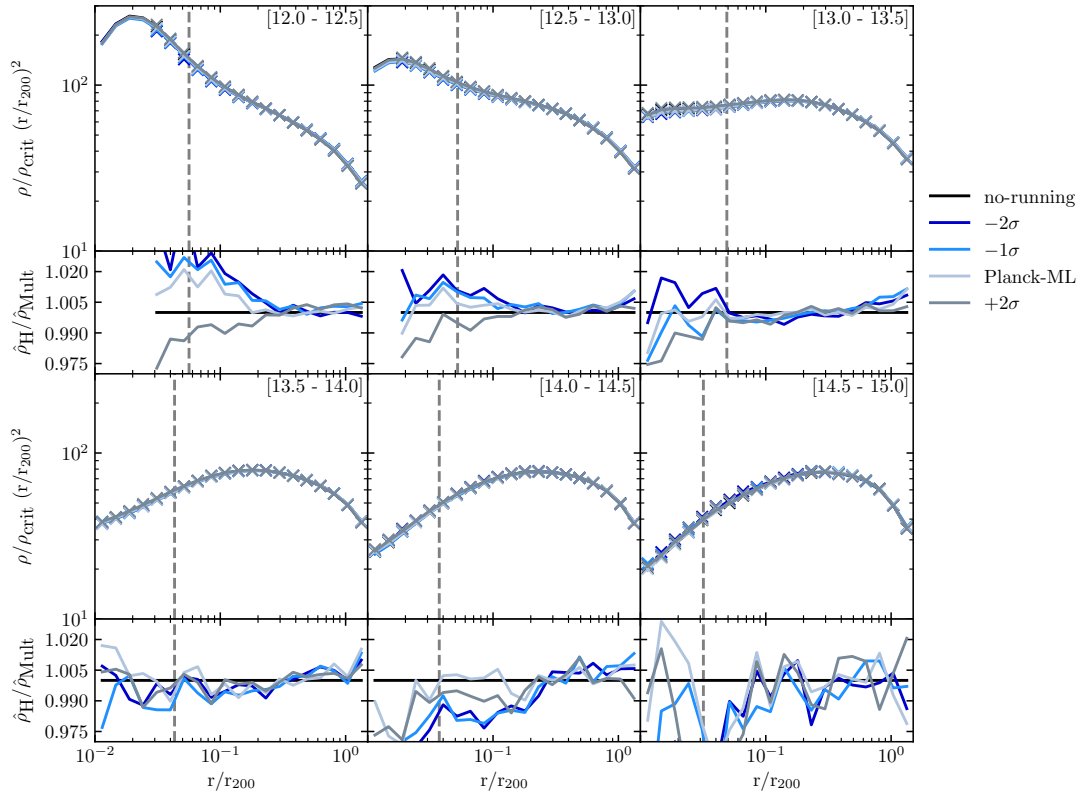

Figure 2.17: Comparison of the median spherically-averaged total-matter halo density profile measured from the hydro simulations, represented by the solid lines in this plot, and calculated using the simple functional form of Equation 2.6, shown by crosses. Haloes are binned using their self-consistent masses, and not that of their matched reference counterparts. The mass-range of each bin is indicated in the top right corner of each panel and is in units of: $\log(M_{200,{\rm c}}/{\rm M}_\odot)$. The vertical dashed line in each panel represents the convergence radius for haloes in the reference simulation. The bottom sub-panels show the ratio of the measured self-consistent density profile to that predicted treating both effects separately. The results agree to better than 2% for the entire radial range for each mass bin.

index simultaneously. The crosses represent the result obtained from using Equation 2.6 and multiplying the effects due to each separately (note that in this case: $\psi \equiv \xi(r)$). The bottom panel(s) shows the measured result from simulating both effects simultaneously normalised with the result obtained from multiplying the effects separately. It can be seen that the clustering signal of haloes in separate mass bins can be recovered to better than $\approx 4\%$ even for the most massive haloes, with the differences being exacerbated due to the low number density of these massive haloes in the sample.

2.5.4 Density profiles

Finally, I examine the separability of the effects due to baryonic physics and allowing the running to be free on the total mass density profile of a halo. As was seen in Fig. 2.15, the effects on halo mass due to baryonic physics and the effect on halo mass due to a running spectral index are largely independent effects. As a result, one might expect that the density profiles of these haloes can also be reproduced relatively well with a simple multiplicative prescription. To test this, I use Equation 2.6 (note that here $\psi = \hat{\rho}$ where $\hat{\rho}$ is the dimensionless re-scaled ρ: $\hat{\rho} \equiv (\rho/\rho_{\rm crit})(r/R_{200,\rm c})^2$). The results are shown in Fig. 2.17. An important note here is that, unlike in Fig. 2.11, here I plot the density profiles of an unmatched set of haloes, meaning that the haloes are binned using their self-consistent masses. Here the lines represent the median spherically averaged total-mass density profiles of each mass bin. The crosses represent the density profiles obtained from treating the effects due to a running scalar spectral index on the density profile of a halo and the effects due to baryonic physics separately. The bottom sub-panels show the ratio of the measured density profiles from the simulations to the self-consistent result obtained from treating the effects separately. The plot shows that even the combined effects on the internal structure of haloes can be reproduced (to typically better than 2%) by treating baryons and running separately.

As mentioned, all of the other statistics examined in the dark matter only simulation were also investigated in the way that has just been laid out in this section to see if the effects of baryonic physics and allowing the running to be free could be treated as separate effects. This includes the comoving halo number density and the c-M relation. Although these are not shown, they were reproduced using the simple functional form of Equation 2.6 to a similar level of accuracy to the tests presented above.

2.6 Summary and Conclusions

This study has made use of a new extension to the BAHAMAS suite of large cosmological hydrodynamic simulations which are 400 comoving Mpc h^{-1} on a side. This extension consists of 5 simulations, corresponding to different values for a running scalar spectral index (α_s), ranging from $-0.02473 \leq \alpha_s \leq 0.00791$ (a complete list of values can be found in Table 2.1). This has allowed an investigation into the effects a cosmology with a freely varying α_s has on the cosmic LSS and into how separable these effects are from those produced by baryonic physics. The statistics which this study focused on include the non-linear total matter power spectrum, the halo mass function (HMF), the two-point halo autocorrelation function, the spherically averaged halo density profiles, and the halo concentration-mass (c-M) relation. This study focuses mainly on haloes in the mass range: $10^{12} \leq M/\mathrm{M}_{\odot} \leq 10^{15}$. The main conclusions that can be drawn from this chapter are as follows:

- On almost all scales probed in these simulations, a cosmology with a negative value for the running of the scalar spectral index leads to an excess of power compared with the standard cosmology, by a maximum of $\approx 10\%$. This holds up to at least $z = 2$ (see Fig. 2.5). Conversely, a cosmology with a positive running leads to a suppression of the matter power spectrum over the entire $k-$range investigated in this study ($0.01 < k[\mathrm{Mpc}^{-1}h] < 8.0$) at $z = 0$. Such an effect should be measurable in upcoming LSS surveys, such as those from LSST, EUCLID and DESI[9] which aim to measure the power spectrum to around 1% accuracy. Naively, one might have expected a negative (positive) running to lead to less (more) power relative to a no-running case. However, the imposed requirement that my adopted cosmologies retain a good fit to the CMB temperature angular power spectrum in the presence of running forces the power spectrum amplitude, A_s, to slightly increase (decrease) for cosmologies with negative (positive) running (see Table 2.1). This effect is retained down to $z = 0$ in the non-linear power spectrum.

[9] https://www.desi.lbl.gov/

- A cosmology with a running scalar spectral index is capable of suppressing the low-mass end ($M \lesssim 10^{13}\mathrm{M}_{\odot}$) of the HMF by nearly 10% in the case of a cosmology with a negative running, but leads to an excess of low-mass haloes for a positive running cosmology (see Fig. 2.7). This effect on the HMF due to a running scalar spectral index depends both on redshift and the mass bin, with a negative running cosmology leading to an excess of high-mass objects ($M \gtrsim 2\times10^{13}\mathrm{M}_{\odot}$) with this effect being pronounced at earlier redshifts. This result is due to the fact that, in a negative running cosmology, the density perturbations which lead to these haloes are amplified and thus lead to higher-mass haloes forming earlier on.

- A cosmology with a running spectral index leads to a change in the spatial distribution of haloes (see Fig. 2.10). A negative running cosmology leads to haloes with $M < 10^{14}\mathrm{M}_{\odot}$ being more clustered compared with a standard cosmology (with a near 10% increase in the clustering signal for the most negative running cosmology) and higher masses being less clustered. This result is reversed for a positive running cosmology, which sees a reduction in the clustering signal of haloes with $M < 10^{14}\mathrm{M}_{\odot}$. This is due to the fact that, in a negative running cosmology, the formation of these low-mass haloes is suppressed, leading them to be a more biased tracer of the underlying matter distribution, and thus have a stronger clustering signal.

- Looking at internal properties of matched haloes, a cosmology with a running spectral index predominantly causes an amplitude shift in the density profiles of haloes, without much of a change to their shape (see Fig. 2.11). The effect of a running scalar spectral index depends both on the mass of the halo and the value of the running. A cosmology with a negative running leads to a reduction in the amplitude of the density profile for haloes with $M < 10^{13.5}\mathrm{M}_{\odot}$, but lead to an increase in the amplitude for high-mass ($M \gtrsim 10^{13.5}\mathrm{M}_{\odot}$) haloes. Conversely a cosmology with a positive running leads to an amplitude increase across the entire mass range investigated here. This is due to the fact that in a negative running cosmology a low-mass halo has its mass decreased, compared with its

matched no-running counterpart. Whereas for the same cosmology, the mass of a high-mass halo (depending on the magnitude of α_s) is increased. Conversely, a cosmology with a positive α_s leads to an increase in mass of a halo across the entire mass range studied here.

- For the c-M relation, it was found that the effect of a $\Lambda\alpha_s$CDM cosmology is once again mass-dependent, with all running cosmologies predicting the higher-mass haloes to be more centrally concentrated than in a no-running cosmology (see Fig. 2.12). Whereas at the low-mass end ($M \lesssim 2 \times 10^{13}\mathrm{M}_{\odot}$), the negative running cosmologies tend to predict slightly lower concentrations, the effect on these scales is small compared to the high-mass end. A similar result was found by Fedeli et al. (2010), who predicted low-mass haloes to have a lower concentration value in a negative running cosmology, but high-mass haloes to have a slightly higher concentration.

  Note that in the calculation of the c-M relation, haloes are binned according to their self-consistent masses, not the masses of their no-running counterparts (as was the case when looking at the density profiles). This is the reason why I see some differences in the c-M relation, with these differences not being obvious from looking at the density profiles of the matched haloes.

- This study also looked into the separability of the effects due to a running scalar spectral index and baryonic physics. I found that these two effects can be treated as separable multiplicative corrections to a standard cosmology. This simple multiplicative procedure is capable of reproducing the combined effects seen for all statistics looked at in this study (such as the non-linear total matter power spectrum in Fig. 2.13, the HMF in Fig. 2.14, and the two-point autocorrelation function in Fig. 2.16) to typically a few percent accuracy.

- As an aside, this study also investigated how well some current approximate methods calibrated on standard ΛCDM cosmologies can predict some of the results found in this study (see Appendix A.2). These include a prescription for the HMF produced by Tinker et al. (2008), as well as a prescription for the

redshift evolution of dark matter halo masses, and the c-M relation, produced by Correa et al. (2015a). I find that for the Tinker et al. (2008) HMF, this is able to reproduce the effects seen due to running out to $z = 2$ very well (Fig. A.4). I also find that qualitatively, the method developed by Correa et al. (2015a), is able to reproduce both the evolution of halo mass across the different simulations in this study (Fig. A.5); as well as the effect a running scalar spectral index has on the c-M relation of haloes at $z = 0$ (Fig. A.7).

This work has shown that a cosmology with a running scalar spectral index, consistent with the observational constraints of the Planck Collaboration XIII (2016) cosmological parameter results, can have relatively large and measureable effects on LSS. However, it is worth noting that, by itself, running is unable to reconcile the current tension involving S_8. For example, all of the $Planck$ CMB-based runs I examined here have $S_8 > 0.85$ (see Table 2.1), whereas many current LSS tests prefer S_8 in the range $[0.75, 0.8]$ (see McCarthy et al. 2018 and references therein). However, I remind the reader that taking account of the internal tensions in the CMB data, by allowing $A_{\rm lens}$ to float, can significantly reduce the tension between the CMB and LSS (see Appendix A.1) and remove it altogether when the neutrino mass is also allowed to float (McCarthy et al., 2018).

Nevertheless, if running is present at the levels suggested by current CMB and Lyman-α forest data, it should be within the detectability range of upcoming surveys such as LSST[10], EUCLID[11], and CMB-S4[12], and allow tangible constraints to be placed on fundamental, early-Universe physics.

Finally, this study has demonstrated that the effects of a running scalar spectral index are largest at low masses which sample far from the pivot scale. This is expected as the pivot scale is where all of the power spectra are normalised, and thus forced to have similar values (with the only differences here on these scales arising due to slight differences in A_s). As mentioned, this scale corresponds to $k_0 = 0.05$ Mpc^{-1} for

[10]https://www.lsst.org/
[11]https://www.euclid-ec.org/
[12]https://cmb-s4.org/

Planck CMB measurements, corresponding roughly to cluster scales which BAHAMAS is designed to sample. Therefore, in a future follow-up study I will explore this larger effect on lower masses in more detail, looking at the impact of running on "near-field" (small-scale) cosmology.

Chapter 3

Exploring extensions to the standard cosmological model and the impact of baryons on small scales

The following chapter appeared in Stafford et al. (2020b). The appendices for this work are included in Appendix B.

In Chapter 1 I introduced some of the apparent tensions which appear to plague the standard model of cosmology with the wealth and quality of observational data being collected recently. In Chapter 2 I detailed some of the apparent large-scale tensions, namely tensions in cosmological parameters when constrained using different observational data sets, and I used these tensions to motivate a minimal extension to the ΛCDM model in the form of a running scalar spectral index. One of the key results of the previous chapters was that when you have a cosmological model with a non-zero value for the running of the spectral index this can have quite large effects, with the magnitude of these effects increasing as you start to observe smaller physical scales and the objects associated with these scales. Therefore, in light of this result, in this chapter, I seek to extend this analysis further and probe the effects of a non-zero running scalar spectral index on lower mass haloes and smaller physical scales. To complement this study I also look into additional minimal extensions to the standard model

of cosmology which are popular due to their ability to preferentially affect small-scale structure. This study is further motivated by the claims that the ΛCDM model cannot easily account for several observations on relatively small scales.

In this chapter, I introduce a new suite of cosmological simulations that systematically explores three plausible extensions: warm dark matter, self-interacting dark matter, and a running of the scalar spectral index of density fluctuations. These extensions introduce 3 new parameters into the standard model of cosmology, $M_{\rm WDM}$, σ/m, α_s respectively. The values that I adopt for these additional cosmological parameters are informed by current observational constraints. We make further use of these simulations, as well as adding additional simulations to this suite, in the following Chapter 4 where we use these simulations to generate cosmic shear power spectrum.

In this chapter, however, I use these simulations to examine a large range of observable metrics on small scales, including the halo mass function, density and circular velocity profiles, the abundance of satellite subhaloes, and halo concentrations, exploiting their higher resolution compared to the simulations introduced in Chapter 2. I find that for any of the above metrics, significant degeneracies can be present between the extensions. In detail, however, the different extensions have quantitatively distinct mass and radial dependencies, suggesting that to place constraints on these parameters using observations a multi-probe approach over a range of scales should be used to break the degeneracies. I also demonstrate that the relative effects on the radial density profiles in the different extensions (compared to the standard model) are converged down to significantly smaller radii than are the absolute profiles. I compare the derived cosmological trends with the impact of baryonic physics using the EAGLE and ARTEMIS simulations. Significant degeneracies are also present between baryonic physics and cosmological variations (with both having similar magnitude effects on some observables). Given the inherent uncertainties both in the modelling of galaxy formation physics and extensions to ΛCDM, a systematic and simultaneous exploration of both is strongly warranted.

3.1 Introduction

The current cosmological paradigm describes a universe which has a matter content that is primarily composed of collisionless cold dark matter (CDM), a cosmological constant (Λ), and normal baryonic matter (Planck Collaboration XIII, 2016). The true nature of dark matter, however, is still an unsolved problem. Aside from there not yet being a confirmed direct detection of dark matter, there are also claimed problems with the current cosmological model (most commonly abbreviated to the ΛCDM model) on small scales which could hint at a deviation from CDM. For example, three of the most widely discussed issues with this model are the 'cusp–core problem' (Flores and Primack, 1994; Moore, 1994), the 'missing satellites problem' (Klypin et al., 1999; Moore et al., 1999), and the 'too-big-to-fail problem' (Boylan-Kolchin et al., 2011). A recent review on these, along with other apparent small-scale issues identified within ΛCDM, can be found in Bullock and Boylan-Kolchin (2017).

These issues have fuelled research into alternatives/extensions to the standard model, particularly modifications to the nature of dark matter. For example, one can relax the assumption that dark matter is purely collisionless, allowing instead for a non-negligible self-interaction with a cross-section that can be constrained by observations. Previous studies on such self-interacting dark matter (SIDM) suggest it may be able to solve the cusp–core problem (Spergel and Steinhardt, 2000; Yoshida et al., 2000; Davé et al., 2001; Colin et al., 2002; Vogelsberger et al., 2012; Rocha et al., 2013; Elbert et al., 2015; Kaplinghat et al., 2016), the too-big-to-fail problem (provided that the self-interaction cross-section is large enough e.g. Zavala et al. 2013; Elbert et al. 2015), and may help to explain the observed diversity of galaxy rotation curves (Kamada et al., 2017; Creasey et al., 2017).

Another popular extension retains the assumption that dark matter is collisionless, but invokes a non-negligible thermal velocity at early times. Termed warm dark matter (WDM), the associated free-streaming erases small-scale density perturbations leading to a characteristic cut-off in the linear matter power spectrum (Bond et al., 1980; Pagels and Primack, 1982; Dodelson and Widrow, 1994; Hogan and Dalcanton, 2000; Viel

et al., 2005; Abazajian, 2006). This leads to WDM potentially being able to resolve the missing satellites problem due to the suppression of structure with masses close to the cut-off scale in the matter power spectrum (Colín et al., 2000; Bode et al., 2001; Polisensky and Ricotti, 2011; Lovell et al., 2012; Anderhalden et al., 2013; Bozek et al., 2016; Horiuchi et al., 2016; Bose et al., 2017). Furthermore, due to the later formation times of haloes in a WDM cosmology, haloes tend to have a lower central density which helps to mitigate the too-big-to-fail problem (Lovell et al., 2012; Horiuchi et al., 2016; Lovell et al., 2017a). Studies have also shown that WDM can produce cores in the density profile of dark matter haloes, however, these are not large enough to solve the cusp–core problem given current constraints on the mass of the dark matter particle (Villaescusa-Navarro and Dalal, 2011; Macciò et al., 2012; Shao et al., 2013).

An alternative mechanism that can alter small-scale structure but which treats dark matter in the standard way (cold and collisionless), is to invoke a change in the primordial power spectrum on small scales. The standard model of cosmology assumes that the primordial power spectrum of density fluctuations, $P(k)$, laid down by inflation is a pure power-law. Measurements of the cosmic microwave background constrain the power-law exponent to be $n_s \approx 0.96$, in excellent agreement with generic inflation models. However, even the simplest single-field inflation models predict some degree of deviation from a pure power-law (Kosowsky and Turner 1995, see also Garcia-Bellido and Roest 2014; Escudero et al. 2016).

A more general treatment of the primordial matter power spectrum allows the spectral index to vary with scale, with this scale-dependence termed the 'running' of the spectral index (α_s). As discussed in Chapter 2, a growing body of observational evidence suggests some preference for a mildly negative value for α_s (Dunkley et al., 2011; Zhao et al., 2013; Hou et al., 2014; Planck Collaboration XIII, 2016; Palanque-Delabrouille et al., 2015; Palanque-Delabrouille et al., 2019), which will act to suppress power on the smallest (and largest) of scales. Garrison-Kimmel et al. (2014) have previously shown that a negative running can help resolve the missing satellite problem as well as alleviate the too-big-to-fail problem.

It is possible, however, that the small-scale crises outlined previously which suppos-

edly exist with the ΛCDM model are instead just a product of conclusions drawn from comparing the observable Universe to the predictions from a series of dark matter-only simulations. Recently there has been extensive research into the possibility that a realistic treatment of baryonic physics in simulations, such as supernovae feedback, stellar winds, and feedback from active galactic nuclei (AGN), may be able to resolve some of these tensions. These studies have shown the importance of including baryonic physics in the simulations, demonstrating the potential to resolve for the cusp–core problem (Mashchenko et al., 2008; Pontzen and Governato, 2012; Macciò et al., 2012; Madau et al., 2014; Oñorbe et al., 2015; Read et al., 2016; Tollet et al., 2016; Wetzel et al., 2016; Fitts et al., 2017), the missing satellites problem (Bullock et al., 2000; Benson et al., 2002; Somerville, 2002; Kravtsov et al., 2004; D'Onghia et al., 2010; Wetzel et al., 2016; Garrison-Kimmel et al., 2017; Sawala et al., 2017), as well as the too-big-to-fail problem (Zolotov et al., 2012; Arraki et al., 2014; Brooks and Zolotov, 2014; Chan et al., 2015; Wetzel et al., 2016; Tomozeiu et al., 2016; Sawala et al., 2016; Dutton et al., 2016; Brooks et al., 2017) and without having to invoke any extensions to the standard model.

To what extent the successes of hydrodynamical simulations in helping to resolve the aforementioned small-scale problems are a natural and robust consequence of the physics implemented in the simulations, or is instead due to calibration (either implicitly or explicitly) of the feedback models to specifically address those issues, remains somewhat unclear[1]. In any case, the correct approach should not to be overly prescriptive about the nature of the cosmological model and the role of baryons, but to use comparisons of simulations to observations to attempt to constrain both.

At present, the literature contains numerous studies that typically explore one cosmological extension at a time, or examine the impact of baryons alone (in ΛCDM), and often in the context of a very small sample of haloes simulated (zooms). Drawing general conclusions from these studies about the relative impact of these effects, their differences and possible degeneracies, is hindered by large study-to-study variations in box

[1] See Schaye et al. (2015) for a discussion of the predictive power of current cosmological hydrodynamical simulations.

size, resolution, differences in feedback calibration schemes, and focus on different aspects of small-scale structure. Here I aim to remedy these issues by simultaneously studying the effects of the different extensions (SIDM, WDM, and a running spectral index) to ΛCDM in a consistent way, using a suite of high-resolution dark matter-only cosmological simulations. To compare to the impact of baryon physics, I make use of the high-resolution EAGLE Recal model (Schaye et al., 2015; Crain et al., 2015) and the new ARTEMIS suite of zoomed hydrodynamical simulations of Milky Way-mass galaxies (Font et al., 2020). Note that ARTEMIS uses the same galaxy formation physics as EAGLE but the stellar feedback has been re-calibrated for the increased resolution to yield an improved match to the stellar masses of haloes with similar mass to the Milky Way. Both of these suites have comparable resolution and statistics to my simulations of the above cosmological extensions. I examine the dark matter-only and hydrodynamical simulations in a consistent way, examining the impact of cosmological variations and baryon physics on a wide range of metrics that characterise the abundance and structure of dark matter haloes and their subhaloes.

The present study is structured as follows: In Section 3.2 I introduce the simulations used as part of this study, covering each cosmological extension in turn. In Section 3.3 I examine some global properties of the simulated volumes, focusing on statistics such as the halo and subhalo mass functions. In Section 3.4 I examine the effects from these various cosmologies on several internal properties of simulated haloes, examining statistics such as the dark matter density profiles of haloes. Finally, in Section 3.5 I summarise and discuss my findings.

3.2 Simulations

For this study, I have run a suite of high resolution, cosmological volumes, sampling different possible extensions to the ΛCDM model. The suite consists of 7 dark matter-only, periodic box simulations which are 25 comoving Mpc h^{-1} on a side, each containing 1024^3 dark matter particles. All of the cosmological parameters for the simulations in this suite use the fiducial $Planck$ 2015 maximum likelihood values, apart

from the simulations which include a running scalar spectral index (this is explained in more detail below). The cosmological parameter values adopted can be found in Table 3.1.

The Boltzmann code `CAMB`[2] (Lewis et al. 2000, August 2018 version) is used to compute the transfer functions and power spectra for all of the simulations (with the WDM power spectra being slightly altered, as explained below), and a modified version of `N-GenIC`[3] is used to create the initial conditions (ICs) for the simulations. The simulations are initialised at a starting redshift of z = 127 and run to z = 0. I use a modified version of `N-GenIC` which includes second-order Lagrangian Perturbation Theory corrections, alongside support for massive neutrinos. Note that when producing the initial conditions (ICs) for the simulations, the same random phases are used for all 7 periodic box runs, removing the effects of cosmic variance when comparing the runs.

The simulations are run using a modified version of the parallel Lagrangian TreePM-SPH code `GADGET3` (last described in Springel, 2005).

The gravitational softening is a fixed physical length of 250 pc h^{-1} at $z \leq 3$, and is a fixed comoving length at higher redshifts. The reference ΛCDM simulation (designated 'Ref') has a dark matter particle mass of $m_{\rm DM}$ = 1.266 $\times$ 10^6 $\rm M_{\odot}$ h^{-1}. The SIDM and WDM simulations also have this particle mass, as they adopt identical cosmological parameters. The two simulations which incorporate a running scalar spectral index have slightly different particle masses, owing to the slightly different values for $\Omega_{\rm m}$ and h for those runs, as described below. I note that for all the $Planck$ 2015 maximum-likelihood cosmologies used in this study, including the cosmologies with a running spectral index, I include massive neutrinos using the minimum summed neutrino mass (equal to ΣM_{ν} = 0.06 eV), derived from atmospheric and solar oscillation experiments and adopting a normal hierarchy of neutrino masses (Lesgourgues and Pastor, 2006). As a result I use a version of `GADGET3` which has the semi-linear algorithm (developed by Ali-Haïmoud and Bird 2013, however see also Bond et al. 1980; Ma and Bertschinger 1995; Brandbyge et al. 2008; Brandbyge and Hannestad 2009; Bird et al.

[2]http://camb.info/
[3]https://github.com/sbird/S-GenIC

2012) which models the effects of massive neutrinos on both the background expansion rate and the growth of density fluctuations implemented into it. This algorithm computes neutrino perturbations on the fly at each time step (see McCarthy et al. 2018 for further details of its implementation). Furthermore, I also include the effects of radiation on the expansion history.

3.2.1 Running of the scalar spectral index

The epoch of inflation seeded small density perturbations in the matter distribution of the Universe, with the power spectrum of these perturbations in the ΛCDM model being of the form (Guth, 1981):

$$P(k) = Ak^{n_s} \tag{3.1}$$

where $P(k)$ is the power spectrum as a function of wavenumber k, A defines the amplitude of the primordial matter power spectrum, and n_s is the scalar spectral index. In the ΛCDM model, n_s is assumed to be constant, with no k dependence. However, as discussed in the Introduction, even the simplest models of inflation predict some level of deviation from a power-law distribution.

Allowing for running, the modified power spectrum, $P(k)$, can be expressed as (Kosowsky and Turner, 1995):

$$P_s(k) = A_s(k_0)\left(\frac{k}{k_0}\right)^{n_s(k=k_0)+\alpha_s'(k)} \tag{3.2}$$

where $\alpha_s'(k) \equiv (\alpha_s/2)\ln(k/k_0)$, α_s is the running of the scalar spectral index, which is defined as $\mathrm{d}n_s(k)/\mathrm{dln}(k)$. The pivot scale, k_0, is the scale at which the amplitude of the power spectrum (A_s) is defined, along with the scale at which the spectral index is measured when $\alpha_s \neq 0$. In this study, I adopt the same pivot scale as that used for the cosmological parameter estimation of Planck Collaboration XIII (2016): k_0 = 0.05 Mpc^{-1}. It is also worth mentioning that this is only a first-order extension to the power spectrum of density perturbations. There can also be a 'running of the running', where

the running of the scalar spectral index also varies with scale [$\alpha_s \rightarrow \alpha_s(k)$] leading to a second-order term being added to the functional form of the spectral index $n_s(k)$. But for simplicity, I focus here on the first order effect.

As mentioned previously, all of the simulations, with the exception of the two simulations that include a running scalar spectral index, adopt the $Planck$ 2015 maximum likelihood cosmological parameters. For the two simulations which include a running scalar spectral index, I adopt the same cosmological parameters as that derived in Chapter 2. Here I will briefly explain how these cosmological parameters were chosen, but more detail is provided in Chapter 2.

To generate a set of parameters which make up a cosmological model, I made use of the $Planck$ 2015 publicly available Markov chains which include α_s as a free parameter. Five values for α_s which sampled the posterior distribution were chosen in Chapter 2, corresponding to the maximum-likelihood value and $\pm 1\sigma$ and $\pm 2\sigma$ values. For a given choice of the running, the values of the other important cosmological parameters were obtained by taking the weighted average of the Markov chain data for all parameter sets with α_s close to the desired value. Choosing the cosmological parameters in this way ensures that the resultant cosmological model is consistent with current measurements of the CMB. In the present study, I use 2 out of the 5 cosmologies generated in this way, corresponding to the $\pm 2\sigma$ values of the posterior distribution of α_s.

3.2.2 Warm dark matter

Instead of modifying the primordial power spectrum, as in the case of a running of the scalar spectral index, the nature of dark matter itself can be modified. Warm dark matter (WDM) differs from CDM in the standard model, in that the subatomic particles that constitute WDM are considerably lighter ($\sim$keV) than CDM particles ($\sim$GeV to TeV masses). Consequently, WDM particles remain relativistic for longer in the early Universe compared with CDM, resulting in non-negligible thermal velocities that allow the particles to free-stream out of small-scale density perturbations, smoothing them out and suppressing the growth of structure on small scales (Bond and Szalay,

1983; Bardeen et al., 1986).

This smoothing out of density perturbations due to the thermal velocity associated with WDM leads to a characteristic cut-off in the WDM power spectrum. This effect can be modelled as a transfer function $T_{\rm WDM}(k)$, relative to the CDM power spectrum:

$$P_{\rm WDM}(k) = T^2_{\rm WDM}(k) P_{\rm CDM}(k). \tag{3.3}$$

Here I make use of the fitting formula of Bode et al. (2001):

$$T_{\rm WDM}(k) = \left[1 + (\alpha k)^{2\nu}\right]^{-5/\nu}, \tag{3.4}$$

with ν being a fitting constant and α corresponding to the scale of the cut-off in the power spectrum, with this being dependent on the mass of the thermal WDM particle. Note that this function assumes the dark matter is entirely composed of WDM. The values adopted for these constants correspond to the best fit values obtained by Viel et al. (2005) (for $k-$scales < 5 Mpc^{-1} h); i.e., ν = 1.12 and (assuming the WDM is composed of thermal relics)

$$\alpha = 0.049 \left(\frac{m_x}{1{\rm keV}}\right)^{-1.11} \left(\frac{\Omega_x}{0.25}\right)^{0.11} \left(\frac{h}{0.7}\right)^{1.22} {\rm Mpc}\ h^{-1}. \tag{3.5}$$

Here m_x corresponds to the mass of the WDM particle, Ω_x is the present-day density of WDM in units of the critical density, and h is the reduced Hubble's constant.

Examining equation 3.5, it can be seen that the warmer the dark matter particle (i.e., the smaller the mass of the particle), the larger the scale of the break in the power spectrum (i.e., the suppression moves to smaller k values).

As well as using a modified power spectrum as outlined previously, one should in principle also assign a thermal velocity to the WDM particles; with the rms velocity dispersion of these WDM particles being around 1.6 (0.6) km s^{-1} in the case of the 2.5 (5.0) keV WDM particle mass at the starting redshift of 127 (Bode et al., 2001), which is a fraction of the rms velocity assigned through the Zel'dovich Approximation

(around 40 km s^{-1} at $z = 127$). Therefore, as the distance scales travelled during the free-streaming of the WDM particles due to their thermal velocities corresponds to $\sim$ tens of comoving kpc for WDM particle masses of $\sim$ keV (Lovell et al., 2012), I neglect these thermal velocities in my simulations. Furthermore, for a given initial power spectrum, the inclusion of thermal velocities tends to introduce spurious noise which can adversely affect early structure formation in the simulations (Leo et al., 2017). Note that the particles are, however, still initialised with a peculiar velocity using the Zel'dovich Approximation (Zel'dovich, 1970) plus 2LPT corrections.

In this study I investigate two different dark matter particle masses: a 2.5 and 5.0 keV thermal relic dark matter mass. The choice for the WDM particle mass is influenced by current astrophysical constraints. For example, a strong lower-limit is placed on the mass of the WDM particles through observations of the Lyman-α forest flux power spectrum, with Viel et al. (2013) placing a lower-limit of $M_{WDM} \gtrsim 3.3$ keV and Iršič et al. (2017) providing a slightly more stringent constraint of $M_{WDM} \gtrsim 5.3$ keV. These limits are consistent with constraints set from the Milky-Way's satellite population, which provide constraints ranging from $M_{WDM} > (1.5 - 3.9)$ keV (Lovell et al., 2014; Kennedy et al., 2014; Jethwa et al., 2018; Nadler et al., 2019; Nadler et al., 2020a).

Note, however, that the limits placed on the WDM particle mass through observations of the Lyman-α forest are somewhat sensitive to the treatment of the thermal history of the intergalactic medium (IGM). For example, Garzilli et al. (2019) demonstrated that the Lyman-α forest constraints can be lowered to $M_{WDM} > 1.9$ keV when marginalising over the plausible temperature range of the IGM.

More recently, time delay measurements of (strong) gravitationally-lensed quasars, which are sensitive to the distribution of substructure around the lens, have been used to derive $M_{WDM} > 5.58$ keV (Hsueh et al., 2019). As such, the thermal relic masses which I choose to simulate are consistent with the current tightest constraints placed on this parameter by various observations.

As this study is focused on dark matter (sub)haloes, it is important that the results are not influenced by numerical artefacts which may form. This is particularly relevant

in the simulations of WDM universes, with some studies having shown an onset of structure formation on small scales in WDM simulations due to spurious fragmentation of filaments. Wang and White (2007) showed this to be due to particle discreteness effects. They provided an empirical cut in halo mass to remove these spurious objects from halo catalogues (see also Lovell et al., 2014). However, as this limiting mass is lower than the the limit I place on resolved (sub)haloes, such spurious structure formation should not impact my results (see Appendix B.1 for more details).

3.2.3 Self-interacting dark matter

Another possible extension to the ΛCDM model is to allow the dark matter particles to self-interact (i.e., scatter with neighbouring particles). Here the dark matter is still assumed to be cold initially as in the standard model.

To simulate the effects of these self-interactions, I use a slightly modified version of the previously mentioned TreePM `GADGET3` N-body code. This version was modified by Robertson et al. (2019) (see also Robertson et al. 2017a,b) to incorporate dark matter self-interactions. I will provide a brief overview of the interaction process here, but refer the reader to the original papers for more details.

At each time-step Δt, particles search for any neighbouring particles that are within some pre-defined radius h. The probability for each pair of nearby particles i and j to scatter is calculated using:

$$P_{ij}^{\text{scat}} = \frac{|\boldsymbol{v}_i - \boldsymbol{v}_j|\Delta t}{\frac{4\pi}{3}h^3} . \left(\frac{\sigma}{m}\right) m_{\text{DM}}. \tag{3.6}$$

Here (σ/m) is the particle physics dark matter scattering cross-section, and m_{DM} is the dark matter particle mass in the simulation. $\boldsymbol{v}_{i,j}$ is the velocity of particle i and j respectively, and h is the search radius which I set to be equal to the gravitational softening length ϵ of the simulations (see Robertson et al. 2017a for discussion). Note this equation leads to the probability of a scattering event between two particles taking place being proportional to the dark matter particle mass. As such, the total probability

of a particle scattering with any other particle is independent of particle mass, as the number of neighbouring particles available to scatter with is inversely proportional to the dark matter particle mass.

The dark matter interactions are assumed to be fully described by an azimuthally-symmetric differential cross-section, defined in the centre of momentum frame of the two particles. Although the code has the functionality for scattering events to be both velocity and angular dependent, in this study I only examine the case where the scattering events are velocity independent and isotropic. Under these assumptions, the interactions are described by a differential cross-section (which is the rate at which particles are scattered into a region of solid angle) equal to:

$$\frac{d\sigma}{d\Omega} = \frac{\sigma}{4\pi}. \tag{3.7}$$

I explore two different values for the total cross-section: $\sigma/m = 0.1$ and 1.0 cm^2 g^{-1}. These values are guided by current observational constraints. Current constraints come from observations of strong lensing arcs, which suggest upper limits of $\sigma/m \lesssim$ (0.1, 1.0) cm^2 g^{-1} (Meneghetti et al., 2001; Robertson et al., 2019, respectively); DM–galaxy offsets in colliding galaxy clusters, which suggest $\sigma/m <$ (0.47 - 2) cm^2 g^{-1} (Randall et al., 2008; Kahlhoefer et al., 2015; Harvey et al., 2015; Kim et al., 2017; Robertson et al., 2017a; Wittman et al., 2018); cluster shapes, have been used to infer $\sigma/m <$ (0.02, 0.1) cm^2 g^{-1} (Miralda-Escude, 2002a; Peter et al., 2013, respectively); as well as from subhalo evaporation arguments that suggest $\sigma/m <$ 0.3 cm^2 g^{-1} (Gnedin and Ostriker, 2001). Note, however, that these constraints are mainly derived from galaxy cluster scales. If the focus is turned instead to the dwarf-galaxy regime, cross-sections as high as 50 cm^2 g^{-1} are within observational constraints and can potentially alleviate some of the small-scale problems associated with ΛCDM (Elbert et al., 2015). As such, a velocity-dependent cross-section may be needed to explain the entire dynamic range of observations. However, as mentioned, this study focuses on velocity-independent cross-sections, with the cross-sections chosen to be representative of the current constraints which exist for this parameter.

3.2.4 Baryonic effects in the standard model

As discussed in the Introduction, many recent studies have concluded that the effects of baryons on 'small-scale' structure are important. A primary aim of the present study is to compare and contrast the effects of baryons with those of changes to the standard cosmological model. I do this by comparing the gravity-only simulations introduced above to one set of simulations from the EAGLE project (the highest-resolution 'Recal' run). I also make comparisons to the ARTEMIS simulations, a new suite of fully hydrodynamic zoom-in simulations of Milky Way-type analogues (Font et al., 2020). This new suite of zoom-in simulations uses the same galaxy formation (subgrid-)physics as the EAGLE project, but the stellar feedback has been re-calibrated for the higher resolution as well as to yield an improved match to observed galaxy stellar masses at halo masses of $\sim 10^{12}\mathrm{M}_{\odot}$.

Note that both sets of hydrodynamical simulations that I use fall within the context of the standard cosmological model. Ideally, one would also like to explore the impact of baryons in non-standard cosmologies, since star formation and feedback-driven winds are observed to be ubiquitous in the Universe. I leave this for future work, noting that it is not likely to simply be a matter of re-running the same galaxy formation model in each cosmological extension, as the properties of the galaxies themselves will likely change. Therefore, re-calibration of feedback prescriptions will presumably be required. In other words, some degree of degeneracy between baryonic effects and cosmological effects is to be expected. I comment on this possibility below, using the simulations in hand.

EAGLE simulation

In this study I make use of the highest-resolution EAGLE run (data from McAlpine et al. 2016), called 'Recal', which is a 25 Mpc on a side cosmological volume (Schaye et al., 2015; Crain et al., 2015). For a full overview of this and other EAGLE runs, including how the initial conditions were generated, I refer the reader to the aforementioned papers. I provide only a brief overview of the Recal simulation here.

The simulation was run in the context of a $Planck$ 2013 maximum-likelihood cosmology (Planck Collaboration XVI, 2014), with the cosmological parameters provided in Table 3.1. The simulation consists of a fully hydrodynamic run, containing 2×752^3 particles, and a complementary dark matter-only run (containing 752^3). This results in particle masses of $m_{\rm DM} = 1.21 \times 10^6$ M$_\odot$ and $m_{\rm gas} = 2.26 \times 10^5$ M$_\odot$. The gravitational softening is 350 pc (in physical below $z = 3$ and is a fixed comoving length at higher redshifts). Thus, the mass and force resolution of this run is very similar to that of my dark matter-only suite introduced above.

The galaxy formation (subgrid-)physics included as part of the EAGLE project include metal-dependent radiative cooling (Wiersma et al., 2009a), star formation (Schaye and Dalla Vecchia, 2008), stellar evolution, mass-loss and chemical enrichment from Type II and Ia supernovae, Asymptotic Giant Branch and massive stars (Wiersma et al., 2009c), black hole formation and growth (Springel et al., 2005; Rosas-Guevara et al., 2015), stellar feedback (Dalla Vecchia and Schaye, 2012) and feedback from active galactic nuclei (AGN) (Booth and Schaye, 2009).

Like the larger (but lower resolution) Reference EAGLE run, the stellar feedback in the Recal model was adjusted to approximately reproduce the local galaxy stellar mass function and the size–stellar mass relation (see Schaye et al., 2015). In practice, the Recal model produces stellar masses that are somewhat below those inferred from the observed galaxy stellar mass function near the knee of the mass function (i.e., for Milky Way-mass halos, the stellar masses are somewhat too low), otherwise the galaxy stellar masses match the observations rather well. I therefore compare the results derived from EAGLE with those derived from the ARTEMIS zooms simulations (described below), for which the stellar masses agree better with observations for Milky Way-mass haloes.

The ARTEMIS simulations

This study also makes use of the ARTEMIS simulations. This is a suite of zoom-in simulations, which are introduced in detail in Font et al. (2020) but I provide a brief overview here.

The simulations were performed using a $WMAP9$ cosmology (Hinshaw et al., 2013), with the cosmological parameters for this run provided in Table 3.1.

Note that the $WMAP9$ maximum-likelihood cosmology does not include massive neutrinos, whereas, as mentioned previously, the $Planck$ 2015 cosmologies used for the cosmological volumes do. However, this should not impact the comparisons made here, as I focus mainly on the relative effects of the cosmological extensions, as well as the relative effects of baryonic physics, compared to a CDM dark matter-only prediction. Furthermore, it was illustrated by Mummery et al. (2017) that the effects of massive neutrinos are separable from the effects of baryonic physics.

The underlying galaxy formation (subgrid-)physics which is included in these full hydrodynamic zoom-in simulations is identical to that used in the EAGLE project (as described in Section 3.2.4). However, the parameters which characterise the efficiency of stellar feedback were adjusted to match the observed stellar mass–halo mass relation, as inferred from abundance matching. The motivation for the adjustment was two-fold: i) the EAGLE Recal model predicted too low stellar masses on the scale of Milky Way-mass haloes (as mentioned above); and ii) the effectiveness of feedback in suppressing star formation tends to increase with increasing resolution for a fixed feedback model, thus the feedback efficiency in the higher-resolution ARTEMIS simulations was reduced with respect to the EAGLE Recal model (see Font et al. 2020 details).

The MW analogues were selected from a parent cosmological volume, 25 Mpc h^{-1} on a side, containing 256^3 particles. These MW analogues were then run at higher resolution, using the zoom-in technique (see e.g Bertschinger, 2001), with the ICs being generated by MUSIC (Hahn and Abel, 2011). The ICs are generated at a starting redshift of $z = 127$, with a transfer function computed using the Boltzmann code CAMB. Furthermore the ICs are generated including 2LPT corrections.

The MW type objects were selected based solely on a mass criterion, with any halo in the original dark matter-only cosmological volume which had a spherical-overdensity mass (defined in Section 3.3.1) in the interval $11.903 \leq \log_{10}(M_{200,\mathrm{crit}}/\mathrm{M}_{\odot}) \leq 12.301$

Table 3.1: The cosmological parameter values for the suite of simulations used in this study are presented here. The columns are as follows: (1) The labels for the different cosmological extensions simulated in this study, as well as the hydrodynamic simulations which I use. (2) Hubble's constant. (3) Present-day dark matter density in units of the critical density of the Universe. (4) Present day baryonic density in units of the critical density. (5) Spectral index. (6) Amplitude of the initial matter power spectrum at a pivot scale of 0.05 Mpc^{-1} for the cosmological variations (corresponding to the $Planck$ pivot scale), and 0.002 Mpc^{-1} for the ARTEMIS simulations (corresponding to a $WMAP9$ pivot scale). (7) linearly evolved present-day amplitude of the matter power spectrum on scales of 8 Mpc h^{-1}. Note that when producing the ICs for the simulations, I use the value for A_s, meaning that the ICs are normalised by the CMB. (8) Simulation DM particle mass.

(1)	(2)	(3)	(4)	(5)	(6)	(7)	(8)
Cosmology	H_0 (km s^{-1} Mpc^{-1})	$\Omega_{\rm DM}$	$\Omega_{\rm b}$	n_s	A_s ($\times 10^{-9}$)	σ_8	$m_{\rm DM}$ ($\times 10^6$ M$_\odot$ h^{-1})
Ref (ΛCDM)	67.31	0.264	0.049	0.966	2.199	0.830	1.063
σ/m = 0.1 cm^2 g^{-1}	67.31	0.264	0.049	0.966	2.199	0.830	1.063
σ/m = 1.0 cm^2 g^{-1}	67.31	0.264	0.049	0.966	2.199	0.830	1.063
$M_{\rm WDM}$ = 2.5 keV	67.31	0.264	0.049	0.966	2.199	0.830	1.063
$M_{\rm WDM}$ = 5.0 keV	67.31	0.264	0.049	0.966	2.199	0.830	1.063
α_s = -0.02473	67.53	0.264	0.050	0.962	2.349	0.851	1.060
α_s = 0.00791	66.95	0.268	0.049	0.965	2.147	0.821	1.079
ARTEMIS	70.00	0.233	0.046	0.972	2.410	0.821	0.118
EAGLE	67.77	0.259	0.048	0.961	3.097	0.829	0.821

being deemed a MW analogue. In total, this suite of zoom-in simulations contains 42 MW-analogues simulated at high resolution, with each hydrodynamic zoom-in having a complementary dark matter-only zoom-in simulation. The resultant resolution of these simulations is a dark matter particle mass equal to $m_{\rm DM} = 1.17 \times 10^5$ M$_\odot$ h^{-1}, and initial baryonic particle mass equal to $m_{\rm gas} = 2.23 \times 10^4$ M$_\odot h^{-1}$. The gravitational softening length for these zoom-in simulations is set to 125 pc h^{-1} in physical coordinates for $z \leq 3$, and is changed to a constant comoving scale at earlier times. Thus, ARTEMIS is somewhat higher resolution than the simulations described previously.

3.3 Global properties

Here I present results for the effects that these different cosmologies have on the structure which forms across the different simulations. I start by examining the effects on global properties of the simulated volume, including the halo and subhalo mass function, and the subhalo V$_{\rm max}$ function.

3.3.1 Spherical-overdensity halo mass function

The first statistic I examine is the spherical-overdensity (SO) halo mass function (HMF), shown in Fig. 3.1. Here I define the SO halo mass function as the number density of haloes which exist per logarithmic mass interval: $\phi \equiv dn/d\log_{10}(M)$, which in this study is plotted as a function of SO mass: $M = M_{\rm 200,crit}$. This is defined as the mass contained within a radius $R_{\rm 200,crit}$, which encompasses an overdensity 200 $\times$ the critical density of the universe.

Haloes in this study are identified using the SUBFIND algorithm (Springel et al., 2001; Dolag et al., 2009). First a standard Friends-of-Friends (FoF) algorithm is run on the dark matter distribution (Davis et al., 1985), linking all particles which have a separation less than some fraction of the mean inter-particle separation (with this fraction being set to 0.2 in this study). With the FoF groups identified, SUBFIND then goes through each group and identifies locally bound substructures (subhaloes). The FoF group is centered on the position of the most-bound particle (lowest gravitational potential) in the central subhalo; i.e., the most massive subhalo in the FoF group. SUBFIND calculates a variety of subhalo parameters, including $M_{\rm sub}$ (the summed mass of all particles deemed to be gravitationally-bound to a subhalo) and $V_{\rm max}$ (the value at which a subhalo's circular velocity profile, $V(r) \equiv \sqrt{GM(<r)/r}$, reaches its maximum). $V_{\rm max}$ is a more stable quantity compared to the mass of a subhalo as it is less sensitive to how the subhaloes are identified and defined and it is more robust to tidal stripping (e.g. Diemand et al., 2007; Springel et al., 2008).

Focusing first on the cosmologies which have a running scalar spectral index as a free parameter, it can be seen in Fig. 3.1 that there is a relatively large suppression ($\approx 10-20\%$) in the number density of haloes with $M_{\rm 200,crit} \lesssim 10^{11}$ M$_\odot$ h^{-1} for the case with a negative running cosmology. This is best illustrated in the bottom panel of this plot, which shows the HMF of each cosmology normalised with respect to the reference simulation[4]. Conversely the opposite is seen for the cosmology which has a

[4]Note that the result shown for the EAGLE hydrodynamical simulation in the bottom panel is normalised by the complementary dark matter-only counterpart to the full hydrodynamical result. This is true for all ratio panels shown throughout this chapter.

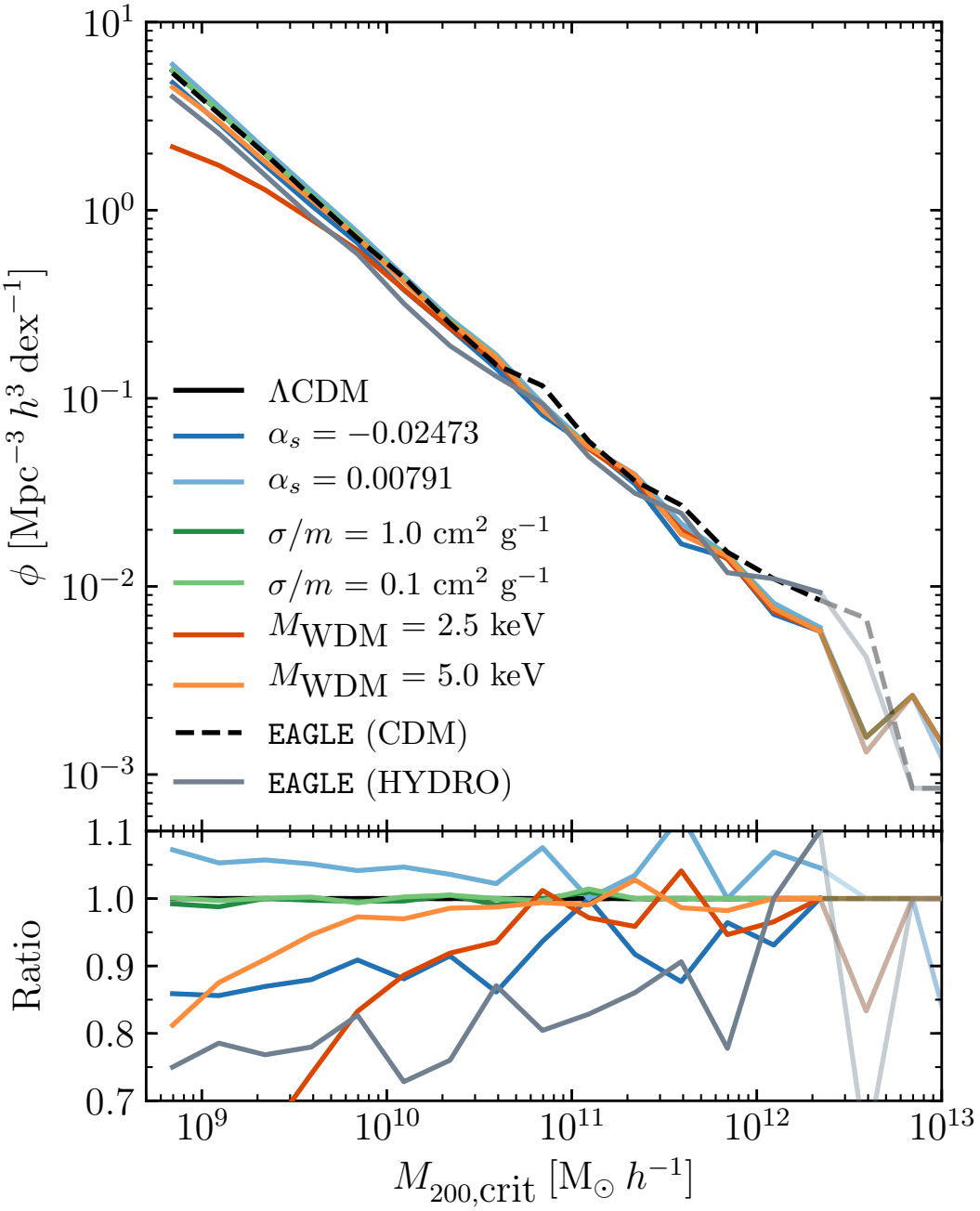

Figure 3.1: Top: number density of haloes per logarithmic mass interval, plotted as a function of their spherical overdensity mass. Bottom: the results in the top panel normalised with respect to the ΛCDM result. Note for the EAGLE simulations, the hydrodynamical simulation result is normalised with respect to the result from the complementary dark matter-only simulation. The lines become transparent for mass bins which have fewer than 10 haloes.

positively-running scalar spectral index, which sees an $\approx 10\%$ increase in the number density of haloes at these masses. These results illustrate how relatively subtle changes to the primordial matter power spectrum are able to have relatively large effects on the growth of structure on small scales.

Similar to the effects of a negative running cosmology, switching to WDM also leads to a significant suppression in the mass function at low masses. As expected, the effect is largest in the simulation with the lighter WDM particle mass. This is a well-known result, having been found for a range of WDM masses and models previously (e.g., Smith and Markovic 2011; Angulo et al. 2013; Bose et al. 2016).

These results illustrate the potential difficulty in constraining some of these cosmological extensions through simply counting the number of low-mass haloes. For example, the cosmology with a negatively-running spectral index can lead to a suppression very similar to that seen in the WDM cosmologies, particular at masses around 10^9 $M_\odot$. Furthermore, if the cosmology happened to be a combination of either WDM + positive α_s or WDM + negative α_s, this could lead to a universe very similar to a ΛCDM universe in the case of the former, and a universe with an apparently much warmer WDM model in the case of the latter.

Examining the simulations where the dark matter is allowed to interact with itself, there is no significant effect on the number density of SO haloes which form. This agrees with previous results that have been found when comparing large-scale statistics in SIDM and CDM cosmologies (e.g. Rocha et al., 2013). However, as I show below, SIDM can strongly affect the abundance of *satellite* haloes embedded within their hosts relative to that of the reference cosmology. In addition, SIDM can have a large effect on the internal properties (e.g., density distribution), which I also discuss below.

I now compare the previous effects, present due entirely to changes in the cosmological model, to those present in fully hydrodynamic simulations in the context of the standard model. Examining the result from the EAGLE simulation, it is interesting that the suppression seen in the HMF is bracketed by the results for the two WDM cosmologies, and the cosmology with a negative running. For example the

EAGLE simulation predicts a suppression of around 20% for haloes with mass around 10^9 $\mathrm{M}_\odot$ h^{-1}, whereas the suppression seen in the different cosmologies range between $\approx (15 - 50)\%$. Note that the suppression of the HMF for EAGLE was also shown previously by Schaller et al. (2015). Physically, the suppression of the halo mass function in the hydrodynamical simulations is the result of ejection of baryons due primarily to stellar feedback at these mass scales (see also, Sawala et al. 2013, who demonstrated this effect for subhaloes).

Another interesting feature is how the suppression of the halo mass function as a function of mass in the EAGLE run is closely mimicked by the result seen for a (dark matter-only) cosmology with a negative running, at least in shape. Furthermore, as was shown in Chapter 2, baryonic effects and the effects from the inclusion of a running spectral index appear to be separable to within a few percent, with each effect treatable as a multiplicative correction to the HMF of a ΛCDM gravity-only simulation. As such, in the presence of an (unaccounted for) positively-running scalar spectral index, one would tend to underestimate the role of baryons in suppressing the HMF. This problem is compounded by the current uncertainty in the suppression of the HMF due to baryonic physics on these scales. This is because current observations measuring the gaseous component of haloes on these scales (e.g. Giovanelli et al., 2005; Brown et al., 2017; Haynes et al., 2018) – which are a proxy for how efficient stellar feedback is at removing baryons from these haloes – are themselves quite uncertain. This propagates through to poor constraints on the stellar feedback implemented into hydrodynamical simulations. For example, as was shown in Davies et al. (2020), there can be a large discrepancy in the gas fractions predicted at halo masses around $10^{11.5}$ $\mathrm{M}_\odot$ in simulations with different feedback implementations. This was shown to be true when comparing the gas fractions seen in the EAGLE simulation and those seen in the IllustrisTNG simulation (Nelson et al., 2018; Springel et al., 2018; Pillepich et al., 2018a,b). However, despite their differences, both of these simulations provide cold gas fractions which are consistent with present constraints (Crain et al., 2017; Stevens et al., 2019).

The change in the SO halo mass function can be more readily understood by examining

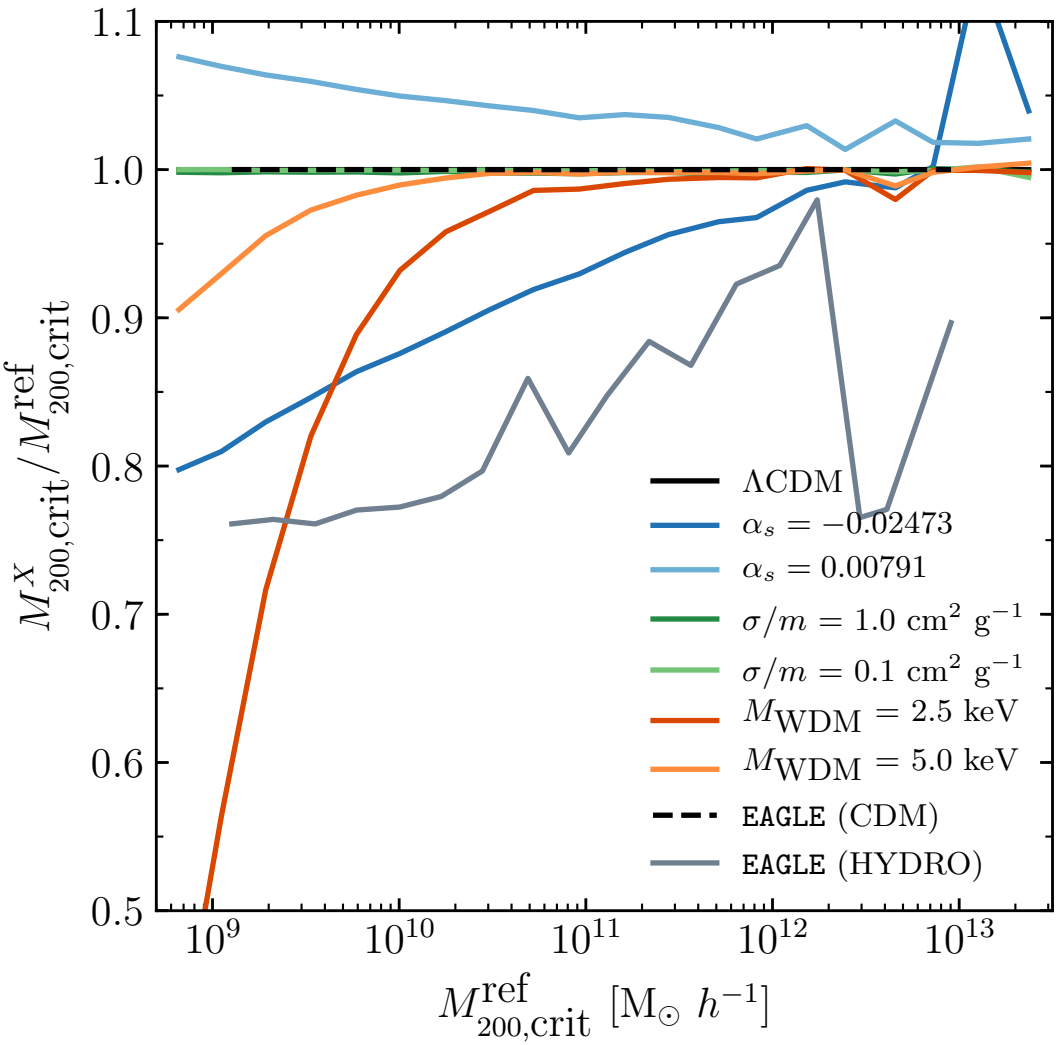

Figure 3.2: The fractional change in mass of a matched set of haloes across the different cosmologies, plotted as a function of the matched mass in the reference simulation, computed at $z = 0$. This result provides an intuitive explanation for the effects seen on the HMF due to the changes in cosmology, or through the inclusion of galaxy formation physics in the simulations.

how individual haloes change their mass across the different cosmologies[5]. In order to calculate the change in mass, I first need to match haloes in different simulations using the unique IDs of the dark matter particles. I do this by bijectively matching the 50 most bound particles of haloes in the reference cosmology to each cosmological extension in turn. I only use haloes which successfully match both forwards and backwards in all simulations.

Using the list of matched haloes, I examine how the masses of individual haloes change across the different simulations. Fig. 3.2 shows the median of the fractional change in mass of haloes in the different cosmologies, alongside the result for the EAGLE simulation.

In terms of the effects of a running scalar spectral index, the positive-running cosmology boosts the halo masses by $\approx 5\%$ compared to its ΛCDM counterpart, whereas the masses are decreased in a negative-running cosmology by $> 10\%$ (with the largest effects coming at low masses). It is worth noting that, although the magnitude of this effect (and the effects seen throughout this chapter on the various statistics examined) is larger in the negative running cosmology, this cosmology is also slightly more extreme than the cosmology with a positive running scalar spectral index (i.e. the initial density field has a larger difference with respect to ΛCDM in the case of the negative running cosmology). The reason for this is because the $Planck$ 2015 results slightly favour a negative running cosmology. As such, the effect on the initial matter distribution in this cosmology is larger than in the positive running cosmology (see e.g. Fig. 2.2). This effect echos what was found in Chapter 2, extending the findings of that chapter down to lower masses and illustrating further how the effects of a cosmology with a running spectral index are more pronounced on smaller scales.

There is also a strong effect on low-mass haloes in the most extreme WDM cosmology, with these haloes being less massive compared to their reference counterpart. This is expected due to the cut-off in the power spectrum on small scales, which preferentially affects low-mass haloes. The two different SIDM cosmologies have little effect on the halo mass over the entire mass-range sampled here.

[5]This is possible since the simulations use the same initial phases.

Examining the results from the EAGLE simulation, again the result seen in the HMF is echoed here, with the mass of a matched set of haloes being reduced in the full hydrodynamic run, compared with its dark matter-only result. The effect is strongest at lower masses, where stellar feedback in particular is able to efficiently blow gas out of the haloes, thus reducing their overall mass. This, in turn, reduces the mass accretion rate onto the haloes, effectively amplifying the change in the final halo mass (Sawala et al., 2013; Schaye et al., 2015). Note that the convergence of the halo mass in the EAGLE hydrodynamical simulation to the matched mass in the dark matter-only simulation, at around $M_{200,\mathrm{crit}} \approx 10^{12}\ \mathrm{M}_{\odot}\ h^{-1}$, likely happens at too low of a mass. Observations show that only haloes above $M_{200,\mathrm{crit}} \sim 10^{14}\ \mathrm{M}_{\odot}\ h^{-1}$ are 'baryonically closed' (e.g., McCarthy et al. 2017), whereas the EAGLE simulations demonstrate convergence to the universal baryon fraction at a considerably lower halo mass (see fig. 15 of Schaye et al. 2015). A more realistic behaviour for the effects of baryons at high halo masses can be found in Velliscig et al. (2014) (see their fig. 2).

As already discussed, the similarity in the magnitude of the change to halo mass and, in some cases its dependence on mass itself (e.g., negative running cosmologies and baryonic effects have a similar mass dependence), strongly suggest that baryonic and cosmological effects on halo mass will be degenerate. As I will show, however, the relative effects depend strongly on the nature of the probe, suggesting that multi-probe data sets are a potential way to break these degeneracies.

3.3.2 The subhalo mass and V_{max} functions

I now examine the subhalo mass function (SMF) and subhalo maximum circular velocity function (SVF). Similarly to the HMF, these quantities are defined as the number of subhaloes of mass M_{sub} (maximum circular velocity V_{max}) that exist per cubic comoving Mpc, per logarithmic mass (velocity) interval: $\phi \equiv dn/d\log_{10}(X)$ (where $X = M_{\mathrm{sub}}$ or V_{max}). As these quantities are well-defined for both central and satellite subhaloes (unlike SO masses), I investigate them separately.

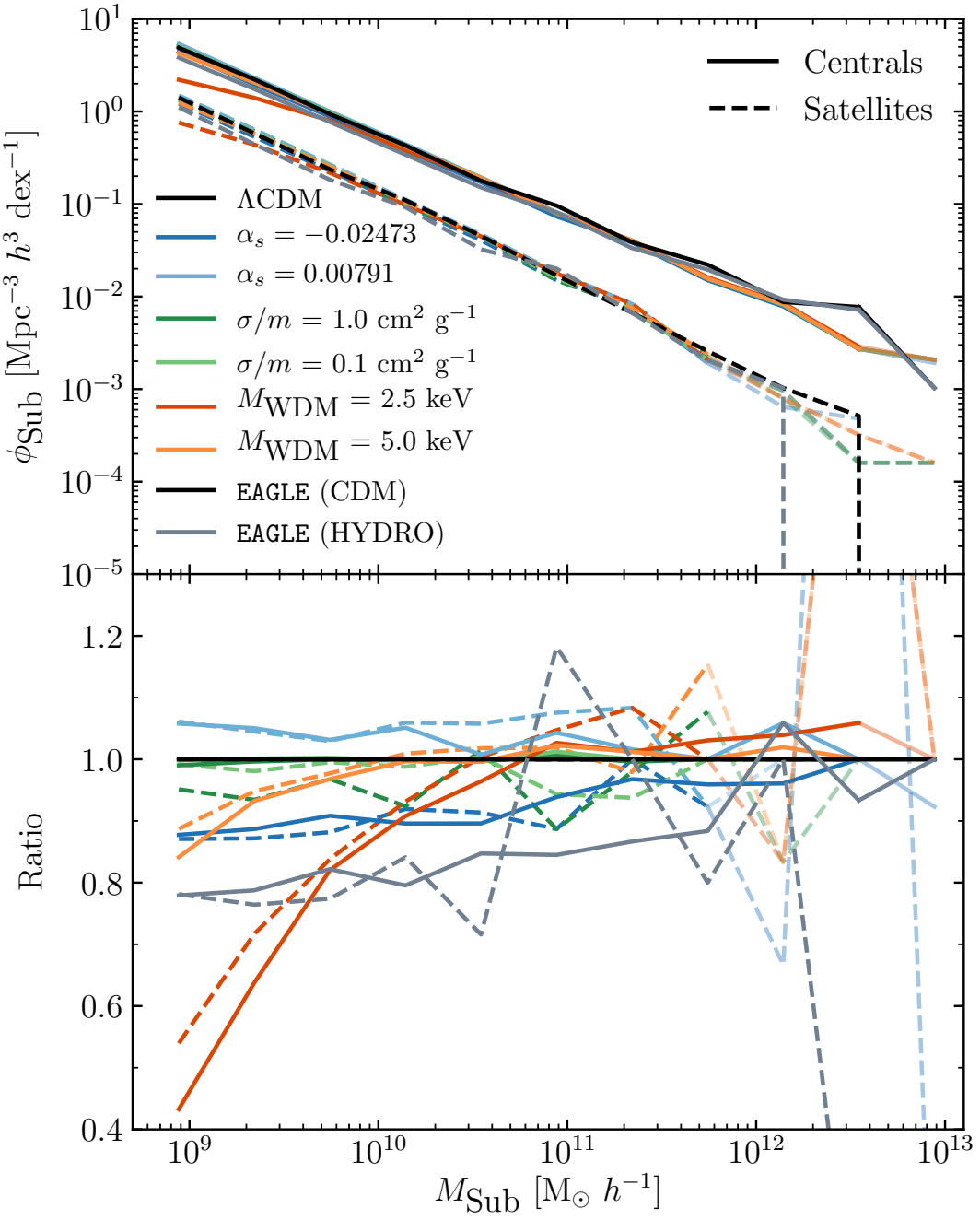

Figure 3.3: Top: the $z = 0$ number density of subhaloes as a functions of subhalo mass, split into the result for central subhaloes (solid) and satellite subhaloes (dashed). Note that this only includes subhaloes which have more than 200 particles bound to them, which was found to be a conservative resolution cut. Bottom: this shows the results in the top panel normalised to the result in the reference simulation, thus highlighting the differences between the simulations. The lines turn transparent for mass bins which have fewer than 10 subhaloes in.

The SMF is shown in Fig. 3.3, which I split into the satellite and central mass functions. A central subhalo is defined as the most massive subhalo contained within a single FoF group, with all other subhaloes in that same FoF group being defined as satellites. The bottom panel in this plot shows the result (be it the satellite or the central mass function) for each cosmology normalised with respect to the corresponding result in the reference ΛCDM simulation. Note that when examining subhaloes in this study, I focus on subhaloes with a mass $> 5 \times 10^8$ M$_\odot$, and $V_{\rm max} > 15$ km s^{-1}. These values were calculated by comparing the $M_{\rm sub}$-$V_{\rm max}$ relation, along with the SMF, between two different resolution simulations. This allows a conservative upper-limit to be placed on the values of $V_{\rm max}$ and $M_{\rm sub}$ for which these parameters are numerically converged (see Appendix B.1).

Focusing on the bottom panel of Fig. 3.3, the results largely mirror those for the SO HMF in Fig. 3.1. Furthermore, in general there are no large differences in the mass change for centrals and satellites for a given variation with respect to the reference ΛCDM model, with the exception of the SIDM simulations. Here, in particular for the simulation with the higher cross-section, satellites appear to be more strongly affected than central subhaloes relative to the reference ΛCDM case. I return to this point below.

Next I examine the subhalo V$_{\rm max}$ function, which is shown in Fig. 3.4. The effect that varying the underlying cosmology has on this is very similar to that seen in the SMF. For example, the WDM models and the negative running cosmology all lead to a large suppression in the number density of subhaloes at fixed $V_{\rm max}$, with the positive running cosmology being the only model which produces an enhancement. Similarly, in the most extreme SIDM cosmology, the number density of satellites is also suppressed, whereas there is little effect on the centrals. The result for the EAGLE simulation is also very similar to that seen in the SMF, in that at fixed $V_{\rm max}$ there is a suppression in the number density of subhaloes in the hydrodynamic simulation. This is true for both centrals and satellites.

Returning now to the difference between the impact of SIDM on satellites relative to central subhaloes, I believe this comes about due to the combination of two effects

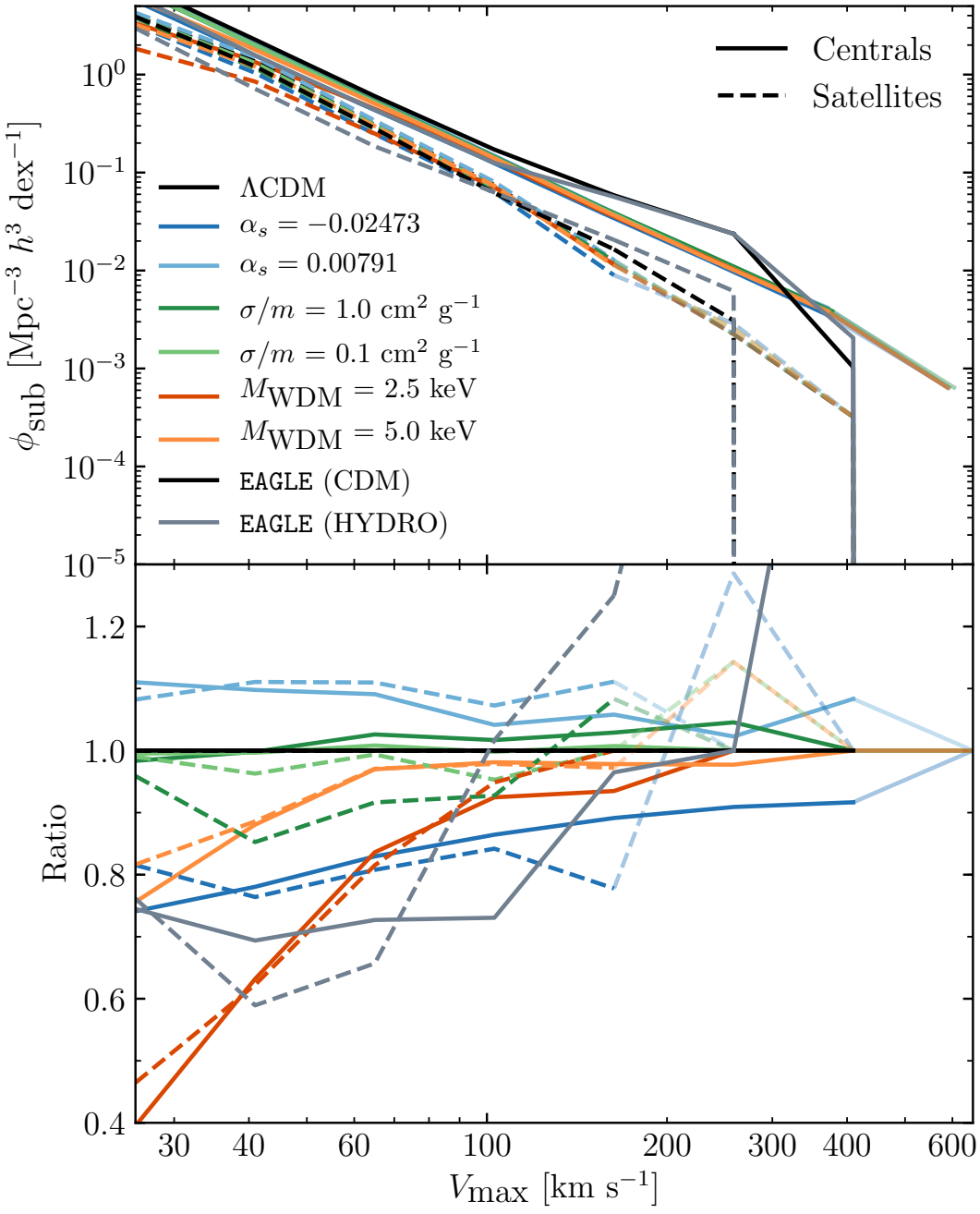

Figure 3.4: Top: the $z = 0$ number density of subhaloes, now as a function of $V_{\rm max}$, once again split up into central subhaloes (solid line) and satellite subhaloes (dashed line) for the different cosmologies examined in this study. Bottom: the above results normalised with respect to the result in the reference cosmology, plotted to make the differences between the effects of each cosmology more apparent. Note the lines are made transparent for mass bins with fewer than 10 subhaloes present.

working in tandem. Firstly, there is the 'evaporation' of the subhaloes, which happens due to elastic collisions between the particles from a subhalo, and the particles of the host halo. These scattering events lead to neither particle being bound to the subhalo (Vogelsberger et al., 2012), causing the subhalo to lose mass as it infalls into the host halo. This evaporation mechanism was the original motivation for using SIDM to solve the missing satellites problem (Spergel and Steinhardt, 2000). However, another effect which causes the subhaloes to lose mass is tidal stripping. Due to the core which forms in subhaloes, they are also more susceptible to tidal stripping (Peñarrubia et al., 2010) (with Dooley et al. 2016 finding this to be the more dominant effect out of the two). As such, both of these effects work to decrease the mass of a subhalo as it travels through its host halo, which is what drives the differences between the central and satellite mass ($V_{\rm max}$) functions in the more extreme SIDM cosmology. I explore this effect further in Fig. 3.8, which shows a strong suppression in the number density of satellite subhaloes in the central regions of their hosts in a SIDM cosmology, relative to the CDM case.

I have also examined the above statistics at early times, corresponding to $z = 0.5, 1.0$. However the results seen at these earlier redshifts are quantitatively very similar to the $z = 0$ result, except that the results become more noisy at the high-mass end due to the finite box size. For this reason, and for brevity, I only show the $z = 0$ results.

3.3.3 Theoretical vs. observable quantities

It is important to note that some of the aforementioned quantities are not strictly observable with current measurements. For example, generally speaking, individual total halo masses can only be estimated with reasonable accuracy on the scale of galaxy groups and clusters[6], where a variety of methods exist for measuring masses (e.g., X-ray, gravitational lensing, and galaxy velocity dispersion measurements). Thus, measurements of the halo mass function are currently very challenging on the scales I am interested in here. On the other hand, observable quantities such as stellar mass are thought to be very good proxies for total halo mass, with a typical scatter in the stellar

[6]Measurements of total masses are possible for lower-mass systems (e.g., with galaxy-galaxy lensing), but generally require the stacking of large numbers of systems to make precise measurements.

mass at fixed halo mass of 0.2 dex (e.g., Behroozi et al. 2013). In terms of the quantity $V_{\rm max}$, while rotation curves are directly accessible observationally, current observations of low-mass galaxies struggle to reach the flat part of the rotation curve, so that estimates of $V_{\rm max}$ can sometimes require significant extrapolation.

Ultimately, in order to make definitive statements about the degeneracies between baryon physics and changes in cosmology for low-mass galaxies, one should make synthetic (or 'mock') observations from the simulations and analyse them in a way that is faithful to what is done for genuine observations. In order to do this, however, a simulation suite which includes baryon physics for all cosmological variations is required. I leave this for future work.

3.4 Internal halo properties

I turn now to the internal structure of host haloes across the different simulations. I stack haloes in 6 equally spaced logarithmic mass bins between $10.0 \leq \log_{10}(M_{\rm 200,crit}\ [{\rm M}_\odot]) \leq 13.5$, with the results shown corresponding to the median result in each mass bin. In particular, I examine the spherically-averaged dark matter density profiles of haloes (which I also use to examine the concentration–mass relation later), along with the circular velocity profiles of the haloes. I also examine how subhaloes are radially distributed in their host haloes.

3.4.1 Dark matter density and circular velocity profiles

The spherically-averaged dark matter density and circular velocity profiles for all of the simulations I consider are shown in Figs. 3.5 and 3.6, respectively. To place the 'dark matter-only' simulations on an equal footing to the hydrodynamical simulations, I rescale dark matter particle masses in the dark matter-only simulations by the ratio $\Omega_{\rm CDM}/\Omega_{\rm m}$ (where $\Omega_{\rm m}$ is the total matter density in units of the critical density). As mentioned, the results shown in this section correspond to the median result of all

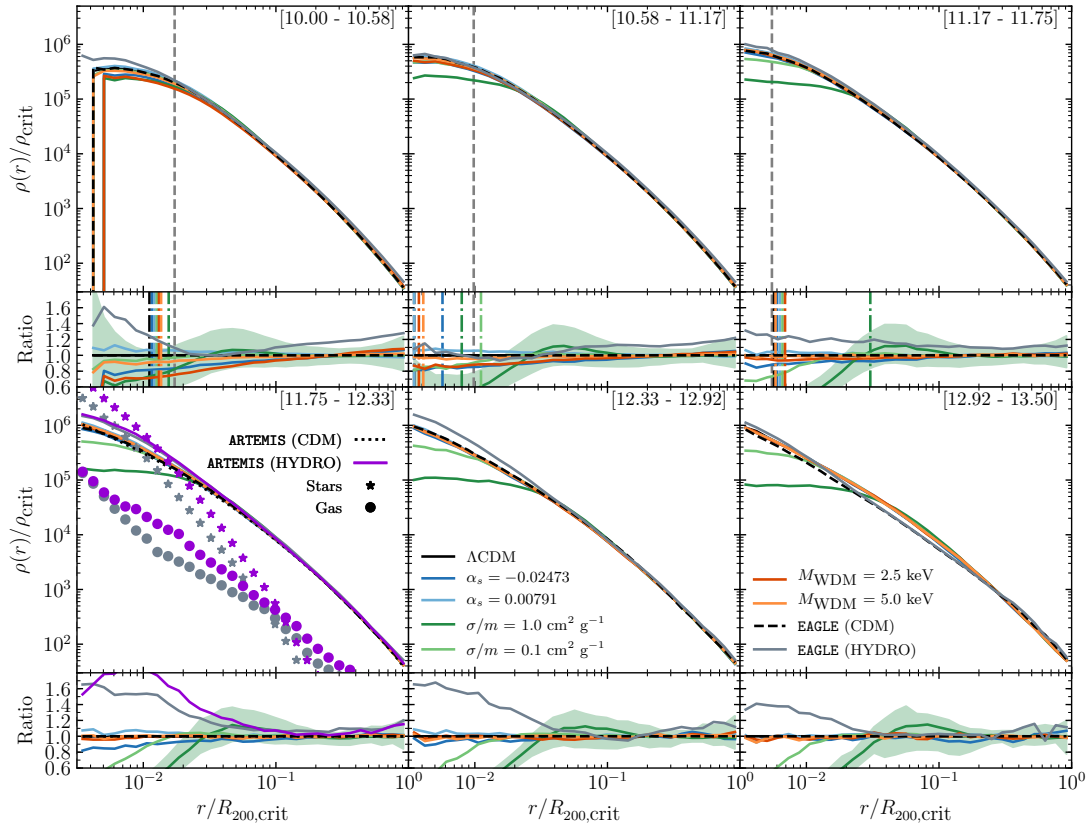

Figure 3.5: Spherically-averaged dark matter density profiles for the different cosmological models at $z = 0$. The different panels here correspond to different mass bins, with the mass window being shown in the top-right hand corner of each panel (equal to $m_1 \leq \log_{10}(M_{200,\rm crit}\ [\rm M_\odot]) < m_2$). The different curves correspond to the median result in that mass bin. The smaller panels below the density profiles show the median density profiles in each mass bin normalised with respect to the median density profile in the reference cosmology in that mass bin. The result is also plotted for haloes in the EAGLE simulation. Alongside this, I also compare these results to the density profiles calculated for the MW analogues from the ARTEMIS simulations. The results for this is shown in the bottom-left panel. I also plot in this panel the stellar (shown by stars) and gaseous (shown by circles) density profiles for the two hydrodynamic simulations. The shaded regions show the 16th-84th percentile result for the most extreme SIDM cosmology. This scatter is representative of the other 6 cosmologies, and shows the significance of the core produced in the SIDM cosmologies' density profiles. The vertical dashed line represents the median convergence radius for that mass bin, calculated in the ΛCDM cosmology. The vertical dot-dashed lined shown in the ratio panel corresponds to the convergence radius calculated using the ratios as a convergence diagnostic rather than the actual density profiles themselves, as described in Section 3.4.2. Note that this radius corresponds to a conservative upper-limit on the convergence of the ratios, as it is calculated based on the minimum radius down to which a lower resolution simulation is converged with the simulations for which these results were extracted. I only plot this result for the first three mass bins, as it is for these mass bins that the absolute profiles are not converged over the entire radial range examined in this study. For instances where this convergence radius is exactly equal for different cosmologies I slightly displace them to larger radii for clarity.

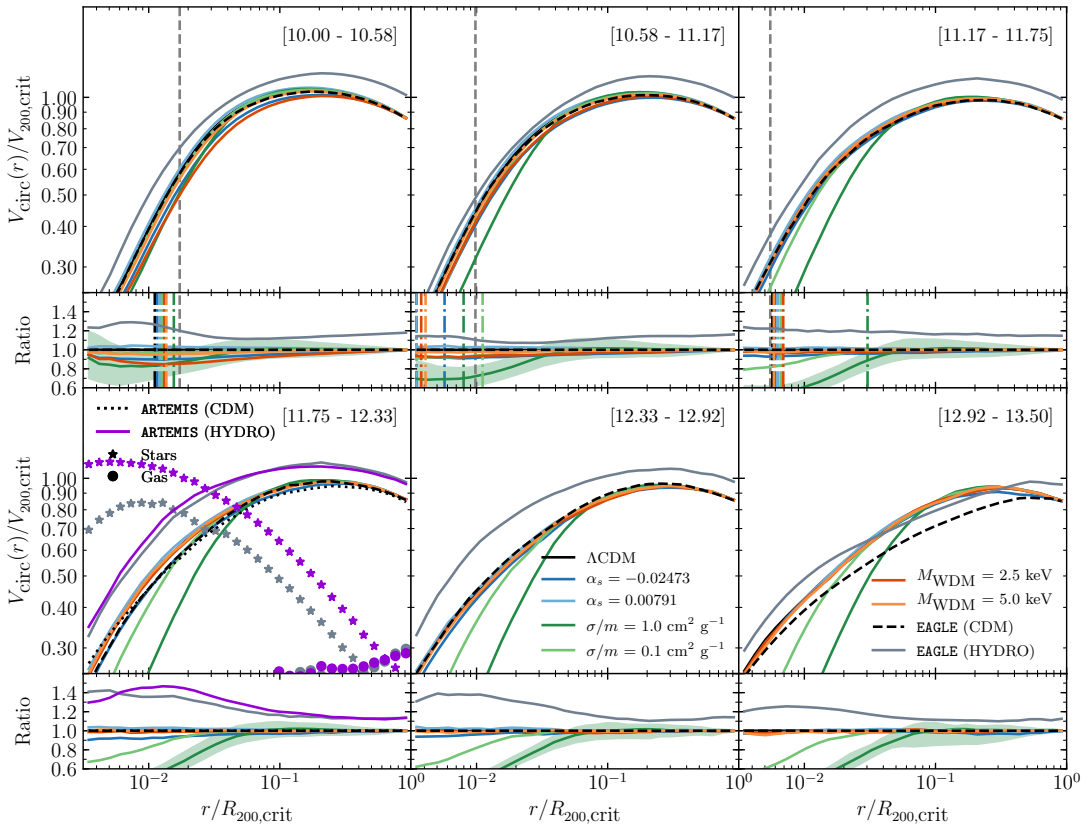

Figure 3.6: The median dark matter circular velocity profile of haloes in 6 separate mass bins for the different cosmologies examined in this study at $z = 0$, scaled by the virial circular velocity. The result is plotted in the same mass bins examined in the previous plot, indicated in the top right-hand corner of each panel. The bottom panel(s) below each main plot show the above result normalised with respect to the median result in that mass bin in the reference cosmology. Once again, the shaded regions correspond to the 16th-84th percentile plotted for the more extreme SIDM cosmology, with this scatter being representative of the other cosmologies. The vertical dashed line corresponds to the median convergence radius of haloes in that mass bin in the ΛCDM cosmology. The vertical dot-dashed line shown in the ratio panels corresponds to the convergence radius obtained from the Section 3.4.2 analysis. Once again, I only show this result for the top three panels, and slightly displace any radii which are exactly equal across different cosmologies for clarity.

haloes in that mass bin, with the mass bin indicated in the top right-hand corner of each panel. The results are shown in dimensionless units, with the density profiles being scaled by the critical density of the universe at $z = 0$ and the circular velocities scaled by the circular velocity at $R_{200,\rm crit}$, $V_{200,\rm crit} = \sqrt{GM_{200,\rm crit}/R_{200,\rm crit}}$. The profiles themselves are computed in 32 logarithmically-spaced radial bins between: $-2.5 \leq \log_{10}(r/R_{200,\rm crit}) \leq 0$.

The plots are split into 6 panels according to halo mass bin. The smaller panels below the main panels correspond to the median density/circular velocity profile in that mass bin normalised with respect to the median density/circular profile in the reference ΛCDM cosmology in the same mass bin. The vertical dashed line in each panel corresponds to the median convergence radius calculated for the ΛCDM simulation. I compute the convergence radius following that advocated by Ludlow et al. (2019) (see their equation 15). This is a follow-up study to that done in Power et al. (2003), where the convergence radius is calculated explicitly for stacks of haloes. Ludlow et al. find that the median result of a stack of haloes (circular velocity profiles in their study) is converged to smaller radii than what was advocated by Power et al. (2003). In this study, however, I am less focused on the absolute value of the density and circular velocity profiles and more on the *relative* effects (shown by the ratio panels in each plot) on the profiles due to changes in cosmology and inclusion of baryons. Therefore, as an aside, I also investigate below (see Section 3.4.2) whether the *ratio* of the density profiles of haloes in non-standard cosmologies with respect to ΛCDM are potentially converged to smaller radii than that advocated by Ludlow et al. (2019). This is particularly relevant for the first three mass bins, which are not converged over the entire radial range which I examine here. I indeed find the ratios are generally converged to small radii and as such I also plot on Figs. 3.5, 3.6 the convergence radii that I advocate for these first three mass bins.

The strongest cosmological effect on the profiles come from the SIDM model, particularly the run with the largest cross-section. The scattering acts as an efficient mechanism for dynamically heating and redistributing the mass in the inner regions, producing a near constant-density core. The size of the core relative to the virial radius is an

increasing function of halo mass, this is expected given the fact that the scattering rate depends on both the local density and velocity. This means that the scattering rate at a fixed fraction of $R_{200,\text{crit}}$, scales with $V_{200,\text{crit}}$; as such, more massive haloes (higher $V_{200,\text{crit}}$) have higher scattering rates, at a certain fraction of $R_{200,\text{crit}}$, resulting in larger cores forming. This effect has been seen in previous studies (e.g. Colin et al., 2002; Rocha et al., 2013; Vogelsberger et al., 2019; Robertson et al., 2019). Interestingly, in the $\sigma/m = 1.0$ cm^2 g^{-1} cosmology, the redistribution of matter from the inner regions to the outer regions tends to lead to a small *enhancement* in the dark matter density on scales of ≈ 0.05–$0.1\ R_{200,\text{crit}}$ relative to the baseline collisionless ΛCDM model.

The next largest cosmological effect is seen in the cosmology with a negative running of the spectral index. Here there is also a suppression in density in the inner-regions, particularly for the lower-mass haloes, with there being an $\approx 20\%$ decrease in the central density of these objects ($M_{200,\text{crit}} < 10^{11}$ M$_\odot$). This effect decreases with increasing mass, with the profile in the highest-mass bin being broadly consistent with the result in the reference cosmology.

This trend, however, continues further, as was shown in Chapter 2; a cosmology with a negative running actually predicts an enhancement in the density profile of haloes with mass $\gtrsim 10^{14}$ M$_\odot$. Conversely to the SIDM models where there is a very sharp drop in the density profile and a small increase in density over a narrow radial range just outside of the core, the decrease in the density profile towards the center in the negative running cosmology is far more gradual.

There is also a slight decrease in the profiles in the inner regions in the two WDM models, particularly at the low mass end, with this effect disappearing quickly with increasing mass; with haloes of mass $M_{200,\text{crit}} \geq 10^{11.17}$ M$_\odot$ having density profiles almost indistinguishable from the ΛCDM result. This agrees with the results of Bose et al. (2016), along with the lower-concentration of low-mass haloes found in Ludlow et al. (2016) (see also Fig. 3.9).

The cosmology with a positive running of the spectral index is the only cosmology which appears to predict an enhancement in the central density (and circular velocity)

profiles of haloes. However, this enhancement is generally quite mild and decreases with increasing halo mass.

I now investigate the impact of baryons on the dark matter density and circular velocity profiles, using the EAGLE and ARTEMIS simulations. For the three lowest-mass bins, the impact of baryons on the dark matter density profiles in the EAGLE simulations is relatively mild. As the stellar mass fractions are very low in this regime (Schaye et al., 2015; Schaller et al., 2015), there is no significant adiabatic contraction of the dark matter. On the other hand, EAGLE may underestimate the effects of repetitive feedback episodes in introducing a core in the dark matter, due to its lack of an explicit cold phase of the ISM and a relatively low density threshold for star formation (e.g., Benítez-Llambay et al. 2019). However, when examining mass bins with $M_{200,\mathrm{crit}} \geq 10^{11.75}$ $\mathrm{M}_{\odot}$, where it is not thought that feedback can produce such cores (e.g., Dutton et al. 2011), the inner density and circular velocity profiles appear far more pronounced in the hydrodynamic result compared to the dark matter-only result. This illustrates the contraction of the dark matter in the central regions due to the presence of stars in the inner regions of the central galaxies of these haloes. A similar result was shown by Schaller et al. (2015) (see their fig. 6), who also showed the density profile of stars in their host haloes, illustrating how these dominate the total matter density in these regions, particularly for these higher mass haloes.

Focusing on haloes in the mass range $10^{11.75} \leq M_{200,\mathrm{crit}}/\mathrm{M}_{\odot} < 10^{12.33}$ (shown in the bottom-left panel of the same figure), I also plot the median result for the dark matter density and circular velocity profiles computed for the 42 MW analogues from the ARTEMIS simulations. Recall that the mass-range sampled by these zoom-in simulations is from: $10^{11.9} \leq M_{200,\mathrm{crit}}/\mathrm{M}_{\odot} < 10^{12.3}$, roughly corresponding to the same range examined for the cosmological extensions [7]. Similarly to the results seen in the EAGLE simulation, at large r, the dark matter density and circular velocity profiles in the hydrodynamic simulations are quite similar to the result seen for the dark matter-only simulation. However, the density and circular velocity profiles in the inner regions

[7] When taking the ratio for the ARTEMIS, I divide the median result for the haloes in the full hydrodynamic run by the median result from the complementary dark matter-only zoom simulations

of the haloes ($r \lesssim 0.1R_{200,\mathrm{crit}}$) are far steeper in the ARTEMIS simulations than their dark matter-only counterpart. This effect is also larger than that seen in the EAGLE simulations and extends to larger radii. I argue that this is the case because ARTEMIS has higher stellar masses than EAGLE for this halo mass range (with the former being in better agreement with observations).

To demonstrate this, I also plot in this panel the density profiles of the stellar and gaseous components of the halo. Here one can see that ARTEMIS has a systematically larger stellar density at all radii compared to the EAGLE result (along with an increased circular velocity). It is these differences which produce the differing profiles between the two hydrodynamical simulations. Note that the apparent offset between the density and circular velocity profiles in the hydrodynamic simulations relative to the gravity-only simulations is due to the former having a larger median mass in each of the mass bins.

These results demonstrate the importance of having simulations which also include a prescription for galaxy formation physics, as baryonic physics has one of the largest effects on the underlying dark matter distribution in Figs. 3.5 and 3.6. This is particularly apparent when examining the panels which also show the stellar density (circular velocity) profiles. These show how the stellar component dominates the profiles in the inner regions and, via adiabatic contraction, produces the changes seen in the dark matter profiles. It is in these regions also where the different cosmological models are seen to have the largest effects. Therefore, as discussed in the Introduction, the ideal scenario is to simulate not only the standard cosmological model, but also plausible non-standard cosmologies using full cosmological hydrodynamical simulations. To date, only a small number of studies have attempted this. For example, recent simulations presented in Despali et al. (2019) explored SIDM hydrodynamical simulations, concluding that the gravitational potential of the stars at the centre of intermediate mass haloes ($M_{\mathrm{vir}} \approx 10^{12}$ M$_{\odot}$) significantly alters the DM distribution, removing the SIDM-induced core, while cores still formed in more massive haloes ($M_{\mathrm{vir}} \approx 10^{13}$ M$_{\odot}$), with this being related to the formation time of the halo. Using zoomed hydrodynamical simulations of clusters, Robertson et al. (2018) found a very complex interplay be-

tween baryons and SIDM, with some haloes showing dark matter cores, and others which do not. How the results of combined baryons + non-standard cosmology runs depend on the method for implementing and calibrating the feedback, the modelling of the cold ISM (or lack thereof), and the resolution of the simulations, has not yet been explored in much detail, but it would not be surprising if the conclusions about the interplay of baryons and cosmological effects were sensitive to these factors and should be explored.

The above analysis of the density and circular velocity profiles was done in bins of halo mass, using the self-consistently computed halo masses from each of the simulations. Since the halo mass itself changes as a result of cosmological and baryonic effects (as I showed in Section 3.3), this implies that, in general, for a given mass bin I am not analysing precisely the same haloes in each simulation. However, I have also examined a versions of Figs. 3.5 and 3.6 where I use matched haloes and binned the profiles according to the mass from the matched reference ΛCDM model. In general, the effects are very similar but are slightly more pronounced in the matched halo plot. For brevity, I do not include these figures here.

3.4.2 Convergence radius of relative cosmological effects

There have been multiple studies which examined the convergence of internal halo properties in numerical simulations (e.g. Power et al., 2003; Diemand et al., 2004; Navarro et al., 2010; Ludlow et al., 2019), which have shown that 2-body relaxation effects impose a lower-limit on the radius to which one can trust mass profiles of haloes. This was most recently investigated by Ludlow et al. (2019), who provided a criterion on the number of particles needed below a radius r for the median mass profiles of a stack of haloes to be converged.

These studies have been extremely useful when interpreting gravity-only N-body simulations. It is noteworthy, however, that they have all been done in the context of a ΛCDM universe and have focused on the convergence of the absolute values for the statistics examined. In this study, I am instead mostly interested in the relative effects

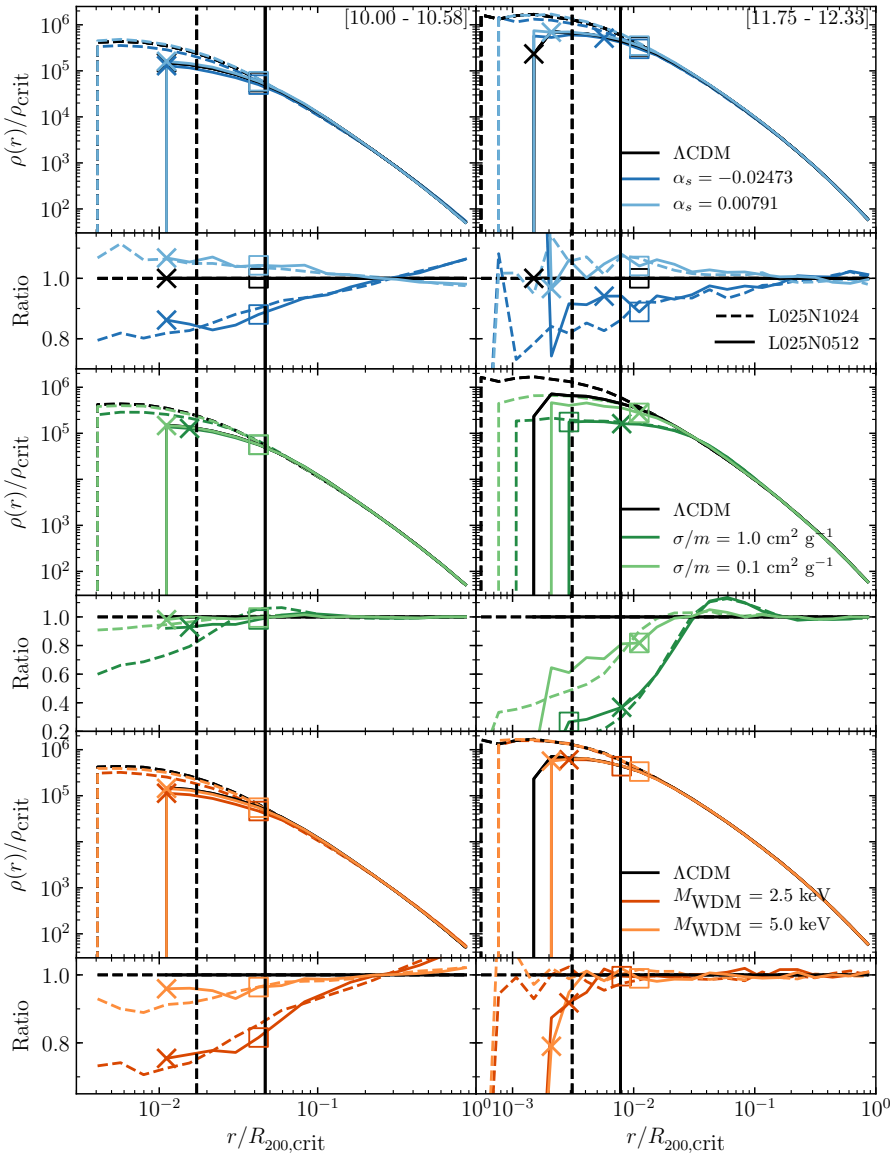

Figure 3.7: Comparison of the convergence of median spherically-averaged dark matter density profiles to the convergence of their ratios with respect to a ΛCDM cosmology. Columns are separated into different mass bins: Left are haloes in the mass range $10 \leq \log_{10}(M_{200,\rm crit}\,[\rm M_\odot]) < 10.58$, right are haloes in the mass range $11.75 \leq \log_{10}(M_{200,\rm crit}\,[\rm M_\odot]) < 12.33$. The different rows show the results for different cosmological extensions: top – running spectral index, middle – SIDM, bottom – WDM. Panels below the absolute density profiles show the ratios with respect to the result in the ΛCDM cosmology. Crosses show the radius at which the ratios diverge by greater than 10% relative to the higher resolution simulation. Hollow squares represent the radius at which the absolute density profiles diverge by greater than 10%. The veritcal solid and dashed lines show the median Ludlow et al. (2019) convergence radius for the ΛCDM cosmology in that mass bin, for the different tiers of resolution.

on certain statistics. In particular the ratio of, for example, the median spherically-averaged density profiles of haloes in non-standard cosmologies with respect to the result in the ΛCDM case. For this reason, as an aside, I briefly explore the convergence of relative cosmological effects. Readers who are less interested in the convergence properties may wish to skip ahead to Section 3.4.3.

To examine the convergence properties, I have run an additional set of simulations but at lower resolution, with 512^3 particles, $m_{\rm DM,\Lambda CDM} = 1.013 \times 10^7$ $\rm M_\odot$ h^{-1}, and $\epsilon = 500$ pc h^{-1}. I compute the density profiles in 32 logarithmically-spaced radial bins, ranging from: $-4.5 \leq \log_{10}\left(r/R_{\rm 200,crit}\right) \leq 0$ (note that this minimum radius is smaller than the minimum radius used in the previous section, this was chosen to test the ratios to as small a radius as possible).

The results are shown in Fig. 3.7, which is set up as follows: the columns represent two different halo mass bins (indicated in the bottom right corner of the top panel), the left column corresponds to the smallest mass bin of main FoF haloes examined in this study. The right column corresponds roughly to a MW analogue mass window. I look at these mass bins because, in the case of the former, these haloes will be most subject to numerical effects, and, in the case of the latter, because much of the emphasis of testing models of dark matter have been at MW scales (for obvious reasons). The rows in this plot correspond to the three different cosmological extensions (running, SIDM, WDM), indicated in the top-right of each right-column panel. I show both the median spherically-averaged dark matter density profiles for each cosmology, as well as, below this, the ratios of the median result taken with respect to the ΛCDM result. I also plot the median convergence radius calculated using equation 14 from Ludlow et al. (2019) for the two different ΛCDM simulations, with their line-styles indicating their resolution.

Similarly to what was done in previous convergence test studies, I define the convergence radius as the minimum radius for which $\left(R_{\rm high} - R_{\rm low}\right)/R_{\rm low} \leq 0.1$ is true, where $R_{\rm high}$ ($R_{\rm low}$) is the ratio in the high-resolution (low-resolution) simulation of the density profile of a cosmological extension with respect to the ΛCDM result. This radius is shown by the coloured crosses. I also show the radius to which the absolute

values of the density profiles in the lower-resolution simulations agree to within 10% of the higher-resolution result (indicated by the open squares).

Focusing first on the left column, it can be seen that in the case of the cosmologies with either a running spectral index or WDM species, that the ratios are converged with the result in the higher-resolution simulation to the smallest possible radius calculable in the lower-resolution simulation. If one focuses on the region between the two vertical lines, where I still trust the absolute value of the density profiles in the higher-resolution simulation, it can be seen that the ratio of the lower-resolution simulations agree extremely well with that in the higher-resolution result. This result is also echoed in the right column, but the ratios are more subject to shot noise due to the fewer number of haloes in this bin used to take a median.

However, this trend breaks in the case of the SIDM cosmologies, which may not be surprising due to the fact that cores develop in the inner regions due to physical processes and not just numerical two-body relaxation effects. In the case of the left column and for the cosmology with the larger cross-section for interaction, it can be seen that the lower-resolution simulation fails to capture both the core-formation due to SIDM (and the resulting density excess at slightly larger radii), which is resolved in the higher-resolution simulation. On the other hand, in the right-column the result is reversed relative to the other cosmologies. Here the absolute density profiles agree all the way to the inner-most radial bin in the case of the lower-resolution simulation, whereas the ratio is converged to the calculated convergence radius. I speculate that the reason for this is that the energy exchange due to the particle collisions is far larger than the small changes in energy due to two-body relaxation. As such, the core formed due to these particles collisions dominates that induced due to discrete sampling effects. The reason the ratio is not converged as well is because the core is now converged to the higher-resolution result, whereas there is an artificial core induced in the ΛCDM result. Consequently, the suppression in the ratio underestimates the core for the lower-resolution simulation.

These results are interesting and motivate us to examine the ratios below the convergence radius of Ludlow et al. (2019) calculated for these simulations. For the case of

SIDM cosmologies, this strategy may result in a slight underestimation of the actual (relative) effects present, as explained above.

Furthermore, these results show that when studying the effects of cosmological extensions on quantities such as the density profiles and circular velocity profiles, it may be possible to run a single high-resolution ΛCDM simulation and use the ratios from interesting cosmological extensions run at considerably lower resolution as a multiplicative adjustment to the high-resolution simulation. This approach can potentially save a great deal of computational expense.

3.4.3 Radial distribution of subhaloes

So far I have focused on the effects that cosmological variations or baryons have on the matter distribution in host haloes. I turn now to the effects on the subhaloes that exist within these host haloes. In particular, I show in Fig. 3.8 the median radial number density of subhaloes as a function of host halo mass. Note that I only include subhaloes which satisfy the $V_{\rm max}$ (> 15 km s^{-1}) and $M_{\rm sub}$ ($> 5 \times 10^8$ M$_\odot$ h^{-1}) convergence criteria. I normalise the resultant value in each mass bin, for each cosmology, by the average number density of subhaloes inside $R_{\rm 200,crit}$ calculated for the reference cosmology. The bottom panels show the results when normalised to the reference ΛCDM cosmology in that mass bin.

It can be seen that the largest effect in all mass bins comes from the cosmology with the lightest WDM mass. This makes sense, as this model has the largest suppression of the SMF (particularly at the low-mass end, which will dominate the signal seen here due to the steepness of the SMF). Adopting a 2.5 (5 keV) WDM particle mass, I see a 40% (20%) suppression in the number density of subhaloes, which is roughly independent of distance from the centre of the host halo (this is in agreement with, for example, the suppression seen in the number of satellites in Lovell et al. 2017b).

A similar effect is seen in the cosmology which has a negative running, in that, for all mass bins there is a suppression at all radii compared with the result in the stan-

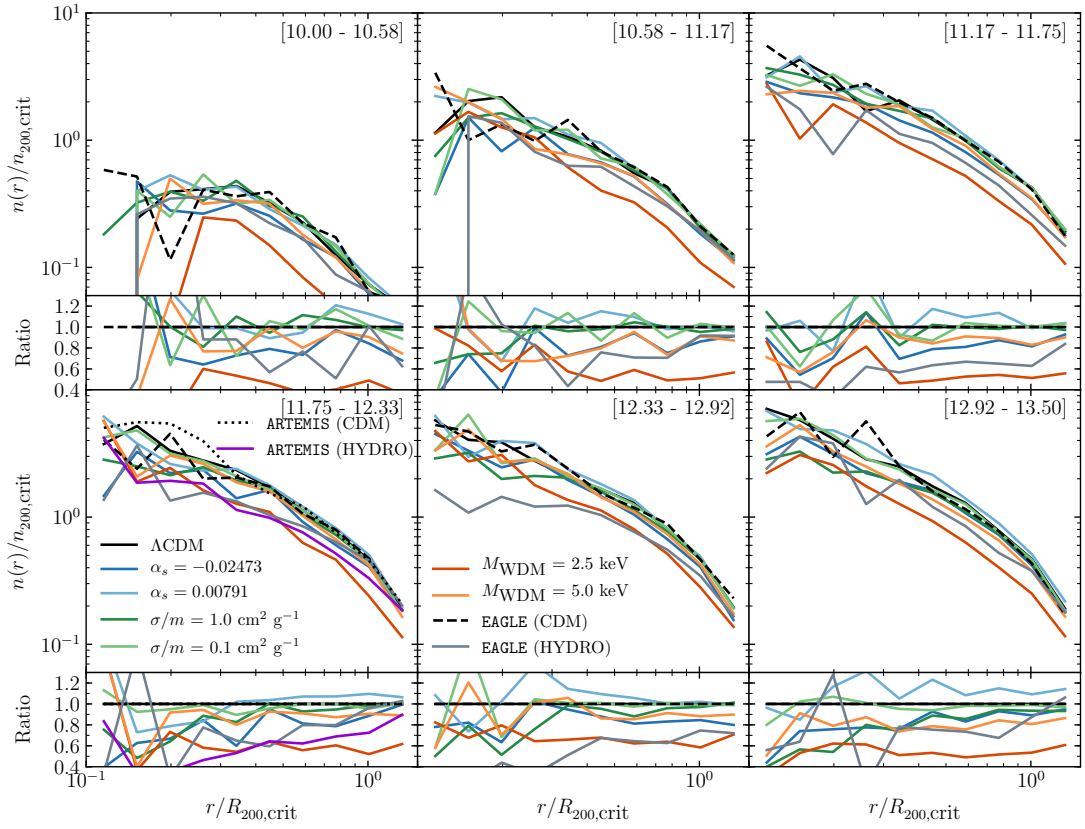

Figure 3.8: The stacked median spherically-averaged radial number density of all satellite subhaloes identified by the SUBFIND algorithm with a mass $> 5 \times 10^8$ M$_\odot$ h^{-1}, and V_{max} > 15 km s^{-1} inside host haloes in different mass ranges (indicated in the top right-hand corner of each panel). The result in each panel is normalised with respect to the average number density of subhaloes inside $R_{200,\mathrm{crit}}$ for that mass bin, in the reference cosmology. The bottom panel(s) below each plot show the result normalised with respect to the median result in the reference cosmology.

dard cosmology. The magnitude of the suppression in the number density ($\approx 20\%$ in this case) is similar to that seen for the 5 keV WDM model. Conversely, for the positive-running cosmology, there does not appear to be much of an effect relative to the reference cosmology, with there being only a very mild hint of an enhancement in the number of subhaloes at all radii in the larger mass bins.

Examining the result for the SIDM cosmologies, in the $\sigma/m = 0.1$ cm^2 g^{-1} cross-section there appears to be no discernible effect in any of the mass bins. When examining the more extreme SIDM model, there is also little to no effect in the low mass bins. However, at the high-mass end it can be seen that there is a clear suppression in the number density of subhaloes in the inner regions of these haloes, which increases with increasing host halo mass and with decreasing distance to the centre of the host halo. As discussed in Section 3.3, this effect is the result of heat transfer (the dark matter equivalent of thermal evaporation) due to scattering between 'hot' host dark matter particles and 'cooler' subhalo/satellite particles. This effect happens in conjunction with enhanced tidal stripping, due to the cored density profiles of these subhaloes (Peñarrubia et al., 2010). This effect was previously observed in Vogelsberger et al. (2012) for a MW-type halo (see also Nadler et al. 2020b; Banerjee et al. 2020).

These results are interesting as they show that, in the case of the WDM cosmologies, there is an almost systematic suppression in the number density of subhaloes as a function of radius in all mass bins. This means that, in principle, a technique where one simply counts the total number of subhaloes (satellite galaxies) could be used to rule out the most extreme WDM models, which as discussed in Section 3.2, is a technique already being used to place constraints on WDM masses (e.g. Lovell et al., 2014). However, this is slightly more complicated in the case of the less extreme WDM model, as this plot shows that the effects present in a cosmology with a negative running of the spectral index are highly degenerate to those in this WDM cosmology[8]. As such, it would be potentially difficult to disentangle these two effects through this

[8]Note that even the more extreme WDM model could effectively masquerade as a less extreme one if one also invokes a positive running scalar spectral index.

type of observation alone. However, going back to the density and circular velocity profiles of the haloes which host these satellites, there are more apparent differences in the underlying matter distribution which could then be used to differentiate these two cosmologies. Similarly, in the case of the most extreme SIDM cosmology, counting subhaloes could also potentially be used to constrain these models, in that for high-mass haloes, there appears to be a clear radial dependence in the suppression of the number density of subhaloes. This is a result which is unique among the cosmological extensions examined here. It is worth noting, however, that these are the signals predicted in the absence of baryonic physics. Including baryonic effects may modify many of these signatures (e.g. Richings et al. 2020), making potential constraints with these observations more difficult.

I can get a sense of the potential impact of baryons by examining the hydrodynamical simulations. For EAGLE, there is a suppression in the number density of subhaloes at virtually all radii and across all mass bins. I speculate that this suppression is due not only to change in subhalo mass and maximum circular velocity, but is also a result of the central region of the host halo being considerably more dense (due to stars and associated contraction of the dark matter), which will result in enhanced tidal stripping of the satellites in the hydrodynamical simulations (see e.g. Samuel et al., 2020). The baryonic effects are therefore similar to those seen for almost all the cosmological extensions explored here (with the exception of the positive-running cosmology). This is also true for the ARTEMIS simulations (lower-left panel of the plot), which shows an almost systematic suppression in the number density of subhaloes. It does appear however that there is a slight radial dependence to this suppression (which is also hinted at in the EAGLE result).

3.4.4 Concentration–mass relation

The concentration–mass relation is of particular interest as it has been shown through cosmological simulations that the inner density profiles of haloes are representative of the conditions of the Universe at the formation time of the halo, at least in a ΛCDM

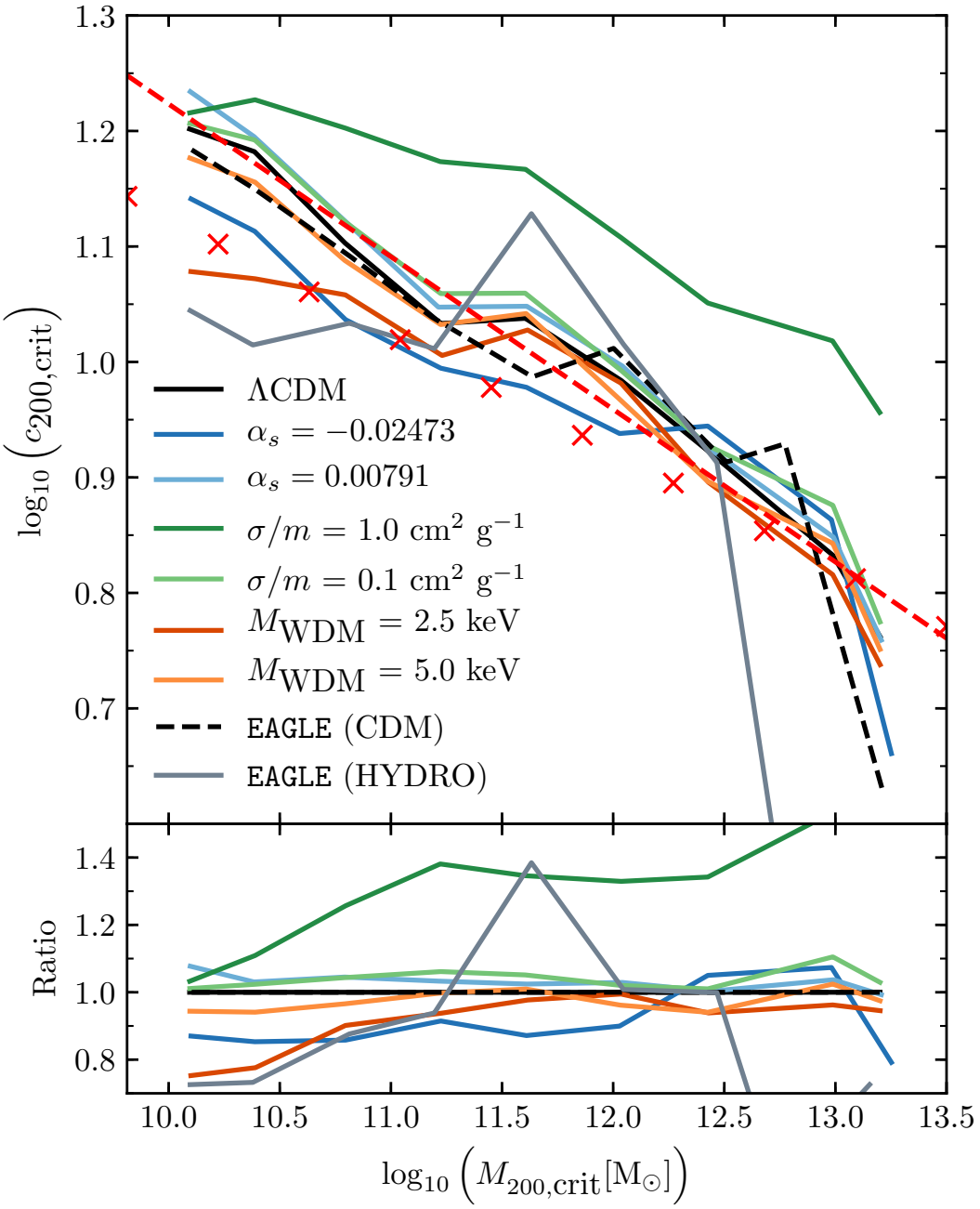

Figure 3.9: Top: the concentration-mass relation computed for stacks of host haloes in the mass range $9.81 \leq M_{200,\mathrm{crit}}/\mathrm{M}_\odot \leq 13.0$ for each cosmology at $z = 0$. The haloes are stacked into 9 equally spaced logarithmic mass bins. The concentration parameter is calculated for each stack by computing the logarithmic slope of the stacked density profile, and finding the radius for which this value is equal to -2. Bottom: the c–M relation normalised with respect to the result in the reference simulation. The red crosses corresponds to the empirical relation found in Dutton and Macciò (2014); with the dashed red line corresponding to this relation, with the parameters tuned to best-fit the reference simulation in this suite.

model. This result (illustrated by Navarro et al. 1996 for example, but confirmed by many additional studies), implies that low-mass haloes, which form first, have a higher central concentration than higher-mass haloes, which tend to assemble most of their mass late on. This is just due to the fact that low-mass haloes formed at a redshift when the mean density of the universe was higher.

It has also been shown that the concentration of low-mass haloes is affected in a WDM cosmology (e.g. Eke et al., 2001; Bode et al., 2001; Avila-Reese et al., 2001; Schneider, 2015; Ludlow et al., 2016), with lower-mass haloes having lower-concentrations compared with the corresponding halo mass CDM haloes, with this difference decreasing with increasing halo mass. Alongside this, it has been shown that a running scalar spectral index can also alter the c–M relation of high-mass haloes (Fedeli et al., 2010; Stafford et al., 2020). It has been shown by Despali et al. (2019) that allowing for self-interactions between the dark matter, also tends to slightly alter the c–M relation. As such, it is interesting to compare and contrast all of these different models in a consistent manner to see the relative effects they have on this important statistic.

It is commonplace when computing the concentration of a halo to fit a Navarro, Frenk & White (NFW) profile (Navarro et al., 1996) to the halo (or equivalently an Einasto profile Einasto 1965). The NFW profile has two free parameters: a scale radius and a scale density, or equivalently to this, a halo mass and a concentration. The concentration is defined as $c_{\Delta} \equiv R_{\Delta}/r_s$ ($r_s \rightarrow r_{-2}$ in the case of the Einasto profile), where Δ corresponds to a choice of spherical overdensity (which in this study is set equal to 200, with respect to the critical density) and r_s is the scale radius, defined as the radius where the logarithmic slope of the density profile is -2.

In this study I take a different approach, as I want to consistently compare the concentration parameter obtained as a function of mass for the different cosmologies examined here. This is not possible using either the Einasto or NFW forms for the SIDM models, as the SIDM models produce prominent cores in the dark matter density profiles (see for example Fig. 3.5). One could instead use a Burkert profile (Burkert, 1995), which is able to fit the cored-region in these dark matter haloes. However, this comes at the expense of poorly fitting the outer regions of SIDM haloes (see e.g. Rocha

et al. 2013) and would also provide a poor fit to the haloes in the other cosmologies. Therefore, I instead take a non-parametric approach and numerically evaluate the logarithmic slope of the computed density profiles using a 2nd-order Savitzky and Golay (1964) filter, smoothing over the 7 nearest bins. I then identify the radius for which the logarithmic slope equals -2. Thus, my non-parametrically estimated concentration parameter is defined in a way which is consistent with the standard definition of concentration using either the NFW or Einasto parametric forms, but it means the same technique can be applied to all the simulations. To check my method, I have compared the concentration parameter obtained for stacked density profiles in 6 different mass bins using this method to that obtained by fitting an NFW and Einasto profile to the stacks of haloes in the reference ΛCDM model. My method provides consistent concentrations with those estimated using the NFW or Einasto forms.

I stack haloes with masses between $9.81 \leq M_{200,\mathrm{crit}}/\mathrm{M}_{\odot} \leq 13.0$ in 9 equally spaced logarithmic mass bins, with the lower mass limit being chosen in order to only include haloes with a minimum of 5000 particles inside $R_{200,\mathrm{crit}}$. The spherically-averaged dark matter-only density profiles are computed in 32 logarithmically spaced radial bins, spanning a radial range: $-2.5 \leq \log_{10}(r/R_{200,\mathrm{crit}}) \leq 0$, as in Ludlow et al. (2016).

The resultant c–M relation can be seen in Fig. 3.9, where the bottom panels in this plot is the c–M relation for each cosmology normalised to the result in the reference ΛCDM simulation. This figure shows that qualitatively lower-mass haloes are more centrally concentrated, with the concentration steadily declining with increasing halo mass, irrespective of the details of cosmology or baryons. However, there are clear quantitative differences between the individual models. For example, as expected, the two different WDM models predict the low-mass haloes to be less centrally-concentrated compared to the standard model result, with this effect being more extreme for the lighter 2.5 keV model. This cosmology predicts a $\approx 20\%$ suppression in the concentration levels of 10^{10} $\mathrm{M}_{\odot}$ haloes. This is a similar level of suppression to that found in previous studies such as Schneider (2015) and Ludlow et al. (2016), who adopted similar WDM masses ([3.0, 3.3] keV respectively).

The magnitude of the effect on the c–M relation in a cosmology with a running spectral

index scales with the magnitude of the running parameter. For example, the cosmology with a negative running produces a suppression of around 10% in the central concentrations of haloes of fixed mass, with this effect extending over almost the entire mass range covered in this study. Whereas a positive running cosmology does not appear to have much of an effect in this mass range, confined to the few percent level. These results extend the trends seen previously in Chapter 2 to lower halo masses with, for example, lower mass haloes being less centrally concentrated in a cosmology with a negative running spectral index relative to the standard model.

The largest effect seen is in the most extreme SIDM model, which produces a large *increase* in the concentration at fixed mass. There also appears to be a change in slope for the c–M relation in the more extreme SIDM cosmology, with the offset between the standard model result and the SIDM result increasing with increasing mass. Naively, this appears to be inconsistent with the cores seen in the density profiles shown earlier (Fig. 3.5). The increase in the concentration, or more specifically the decrease in the radius where the logarithmic slope equals -2, is a consequence of the enhancement in the density just outside the core. The enhancement causes the transition radius from a constant density core in the inner regions of a SIDM halo to an NFW-like logarithmic slope of -3 in the outer regions to move inwards.

When examining the result in the EAGLE Recal simulation, there appears to be a change in slope for the c–M relation, compared to the result in the dark matter-only simulation. In particular the c–M relation in the full hydrodynamic simulation is somewhat flatter, in agreement with that found in Schaller et al. (2015). This is because the decrease in $M_{200,\mathrm{crit}}$, seen in Fig. 3.2, also results in a decrease in a haloes' $R_{200,\mathrm{crit}}$. This causes a decrease in concentration, preferentially at low halo masses.

Previous studies have shown that simple power-laws or functions are able to describe well the average c–M relation of haloes over a narrow range in halo masses (e.g. Avila-Reese et al., 1999; Neto et al., 2007; Duffy et al., 2008; Dutton and Macciò, 2014; Child et al., 2018). I highlight one such result here, that by Dutton and Macciò (2014), who found that the c–M relation of haloes in a Planck Collaboration XVI (2014) cosmology

is well described by a power-law of the form:

$$\log_{10}(c) = a + b \log_{10}\left(\frac{M}{M_{\rm pivot}\ [\mathrm{M}_\odot\ h^{-1}]}\right), \tag{3.8}$$

where a, b are fitting constants, found to be 0.905, -0.101 respectively in Dutton and Macciò (2014), $M_{\rm pivot}$ is a reference mass-scale, set to be 10^{12} $\mathrm{M}_\odot$ h^{-1}. I show this result as red crosses in Fig. 3.9. I also show an updated fit to the reference cosmology, which provides best-fitting parameters a = 0.936, b = -0.132. The reasons for the slight change in these parameters are two-fold. Firstly, the cosmologies are slightly different, for example the values for $\Omega_{\rm m}$ and σ_8 which the c–M relation is particularly sensitive to (Duffy et al., 2008; Dutton and Macciò, 2014). Also, the method of taking the logarithmic slope of the median density profile in a mass bin predicts slightly higher values for the concentration than what one typically gets when fitting an NFW profile to that same stack. This is particularly true at low-masses, which is where the two best-fitting relations differ most.

3.5 Discussion and Conclusions

In this study I have systematically explored different proposed mechanisms for altering the distribution of matter on small scales. This includes alterations to the standard model of cosmology or including baryonic effects within the standard model (but not yet both simultaneously). These mechanisms are motivated in part by apparent tensions between the standard model and observational data in the local Universe (see the Introduction).

In terms of the alterations to the standard model, I consider three scenarios: warm dark matter (WDM), self-interacting dark matter (SIDM), and a running of the scalar spectral index of the power spectrum of primordial density fluctuations. These cosmological alterations come with additional free parameters (e.g., WDM particle mass, SIDM cross-section, value of the running) and I use current observational constraints to guide my choice of the parameter values. To characterise the potential role of baryons within

the standard model, I use the high-resolution EAGLE 'Recal' run and the ARTEMIS suite of zoom-in simulations of Milky Way-mass haloes. Using all of the simulations, I compare and contrast the effects of altering the standard model in different ways and I frame this within the context of the potential role of baryons, highlighting potential degeneracies between the different effects for different observables.

The main findings of my study may be summarised as follows:

- Baryon physics, WDM, and a running spectral index alter the spherical-overdensity (SO) halo mass function (Fig. 3.1) in similar ways and are expected to be degenerate if they are constrained solely using this metric. A cosmology where the DM is allowed to self-interact (SIDM) is the only cosmological extension examined here which has no significant effect on the SO halo mass function. There are, however, noticeable effects present when examining the subhalo population in SIDM cosmologies (Fig. 3.3). Specifically, while the central subhalo mass function resembles the SO mass function strongly, the satellite subhalo mass function can be strongly suppressed, particularly for satellites that are located close to the centres of their host halo (Fig. 3.8). This effect is plausibly due both to a form of evaporation in which energetic DM particles from the host halo scatter off satellite DM particles (and thus unbinding them) and enhanced tidal stripping as a result of the cored density profiles of SIDM subhaloes.

- When examining the radial dark matter distribution within host haloes, WDM and a (negative) running spectral index can behave similarly (Figs. 3.5, 3.6). This degeneracy is only prevalent for haloes with mass $\lesssim 10^{11.75}$ $\mathrm{M}_{\odot}$, however, with there being no significant suppression in the density profiles in the WDM cosmologies for haloes with mass greater than this, but still an $\approx 10\%$ suppression in the inner regions for the negative running cosmology. The SIDM cosmologies produce large cores, strongly distinguishing them from any of the other cosmological extensions. These results are echoed in the concentration–mass relation of haloes (Fig. 3.9). Consistent with previous works, there is a large enhancement in the dark matter density profile for the hydrodynamical sim-

ulations, shown both for the EAGLE Recal simulation, as well as the ARTEMIS zoom-in simulations. Interestingly, among the cosmological extensions I also find that a positive running scalar spectral index is able to produce an enhancement in the dark matter density profiles relative to the ΛCDM case, but at a much reduced level (around 10%) for haloes of mass $\leq 10^{12.33}$ $M_{\odot}$.

- I have shown that for cosmological extensions such as a running scalar spectral index and WDM, the *relative* effects on the density profiles with respect to the standard model are reliably followed down to significantly smaller radii than standard 'convergence' radii (for absolute quantities) would suggest (Fig. 3.7). This potentially allows one to save a great deal of computational expense, by running only a single ΛCDM simulation at very high resolution and then using the ratios of cosmological extensions to ΛCDM from lower-resolution simulations to produce high-resolution non-standard cosmologies.

- There is a strong degeneracy for the suppression in the radial distribution of subhaloes in their host haloes for WDM, running, and hydrodynamical effects (Fig. 3.8). For example, the results for the 5.0 keV WDM model are nearly identical to those with the negative running cosmology. In the high halo-mass bins ($M \gtrsim 10^{11.75}$ $M_{\odot}$) there is also a suppression in the number density of subhaloes in the SIDM cosmology with the larger cross-section for interaction, due to evaporation of the satellites and enhanced tidal stripping of cored subhaloes.

The different cosmological extensions explored here are able to produce large, and potentially measureable effects on the structure which forms in the Universe. All of the cosmological extensions examined are within current observational constraints, and are able to potentially help alleviate some of the small-scale crises which (may) exist with the standard model of cosmology. An interesting problem arises, however, in that some of the models have highly degenerate effects.

As such, when making constraints on these different cosmological extensions, it is potentially necessary to combine probes which examine different aspects of haloes and their satellite subhaloes in order to break degeneracies between the different exten-

sions. This is because, in detail, the different extensions do have different mass and radial dependencies which can be exploited to simultaneously constrain them.

However, it is important to note that this study has focused on dark matter-only simulations when extending ΛCDM. I examined the EAGLE 'Recal' and ARTEMIS simulations to compare the results from these gravity-only simulations to those from full hydrodynamical simulations (in the context of the standard model). I find that baryonic physics can also be highly degenerate with varying the cosmological model. Furthermore, there are inherent differences in the results predicted by the inclusion of baryonic physics, due to the uncertainty associated with the subgrid implementation of this physics. This is highlighted by the differences present between the ARTEMIS results and the EAGLE results. Even though these simulations have the same subgrid physics implementations, they were calibrated slightly differently, leading to somewhat different results. While it is clear that baryonic effects are important, how robust the predictions are remains an open question. Since feedback efficiencies cannot be predicted from first principles and must therefore be calibrated against some set of observable properties of galaxies (Schaye et al., 2015), there is a danger that we may come to erroneous conclusions about the role of baryons if those calibration observables also depend on cosmology.

Thus, given the degeneracies that exist between cosmological extensions and also that of baryon effects and the uncertainties inherent to galaxy formation modelling, it seems the best approach is to *simultaneously* explore variations to cosmology and baryon physics, using a multi-observational probe approach to constrain both. I am adopting such a strategy in forthcoming work.

Chapter 4

Testing extensions to ΛCDM on small scales with forthcoming cosmic shear surveys

The following chapter appeared in Stafford et al. (2021). The appendices for this paper are included in Appendix C.

In this chapter, I investigate the constraining power of forthcoming Stage-IV weak lensing surveys (EUCLID, LSST, and NGRST) for extensions to the ΛCDM model on small scales, via their impact on the cosmic shear power spectrum. The extensions explored in this chapter are the same as those introduced in Chapter 3 and I make use of the same high-resolution cosmological simulations to calculate how warm dark matter (WDM), self-interacting dark matter (SIDM) and a running of the spectral index affect the non-linear matter power spectrum, $P(k)$, as a function of scale and redshift. One difference in the suite of simulations used in this chapter, compared to the previous chapter, is that I have added an additional, more extreme, run for both the warm dark matter simulations (smaller thermal relic mass) and the self-interacting dark matter (larger cross-section for interaction) to the suite.

I evaluate the cosmological constraining power of cosmic shear using synthetic weak

lensing observations derived from these power spectra and that take into account the anticipated source densities, shape noise and cosmic variance errors of upcoming surveys. I show that upcoming Stage-IV surveys will be able to place useful, independent constraints on both WDM models (ruling out models with a particle mass of $\lesssim 0.5$ keV) and SIDM models (ruling out models with a velocity-independent cross-section of $\gtrsim 10$ cm^2 g^{-1}) through their effects on the small-scale cosmic shear power spectrum. Similarly, they will be able to strongly constrain cosmologies with a running spectral index.

Finally, in this chapter, I explore the error associated with the cosmic shear cross-spectrum between tomographic bins, finding that it can be significantly affected by Poisson noise (the standard assumption is that the Poisson noise cancels between tomographic bins). I provide a new analytic form for the error on the cross-spectrum which can accurately capture this effect. I exploit this new analytic form in my analysis by using it to predict the Gaussian errors associated with the cosmic shear power spectrum up to an $\ell_{\rm max}$ = 20,000 which otherwise would have been prohibitively expensive.

4.1 Introduction

In the current concordance cosmological framework, termed the ΛCDM (Λ-cold dark matter) model, structure in the Universe forms hierarchically. The initial density perturbations laid down by inflation eventually grow large enough that they become gravitationally unstable and collapse to form low-mass 'haloes'. These low-mass haloes merge to build up progressively larger systems, eventually culminating in the large-scale structure (LSS) that we observe today (see, e.g., Davis et al. 1985). This theoretical picture has been immensely powerful in describing observations of our Universe, accurately reproducing the observed properties of the cosmic microwave background (see e.g. the recent results from Planck Collaboration et al. 2020) as well as low-redshift probes such as baryon acoustic oscillations (Eisenstein et al. 2005; Cole et al. 2005) and redshift-space distortions (see e.g. Alam et al. 2017). Given its success, this

theoretical framework has come to be known as the 'standard model of cosmology'.

It is noteworthy that, while the ΛCDM model accurately describes many observables on large scales, there have been a number of recent mild tensions reported in the best-fit parameter values for certain cosmological parameters, including the Hubble constant (see Verde et al. 2019 for a review) and the LSS parameter $S_8 \equiv \sigma_8\sqrt{\Omega_m/0.3}$ (see, e.g., discussion in McCarthy et al. 2018) as derived from independent measurements. Whether these tensions are signaling the presence of unaccounted for systematic errors in some of the cosmological analyses, that there is new physics (i.e., beyond the standard model), or that they are merely the result of statistical fluctuations, is presently unclear and the subject of much investigation.

Although the ΛCDM model does remarkably well at describing observations of our Universe on large scales (tens to hundreds of Mpc, modulo the recent mild tensions described above), the last decade or so has seen a ramping up of detailed comparisons on smaller scales (typically kpc to Mpc), some of which have reported significant tensions with the predictions of ΛCDM-based cosmological simulations. Three of the most widely discussed tensions are the 'cusp-core' problem (Flores and Primack, 1994; Moore, 1994), the 'missing satellites' problem (Klypin et al., 1999; Moore et al., 1999) and the 'too-big-to-fail' problem (Boylan-Kolchin et al., 2011). The common thread between these tensions is that the ΛCDM model appears to predict too much structure (and too high densities) on small scales compared with what is inferred from observations. These tensions are often evaluated with respect to gravity-only calculations in the context of ΛCDM, but recent work has suggested that neglecting important baryonic physics may have significant implications for these tensions. For example, including processes such as reionisation, star formation, stellar feedback through supernovae and winds, and feedback associated with active galactic nuclei in the models have been shown to help alleviate some of these problems with ΛCDM on small scales (see e.g. Efstathiou 1992; Navarro et al. 1996; Bullock et al. 2000; Benson et al. 2002; Mashchenko et al. 2008; Pontzen and Governato 2012; Wetzel et al. 2016; Sawala et al. 2016).

Nevertheless, it is worthwhile to consider other possibilities, which may act in con-

junction with baryon physics, for these small scale problems, not least because the modelling of baryon physics on small scales is quite complex and requires a degree of fine tuning to resolve some of the aforementioned tensions. Also, it is important that we continue to test the standard model as rigorously as possible on small scales, in order to shed light on the nature of dark matter.

The apparent deficit of small-scale structure has led to the study and development of many extensions to the ΛCDM model which aim to reconcile these differences. Promising extensions to the current ΛCDM paradigm, such as warm dark matter (WDM) and self-interacting dark matter (SIDM), can reduce the formation of structure on small scales. These different cosmological models focus on changing one of the assumed aspects of dark matter. In the case of the former, dark matter decouples in the early universe whilst still relativistic leading to non-negligible thermal velocities and free-streaming, while in the latter case dark matter is allowed to have strong self-interactions (scattering). Both of these extensions have been shown to have success in alleviating the outlined challenges which exist with ΛCDM (see e.g. Colín et al. 2000; Lovell et al. 2012 for the case of WDM and Spergel and Steinhardt 2000; Zavala et al. 2013 for the case of SIDM). One further extension which has not been studied quite so extensively is a running scalar spectral index. A running spectral index is different from the previous two extensions as it does not alter the nature of dark matter but instead changes the initial conditions for structure formation, which is motivated by certain classes of inflation models. Previously this has also been demonstrated to be a promising candidate for reducing the formation of small-scale structure (see e.g. Garrison-Kimmel et al. 2014; Stafford et al. 2020b).

In Chapter 3, I compared how effective these three different extensions were in altering various small-scale structure statistics. To do this I used gravity-only cosmological simulations with the values adopted for the additional parameters associated with each extension being guided by current observational constraints. I found that all of the models can have similar effects on certain statistics, such as the abundance of satellite galaxies inside hosts (which is one of the primary tests of ΛCDM on small scales). As such, it is of interest to explore new observables which could help differentiate these

models and the effects they have on structure formation.

In this study, I exploit the fact that these different models alter the non-linear matter power spectrum along with its redshift evolution in different ways (as I will show). Consequently, observational probes which are directly sensitive to the non-linear matter power spectrum may provide a strong test of these extensions and of ΛCDM. One potentially promising observable is the cosmic shear power spectrum. As the light emitted from distant galaxies travels towards us on Earth, its path becomes distorted due to intervening matter, a phenomenon known as gravitational lensing. One can use the correlated effect this has on galaxy shapes to extract information about the non-linear matter power spectrum. This can be done either through the two-point auto-correlation function of galaxy shapes or its Fourier analogue, the cosmic shear power spectrum. It is this latter statistic that I examine in this chapter and how it is affected by SIDM, WDM and a running spectral index in comparison with the ΛCDM result.

The impetus for this study stems from the increasing quantity and quality of cosmic shear observations being made by current Stage-III surveys, such as the Dark Energy Survey (DES)[1] (DES Collaboration et al., 2021), the Hyper Suprime-Cam Subaru Strategic Survey (HSC)[2] (Hamana et al., 2020), and the Kilo-Degree Survey (KiDS)[3] (Asgari et al., 2021), and forthcoming Stage-IV cosmic shear surveys, such as EUCLID[4] (Euclid Collaboration et al., 2020a), the Rubin Observatory Legacy Survey of Space and Time (LSST)[5] (Zhan and Tyson, 2018), and the Nancy Grace Roman Space Telescope (NGRST)[6] (Spergel et al., 2015). Stage-IV surveys will greatly improve on current observations, by covering a much larger area of the sky and/or being significantly deeper, ultimately resulting in greatly improved measurements of the cosmic shear power spectrum.

To date most of the forecasting work for Stage-IV surveys has been with regards to anticipated constraints on the standard model of cosmology and extensions that affect

[1] https://www.darkenergysurvey.org/
[2] https://hsc.mtk.nao.ac.jp/ssp/survey/
[3] http://kids.strw.leidenuniv.nl/overview.php
[4] https://www.euclid-ec.org/?page_id=2581
[5] https://www.lsst.org/scientists/
[6] https://www.jpl.nasa.gov/missions/the-nancy-grace-roman-space-telescope

large-scale structure (such as evolving dark energy and massive neutrinos). Only a small number of studies have been dedicated to the possible constraints that may be obtained for small-scale extensions. For example, Markovic et al. (2011) explored how future cosmic shear surveys can be used to place constraints on the mass of thermal relic particles. More recently, Hubert et al. (2021) explored constraints on decaying dark matter models. The present chapter seeks to examine the impact of the three cosmological extensions described above (WDM, SIDM, and a running scalar spectral index) on the cosmic shear power spectrum using the non-linear matter power spectrum extracted from numerical simulations. I then explore the prospect of these upcoming Stage-IV surveys in differentiating these extensions from ΛCDM.

The chapter is structured as follows. In Section 4.2 I describe in more detail the extensions studied in this chapter. I also discuss the numerical simulations which I use as well as how I create a non-linear matter power spectrum which covers the full dynamic range of interest for this weak lensing study. In Section 4.3 I discuss how I compute the cosmic shear power spectrum and the associated uncertainties. In Section 4.4 I present my results for the cosmic shear auto- and cross-correlation power spectra for each cosmological model and finally in Section 4.5 I discuss and summarise my results.

4.2 Cosmological Extensions

In this study, I analyse three separate cosmological extensions, a running scalar spectral index, warm dark matter and self-interacting dark matter. I briefly describe these in the following subsections, with more details provided in Chapter 3. Note, however, in Chapter 3 I only examined two WDM models and two SIDM models, whereas in this study I extend my analysis slightly and look at an additional, more extreme, case for both of these extensions.

4.2.1 Extensions

Running of the scalar spectral index

In the standard model of cosmology, the power spectrum for scalar perturbations generated by inflation is assumed to follow a simple power-law of the form (Guth, 1981; Kosowsky and Turner, 1995):

$$P(k) = Ak^{n_s}, \tag{4.1}$$

where A is the amplitude of the primordial matter power spectrum, k is the wavenumber and n_s is the spectral index. A first order extension is that the spectral index has some level of scale dependence, which results in a modification to the functional form of the primordial matter power spectrum (Kosowsky and Turner, 1995):

$$P(k) = A_s(k_{\text{pivot}}) \left(\frac{k}{k_{\text{pivot}}}\right)^{n_s(k_{\text{pivot}}) + \frac{\alpha_s}{2} \ln\left(\frac{k}{k_{\text{pivot}}}\right)}. \tag{4.2}$$

Here, α_s is termed the 'running' of the scalar spectral index and is defined as $dn_s(k)/d\ln(k)$[7]. Here, $n_s(k)$ is still equal to the logarithmic slope of the power spectrum, however, it now has a k-dependence due to the $(\alpha_s/2)\ln(k/k_{\text{pivot}})$ term in equation 4.2. The value adopted for k_{pivot} here corresponds to that for the Planck satellite mission, k_{pivot} = 0.05 Mpc^{-1}, and corresponds to the $k-$scale at which values for A_s and n_s are quoted. In this work I explore the effects that a positive value for the running (with $\alpha_s = 0.00791$) and a negative value for the running (with $\alpha_s = -0.02473$) have on the non-linear matter power spectrum and how these propagate through to an observable impact on the cosmic shear power spectrum. Note the cosmological parameter values chosen for the running simulations are in the context of a Planck 2015 cosmology; the maximum-likelihood values are computed from the Markov chains which includes α_s as a free cosmological parameter in the analysis. This results in slight differences to the quoted values of the other cosmological parameters in Section 4.2.2 (a table of all of the pa-

[7] Although in the ΛCDM model α_s is assumed to be zero, virtually all models of inflation predict some level of scale dependence for n_s. However, the simplest single field slow-roll inflation models predict that this scale-dependence should only be of the order 10^{-3} (Kosowsky and Turner, 1995).

rameter values for each cosmology can be found in Chapter 3). The values chosen for α_s are discussed in detail in Chapter 2, but in summary represent the $\pm 2\sigma$ values of the posterior distribution extracted from the Planck 2015 Markov chains[8] (Planck Collaboration et al., 2014).

These two cosmological models with a running scalar spectral index were chosen in Chapter 2, prior to the release of the Planck 2018 cosmological parameter constraints (Planck Collaboration et al., 2020). The updated CMB constraints on α_s are tightened somewhat to $\alpha_s = -0.0045 \pm 0.0067$ (68% CL TT,TE,EE+lowE+lensing) making the posterior distribution for α_s used in Chapter 2 slightly out of date. However, it is worth noting that, even with the updated CMB constraints from the Planck team, a mildly negative value for the running of the spectral index is not ruled out (see the discussion in section 7.2.1 in Planck Collaboration et al. 2020). Furthermore, updated constraints from the Lyman-α forest find a $\approx 3\sigma$ detection for a negative α_s with $\alpha_s = -0.010 \pm 0.003$ (Palanque-Delabrouille et al., 2020)[9]. Therefore, the values I simulate are still compatible with current observations, even if they lie on the more extreme end of current constraints. Furthermore, as discussed later on in the chapter in the context of warm dark matter models, this work seeks to answer the question whether cosmic shear can be used as a complementary probe to place *independent* constraints on these additional cosmological parameters (α_s, $M_{\rm WDM}$, σ/m).

Warm dark matter

Another assumption of the standard model of cosmology is that dark matter decoupled from the primordial plasma after it became non-relativistic. This results in negligible thermal velocities at early times (hence "cold" dark matter) and would be expected if dark matter was composed of particles with masses in the GeV range (or larger), such as the currently favoured candidate, the WIMP (Weakly Interacting Massive Particle). If, however, dark matter is made up of lighter particles with masses in the keV range,

[8] http://pla.esac.esa.int/pla/#home

[9] Note, however, that Palanque-Delabrouille et al. (2020) marginalise over neutrino mass at the same time as α_s, whereas the Planck analysis fixed ΣM_ν to 0.06 eV when constraining α_s.

such as thermal relic sterile neutrinos, the dark matter particles decouple whilst still relativistic. This type of model is referred to as a thermal relic warm dark matter (WDM) model. The resulting larger thermal velocities that these dark matter particles have (compared to CDM) at early times allows them to free-stream out of density perturbations. The free-streaming of dark matter particles works to suppress the growth of structure on small scales (Bond and Szalay, 1983; Bardeen et al., 1986).

The suppression of small-scale density perturbations due to the thermal velocity associated with the dark matter particles leads to a characteristic cut-off in the WDM power spectrum below a $k-$mode corresponding to the free-streaming scale. In this work I model the suppression of the initial linear matter power spectrum as a transfer function relative to the corresponding cold dark matter power spectrum:

$$P_{\rm WDM}(k) = T^2_{\rm WDM}(k) P_{\rm CDM}(k). \tag{4.3}$$

I compute $T_{\rm WDM}$ using the fitting formula developed in Bode et al. (2001):

$$T_{\rm WDM}(k) = \left[1 + (\alpha k)^{2\nu}\right]^{-5/\nu}, \tag{4.4}$$

where ν is a fitting constant and α dictates the scale of the cut-off in the power spectrum, with this being dependent on the mass of the thermal relic particle. I follow Viel et al. (2005), adopting ν = 1.12 and (assuming the WDM is composed of thermal relics) and computing α as:

$$\alpha = 0.049 \left(\frac{M_{\rm WDM}}{1{\rm keV}}\right)^{-1.11} \left(\frac{\Omega_{\rm WDM}}{0.25}\right)^{0.11} \left(\frac{h}{0.7}\right)^{1.22} {\rm Mpc}\ h^{-1}, \tag{4.5}$$

where $M_{\rm WDM}$ corresponds to the mass of the WDM particle, $\Omega_{\rm WDM}$ is the present-day density of WDM [10] in units of the critical density and h is the reduced Hubble's constant.

It is evident from equation 4.5 that for lighter WDM particles α increases, pushing the scale of the cut-off in the matter power spectrum to smaller $k-$modes (larger physi-

[10] I assume all of the dark matter is in the form of WDM and so $\Omega_{\rm WDM} = \Omega_{\rm CDM}$.

cal scales). In this study I examine $M_{\rm WDM}$ = (0.5, 2.5, 5.0) keV. My choice for the parameter values investigated in this study aims to bracket the current observational constraints placed on the mass of a WDM particle from different probes such as the Lyman-α forest (Viel et al., 2013; Iršič et al., 2017), the Milky-Way's satellite population (Lovell et al., 2014; Kennedy et al., 2014; Jethwa et al., 2018; Nadler et al., 2019; Nadler et al., 2020c) and time-delay measurements of strongly gravitationally lensed quasars (Hsueh et al., 2019; Gilman et al., 2019). Although the 0.5 keV model is perhaps currently in tension with constraints from the previous observations, I examine it here to see if cosmic shear, as an independent test with very different systematics compared to previous methods, can also rule out such a model.

Self-interacting dark matter

In terms of the possible interactions that dark matter particles can experience, the standard model of cosmology adopts the simplest assumption that dark matter interacts only via gravity and is therefore 'collisionless'. The final extension that I investigate is a relaxation of this assumption, allowing the dark matter particles to have strong self-interactions. SIDM was proposed to alleviate the 'cusp-core problem' (Flores and Primack, 1994; Moore, 1994) by Spergel and Steinhardt (2000) and has indeed been shown in the literature to produce strong cores inside dark matter haloes and can have particularly large effects on satellite subhaloes, strongly reducing their masses (see e.g. Peñarrubia et al. 2010; Vogelsberger et al. 2012; Dooley et al. 2016). I explore how these effects translate through to the non-linear matter power spectrum.

To study the effect of strong self-interactions I use a version of the `GADGET3` N-body code (discussed in Section 4.2.2) which was modified in Robertson et al. (2019) to include dark matter self-interactions, which are assumed to be elastic. The additional parameter this adds to the standard 6 free parameters of the ΛCDM model is (σ/m), which is the cross-section for interaction of dark matter particles. In this study the values which I explore are (σ/m) = (0.1, 1.0, 10.0) cm^2 g^{-1}. Again, my choices for the values adopted for this cosmological parameter are guided by the current observa-

tional constraints. In the case of the self-interaction cross-section, these constraints are placed by probes such as perturbations in strong lensing arcs (Meneghetti et al., 2001; Robertson et al., 2019), dark matter-galaxy off-sets in colliding galaxy clusters (Randall et al., 2008; Kahlhoefer et al., 2015; Harvey et al., 2015; Kim et al., 2017; Robertson et al., 2017c; Wittman et al., 2018), cluster shapes (Miralda-Escude, 2002b; Peter et al., 2013) group shapes (Sagunski et al., 2021) and also from subhalo evaporation arguments (Gnedin and Ostriker, 2001). Furthermore, Banerjee et al. (2020) showed that constraints of the order $\sigma/m \lesssim 2$ cm^2 g^{-1} can be placed on the cross-section for self interaction when combining observations of the distribution of subhaloes and weak lensing measured density profiles.

The largest cross-section I examine is somewhat in tension with some of the observations listed here, but it is worth noting that these are primarily focused on large scales (galaxy clusters). There is evidence to suggest that SIDM models with cross-sections as high as 50 cm^2 g^{-1} are viable when using constraints coming from dwarf galaxies (Elbert et al., 2015; Correa, 2021). As my focus is on small scales, the range of cross-sections I explore is therefore plausible given current constraints. Note, although the simulation code developed by Robertson et al. (2019) has the functionality for scattering events to be both angular and velocity dependent, for simplicity I focus on the case where scattering events are velocity-independent and isotropic.

4.2.2 Simulations

The simulations used in this study are those first introduced in Chapter 3. All of the simulations follow dissipationless physics only, meaning they follow either just the gravitational evolution (for CDM, WDM, and the running spectral index models) or the gravitational and self-scattering (SIDM) evolution. The impact of physical processes associated with the baryonic component (i.e., radiative cooling, star formation, feedback processes) is not included but is discussed further in Section 4.5.

The simulations are run with the `GADGET3` code (last described in Springel 2005). Each simulation is 25 comoving h^{-1}Mpc on a side and contains 1024^3 dark matter

particles. I adopt a fixed physical gravitational softening length of 250 h^{-1} pc at $z \leq 3$, with this being a fixed comoving length at higher redshifts. The particle mass for all of the simulations, with the exception of the two with a running spectral index, is $m_{\rm DM}$ = 1.266 $\times$ 10^6 $\mathrm{M}_\odot$ h^{-1}. For the two 'running' simulations, the particle mass is slightly different, owing to the slightly different values adopted for $\Omega_{\rm m}$ and h (see Table 3.1 in Chapter 3). Alongside these main simulations, I also use a secondary suite of simulations of varying box size and resolution. These include a suite of simulations which are 400 comoving h^{-1}Mpc on a side, as well as a suite which are 100 comoving h^{-1}Mpc on a side. Both suites contain 1024^3 collisionless particles. Note, however, that I only run the cosmologies with a running scalar spectral index (as well as the reference ΛCDM cosmology) in these larger volumes, as they are required for the process of creating a spliced power spectrum (see Section 4.2.3).

The initial conditions (ICs) for the simulations are generated using a modified version of the `N-GenIC`[11] code (Springel et al., 2005) which was modified to include second-order Lagrangian Perturbation Theory corrections. The ICs are generated at a starting redshift of z = 127 with each simulation being initialised with the same random phases. The input linear theory matter power spectrum and transfer functions are computed with the Boltzmann code `CAMB` (Lewis et al. 2000, August 2018 version). The initial conditions and the background expansion rate in the simulations are computed assuming the Planck 2015 maximum-likelihood cosmological parameters (Planck Collaboration et al., 2014) ($H_0 = 67.31$ km s^{-1} Mpc^{-1}; $\Omega_{\rm DM} = 0.264$; $\Omega_{\rm b} = 0.049$; $n_s = 0.966$; $\sigma_8 = 0.830$; $\Sigma M_\nu = 0.06$ eV), with the exception of the two running simulations (as explained above).

Note that I use a version of the `GADGET3` code (see McCarthy et al. 2018) that includes the impact of massive neutrinos on the expansion rate and the growth of fluctuations (i.e., accounts for their free streaming), using the semi-linear algorithm of Ali-Haïmoud and Bird (2013). As the simulations employed here adopt the minimum allowed neutrino mass ($\Sigma M_\nu = 0.06$ eV), consistent with what is assumed in the Planck analysis, their incorporation will not have important consequences for the

[11] https://github.com/sbird/S-GenIC

present study, but I include them for consistency.

4.2.3 Matter power spectra

In this study I probe the theoretical cosmic shear power spectrum over a large range of multipoles/angular scales. This requires that I have a model for the non-linear matter power spectrum which spans a large range of wavenumbers/physical scales. However, the high-resolution 25 h^{-1}Mpc simulations that I use to probe the non-linear effects only have a k-range spanning from ≈ 0.25 hMpc^{-1} to 257.36 hMpc^{-1}. While the simulations extend to large enough k (i.e., small scales) for upcoming lensing surveys, they are clearly too small to capture all of the relevant structure on large scales. Even though my interest is primarily focused on small scales, I nevertheless want to construct realistic synthetic cosmic shear observations. (Furthermore, as I will show, the running of scalar spectral index models have important contributions from large scales.) I thus require a way of modelling the non-linear matter power spectrum over a wide range of scales.

Method for constructing matter power spectra

In order to model the non-linear matter power spectrum over a wide range of wavenumbers, I combine the direct simulation measurements with predictions from `Halofit` (Smith et al., 2003; Takahashi et al., 2012) on larger scales. Briefly, the `Halofit` algorithm provides an empirical correction for scaling the linear power spectrum (e.g., from a Boltzmann code) for a given cosmology to the non-linear power spectrum. The empirical corrections were derived from fits to a large suite of CDM-based cosmological (N-body) simulations. I use the Boltzmann code `CAMB` to compute the `Halofit` prediction at a given redshift. This provides us with the fiducial non-linear ΛCDM power spectrum. To construct a full power spectrum for each of the extensions to ΛCDM, I use the ratios of the non-linear matter power spectra extracted directly from the simulations (with respect to the ΛCDM case) as a multiplicative 'boost factor' for

the non-linear Halofit ΛCDM prediction via:

$$P_C(k,z) = P_{\Lambda\mathrm{CDM}}^{\mathtt{Halofit}}(k,z) R_C(k,z), \tag{4.6}$$

where $P_C(k,z)$ is the non-linear matter power spectrum in a given cosmological extension, and $R_C(k,z)$ is the constructed ratio (boost factor) for a given cosmology.

This approach allows us to combine multiple simulations of varying box size or resolution (by combining their ratios), following in a similar vein to the power spectrum splicing in previous Lyman-alpha forest work (e.g., Palanque-Delabrouille et al. 2015). The combined ratios can then be used to seamlessly scale the power spectra derived on very large scales (e.g., via linear theory, perturbation theory, Halofit, etc.) via equation 4.6 to produce an absolute power spectrum for a cosmological model.

Note that previous studies have shown that cosmological simulations which do not simulate the smaller $k-$modes (larger physical scales) do not accurately represent the intermediate $k-$modes sampled in the cosmological volume (see e.g. Power and Knebe 2006; Heitmann et al. 2010; Klypin and Prada 2018; Euclid Collaboration et al. 2019), making it difficult to combine the absolute matter power spectra from simulations of different box sizes. This motivates the use of combining ratios of power spectra rather than splicing the absolute power spectra themselves. I have explicitly tested how sensitive the ratio of the different power spectra are to resolution as well as box size effects (see Fig. C.1 in Appendix C.1), concluding that they are more robust to such effects than are the absolute power spectra.

To explain how I construct the non-linear matter power spectrum in a bit more detail, firstly, I compute the matter power spectra for the different simulations using GENPK[12] (Bird, 2017). I then re-bin the matter power spectra to have 10 k-modes per bin (corresponding roughly to rebinning the power spectra in logarithmic bins of width 0.0143 dex), in order to smooth out some of the associated noise. I compute the mean power in each bin, as well as the mean wavenumber. The ratios of the power spectrum for each cosmological extension with respect to the ΛCDM result are then computed. In

[12]https://github.com/sbird/GenPK

the case of the SIDM and WDM models, all six of these simulations have ratios which tend to 1 within the simulated volume (i.e., the physical effects of these modifications are confined to small scales), as such I simply extrapolate these ratios to smaller k-values (larger physical scales) assuming they are fixed at unity over the entire range. In the case of the two simulations which have a running scalar spectral index, the ratios of these power spectra do not tend to unity within the high-resolution 25 h^{-1}Mpc boxes, as such I need to simulate the ratio over a wider k-range. To do this I use two further sets of simulations of size 100 h^{-1}Mpc and 400 h^{-1}Mpc, each with 1024^3 dark matter particles, to compute the ratio of these models with respect to a corresponding ΛCDM result. As a result, I can accurately probe the non-linear matter power spectrum in these simulations up to approximately linear scales where I can then make use of the theoretical prediction from `Halofit`. The reason I do not use the `Halofit` prediction over the entire k-range for the simulations with running is because it does not tend to reproduce the effects I see in the running simulations on non-linear scales (as shown by the dotted line in Fig. C.1), discussed in Chapter 2 (see also Smith and Angulo 2019).

With a combined ratio spanning the entire desired k-range for each cosmological model, I fit a cubic spline to the the data, which is smoothed with a 3rd order Savitsky-Golay filter (Savitzky and Golay, 1964) over the nearest 51 wavenumbers. These two steps are done to ensure a smooth continuous function describing the ratio over the entire k-range. I repeat this process at each redshift for which I have a simulation snapshot. Once I have the ratio for each cosmology at each redshift relative to the ΛCDM prediction, I use it as a multiplicative boost factor to a ΛCDM matter power spectrum (at the corresponding redshift) to obtain the absolute power spectrum for each cosmology. Note that I have simulation snapshots at $z = \{0.0, 0.125, 0.25, 0.375, 0.5, 0.75, 1.0\}$ for which I compute the non-linear total matter power spectrum. When I compute the shear power spectra described in Section 4.3.1, I use a cubic spline to interpolate between both redshift and $k-$modes. I set the power to zero for $k-$modes outside of the range sampled by the above constructed matter power spectrum.

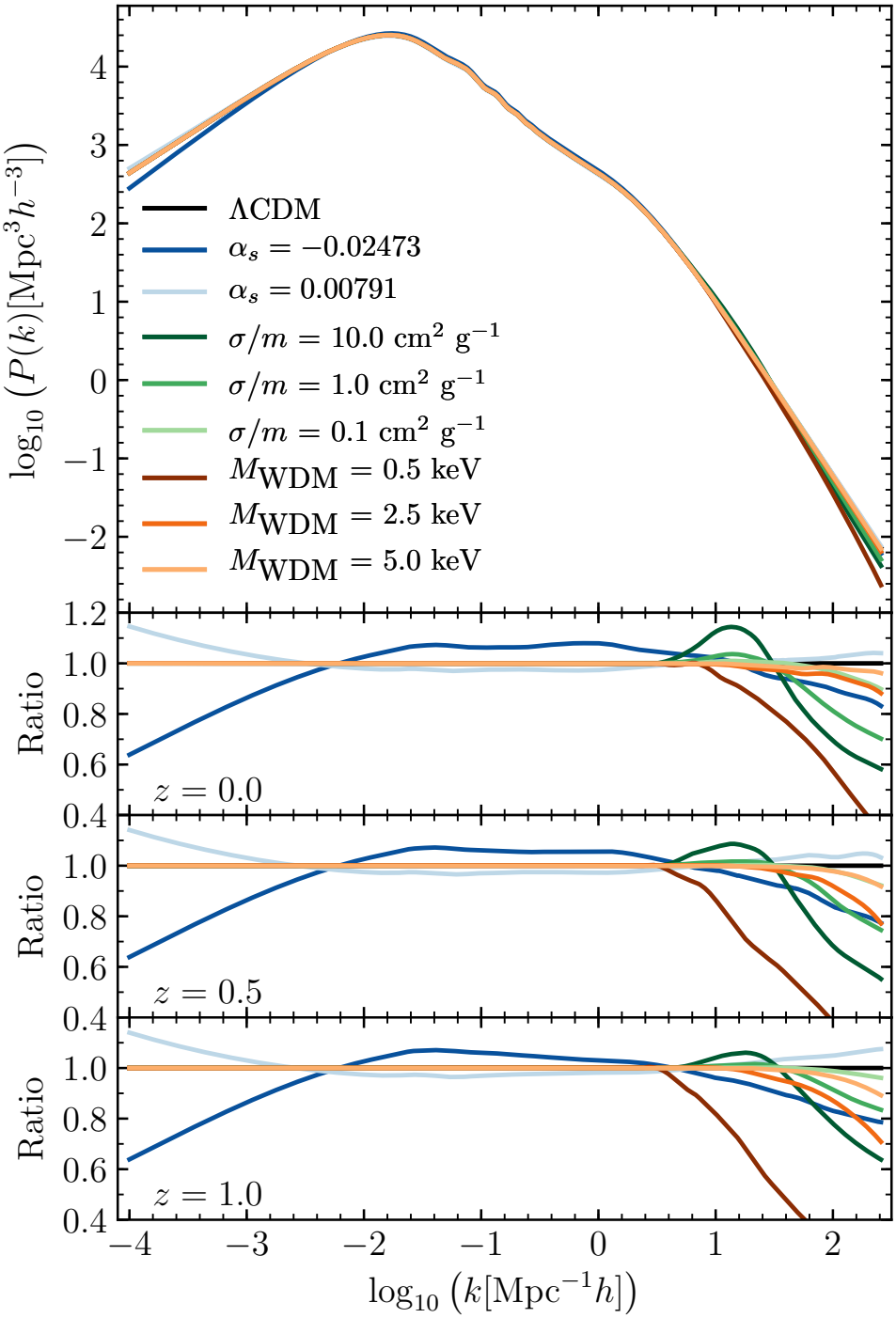

Figure 4.1: Top: the constructed non-linear matter power spectrum for each cosmological extension indicated with varying colours, computed at $z = 0$. Bottom (three panels): the matter power spectrum of each cosmological extension normalised to the ΛCDM case. Redshifts 0, 0.5 and 1.0, respectively, are shown, demonstrating the redshift evolution of the ratios for each cosmological model. All models, with the exception of a cosmology with a positively running scalar spectral index, result in some level of suppression of the non-linear matter power spectrum compared to the ΛCDM prediction on small physical scales. This suppression ranges from around 5% in the case of the less extreme WDM cosmology to $\approx 60\%$ for the more extreme WDM cosmology for the smallest scales examined here at the present day.

Resulting non-linear matter power spectra

The resultant constructed matter power spectra can be seen in Fig. 4.1, where I show the absolute power spectra at redshift z = 0 in the top panel, and the redshift evolution of the ratios computed with respect to the ΛCDM result in the bottom three panels. I only show here the results up to a maximum redshift of $z = 1.0$ as this is the maximum source redshift I use in my weak lensing calculations (I discuss my choice of a maximum source redshift of $z = 1.0$ in Section 4.4.1).

A feature common to most of the cosmological extensions examined here is the suppression of small-scale power at $k > 10\ h\text{Mpc}^{-1}$. A cosmological model with a negatively running scalar spectral index has less power on small scales due to a dampening effect on the initial density perturbations generated by inflation. WDM cosmologies have small-scale density perturbations erased due to free streaming. Finally, SIDM cosmologies have small-scale clustering erased at late times due to the self-interactions creating cores (and generally erasing structure) in otherwise high-density dark matter haloes. In detail, however, differences between the three models do exist. For example, whereas the suppression in the matter power spectrum decreases with decreasing redshift for WDM and a negative value for α_s, the suppression increases with time in a SIDM cosmology. The suppression reduces with time for the other two cosmological models due to mode mixing transferring power from large scales to smaller scales. A similar result to this was seen in Chapter 2 for the case of a running spectral index and in Viel et al. (2012) for the case of WDM. However, in the case of SIDM the effect seen in the non-linear matter power spectrum of the suppression becoming larger with decreasing redshift, which is a feature unique to SIDM, occurs due to the higher virial velocities present at late times. This causes scattering events to be more efficient at redistributing the mass inside the inner regions of haloes. Furthermore, there is a cumulative number of scattering events which occur with decreasing redshift. These combined effects result in the suppression in the matter power spectrum extending to smaller k-modes. The differences seen in the redshift evolution of the matter power spectrum are important as measurements at a single fixed redshift could result in different cosmological models having very similar effects. See, for example, the z = 0.5

panel in Fig. 4.1 where the $M_{\rm WDM}$ = 5.0 keV and the σ/m = 0.1 cm^2 g^{-1} are predicted to have an almost indistinguishable effect on the non-linear matter power spectrum. However, at earlier and later redshifts the predictions for their suppression of the matter power spectrum are noticeably different.

The model with a positive running scalar spectral index is the only model to predict an enhancement in power on these same scales, except for the slight increase in power seen in the more extreme SIDM models on $k-$scales $\approx$ 25 hMpc^{-1}. The increase in power on small-scales in the SIDM models is due to the re-distribution of dark matter in the central regions of dark matter haloes. In particular, the enhancement mainly occurs due to the outward scattering of dark matter particles from the very central regions to somewhat larger radii (see Figure 3.5 in Chapter 3, for example). This outer radii, where particles tend to gather in stable orbits corresponds approximately to the radius where one would expect each particle to have interacted at least once per Hubble time (see section 5.3 of Rocha et al. 2013, for example, for a discussion on this).

One obvious feature of the two cosmologies with a running scalar spectral index is the cross-over regions seen in the ratio panels (in the range $-2 \leq \log_{10}(k[h\text{Mpc}^{-1}]) \leq 1$). The reason these cross-over regions exist is because of differences in the amplitude of the primordial matter power spectrum, A_s, which is larger in the case of the positive running cosmology and smaller in the negative running case with respect to A_s for the fiducial ΛCDM case. (Note that A_s varies between the models in order to retain a good match to the Planck CMB angular power spectrum, see discussion in Chapter 2.) This amplitude difference produces an additional offset with respect to the ΛCDM power spectrum on top of the the resulting increase (decrease) in power on large and small scales due to the positive (negative) running of the spectral index.

4.3 Tomographic Weak Lensing

In this section I describe my methodology for computing cosmic shear power spectra from the non-linear matter power spectra described above and how I generate noisy

realisations (synthetic observations) of the cosmic shear power spectra.

4.3.1 Theory

Weak lensing describes the deflection of light rays due to the presence of large-scale structure in the Universe, which results in slight correlated distortions in the observed shapes of galaxies (Blandford et al., 1991; Miralda-Escude, 1991; Kaiser, 1992). The lensing of galaxies leads to two effects: the dilation or magnification of an image which can be described by the convergence, κ, and the stretching (shearing) of an image, $\gamma_{1,2}$. In this study I focus on the shears of galaxies which can be used to probe the projected mass distribution via the galaxy shape correlation functions. Additional information on the growth of structure over cosmic time can be obtained if one has redshift measurements of the background galaxies. In this case, the source distribution can be discretized into redshift (or tomographic) bins, allowing one to probe the three-dimensional matter distribution (see Kilbinger 2015 for a recent review).

The 2-point correlation function of galaxy shapes, and its Fourier analogue the power spectrum, are directly linked to the underlying matter distribution and its power spectrum integrated along the line of sight. I compute the cosmic shear power spectrum via:

$$P_{ij}^{\gamma}(\ell) = \int_0^{\chi_{\rm H}} d\chi_{\rm l}(1+z_{\rm l})^2 W_i(\chi_{\rm l}) W_j(\chi_{\rm l}) P_{\rm 3D}\left(k=\frac{\ell}{\chi_{\rm l}},\chi_{\rm l}\right) \quad , \tag{4.7}$$

where $\chi_{\rm l}$ is the comoving distance to the lens at redshift $z_{\rm l}$, $\chi_{\rm H}$ is the comoving distance to the horizon, which in this case is the comoving distance associated with a maximum lens redshift of 1, $P_{\rm 3D}$ is the non-linear matter power spectrum, and W_i and W_j are the lensing efficiencies in the tomographic bins i and j, defined as:

$$W_{i,j}(z_l) = \frac{3}{2}\Omega_{\rm m}\left(\frac{H_0}{c}\right)^2 \int_{z_{\rm l}}^{z_{\rm max}} \frac{\chi_{\rm l}-\chi_{\rm s}}{\chi_{\rm s}} n_{i,j}(z_{\rm s}) dz_{\rm s}. \tag{4.8}$$

Here $\chi_{\rm s}$ corresponds to the comoving distance to the source at redshift $z_{\rm s}$ and n_i is the

normalized homogeneous source distribution in tomographic bin i given by:

$$n_i(z) = \frac{n(z)}{\int_0^{z_{\max}} n(z)dz}, \tag{4.9}$$

It is worth mentioning that equation 4.7 is predicated upon some important assumptions. These include the Limber approximation (Limber, 1953; Kaiser, 1992), which only includes modes in the plane of the sky, neglecting those between structures at different epochs in the line of sight integration. The small-angle and flat-sky approximations have also been adopted, which allows one to replace a spherical harmonics transform with a Fourier transform (Hu, 1999). Other assumptions which are embedded inside the lensing efficiency $W_{i,j}$ (see equation 4.8) is that of a homogeneous galaxy distribution, which ignores source-source clustering (Schneider et al., 2002) as well as source-lens clustering (Bernardeau, 1998; Hamana et al., 2002). Spatial flatness has also been assumed in equation 4.7.

Although the previous assumptions may introduce some level of systematic error in the calculation of the shear power spectrum, I neglect them here owing to the fact that, firstly, they will be common to each cosmology and should therefore be less important when I focus on the ratios of the cosmic shear power spectra, and, secondly, they mainly affect the largest angular scales ($\ell \lesssim 10$) (see for example Schmidt, 2008; Giannantonio et al., 2012; Kilbinger et al., 2017) which is not my focus.

The uncertainty in the shear power spectrum can be expressed as (Kaiser 1998; Hu 1999; Euclid Collaboration et al. 2020a):

$$\Delta P_{ij}^{\gamma}(\ell) = \sqrt{\frac{2}{(2\ell+1)\,\Delta\ell f_{\text{sky}}}}\left[P_{ij}^{\gamma}(\ell) + \delta_{ij}\frac{\langle\gamma_{\text{int}}^2\rangle}{\overline{n_i}}\right], \tag{4.10}$$

where $\Delta\ell$ is the multipole bandwidth, f_{sky} is the fraction of sky surveyed, δ_{ij} is the Kronecker delta symbol, $\langle\gamma_{\text{int}}^2\rangle$ is the shape noise, representing the variance of observed galaxy ellipticities (which I take to have a value of 0.261, motivated by Gatti et al. 2021), and $\overline{n_i}$ is the surface density of source galaxies in the tomographic bin, expressed in steradians^{-1}. The term under the square root accounts for the limited

number of available independent ℓ modes. The first term in the square brackets corresponds to the cosmic variance and the second term is a Poisson noise term. In addition to introducing scatter in the cosmic shear power spectrum (via the Poisson noise term), the shape noise also contributes to an additive shot noise term that biases the auto power spectrum but not the cross-power spectrum, as the shot noise in different tomographic bins is uncorrelated. Thus, the shot noise must be subtracted from the estimated auto power spectra.

As written in equation 4.10 (see also Euclid Collaboration et al. 2020a, eqns. 118 and 125), it appears that the Poisson noise only applies to the uncertainty in the autocorrelation power spectrum and not the uncertainty in the cross-correlation power spectrum, in analogy to the way shot noise contributes to the measured power spectrum but not the cross-spectrum. While the Poisson noise is uncorrelated between tomographic bins and therefore does not bias the cross-spectra, I find that there is a significant contribution to the *uncertainty* in the measured cross-spectra due to Poisson noise. Furthermore, equation 4.10 only provides an estimate of the Gaussian errors; i.e., the diagonal elements of the covariance matrix, but in principle there could be significant non-Gaussian contributions. For these reasons, instead of using the standard analytic error estimate in equation 4.10, I instead generate synthetic weak lensing observations using the `FLASK` software package, as described below.

I note that cosmic variance, shape noise, and Poisson errors are not the only sources of uncertainty for the cosmic shear power spectrum. One of the major astrophysical sources of uncertainty stems from the intrinsic alignment of galaxy shapes. This stems from tidal interactions during the formation period of nearby galaxies which induces an intrinsically correlated orientation of the galaxies' shapes (Joachimi et al., 2015; Kiessling et al., 2015; Kirk et al., 2015) which works to dilute the cosmological signal in the two-point correlation function of these shapes. Additionally, another important source of error stems from photometric redshifts being used for source galaxies. This leads to some galaxies being ascribed the wrong redshift and blurring the edges of tomographic bins. A comprehensive discussion on the systematic errors affecting weak lensing surveys can also be found in Mandelbaum (2018). For simplicity I ignore these

effects in the present study.

4.3.2 Synthetic cosmic shear observations

For my cosmic shear analysis there are several choices one needs to make to specify the setup. For example, as seen in equation 4.7, the shear power spectrum will directly depend on the redshift distribution of the source galaxies. It will also depend on how many tomographic bins are used in the analysis. Furthermore, the associated uncertainty on the shear power spectrum will depend on the density of source galaxies as well as on the survey sky coverage.

In this study I am interested in whether or not future Stage-IV weak lensing surveys such as EUCLID, LSST, and NGRST would be able to rule out, or help place constraints on, the different cosmological extensions examined in this study. For my fiducial results I compute the shear auto- and cross-power spectra for a EUCLID-like setup, however, the survey parameters of an LSST-like setup would be very similar, and so the results I present below would not differ much (I have explicitly verified this). I discuss the differences with respect to an NGRST setup in Section 4.4.1.

When constructing the EUCLID-like setup, I follow as closely as possible that described in Euclid Collaboration et al. (2020a). In particular, the source galaxy distribution is defined via:

$$n(z) = z^{\alpha} \exp\left(-\left[\frac{z}{z_0}\right]^{\beta}\right), \tag{4.11}$$

where α, β and z_0 are survey specific parameters which describe the source distribution. I adopt values of 2, 1.5 and 0.636, respectively, to be similar to the source distribution expected for the EUCLID survey.

The planned analysis of the EUCLID survey splits the galaxy distribution up into 10 tomographic bins with a redshift range of $0.001 \leq z_s \leq 2.5$. However, in this study I focus on redshifts ≤ 1, which approximately corresponds to the first 6 tomographic bins in the EUCLID setup. As such, I split my galaxy distribution up into 6 tomographic bins between $0.001 \leq z_s \leq 1.0$. The edges of each tomographic bin are z_i

= $\{0.001, 0.414, 0.554, 0.669, 0.777, 0.885, 1.0\}$ and are defined such that there is an equal number of galaxies in each bin, essentially fixing the associated shot noise in each bin. I choose a maximum source redshift of 1 as, for a fixed range of angular scales, higher redshift measurements correspond to larger physical scales.[13] As the extensions I explore mostly affect small physical scales, I do not expect them to be easily distinguishable from ΛCDM at high redshifts (the exception to this are the models which have a running of the scalar spectral index, as I discuss below). Specifically, I compute the cosmic shear power spectrum up to an $\ell_{\rm max} = 4,000$, which lies close to the 'optimistic' case for the EUCLID survey of $\ell_{\rm max} = 5000$ (with their 'pessimistic' case being $\ell_{\rm max}$=1500, if one does not include non-Gaussian contributions to the covariance matrix). This $\ell_{\rm max}$ corresponds to angular scales of around 0.44 arcmin, or k [hMpc^{-1}] = 2.18, at $z = 1$.

Note that, as surveys such as EUCLID and LSST will make use of photometric redshifts (see e.g. Euclid Collaboration et al. 2020b), one needs to account for the associated uncertainty by convolving the number density distribution in equation 4.9 with a probability distribution function accounting for uncertainties in the photometric redshifts, along with accounting for catastrophic outliers (see for example equation 115 in Euclid Collaboration et al. 2020a). These are galaxies which have a severely incorrect measurement of their redshift and have therefore been placed in the wrong tomographic bin. I ignore this effect in this chapter, however.

To generate the synthetic weak lensing observations using the cosmic shear power spectra computed in Section 4.3.1 and the details of the EUCLID survey choices above, I use the publicly available software package `FLASK`[14] (Xavier et al., 2016). `FLASK` can generate lognormal (or Gaussian) realisations of correlated fields on spherical shells. I make use of its ability to generate weak lensing shear fields. Each field can be generated tomographically, with the statistical properties of these fields (including their cross-correlations) being defined via input angular power spectra (where one provides as input the auto- and cross-spectra that they want maps created for). I provide as input

[13] Note, the minimum source redshift of 0.001 was chosen to coincide with the minimum redshift used in Euclid Collaboration et al. (2020a).

[14] https://github.com/hsxavier/flask

Table 4.1: The shift parameters used to define the lognormal realisations of each shear field. The columns from left to right are the tomographic bin number, the mean redshift of the tomographic bin, the calculated shift parameter for that bin.

i	z_{mean}	λ
1	0.3003	0.0048
2	0.4874	0.0099
3	0.6126	0.0141
4	0.7233	0.0181
5	0.8307	0.0224
6	0.9417	0.0272

the theoretical cosmic shear power spectra as computed in equation 4.7, which in the flat-sky approximation is equivalent to the convergence power spectrum (Hu, 2000; Kilbinger et al., 2017; Bartelmann and Schneider, 2001). I use `FLASK` to produce many realisations of my theoretical shear power spectra, allowing us to evaluate the full covariance matrix in the error analysis, rather than just using the Gaussian errors computed using equation 4.10, and to evaluate the potential Poisson noise contribution to cross-power spectra between tomographic bins. Note that the measured power spectra computed from the `FLASK` maps will contain a shot noise contribution. Therefore, when computing the full covariance matrix I subtract this shot noise from the autocorrelation power spectra.

In order to define the log-normality of the shear field, one needs to specify a shift parameter. I compute this shift parameter (λ) following Hilbert et al. (2011) who used the Millennium Simulation (Springel, 2005) to produce synthetic convergence and shear maps (see, for example, equation 22 in this paper for how this relates to the definition of a lognormal distribution). From these maps they measure the convergence distribution and find that it is best fit with a zero-mean shifted log-normal distribution. They do this at multiple redshifts and provide an empirical formula, which I use here, that captures the redshift evolution of the shift parameter λ (κ_0 in Hilbert et al. 2011)

$$\lambda(z) = 0.008z + 0.029z^2 - 0.0079z^3 + 0.00065z^4. \tag{4.12}$$

I substitute in the mean redshift of each tomographic bin to calculate the associated shift parameter for that field. The values calculated can be found in Table 4.1.

I want FLASK to output shear maps which will also capture the noise associated with measurements of the cosmic shear power spectrum (see Section 4.3.1). Therefore, I also supply FLASK with an angular selection function, such that the map will be masked to reproduce a survey's specific $f_{\rm sky}$, as well as providing a redshift selection function so that the number of galaxies in a tomographic bin is reproduced. One also needs to supply the software with a value for the ellipticity dispersion of galaxy shapes, $\langle\gamma^2_{\rm int}\rangle$, in order to incorporate shape noise into the shear maps created. As already noted, I adopt $\langle\gamma^2_{\rm int}\rangle = 0.261$.

The maps output by FLASK, which are output in HEALPix[15] format, contain the mean source ellipticity in each pixel, calculated via:

$$\epsilon(j) = g(j) + \frac{\epsilon_s}{\sqrt{N_{\rm gal}}}, \tag{4.13}$$

where $g(j)$ is the reduced shear associated with pixel j, $\epsilon_{\rm s}$ is a value for the intrinsic ellipticity associated with galaxy shapes randomly sampled from a zero-mean Gaussian distribution with width equal to $\langle\gamma^2_{\rm int}\rangle$, and $N_{\rm gal}$ is the number of galaxies that fall within that pixel. I produce 200 map realisations of each tomographic power spectrum in this way. Following this I compute the auto- and cross-correlation power spectra of these maps using the PYTHON package HEALPY[16]. I use these power spectra to evaluate the covariance matrix in 14 multipole bins in the range $10 \leq \ell \leq 4,000$, which I calculate as:

$$\mathrm{cov}\left[P^{\gamma}_{ij}(\ell), P^{\gamma}_{i'j'}(\ell')\right] \quad = \quad \left\langle \left(P^{\gamma}_{ij}(\ell) - \left\langle P^{\gamma}_{ij}(\ell)\right\rangle\right)\left(P^{\gamma}_{i'j'}(\ell') - \left\langle P^{\gamma}_{i'j'}(\ell')\right\rangle\right)\right\rangle \tag{4.14}$$

The resultant cosmic shear auto- and cross-power spectra can be seen in Fig. 4.2 for all cosmologies, along with the associated uncertainties on the cosmic shear power

[15] https://healpix.sourceforge.io/
[16] https://github.com/healpy/healpy

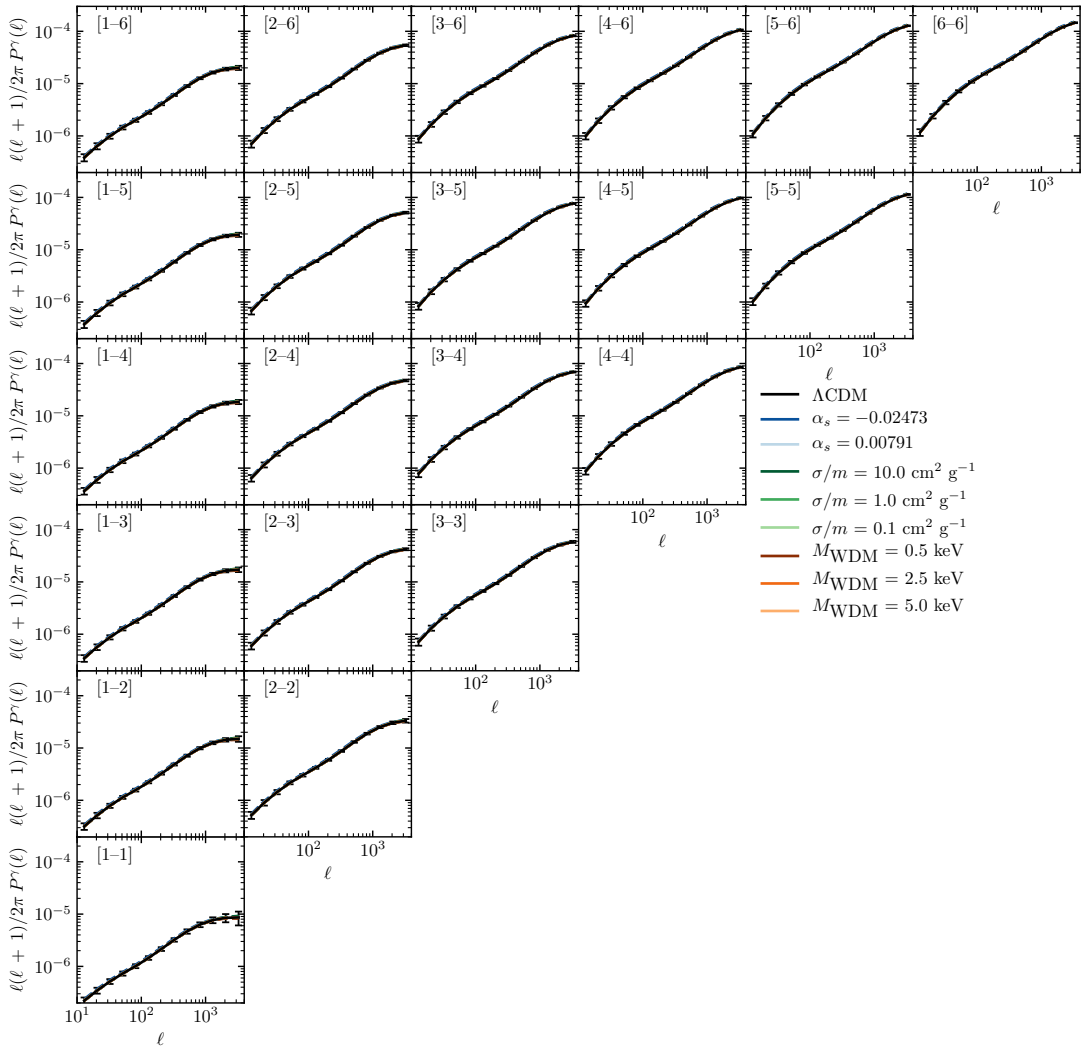

Figure 4.2: The shear auto- and cross-correlation power spectra computed for each cosmological model. The source galaxy tomographic bins are distributed between a minimum source redshift of 0.001 and a maximum source redshift of 1.0 and such that each tomographic bin has the same number density of source galaxies. I split the distribution up into 6 tomographic bins to mimic a EUCLID-like survey and plot up to $\ell_{\rm max}$=4,000, which lies between the pessimistic and optimistic case for the EUCLID survey. Here the error bars show the standard deviation of the realisations of each power spectrum evaluated using the `FLASK` package (see text). In general, the deviations to ΛCDM case are subtle and require a quantitative evaluation of the signal-to-noise ratio.

spectrum, which serves to illustrate the absolute power spectra and how the associated changes due to the different cosmological models are generally quite subtle. The differences in the cosmic shear power spectra are better highlighted in Fig. 4.3, which shows the ratio of each auto- and cross-correlation power spectrum with respect to the ΛCDM prediction in that same tomographic bin. I discuss here the calculation of the error bars in Figs. 4.2 and 4.3 and leave the scientific interpretation of these results for Section 4.4.

The red error bars in Fig. 4.3 show the theoretical uncertainty associated with the shear power spectrum as computed using equation 4.10. The black error bars represent the diagonal elements of the covariance matrix for a ΛCDM cosmology calculated using multiple realisations of each shear power spectrum as generated by `FLASK`. Note here that the error bars which are shown are normalised to the ΛCDM power spectrum in each tomographic bin, i.e., $\Delta P_{ij}^{\gamma}(\ell)/P_{ij}^{\gamma}(\ell)$.

It can be seen in Fig. 4.3 when comparing the theoretical error bars shown in red to the black error bars extracted from the covariance matrix computed with the assistance of `FLASK`, that the errors are in excellent agreement (as one would expect) for the autocorrelation power spectra. There is some disagreement at low multipoles, which stems from cosmic variance issues associated with the maps.[17] However, importantly, this agreement does not hold for the cross-correlation power spectra, with significant disagreements at large multipoles (small angular scales). Specifically, the analytic calculation in equation 4.10 ignores the effects of Poisson noise on uncertainty in the cross-spectrum, but I find there is always a non-negligible Poisson error.

In Appendix C.2 I use realisations of pure shape noise fields generated with `FLASK` to derive a more accurate and general equation for incorporating the impact of shape noise

[17] I tested whether the error bars at small multipole were brought into better agreement if one created full sky realisations of the power spectra using `FLASK` rather than a masked version and found that this was indeed the case. Therefore, it is likely that the masking is adding some additional spurious noise to the signal on large angular scales.

(Gaussian errors only) on the cross-spectrum, namely:

$$\Delta P_{ij}^{\gamma}(\ell) \quad = \quad \sqrt{\frac{2}{(2\ell+1)\, f_{\rm sky}}} \left[P_{ij}^{\gamma}(\ell) + \delta_{ij} \frac{\langle \gamma_{\rm int}^2 \rangle}{\overline{n_i}} + (1-\delta_{ij}) \frac{\langle \gamma_{\rm int}^2 \rangle}{\sqrt{2 \overline{n_i n_j}}} \right] . \quad (4.15)$$

The new term (right most in the square brackets) represents the contribution of Poisson noise to the uncertainty in the cross-power spectrum. Note the similarity of the noise terms for the auto- and cross-spectra, which is expected because they are caused by the same effect: random alignments of galaxy shapes. The only difference is that for the cross-spectrum term I allow for the possibility of different source densities in the tomographic bins being cross-correlated, and the extra factor of square root of 2, which is the result of having more galaxy pairs to evaluate in the cross-spectrum compared to the power spectrum (the error scales as the number of pairs).

Finally, I note that the black error bars plotted in Figs. 4.2 and 4.3 correspond to just the diagonal elements of the covariance matrix, but I use the full covariance matrix when evaluating signal-to-noise ratios in in Section 4.4.

4.3.3 Summary of theoretical cosmic shear pipeline

Here I provide a very brief summary of the steps described above in generating cosmic shear power spectra for the different cosmological models in this study, alongside a realistic estimate of the uncertainties.

- Compute $P(k)$ for each cosmological simulation (including box size variations for the two α_s simulations) and re-bin to smooth out some of the initial numerical noise associated with the power spectra.
- Compute the ratio of each power spectrum with respect to a corresponding ΛCDM simulation (of same box size and resolution).
- For cosmologies with a running spectral index, combine the ratios computed from the 400, 100, 25 Mpc h^{-1} box simulations along with the `Halofit` pre-

diction to a $\log(k_{\rm min}) = -4$. For all other cosmologies, extrapolate $R_C(k, z) = 1$ for large scales not sampled in the 25 Mpc h^{-1} box. Fit a cubic spline to the constructed ratios and smooth.

- Calculate the absolute $P(k)$ for each cosmology using the constructed ratio as a boost factor to modify the ΛCDM prediction computed using `Halofit` (equation 4.6).
- Generate theoretical tomographic shear power spectra for each cosmological model using equation 4.7.
- Construct multiple synthetic tomographic weak lensing shear maps for a ΛCDM universe including galaxy shape noise using the `FLASK` package. Compute $C(\ell)$ for each realisation to construct a covariance matrix for the ΛCDM prediction using equation 4.14.

4.4 Results

In this section I present the main results of this work. This includes predictions for the tomographic cosmic shear auto- and cross-power spectra for each cosmological model, along with their respective ratios with respect to ΛCDM. I also explore how large the differences in the cosmic shear power spectrum due to a change in cosmology are compared to the expected error associated with the cosmic shear power spectrum.

4.4.1 Comparisons up to $\ell_{\rm max} = 4,000$

I now discuss the main results of my investigation for the fiducial EUCLID-like setup, examining the cosmic shear power spectrum up to a maximum multipole of $\ell_{\rm max} = 4,000$.

Examining the ratios of the various cosmological extensions with respect to ΛCDM shown in Fig. 4.3, I can immediately conclude (by eye) that all of the cosmological

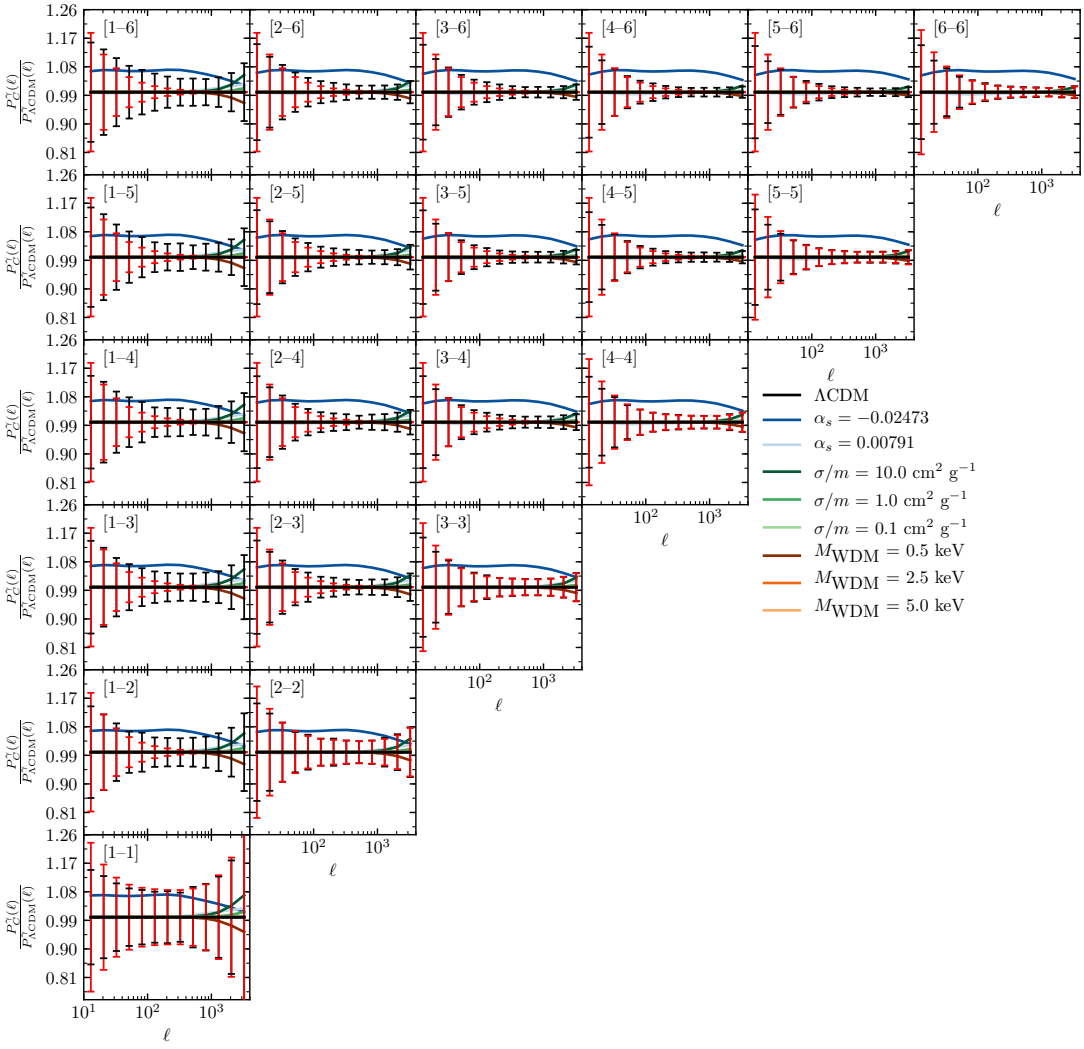

Figure 4.3: The shear auto- and cross-correlation power spectrum for each cosmological model normalised to the corresponding ΛCDM auto/cross-correlation power spectrum. The different coloured lines represent the different cosmological modes, indicated in the legend. The red error bars show the standard theoretical (analytic) prediction for the noise on the shear power spectra (which does not include the effects of Poisson noise on the shear cross-spectra), and the black error bars show the noise computed using multiple realisations of each auto and cross power spectrum in a ΛCDM cosmology with the `FLASK` package. This plot helps highlight the resultant changes to the cosmic shear power spectrum, particularly due to the inclusion of a running scalar spectral index as a free parameter in the standard model. The numbers in square brackets in the top left of each panel indicate the tomographic bin number. Increasing tomographic bin number corresponds to higher redshifts (see Table 4.1 for the mean redshift of each bin).

extensions studied here are capable of producing some level of deviation in the cosmic shear power spectrum compared to the ΛCDM prediction over this range of multipoles. However, in the case of WDM and SIDM, these changes appear most noticeable for the two extremest models examined in this study. The other models do produce differences as well, but they are comparatively smaller and a more quantitative analysis of their 'detectability' is thus required.

I quantitatively characterise the constraining power of the cosmic shear observations via a signal-to-noise ratio (SNR), which I evaluate as:

$$(S/N)^2 = \sum_{\ell,\ell' \leq \ell_{\rm max}} (|R(\ell) - 1|) \left(\frac{\mathrm{Cov}[\mathrm{P}^{\gamma}_{\rm ij}(\ell), \mathrm{P}^{\gamma}_{\rm ij}(\ell')]}{P^{\gamma}_{ij}(\ell) P^{\gamma}_{ij}(\ell')} \right)^{-1} (|R(\ell') - 1|) \quad , \quad (4.16)$$

where $R(\ell)$ is the ratio of each cosmological extension with respect to ΛCDM as plotted in Fig. 4.3. I make use of the full covariance matrix calculated using equation 4.14, which I normalise with respect to the absolute power spectra themselves. I do this because I am comparing the error bars to the ratios rather than the absolute power spectra.

The resultant plot of the integrated SNR as a function of $\ell_{\rm max}$ can be seen in Fig. 4.4. The solid curves represent the integrated SNR as a function of scale when using the full covariance matrix to estimate the uncertainties. For comparison, the dashed curves show the integrated SNR when using only the Gaussian (diagonal elements) errors. A legend is provided which lists the integrated SNR when summed (in quadrature) over all tomographic bins for the full covariance matrix case and for the diagonal errors only (the latter is in parentheses).

As expected from Fig. 4.3, the cosmology with a negative value for the running of the spectral index shows strong deviations from the ΛCDM prediction over almost the entire multipole range, with these differences becoming larger at higher redshift. The reason for this stems mainly due to an increase in the absolute power on these multipoles in the later tomographic bins, as seen in Fig. 4.2. This causes the relative error bars to decrease with increasing redshift resulting in a larger SNR. When summed over

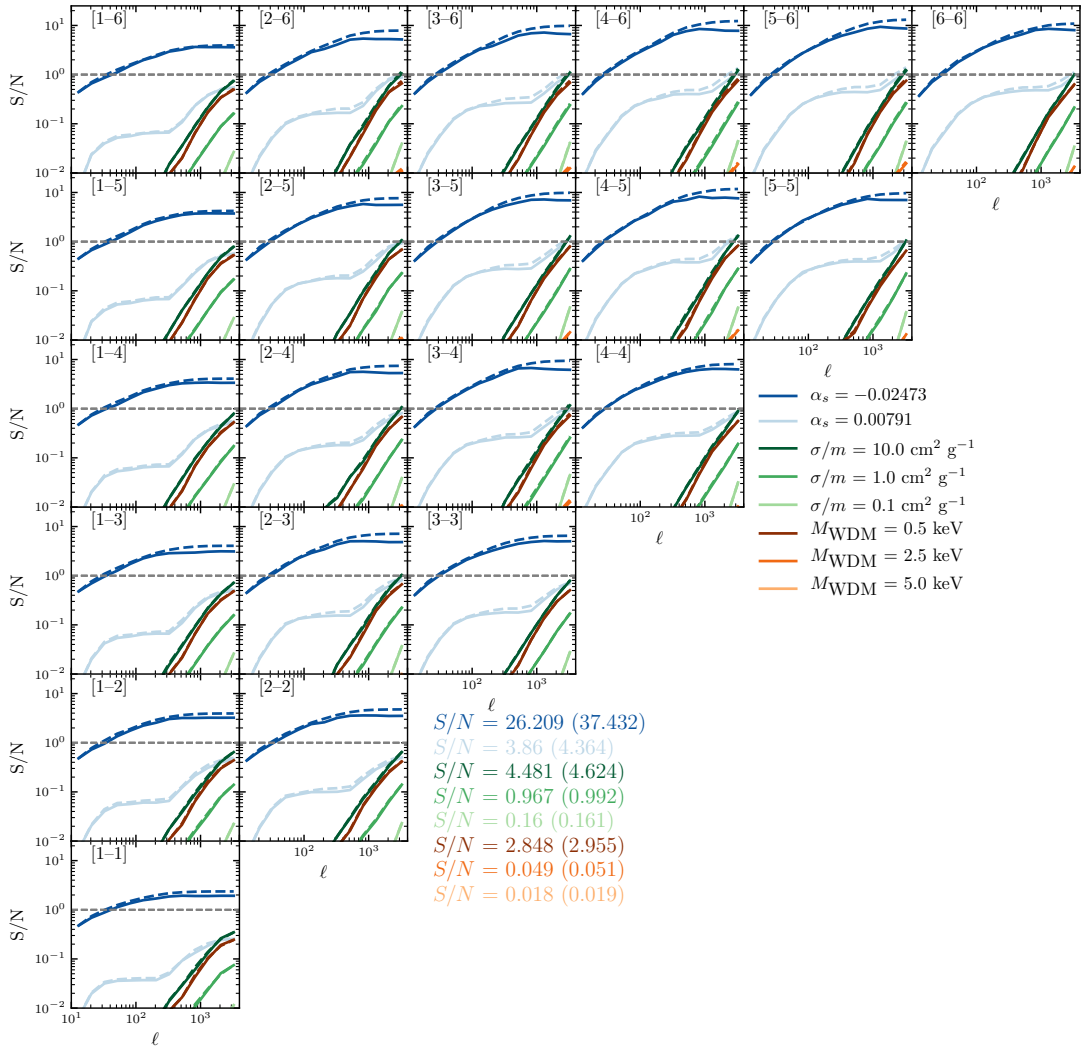

Figure 4.4: The integrated signal to noise ratio (SNR) as a function of $\ell_{\rm max}$ to demonstrate how significant the deviations in the shear power spectra are for the different cosmological models relative to ΛCDM. I plot here two variants of this statistic shown by solid and dashed lines. In the first case (solid line), the SNR is calculated using the entire covariance matrix, whereas the dashed line only uses the diagonal elements of the covariance matrix. The total integrated SNR, summed (in quadrature) over the tomographic bins, is shown next to the bottom left panel with the values in brackets indicating the SNR if one only uses the diagonal elements of the covariance matrix.

all tomographic bins, a Planck-based cosmology with a negative running of the scalar spectral index will likely be easily distinguishable from a Planck-based ΛCDM cosmology with a EUCLID-like cosmic shear survey.

One apparent feature in the SNR for the negative running cosmology is the plateau towards higher multipoles. The reason for this behavior is that the signal I see here is dominated by the region of the power spectrum for which a negative running cosmology produces an enhancement in power (due to the increase in A_s) relative to ΛCDM. However, on the largest multipoles the ratio begins to turn over and decrease, where it would eventually cross over the ΛCDM prediction and predict a suppression in the cosmic shear power spectra, rather than the enhancement that I see on these scales. Therefore, the signal, relative to the error bars, decreases over this range of scales yielding a plateau in the integrated SNR. The same effect is also seen, perhaps somewhat more clearly, in the cosmology with a positively running scalar spectral index where the opposite is true. In this case, there is initially a slight suppression in the cosmic shear power spectra which flips and becomes an enhancement at high multipoles, producing the initial increase in the SNR, followed by a plateau and then a second increase after the ratio has crossed unity. As a result, the positive running cosmology has an integrated SNR in the later multipole bins exceeding 1, showing that upcoming future surveys such as EUCLID and LSST are perhaps able to put constraints on a value for the running of the scalar spectral index that are competitive to those from cosmic microwave background and Lyman-α forest constraints.

Note that the SNR would likely continue to increase if I increased the maximum source redshift beyond the limit of z_s=1.0 that I adopt here, at least for the running cosmologies. If one was to include tomographic redshift bins beyond $z_{\rm s}$ = 1.0 the relative error bars shown in Fig. 4.3 would decrease (due to the increase in the cosmic shear signal); hence this would enhance the SNR seen here. The reason I do not include these higher redshift tomographic bins in this study is because, as mentioned, at fixed $\ell_{\rm max}$, but increasing $z_{\rm s}$ the region of the matter power spectrum one becomes sensitive to tends towards smaller $k-$modes. As such, although this would still result in a measurable signal for the two models with a running spectral index, it would not result in a mea-

surable signal for the WDM and SIDM cosmologies (their effects are confined to small physical scales). However, these higher redshift tomographic bins will be included in future weak lensing surveys, resulting in potentially increased constraining power on α_s compared to what is shown here.

For the SIDM and WDM cosmologies it appears that one needs to probe to much smaller scales (higher multipoles) to be able to distinguish most of the models I explored from ΛCDM. The only exceptions are the most extreme WDM (0.5 keV) and SIDM ($\sigma/m = 10$ cm^2 g$^-$1) models. My calculations suggest that a EUCLID-like survey with realistic source densities and shape noise may be able to (marginally) distinguish these models from ΛCDM. Pushing to higher multipoles would help in these cases as well.

An important aspect of a EUCLID-like survey is the fact that it has a large sky coverage, meaning the cosmic variance error associated with the measurements of the cosmic shear power spectrum is strongly reduced on all but the largest angular scales. Therefore, the limiting factor in the ability of detecting a difference between some of these cosmological models and ΛCDM, particularly at the upper-end of the multipole range I analyse in this study, is a result of the uncertainty in galaxy shapes. Thus, I have also investigated a similar tomographic setup as that expected for the NGRST survey which instead of a large $f_{\rm sky}$ (NGRST is envisioned to have $f_{\rm sky}$ = 0.0485), is expected to have a larger number density of source galaxies equal to n_s = 51 galaxies/arcmin^2 compared to $n_s = 30$ galaxies/arcmin^2 for a EUCLID-like (or LSST-like) setup.

For the NGRST setup I use five tomographic bins up to redshift 1.0, defining the source galaxy distribution using equation 4.11 (here I adopt the parameter values: $\alpha = 2$, $\beta = 0.9$, $z_0 = 0.28$ in order to closely mimic the galaxy distribution described in Eifler et al. 2020). I find that, although the shot noise error is decreased in such a survey setup, the increase in the cosmic variance error due to the reduction in sky coverage compensates, resulting in no improvement on the SNR[18]. Therefore, it seems

[18]The total integrated SNRs calculated for a NGRST-like setup for each cosmology, using the full covariance matrix are: {9.657, 1.733, 2.203, 0.481, 0.082, 1.39, 0.023, 0.009}, in the same order as that displayed in Fig. 4.4.

that one would need both a large $f_{\rm sky}$ (although potentially not as large as EUCLID or LSST), and a large number density of source galaxies, n_s, to use cosmic shear to better constrain these cosmological models without having to push to higher multipoles.

It is apparent from the above analysis that, if it was possible to push to higher multipoles, this could considerably increase the constraining power for the SIDM and WDM scenarios. However, if I were to evaluate the uncertainties using a full covariance matrix approach this would be much more computationally expensive, as each realisation has around 2×10^8 pixels in each tomographic map and $(N_{\rm T}(N_{\rm T}+1)/2)$ auto- and cross-correlation power spectra (where $N_{\rm T}$ is the number of tomographic bins)[19]. However, I can considerably simplify the process if the Gaussian errors (in equation 4.15) are sufficient to calculate a SNR. Comparing the solid and dashed curves in Fig. 4.4, I conclude that the difference in the integrated SNRs are fairly significant for the running cases (particularly the negative running scenario), but not for the SIDM or WDM cases, at least over the range of multipoles examined here. As such, below I examine if pushing to $\ell_{\rm max} = 20,000$ improves the SNR for the models with WDM, SIDM and positive running scalar spectral indices, using the estimated Gaussian errors rather than a full covariance matrix approach.

4.4.2 Comparisons up to $\ell_{\rm max} = 20,000$

I show in Fig. 4.5 the new integrated SNR, extended up to an $l_{\rm max}$ = 20,000, with the vertical dashed grey line in each panel showing the previous $l_{\rm max}$. Note that I have replaced the reduced covariance matrix term in equation 4.16, with simply $\left(\Delta P^{\gamma}_{ij}/P^{\gamma}_{ij}\right)^{-2}$, where ΔP^{γ}_{ij} is calculated using equation 4.15, which includes the additional Poisson error on the cross-correlation power spectra.

Pushing to higher multipoles does indeed reveal regions of the cosmic shear power spectrum where the differences due to changes in cosmology are not yet completely drowned out by the associated noise. This is particularly true for the positive running cosmology and the two SIDM cosmologies with the smallest cross-sections, which

[19]Note that I produce 200 unique realisations in order to evaluate the covariance matrix.

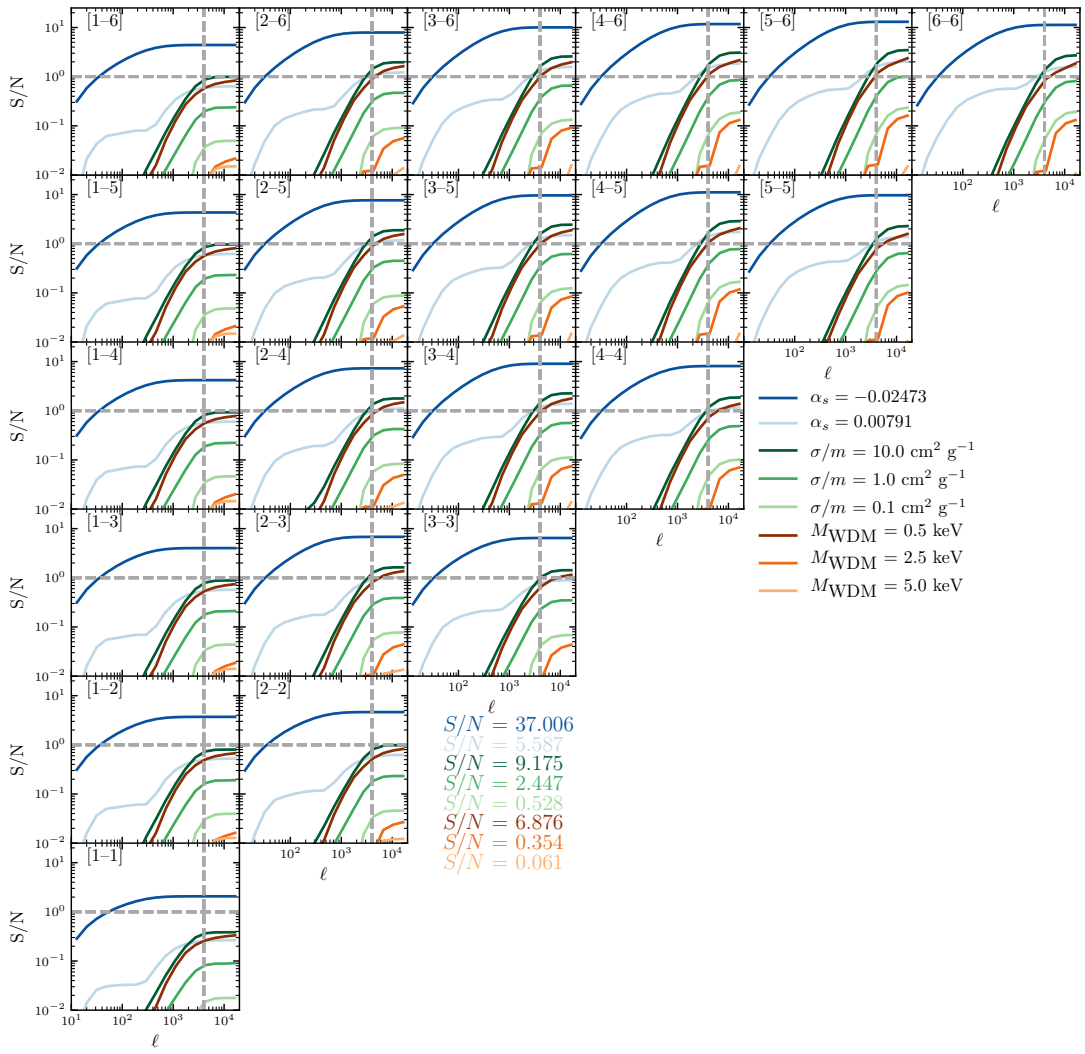

Figure 4.5: Same as Fig. 4.4, however, here I plot the integrated SNR up to an increased $\ell_{\rm max}$ of 20,000. To do this I only make use of the Gaussian terms of the covariance matrix, computed using the updated error equation shown by equation 4.15. This shows that if one was able to push to these smaller angular scales, these observations could potentially be fruitful in putting constraints on the the cross-section for interaction of dark matter particles, as well as increased constraining power on the running of the spectral index. The vertical grey dashed line corresponds to the previous $\ell_{\rm max}$ = 4,000.

all show a marked improvement in the total integrated SNR when summed over tomographic bins, as shown at the bottom of Fig. 4.5. However, although the total integrated SNR is now > 1 for the less extreme SIDM cosmology of the two, the integrated SNR never exceeds 1 in any single tomographic bin, meaning the full tomographic information will be needed to place constraints on the cross-section for interaction.

Note that the signal present in each tomographic bin will be somewhat sensitive to the tomographic binning strategy. For example, at fixed source density for a given survey, the fewer tomographic bins one has the larger the effective number density of source galaxies in each tomographic bin. This will work to decrease the shot noise associated with each tomographic power spectrum, thus increasing the integrated SNR in an individual bin. The integrated SNR when summed over all bins, though, should be a more robust quantity.

In the case of the WDM cosmologies, pushing to these higher multipoles does not result in a significant gain in SNR, insofar as detection is concerned. As explained previously, this is in part because the suppression in the matter power spectrum in a WDM cosmology is maximal at larger redshifts. However, the $k-$scales affected in a WDM cosmology move out of range of the $\ell-$modes covered in this study at higher redshifts.

While it is clear from the above analysis that pushing to higher multipoles in general results in increased SNRs, a potentially important caveat is that my analysis does not take into account additional sources of uncertainty that may be prevalent on such small angular scales, including source deblending difficulties. This refers to the phenomenon where sources (be them galaxies or stars) overlap on the sky, disrupting the shear estimation of a source galaxy. This can be accounted for by rejecting objects which are flagged as blended. However, as was shown in, for example Hartlap et al. (2011) and MacCrann et al. (2017), this can lead to a selection bias on the source galaxies used in the cosmic shear analysis. In particular, this selection bias works to exclude galaxies in high density environments, which will have a higher convergence than average, resulting in a biased (low) two-point correlation function of galaxy shapes, particularly on small-scales (see e.g., fig.8 in MacCrann et al. 2017). However, recently Hoek-

stra et al. (2021) showed that this bias can be effectively mitigated using a process of METADETECTION (Sheldon et al., 2020). In addition to this, an effective modelling of baryonic physics will be needed on these scales to fully extract the cosmological information on these small scales (see below).

4.5 Discussion & Conclusions

In this study I have explored the effects that different extensions to the standard model of cosmology have on the non-linear matter power spectrum, particularly on small scales. This was achieved using a suite of numerical simulations which contain three cosmological variations (in addition to the fiducial ΛCDM realisation): i) a running scalar spectral index (α_s), warm dark matter ($M_{\rm WDM}$) and self-interacting dark matter (σ/m). I focus on these extensions in particular as they have previously been shown to suppress small-scale structure and therefore offer a potential means to mitigate small-scale challenges which have been highlighted with the ΛCDM model. I combined the small-scale power spectra extracted from the simulations with the predictions of Halofit on large scales to construct non-linear matter power spectra for the different extensions spanning over six orders of magnitude in wavenumber ($-4 \leq \log_{10}(k[h\text{Mpc}^{-1}]) \leq 2.4$). These power spectra were used to compute the cosmic shear power spectrum. Finally, I evaluated via synthetic lensing observations (generated with FLASK) whether forthcoming Stage-IV lensing surveys (EUCLID, LSST, and NGRST) will potentially be able to differentiate these extensions from the standard ΛCDM model.

The main findings of my study are as follows:

- A negative running spectral index, WDM and SIDM are all capable of producing a significant suppression in the non-linear matter power spectrum at late times (Fig. 4.1). At $z = 0$, this suppression can range from $\approx 5\%$ to $\approx 40\%$ in the case of WDM, at $k \approx 100\ h\text{Mpc}^{-1}$. Furthermore, in the case of WDM, the suppression in the matter power spectrum increases with increasing redshift, rising

to $\gtrsim 60\%$ at $z = 1$. A similar trend is seen for the negative running cosmology, although not to the same extent as for WDM. Conversely, the suppression in the matter power spectrum increases with decreasing redshift in an SIDM cosmology. This is due to the strong cores developing in the density profiles of haloes as structures collapse and the relative velocities of particles increase.

- From the different cosmological extensions I have examined, a running scalar spectral index looks the most promising in having a measurable effect on the cosmic shear power spectrum for upcoming surveys such as EUCLID. This can be seen, somewhat counter-intuitively, in the enhancement that is produced in the cosmic shear signal on intermediate scales, due to the change in the amplitude of the non-linear power spectrum with respect to ΛCDM on the important scales (Fig. 4.3). I find that there is a significant signal for both a negatively running spectral index and a positively running one, shown through the signal-to-noise ratio (Fig. 4.4). This illustrates that cosmic shear could be an additional probe which, if used in combination with other probes such as the CMB, could help place strong constraints on the running α_s.

- The constraining power for the other two cosmological extensions of interest here, the mass of the WDM particle and the self-interaction cross-section, is slightly weaker, owing to the fact that these extensions affect only the smallest scales. I have shown that upcoming cosmic shear measurements should be able to rule out SIDM models with $\sigma/m > 10$ cm^2 g^{-1} or WDM models with thermal relic masses $M_{\rm WDM} < 0.5$ keV. While these are perhaps weaker constraints than what can be obtained from other methods (e.g., satellite abundances, strong lensing time delay, Lyman-α forest), I note that cosmic shear is independent test that has very different systematics than previous small-scale probes, making it still a very worthwhile test of these small-scale extensions. In addition, I have demonstrated that, if it is possible to push to higher multipoles with these experiments, there is the potential that cosmic shear could help place some of the strongest constraints on the SIDM cross-section (σ/m) (Fig. 4.5).

- Finally, I have illustrated that the standard analytic prediction for the error asso-

ciated with the cosmic shear cross-correlation power spectrum (between tomographic bins) significantly underestimates the true error that one recovers when computing the same power spectrum from a map which includes a prescription for galaxy shape noise by a factor of around 20 at $\ell \approx 1,000$ (Fig. C.2) . This is because the standard prescription ignores the associated Poisson error. I have introduced a modification to the analytic form of the error which modifies the error associated with cross-correlation power spectrum (equation 4.15) and is found to bring the analytic errors into much better agreement with my empirical findings based on cross-correlating shape noise maps.

One of the main focuses of upcoming weak lensing surveys, such as EUCLID, LSST and NGRST, is to help place constraints on the dark energy equation of state parameter w, or the time varying dark energy equation of state parameters w_0, w_a. It is well-established that cosmic shear tomography provides a sensitive probe of the growth of structure which, in turn, depends on the evolution of dark energy. However, here I illustrate that the constraining power of cosmic shear measurements also extends beyond dark energy and the other Friedmann parameters. Specifically, I have shown that cosmic shear observations can potentially place constraints on the running of the spectral index, as well as the cross-section for interaction of dark matter particles (SIDM) and the thermal relic mass (WDM). As a final test, I have calculated the source density required to improve constraints on the less extreme cosmological models such as the $M_{\rm WDM} = 2.5, 5.0$ and $\sigma/m = 0.1$ cm^2 g^{-1} models. I find that for a sky coverage equal to that of EUCLID, the required source density of background galaxies should be $\approx$ $\{85, 525, 60\}$ galaxies/arcmin^2, respectively, in order to obtain a SNR of > 1, when pushing the analysis to $\ell_{\rm max}$=20,000.

The tests performed in this study consisted of whether forthcoming cosmic shear surveys could distinguish (on the basis of SNR) a number of extensions, with specific parameter values, from the baseline ΛCDM model. The tests were particularly simple in that, in most cases, all of the cosmological parameters were held fixed, apart from the new parameters describing the extension. A more realistic test would be to allow the various parameters to be free and to marginalise over them when estimat-

ing the uncertainty (and potentially bias) in the recovered extension parameters (e.g., WDM particle mass). However, to achieve this requires many more simulations than produced here and potentially sophisticated methods (e.g., emulators) for interpolating the results for arbitrary cosmological parameter values. While my promising results demonstrate that this is clearly worthwhile, it is a large undertaking and I leave this for future work.

In this study I focused on the constraining power of future cosmic shear measurements. However, there are additional complementary two-point statistics that may be helpful in placing constraints on these cosmological extensions. In particular there is galaxy clustering, which describes the clustering between lens galaxies, and galaxy–galaxy lensing, which describes the over-density of mass around lens galaxies. Together with cosmic shear, these 3×2pt statistics have been shown to help place tighter constraints on the cosmological parameters $\Omega_{\rm m}$ and σ_8 (see e.g. fig. 6 of DES Collaboration et al. 2021). However, combining all three of these probes is beyond the scope of this work, which focused on the constraining power of cosmic shear alone. In future work, I will explore how the constraints in this paper change when combining these 3×2pt statistics.

An important caveat to the work I have presented is that the simulations I used neglected the effects of baryonic physics. Previous work has demonstrated that when numerical simulations include complex galaxy formation physics, such as feedback from supernovae and active galactic nuclei, they can produce relatively large effects (typically 5-20%) on the non-linear matter power spectrum (e.g., van Daalen et al. 2011; Chisari et al. 2018; Springel et al. 2018; van Daalen et al. 2020). Furthermore, these effects due to galaxy formation physics have been shown to be visible in the cosmic shear two-point correlation functions at a similar level (Semboloni et al., 2011). My work has focused mostly on small scales where, as opposed to baryons suppressing the power spectrum via the expulsive effects of feedback on relatively large scales (the focus of most previous studies), it is more likely that cooling and star formation will lead to an *enhancement* in the power spectrum. Regardless of whether baryons produce a suppression or an enhancement, the effects may be degenerate with the cos-

mological extensions I have examined here. As discussed in Chapter 3, ultimately what is required is a systematic and simultaneous exploration of the (uncertain) impact of baryons and cosmological variations on small scales and an understanding of how these effects propagate through to observables on small scales such as the cosmic shear power spectrum.

In closing, to help mitigate potential degeneracies, recent studies have shown the power of combining complementary probes when placing constraints on additional cosmological (and baryon) parameters. For example, Enzi et al. (2020) and Nadler et al. (2021) have illustrated the power of combining multiple probes (Lyman-α forest, strong lensing and the abundance of Milky Way satellites) in placing constraints on the WDM particle mass. Measurements of cosmic shear on small scales provide an important new tool in this regard and one that has very different systematic uncertainties from currently used small-scale probes. Forthcoming Stage-IV lensing surveys therefore offer a promising new window to study cosmological and galaxy formation physics on small scales.

Chapter 5

Conclusions and Future Work

5.1 A summary

The ΛCDM model is able to successfully predict a remarkably wide range of observations of our Universe and this is in spite of it having only six free parameters. With this in mind, it is no wonder it has come to be known as the standard model of cosmology. However, we are currently living in very exciting times for the field of cosmology, with several apparent tensions with ΛCDM now reaching the threshold of statistical significance, potentially heralding unaccounted for physics beyond that contained within the currently accepted standard model. Over the previous chapters in this thesis, I have outlined several possible extensions to the standard model. These extensions have been motivated using tensions associated with cosmological parameter constraints from large-scale structure observations, as well as tensions associated with the apparent under-abundance of structure on small-scales in the real Universe compared with ΛCDM simulations.

5.1.1 Effects of a running scalar spectral index on large-scale structure

In Chapter 2, I introduced an extension to the BAHAMAS suite of cosmological hydrodynamical simulations (first presented in McCarthy et al. 2017). This suite consists of 5 hydrodynamical simulations (along with complementary dark matter only realisations) exploring different values for the running of the scalar spectral index which is usually assumed to be zero in the standard model of cosmology. I found that the matter power spectrum in a $Planck$-constrained running cosmology is affected on all $k-$scales examined in this study. These effects on the matter power spectrum should be detectable with upcoming surveys such as LSST and EUCLID (which is supported by the results of Chapter 4). A cosmology with a positive value for the running leads to an increase in the mass of galaxy groups and clusters, with the favoured negative running leading to a decrease in mass of lower-mass ($M \lesssim 10^{13}\mathrm{M}_{\odot}$) haloes, but an increase for the most massive ($M \gtrsim 10^{13}\mathrm{M}_{\odot}$) haloes. Changes in the mass are generally confined to 5-10% which, while not insignificant, cannot by itself reconcile the claimed tension between the primary CMB and cluster number counts. Furthermore, this change in the mass of haloes results in a change to the linear bias, which manifests itself in changes to the clustering signal of haloes in different mass bins.

5.1.2 Separability of cosmological effects and baryonic effects

Additionally, in Chapter 2, I examined whether or not the effects present due to changes in cosmology are separable from the effects seen when incorporating galaxy formation physics in the simulations. In detail, I found that the observed effects on LSS due to a running scalar spectral index are separable from those of baryonic effects to typically a few percent precision. This is particularly relevant for the non-linear matter power spectrum and the halo mass function, both of which are sensitive probes of cosmology. Therefore these results showed that one can marginalise over baryonic effects without compromising any constraining power on the underlying cosmological parameters.

5.1.3 Effects of non-standard cosmologies on small-scale structure formation

In Chapter 3, I introduced a new suite of high-resolution dark matter only cosmological simulations exploring 3 different extensions to the standard model of cosmology. I used these high-resolution simulations to examine a large range of observable metrics on small scales, including the halo mass function, total matter density and circular velocity profiles, the abundance of satellite subhaloes, and halo concentrations. For any given metric, significant degeneracies can be present between the extensions examined in this chapter (non-zero α_s, WDM and SIDM). In detail, however, the different extensions have quantitatively distinct mass and radial dependencies, suggesting that a multi-probe approach over a range of scales can be used to break the degeneracies. I also demonstrated that the relative effects on the radial density profiles in the different extensions (compared to the standard model) are converged down to significantly smaller radii than are the absolute profiles. Additionally to comparing the effects present between different cosmological models, I also compared the derived cosmological trends with the impact of baryonic physics using the EAGLE and ARTEMIS simulations. Significant degeneracies are also present between baryonic physics and cosmological variations (with both having effects of similar magnitude on certain observables). Given the inherent uncertainties both in the modelling of galaxy formation physics and extensions to ΛCDM, a systematic and simultaneous exploration of both is strongly warranted.

5.1.4 Constraining power of stage-IV cosmic shear surveys

In Chapter 4, I investigated the constraining power of forthcoming Stage-IV weak lensing surveys (such as EUCLID, LSST, and NGRST) for extensions to the ΛCDM model, via their impact on the cosmic shear power spectrum. This was done using high-resolution cosmological simulations which were introduced in Chapter 3 to calculate how warm dark matter (WDM), self-interacting dark matter (SIDM) and a running of the spectral index affect the non-linear matter power spectrum, $P(k)$, as a function

of scale and redshift. To evaluate the cosmological constraining power of these future surveys I created synthetic weak lensing observations derived from these measured power spectra taking into account the anticipated source density, shape noise and sky coverage of each survey. I showed that upcoming Stage-IV surveys will be able to place useful, independent constraints on both WDM models (ruling out models with a particle mass of $\lesssim 0.5$ keV) and SIDM models (ruling out models with a velocity-independent cross-section of $\gtrsim 10$ cm^2 g^{-1}) through their effects on the small-scale cosmic shear power spectrum. Similarly, they will be able to strongly constrain cosmologies with a running spectral index. Finally, I explored the error associated with the cosmic shear cross-spectrum between tomographic bins, finding that it can be significantly affected by Poisson noise (the standard assumption is that the Poisson noise cancels between tomographic bins).

5.2 Future Work

To conclude this thesis I will briefly outline some of the ways I foresee the research I have presented being extended in the future. The thrust of the work in this thesis has been to explore extensions to the standard model of cosmology which are able to reproduce the many successes of the ΛCDM model while also possibly reconciling some of the highlighted tensions with the model. The results of this work, however, have relied extensively on dark-matter only simulations. However, as highlighted in this thesis, and shown in other works (e.g. Mummery et al. 2017; Schaller et al. 2015), galaxy formation physics plays an important role in the evolution of structure in the universe. Therefore, to fully understand the interplay between galaxy formation physics and cosmological effects, a similar study as that done in Chapter 2, where one self-consistently models galaxy formation physics as well as changes to the underlying cosmological model, is warranted. This will enable a study on the separability between the two effects on statistics such as the number of satellite haloes, and the internal structure of haloes providing a more detailed understanding of the interplay between cosmological and baryonic effects on structure formation; one could do this

in the context of zoom-in simulations. Similar studies have been done in the past (see e.g. Lovell et al. 2017b; Macciò et al. 2019; Sameie et al. 2021), however, they often look at individual extensions in isolation and compare the results to a ΛCDM prediction. Furthermore, these past studies have only looked at a very small number of systems, focusing mainly on dwarf galaxies, therefore there is scope to expand this by looking at a much more diverse range of systems, with more statistically significant samples. I advocate the process done by (Fitts et al., 2019) where they simulate SIDM and WDM in the context of a hydrodynamical simulation and compare the results to ΛCDM. However, again this was done in the context of dwarf galaxies, and so exploring the effects of the extensions discussed in this thesis, in the context of hydrodynamical simulations, over a broad range of host halo masses will potentially help when placing observational constraints on these cosmological extensions, or at the very least will help better understand the uncertainty introduced due to baryonic physics.

The extensions to ΛCDM explored in this thesis are all independent of one another, but there is no theoretical reason that they cannot be combined, and in fact, when combined they may help better describe observations of the Universe we live in. Therefore, another potential avenue of research is to investigate the effects on structure formation in cosmological models which combine these extensions. For example, Hannestad and Scherrer (2000) noted that having a WDM particle that can also self-interact increases the amount of power on small-scales than that predicted by the same standard WDM model. This could have interesting consequences for certain cosmological combinations, for example, a positive running of the spectral index which increases the amount of small-scale power could be paired with WDM models, which produces a suppression. In conjunction with one another, this would potentially significantly loosen the constraints on both α_s and $M_{\rm WDM}$. Or for example, WDM does an excellent job at reducing the amount of small-scale structure but struggles to produce a core in dwarf galaxies in-line with observations (Macciò et al., 2012). As such one could combine a WDM model with a velocity-dependent SIDM model to produce both a core, and reduce the number of satellite haloes, whilst on large-scales being almost indistin-

guishable from a ΛCDM universe.

One final avenue of research I think would be interesting is to extend the analysis done in Chapter 4 into a full parameter forecast, which could be done in a couple of ways, either through a Fisher matrix prediction, or a full MCMC analysis. However, in the case of a Fisher matrix analysis, this would require many more realisations of the predicted observables (in this case either the cosmic shear power spectrum or the non-linear matter power spectrum), more finely sampling the available parameter space. Whereas in the case of a full MCMC analysis, in theory, this would require a numerical simulation to be run for every point sampled in the parameter space to get an accurate prediction of the observables. To do either of these methods would quickly become very computationally expensive. To help reduce the computational cost one could instead build an emulator to predict the non-linear matter power spectrum for these non-standard cosmologies (as done for example in, Heitmann et al. 2014; Lawrence et al. 2017; Euclid Collaboration et al. 2019, but not in the context of WDM, SIDM or α_s). Having an emulator would drastically reduce the number of simulations needed to accurately predict the non-linear matter power spectrum over a large parameter space sufficient for either a Fisher matrix analysis or MCMC. Furthermore, this work could be combined with the results shown in Chapter 2, and the first point made in this section, wherein you first investigate the separability of cosmological and baryonic effects on the non-linear matter power spectrum. Such a study would be interesting for the non-linear matter power spectrum, as on small physical scales, at large values of k, there is an enhancement in the non-linear matter power spectrum extracted from hydrodynamical simulations due to the presence of stars (see e.g. van Daalen et al. 2020). However, Lovell et al. (2020) recently showed that in local group analogues, WDM delays star formation by ≈ 200 Myrs, therefore, an investigation into the separability of these two effects on the non-linear matter power spectrum may produce different results than those found for large scales in Chapter 2 for a running spectral index. If, however, the effects are separable, one could also build an emulator for the baryonic effects on these very non-linear scales, to use as a correction factor for the cosmological emulator, this would allow baryonic effects to be marginalised over in the parameter forecast.

Appendix A

This appendix contains all of the material from the appendices of Stafford et al. (2020a) copied verbatim.

A.1 Supplementary

Here I provide the particle mass for each of the 5 simulations, note, the slight differences in the particle masses between the different simulations is due to their slightly different values for $\Omega_{\rm m}$ and H_0.

As mentioned in Section 2.2.4, as a test of my cosmological parameter selection I examined the predicted CMB angular power spectra measurements of $Planck$. The result of this can be seen in Fig. A.1 and demonstrate that the adopted cosmologies are

Table A.1: (1) Simulation label, (2) the dark matter particle mass in the full hydro simulations, (3) the dark matter particle mass in the dark matter only simulations and (4) the initial baryonic particle mass in the hydro simulations.

(1)	(2)	(3)	(4)
Label	$M_{\rm DM,HYDRO}$ (10^9 M$_\odot$ h^{-1})	$M_{\rm DM,DMONLY}$ (10^9 M$_\odot$ h^{-1})	$M_{\rm bar,init}$ (10^8 M$_\odot$ h^{-1})
-2σ	4.37	5.19	8.2
-1σ	4.31	5.12	8.11
$Planck$ ML	4.32	5.15	8.25
no-running	4.36	5.17	8.11
+1σ	4.44	5.26	8.13

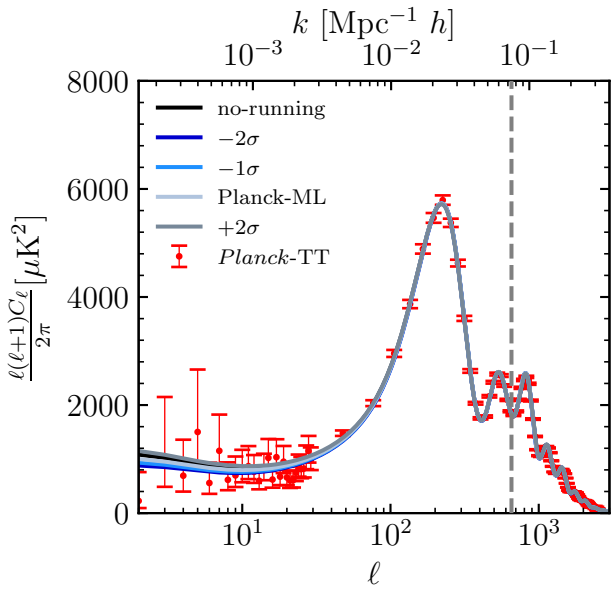

Figure A.1: The angular power spectrum of temperature anisotropies of the CMB. Data points here are the measurements made by the $Planck$ satellite, and the solid lines represent the theoretical prediction for the different cosmological models. All models are virtually indistinguishable at high-multipoles, with the results at low-multipoles still within observational errors. The corresponding $k-$scales which the $Planck$ observations cover are indicated at the top of the plot. The $Planck$ pivot scale ($k = 0.05 Mpc^{-1}$) is indicated by the vertical grey dashed line.

indistinguishable with regards to current $Planck$ measurements[1] for high-multipoles ($\ell \gtrsim 100$), and consistent with $Planck$ measurements at low-multipoles ($\ell \lesssim 100$).

Lastly here, I present results from allowing both $A_{\rm lens}$ and α_s to be free. As mentioned in the main text, for a standard ΛCDM cosmology, $A_{\rm lens}$ assumes the value of 1. However, when also treated as a free parameter in the standard model there is a mild preference for a value greater than unity (Planck Collaboration XIII, 2016), which has a knock on effect on other cosmological parameters, such as H_0, σ_8, and $\Omega_{\rm m}$. Therefore, I test whether the mild preference for a non-zero negative running which also exists in the $Planck$ 2015 results is mitigated if you no longer fix $A_{\rm lens}$ and α_s to their assumed values of: 1, and 0 respectively. To do this, I create a new set of chains using the publicly available $Planck$ 2015 likelihood function. I give these parameters the following flat prior ranges:

[1] https://pla.esac.esa.int/

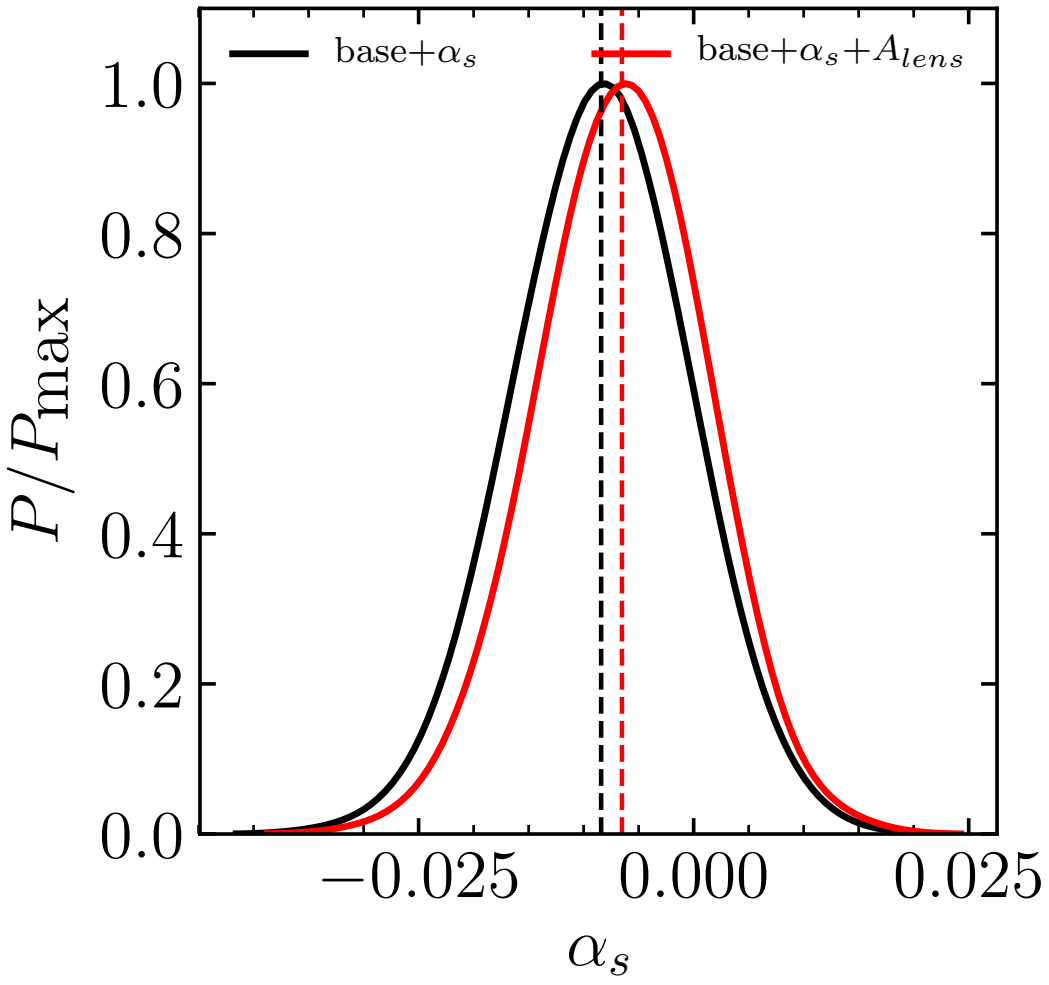

Figure A.2: Posterior distribution for the running of the spectral index parameter when included in the $Planck$ MCMC analysis, along with $A_{\rm lens}$. Here, the black curve corresponds to constraints on α_s using the $Planck$ 2015 $TT + lowTEB$ dataset, while the red curve shows the same only now $A_{\rm lens}$ is also allowed to vary. The vertical dashed lines correspond to the maximum likelihood value for each distribution. This shows how allowing $A_{\rm lens}$ to also vary in the cosmological model does not affect the constraints on α_s much.

Table A.2: Cosmological parameter values obtained when treating both $A_{\rm lens}$ and α_s as free parameters. All symbols have their previous meaning, with definitions for all excluding (3) $A_{\rm lens}$ (the lensing amplitude of the CMB TT angular spectrum) present in Table 2.1.

(1)	(2)	(3)	(4)	(5)	(6)
σ	α_s	$A_{\rm lens}$	$\Omega_{\rm m}$	σ_8	S_8
-2	-0.02232	1.19141	0.29153	0.82160	0.80991
-1	-0.01442	1.19927	0.29681	0.81539	0.81104
Max Likelihood	-0.00652	1.21847	0.29476	0.80750	0.80042
+1	0.00138	1.22956	0.29371	0.80025	0.79182
+2	0.00928	1.24425	0.28979	0.79459	0.78094

$$A_{\rm lens} \in [0.0, 10.0]$$

$$\alpha_s \in [-1.0, 1.0]$$

I then select values for α_s and the other important cosmological parameters, including $A_{\rm lens}$ this time, in the same way as that described in Section 2.2. The results on the 1D density distribution for α_s are shown in Fig. A.2, with the effects on other key parameters for LSS shown in Table A.2. Looking at Fig. A.2, it can be seen that when allowing $A_{\rm lens}$ to also be free, the mild preference for a negative running value is maintained, although the maximum likelihood value is shifted slightly closer to 0.

As allowing $A_{\rm lens}$ to be free does not drastically impact the resultant values for α_s one would simulate, I focus this study on the one parameter extension to ΛCDM where I only allow α_s to vary.

Finally in this section I show in Fig. A.3 the redshift evolution of the fractional change in halo mass. This helps explain the results which were seen in the redshift evolution of the HMF (Fig. 2.7).

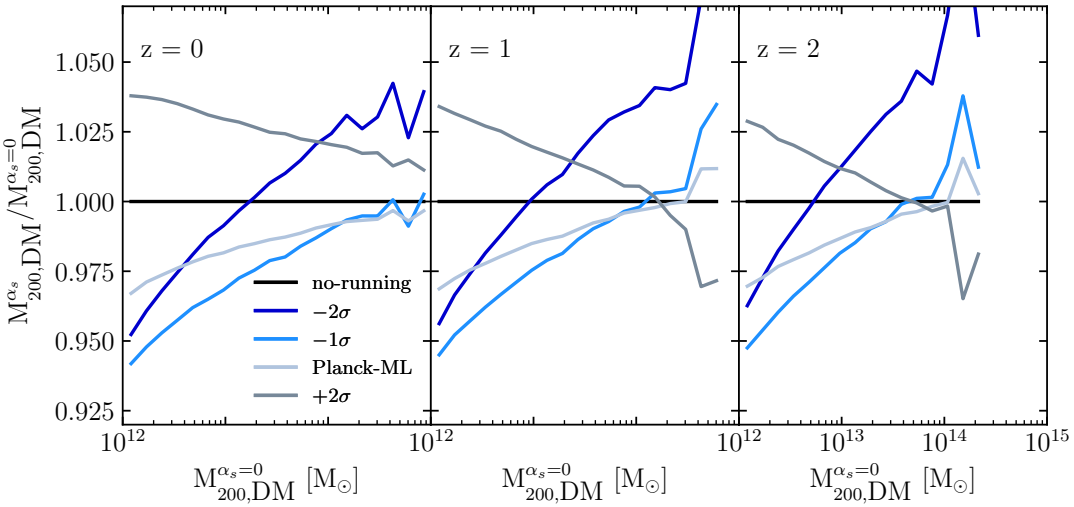

Figure A.3: The fractional change in halo mass for a matched set of haloes across the 5 different cosmologies for 3 separate redshifts (indicated in the top-left corner of each panel). This shows that a halo in a negative running cosmology is more massive than it would be in a no-running cosmology, with this effect amplified with redshift. Conversely a halo in a positive running cosmology is more massive at the present day, but less massive as you go back in redshift.

A.2 Approximate Methods

Although a systematic exploration of the effects a running scalar spectral index on LSS in the Universe using large cosmological hydrodynamic simulations has not been conducted, research has gone into the effects of running using semi-analytic models (e.g. Fedeli et al. (2010)). Here, I explore how well these approximate methods work in reproducing the HMF, and the redshift evolution of dark matter haloes.

A.2.1 Halo mass function

First, I look at how well the prescription for the HMF provided in Tinker et al. (2008) (T08) is able to describe the HMF that I measure for the 5 separate cosmologies from the simulations. The resultant plot can be seen in Fig. A.4, which shows the HMF at three separate redshifts generated using the prescription of T08, represented with the different curves. Also shown is the actual HMF measured from the simulations. Note that here, I plot the HMF as a function of $M_{200,mean}$ instead of $M_{200,\mathrm{crit}}$ as was done previously. Here $M_{200,mean}$ describes the mass enclosed in a spherical overdensity,

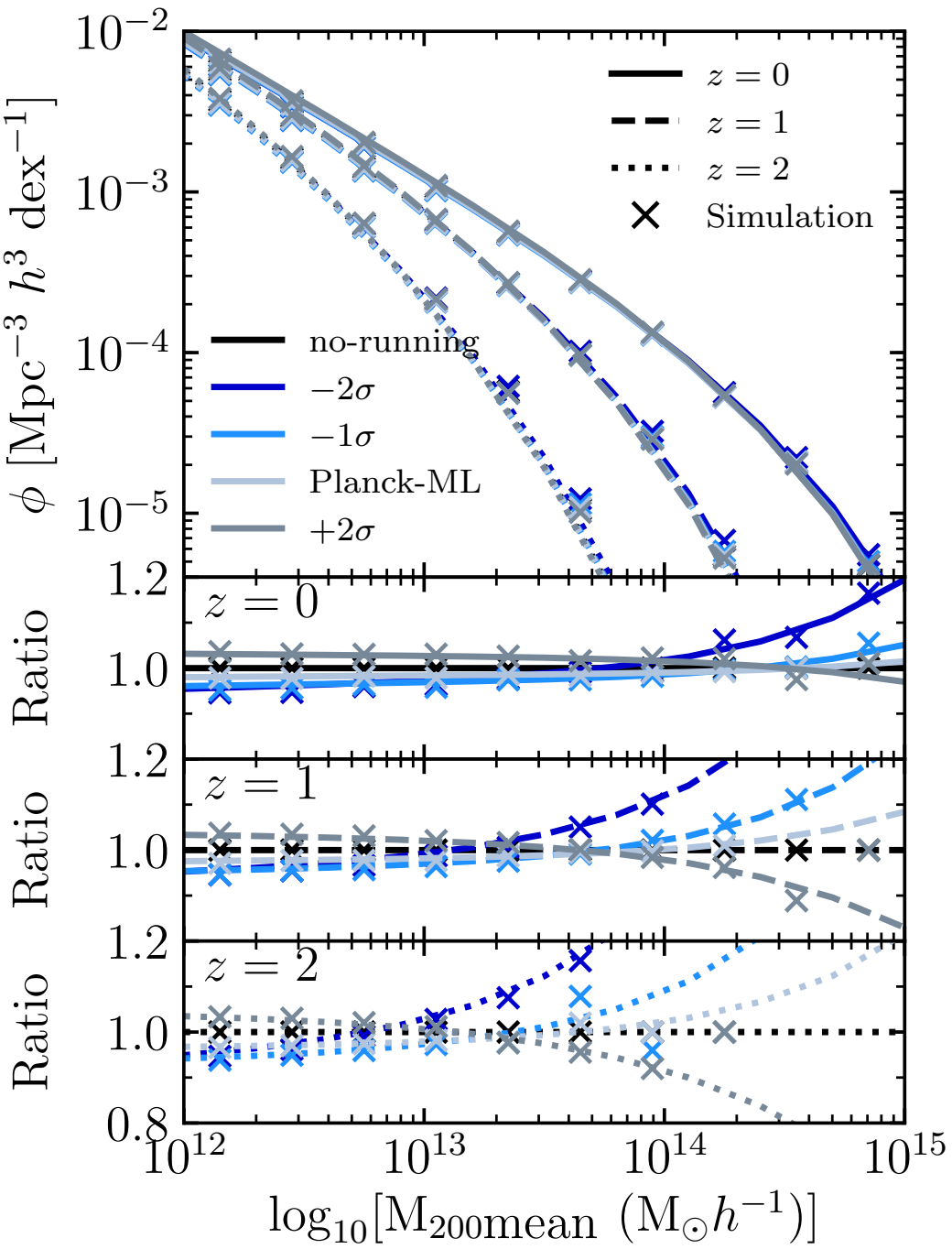

Figure A.4: Top: the halo mass function (HMF) for the 5 separate cosmologies looked at in this study. Here, the lines represent the halo mass function calculated according to the Tinker et al. (2008) prescription, with the linestyles indicating the different redshifts for which the HMF was computed. Also shown in this plot is the HMF measured from the simulations themselves, indicated by the crosses. Note that here, unlike the HMF shown in Fig. 2.7, the HMF is plotted in terms of $M_{200,\mathrm{mean}}$ and not $M_{200,\mathrm{crit}}$. The bottom panel shows the HMF normalised with respect to the $\alpha_s = 0$ case, for each respective method, at each redshift. It can be seen that the Tinker et al. (2008) HMF reproduces the effects due to a running scalar spectral index remarkably well.

whose radius contains an overdensity equal to 200 $\times$ the mean density of the Universe ($\rho_{\rm c}\Omega_{\rm m}$). The bottom panel of this plot shows the HMFs normalised with respect to the $\alpha_s = 0$ model, for each case, and at each redshift. This plot shows that the T08 HMF can reproduce the measured HMF remarkably well at $z = 0, 1, 2$. There is a hint from the top plot that there is a slight under prediction of the number of high-mass haloes at $z = 2$, but the relative effect shown in the bottom panel is almost perfectly reproduced.

It is important to highlight that, the above T08 mass function was computed by using the linear matter power spectrum output using `CAMB` to compute the mass variance $\sigma(M)$. Off the shelf packages such as `HMFCALC`[2] are not able to reproduce the observed HMF, due to the fact that they are hardwired to use the transfer function when computing the power spectrum at a certain redshift, with their primordial matter power spectrum assuming a constant power law.

A.2.2 Mass accretion histories

I now look at the effects a running scalar spectral index has on the the evolution of dark matter haloes. I do this using the method developed by Correa et al. (2015b) (see also Correa et al., 2015c,a) to reproduce the mass-accretion histories of haloes, along with the concentration-mass relation.

I used a slightly modified version of the python package developed by Correa et al. (2015b): `COMMAH`[3]. I modify it to account for a running scalar spectral index in its calculation of the $z = 0$ linear matter power spectrum. Following Correa et al. (2015a), I also calculate a value for $A_{\rm cosmology}$, for each cosmology in order to compute the c-M relation.

The redshift evolution of halo mass can be seen in Fig. A.5. Here the dashed curves show the result obtained using the modified `COMMAH` code, with crosses representing the evolution of halo mass with redshift computed from the actual simulations. To compute this, I choose haloes in a narrow mass bin centered on the desired redshift 0

[2] http://hmf.icrar.org/

[3] https://bitbucket.org/astroduff/commah/src/master/

mass. I then find that halo's progenitor at each snapshot up to $z = 3$. This is done by matching the 50 most bound particles from the $z = 0$ halo, and selecting the halo at each redshift which contains the most of these particles. It can be seen that there is a qualitatively good agreement between the simulation's result and that predicted using `COMMAH`. The bottom panels on this plot show the predicted redshift evolution of three haloes of different mass, normalised with respect to the no-running evolution for that mass. It can be seen that the introduction of a running spectral index affects how these haloes evolve. For example, the -2σ cosmology predicts a $10^{15}M_{\odot}$ halo to be around 10% more massive at $z = 3$, compared with a no-running cosmology. Whereas, for that same cosmology, a $10^{13}M_{\odot}$ is near 5% under-massive compared with a no-running cosmology. This general trend agrees with the mass-dependent effects seen in this study for the HMF. It also implies that the MAH of these objects are going to be different, which I examine next.

The predicted MAH for the same set of halo masses as examined previously is shown in Fig. A.6. The bottom panels in this plot show the MAH for the 5 cosmologies, normalised with respect to the result in the no-running cosmology at that mass. This result helps explain Fig. A.5. For example, looking at the $10^{15}M_{\odot}$ halo's MAH, it can be seen that for the -2σ cosmology, it accretes a lot of its mass at early times, causing it to be more massive earlier on. Conversely, in the positive running cosmology, it has a steady incline in its mass accretion rate, compared with the no-running cosmology, and has a higher accretion rate at present. This allows haloes of this mass, in a positive running cosmology, to start with a smaller seed mass, compared to no-running. Similarly, for the $10^{13}M_{\odot}$ halo, for all negative running cosmologies, $M(z)$ is lower than the no-running prediction, but this is made up for, by an increase in the MAH of these haloes as z approaches 0.

Finally, I show the predicted halo concentration-mass relation for these 5 separate cosmologies in Fig. A.7. The bottom panel shows the halo concentration-mass relation normalised with respect to the no-running cosmology. Qualitatively, the results are similar to what was found from the simulations. For example, a positive running cosmology predicts all haloes in the mass-range examined here to have a higher

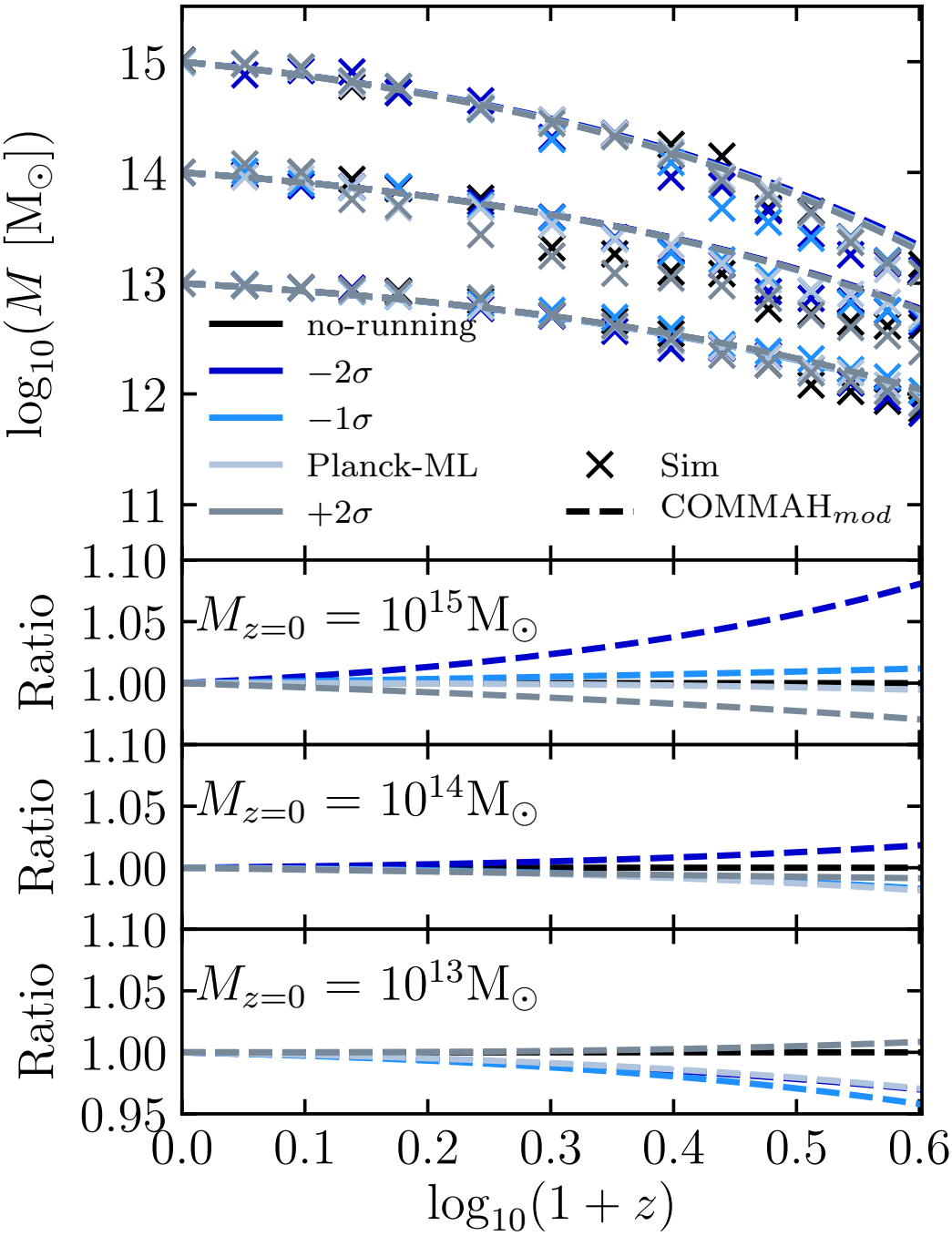

Figure A.5: Evolution of halo mass, with redshift. Top: the dashed lines here indicate the predicted $M(z)$. The crosses show the results obtained directly from the simulations. The general trend of these results are in qualitative agreement. Bottom: the ratio of the COMMAH predicted $M(z)$, with respect to the no-running cosmology, for three separate halo masses, indicated in each panel. It appears to show again, that a running scalar spectral index has a mass dependent effect on haloes. With larger-mass haloes being more massive at early times in a negative running cosmology, and lower-mass haloes, less massive. This effect is reversed somewhat for the positive running cosmology.

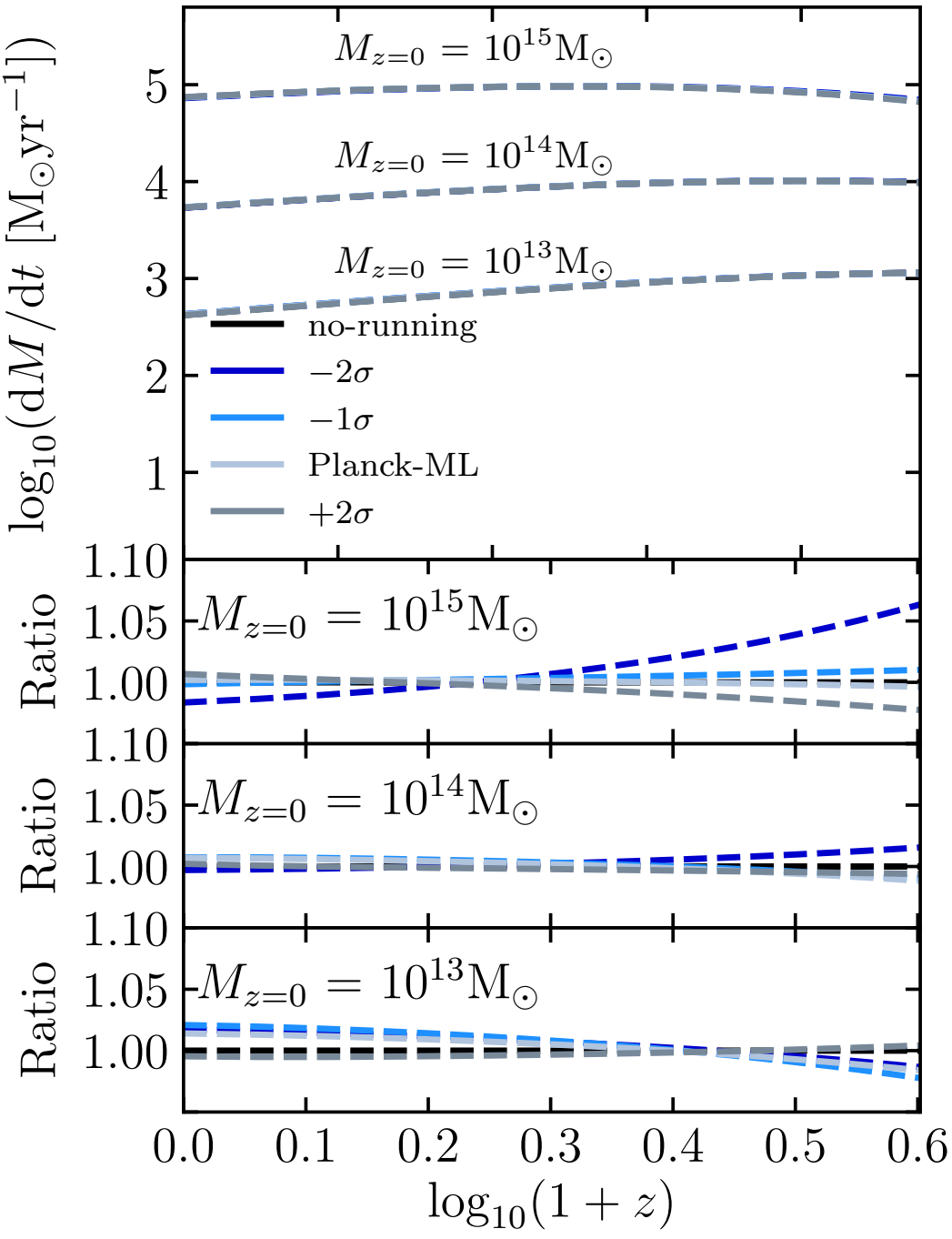

Figure A.6: Mass accretion histories (MAHs) predicted using the slightly modified version of the `COMMAH` python package for 3 different halo masses for each cosmology examined here. Top: MAH predicted for 3 different halo masses, indicated above each curve. The bottom panels how the MAH of each halo normalised to its respective no-running counterpart. How a halo forms in a cosmology which has a running scalar spectral index depends on both the sign and magnitude of the running, along with the mass of the object.

concentration, compared to the no-running cosmology. Alongside lower-mass haloes ($M \lesssim 2 \times 10^{13}\mathrm{M}_{\odot}$) having lower concentrations in a negative running cosmology. However, whereas in the simulations all haloes above $M \approx 10^{14}\mathrm{M}_{\odot}$ were found to have higher concentrations, here they are predicted to have slightly lower concentrations, with the results converging towards (but not exceeding) the no-running prediction at the high-mass end.

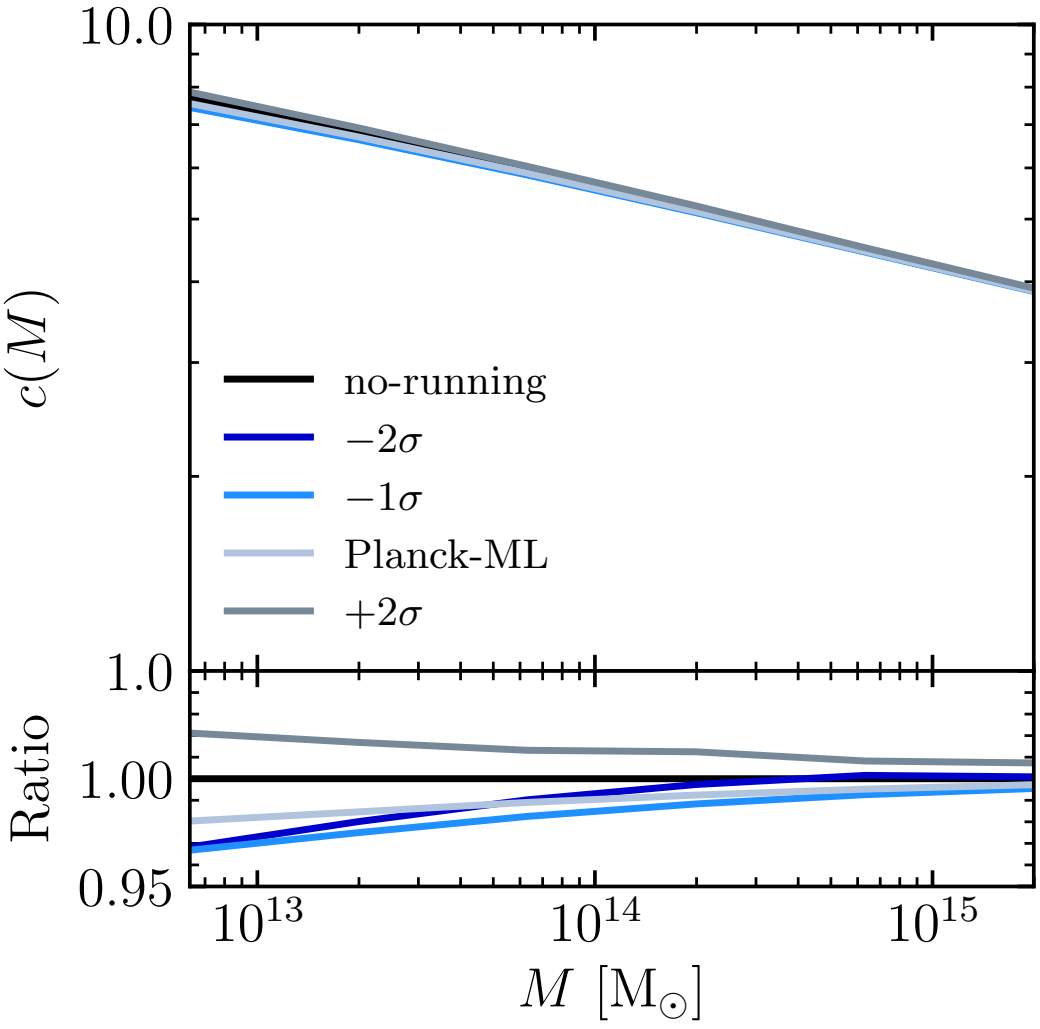

Figure A.7: The halo concentration-mass relation for the different running cosmologies predicted using the slightly modified `COMMAH` python package. The bottom panel of this plot shows the result normalised with respect to the no-running cosmology. A negative running cosmology is predicted to have less concentrated lower-mass haloes, whereas a positive running yields higher concentrations. This is in qualitative agreement to the results found in this study (see Fig. 2.12). Conversely, for larger-mass haloes only a positive running cosmology predicts higher concentrations, whereas it was found in this study that all cosmologies with a non-zero running spectral index had higher concentrations compared to the no-running result.

Appendix B

This appendix contains all of the material from the appendices of Stafford et al. (2020b) copied verbatim.

B.1 Convergence tests

Here I determine the mass and maximum circular velocity limits for the subhaloes that I include in the statistics examined in this paper.

I examine the $M_{\rm sub}$-$V_{\rm max}$ relation, shown in Fig. B.1, for two different resolution levels. Following Boylan-Kolchin et al. (2010), I fit a power-law to this relation of the form:

$$\log_{10}\left(M_{\rm sub}\ [{\rm M}_{\odot}\ h^{-1}]\right) = 11.04 + 3.38\log_{10}\left(\frac{V_{\rm max}}{100\ {\rm km\ s^{-1}}}\right), \qquad \text{(B.1)}$$

which is shown as crosses in the plot. It can be seen that the higher-resolution simulations used throughout this study follow the power-law down to a $V_{\rm max} \approx 15$ km s^{-1} ($\approx 3 \times 10^{8}$ M$_{\odot}$ h^{-1}), before the turn-up indicative of resolution effects. The same effect is seen in the lower-resolution simulation, but at a lower value for $V_{\rm max} \approx 28$ km s^{-1}. In addition, I plot the subhalo mass function, shown in Fig. B.2, for both centrals and satellites, for two tiers of resolution. Here, I examine at what particle limit does the subhalo mass function in the lower-resolution simulation start to significantly differ from the higher-resolution simulation. This is illustrated in the bottom panel of this figure, which shows the ratio of the lower-resolution simulation, with respect to

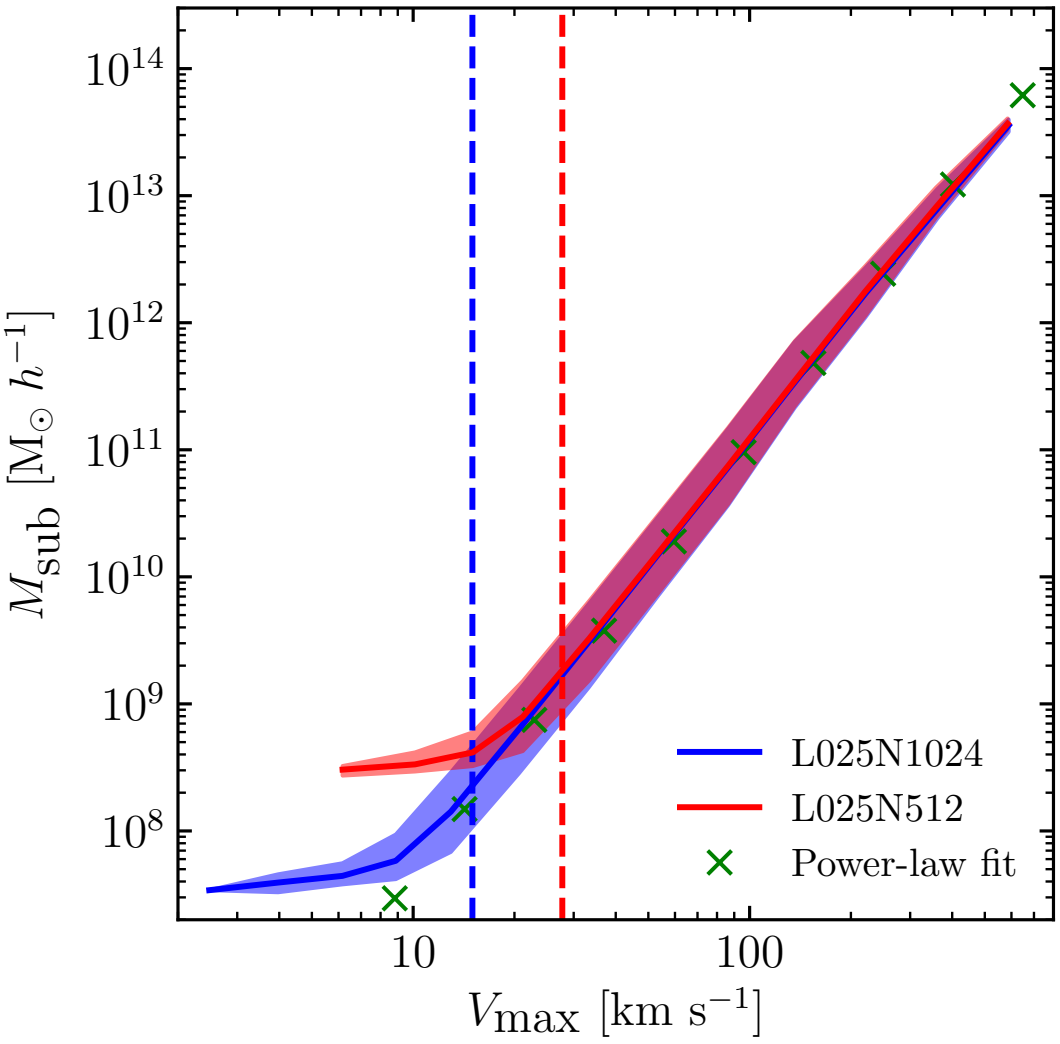

Figure B.1: $M_{\rm sub}$-$V_{\rm max}$ relation for subhaloes in simulations ran at two different resolution levels indicated by colour. These simulations correspond to the reference cosmology used through this study. The green crosses correspond to the power-law fit calculated using equation B.1, as done in Boylan-Kolchin et al. (2010). The vertical dashed lines correspond to the resolution limit for these simulations, beyond which numerical effects become important. The shaded regions show the 16th and 84th percentiles.

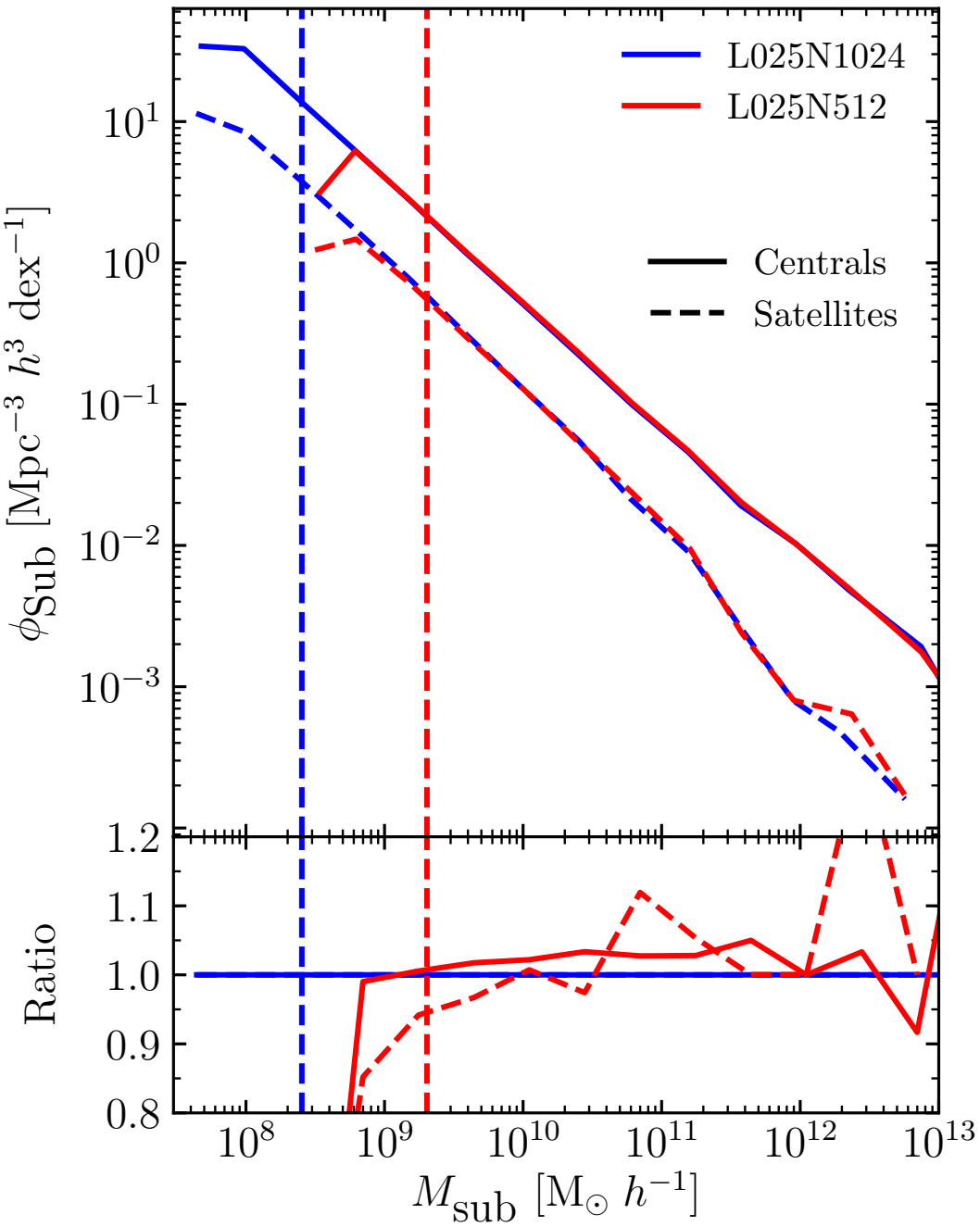

Figure B.2: Top: the subhalo mass function for two different resolution tiers (indicated by colour). The solid line corresponds to this quantity calculated for centrals, with the dashed line corresponding to satellites. Bottom: the above result normalised with respect to the result in the higher resolution simulation. The vertical dashed line corresponds to the lower-mass limit for each simulation, calculated using the mass at which the lower-resolution simulation diverges from the higher-resolution case.

the higher-resolution simulation. I place a conservative lower-limit on the number of particles, for which I deem this quantity to be converged, which is indicated by the vertical dashed lines, and corresponds to subhaloes containing at least 200 particles. This corresponds to a mass-limit of 2.5×10^8 M$_\odot$ h^{-1}. Therefore, throughout this paper, I only select subhaloes with $M_{\rm sub} > 5 \times 10^8$ M$_\odot$ h^{-1}, and $V_{\rm max} > 15$ km s^{-1}, satisfying both convergence tests.

As mentioned in the main text, it was shown by Wang and White (2007) that spurious fragmentation of filaments is a significant problem in WDM simulations due to discreteness effects. They derived an empirical mass cut to remove these spurious objects: $M_{\rm lim} = 10.1\overline{\rho}dk_{\rm peak}^{-2}$, where $\overline{\rho}$ is equal to the mean density of the universe ($\Omega_{\rm m}\rho_{\rm crit}$), d is the mean inter-particle separation, and $k_{\rm peak}$ is equal to the maximum of the dimensionless linear theory matter power spectrum ($\Delta^2(k) = k^3P(k)/(2\pi^2)$). Therefore, I show in Fig. B.3 the cumulative abundance of haloes above a certain mass M, with this mass limit shown with a vertical dashed line. I plot this for both of the WDM models simulated as part of this study, at two different resolutions, illustrating the resolution dependence of this effect. The resultant mass-cut advised is equal to $\approx$ (0.5, 2) $\times 10^8$ M$_\odot$ h^{-1} for the the $M_{\rm WDM}$ = 5.0, 2.5 keV cosmologies respectively. Both of these mass limits lie below the resolution cut I derived above. I therefore do not need to make an additional cut for the WDM simulations.

One additional note worth mentioning here is the apparent lack of spurious haloes in the lower-resolution simulation, which at first sight seems to contradict the expectation that they should be more prevalent at lower resolution. However, the reason for this behaviour is that the WDM models which I explore have a cut-off in their initial matter power spectrum that results in a sufficiently large $k_{\rm peak}$ that the spurious halo mass limit is barely resolved in the lower resolution simulation. For example, $M_{\rm lim}$ corresponds to $\approx$ 10 (40) particles for the $M_{\rm WDM}$ = 5.0 keV (2.5 keV) model. As such, the vast majority of these haloes will not be identified as FoF groups (I require there to be at least 20 particles in identified FoF groups), which is why the characteristic turn up in the mass function is not seen for the lower-resolution simulations.

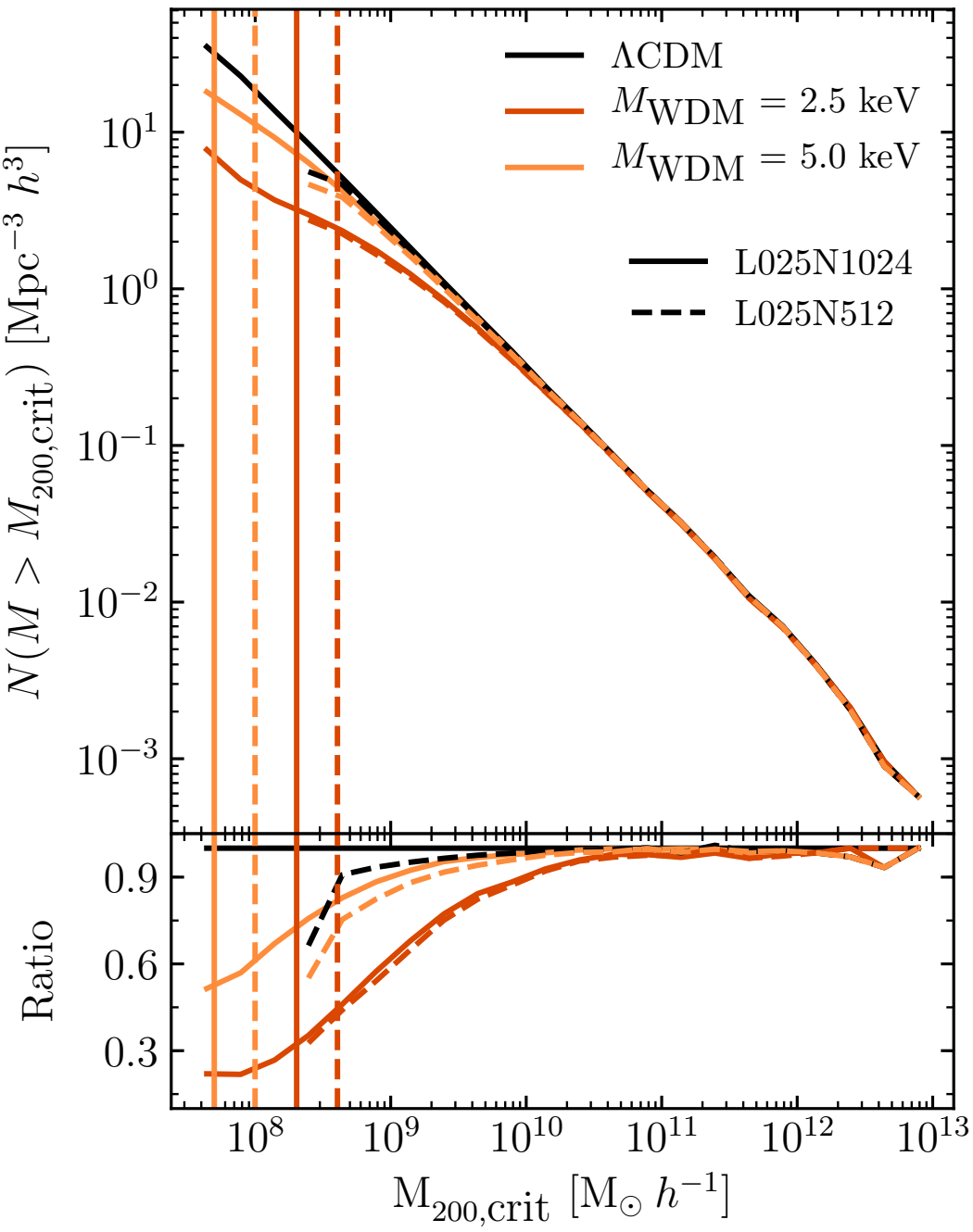

Figure B.3: Top: cumulative abundance of subhaloes above a mass M for the different WDM cosmologies, along with the reference cosmology. Bottom: the above result normalised with respect to the reference simulation. The vertical dashed lines indicate the mass cut advocated by Wang and White (2007) for the two different WDM models.

Appendix C

This appendix contains all of the material from the appendices of Stafford et al. (2021) copied verbatim.

C.1 Resolution and box size study

In Section 4.2.3 I detail my method for constructing the non-linear matter power spectrum spanning a large range of k-modes, which is done using the ratio of the matter power spectrum extracted from the numerical simulations with respect to the result from the ΛCDM simulations. As I show here, splicing ratios of power spectra, rather than absolute power spectra, is more robust to changes in resolution and box size. I do this using an additional sub-suite of simulations, examining the running spectral index cosmological extensions, which consists of various box sizes and resolutions. Firstly, there are two setups which are used in the analysis detailed in the paper, which have box sizes of 25 and 400 h^{-1}Mpc, each with 1024^3 particles. I then compare the non-linear matter power spectrum extracted from these simulations to that extracted from simulations which are a step down in resolution. These simulations are 25 and 100 h^{-1}Mpc on a side and have 512^3 and 256^3 particles respectively. Thus, this allows us to explore the effects of both box size and resolution on both the absolute matter power spectrum and the ratio with respect to ΛCDM.

Fig. C.1 shows the non-linear matter power spectrum for two running of the spectral index models. In the left panel I show how the simulation box size affects the absolute

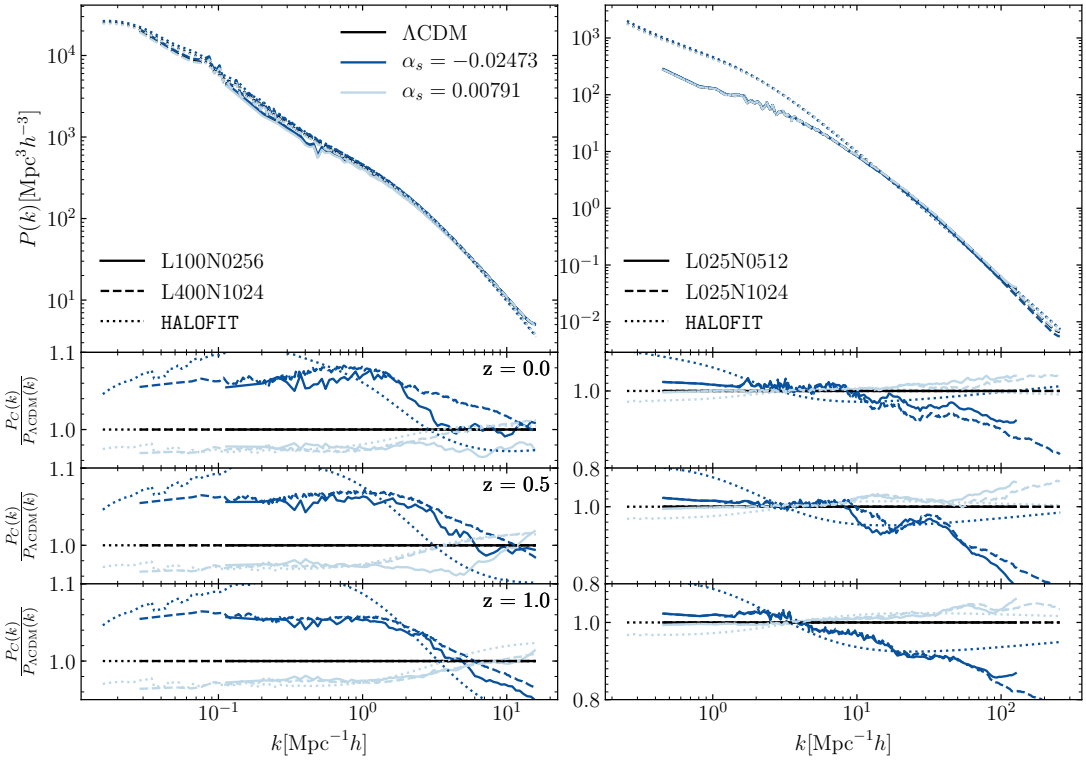

Figure C.1: Testing how both box size and resolution affect the ratios of the power spectrum extracted from a cosmology with a running spectral index with respect to the ΛCDMresult. Left panels show the results for fixed resolution and varying box size, while the right panels show the opposite. The top panel in each case shows the absolute power spectra at $z = 0$. The three sub-panels below show the ratio as a function of redshift. The ratio is computed with respect to the power spectrum from the ΛCDM simulation with the same box size and resolution as in the running spectral index case. The ratio of the power spectra appears to be well converged for the various box sizes and resolutions examined here which motivates us to combine the ratios over the extended $k-$scale, as described in Section 4.2.3, rather than the absolute power spectra.

power spectra (top) and the ratio with respect to a complementary ΛCDM simulation of the same box size (bottom), both at fixed resolution. In the right panel, I show how resolution affects these two statistics at fixed box size. Therefore, it is important to note that when comparing the solid to dashed lines (or dotted) in the bottom panels, both the numerator and denominator have changed. Comparing the different linestyles allows us to assess the convergence of the ratio of power spectra from the running cosmologies with respect to a ΛCDM power spectrum as a function of varying box size at fixed resolution, or vice versa.

One can see that while the absolute power spectra tend to disagree with each other on the largest scales sampled in the box, the ratio is a much better converged quantity. This is particularly relevant for the smaller volume boxes, where the size of the simulations cause an almost order of magnitude suppression in the matter power spectrum on the largest scales sampled by the simulated volume (comparing the simulation curves to the `HALOFIT` curve). Conversely, if I compare the ratios at a $k-$scale of around 10 $h\text{Mpc}^{-1}$, one can see that these agree to within a few percent across the varying box sizes and resolutions.

C.2 Analytic error on cross power spectra

As discussed in Section 4.3.1, there are two sources of error associated with measurements of the cosmic shear power spectrum (ignoring other systematic errors which exist such as intrinsic alignment errors), these being cosmic variance and Poisson noise. It is commonplace to assume that Poisson noise only affects the uncertainty in the autocorrelation power spectrum. However, as I show here, cross-power spectra can still have a significant Poisson noise term.

As shown in Fig. 4.3, I find there to be a significant difference in the error bars on small angular scales (large multipoles) when comparing equation 4.10 to the error bars I derive from synthetic weak lensing maps using `FLASK`. The level of disagreement between the two sets of error bars is more clearly illustrated in Fig. C.2, which shows

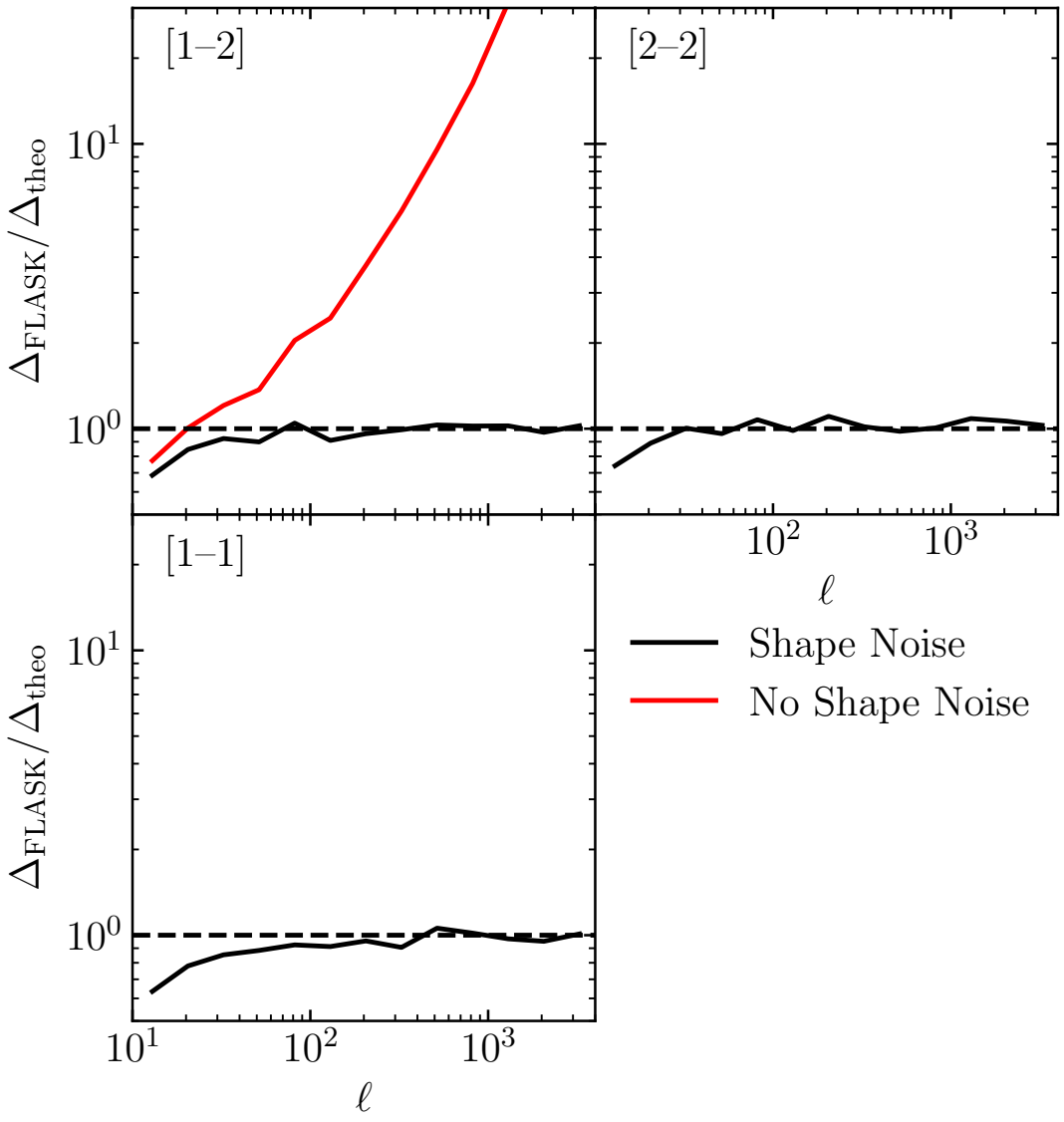

Figure C.2: The ratio of the errors extracted directly from the multiple realisations of a given ΛCDM auto/cross-correlation power spectrum as computed by FLASK with respect to the theoretical error bars computed using equations 4.10 & 4.15. Note the tomographic bins shown here are the same as those in the previous plots, however, I do not show the full tomographic setup for brevity as I only need to focus on one cross-correlation power spectrum (with the result being the same for the rest). The black line shows the result when one includes a prescription for the error associated with Poisson noise in the theoretical calculation of the error on the auto/cross-correlation power spectrum, i.e. computed using equation 4.15, with the red line being the result if one does not, i.e. computed using equation 4.10.

the ratio of the errors extracted directly from the FLASK power spectra to the errors computed using equation 4.10. Note that for clarity I only show here the result for the bottom three panels of Fig. 4.3, although the results presented here is true for the other auto- and cross-correlation spectra. This shows how well the two sets of errors agree with one another in the case of the autocorrelation power spectra, whereas, examining the red curve in the cross-correlation power spectrum panel, the error bars diverge significantly at high multipoles, due to equation 4.10 having no treatment for Poisson noise on the cross-correlation power spectrum.

The fiducial error associated with the cosmic shear power spectrum (shown in equation 4.10) is unable to capture the residual error which exists on the cross-correlation power spectrum. This motivates us to produce a more general formula which is able to capture this residual error without having to rerun FLASK for each possible tomographic setup. For this reason, I have run a set of FLASK noise-only realisations (with the weak lensing signal due to gravity removed) to derive a functional form for the residual Poisson noise error on the cross-correlation power spectrum. The maps were produced using the same tomographic setup described in Section 4.4.1, for varying levels of the source density of galaxies. In total I produced four sets of realisations sampling: $n_s = 15, 30, 45, 60$ galaxies/arcmin^2, with each set having 100 realisations of each tomographic bin. I then computed the auto- and cross-correlation power spectra of these maps, along with cross-correlation power spectra of maps with varying source densities (to test the case where two tomographic bins may not have the same effective number density of galaxies).

I find that an additional term, which only contributes to the cross-correlation power spectrum, is required. See equation 4.15. This term includes a multiplicative combination of the two effective source densities in each tomographic bin and is able to reproduce the additional error on the cross exceptionally well. This is illustrated again in Fig. C.2 in the cross-correlation power spectrum panel (top left), where the black line now shows the ratio of the theoretical error bars, now computed using equation 4.15, with the error bars extracted from FLASK. Note that here I show the results from the full analysis (i.e., including an intrinsic lensing signal, as well as the noise). Note

that the slight disagreement which exists between the errors on large angular scales is strongly dependent on the sky coverage of the survey. I computed this same test where I had a EUCLID-like galaxy sample, but a full sky survey and this brought the errors into excellent agreement even at low multipoles.

Bibliography

V. M. Slipher. Spectrographic Observations of Nebulae. *Popular Astronomy*, 23:21–24, January 1915.

Edwin Hubble. A Relation between Distance and Radial Velocity among Extra-Galactic Nebulae. *Proceedings of the National Academy of Science*, 15(3):168–173, March 1929. doi: 10.1073/pnas.15.3.168.

Edwin Hubble and Milton L. Humason. The Velocity-Distance Relation among Extra-Galactic Nebulae. *ApJ*, 74:43, July 1931. doi: 10.1086/143323.

G. Gamow. Expanding Universe and the Origin of Elements. *Physical Review*, 70 (7-8):572–573, October 1946. doi: 10.1103/PhysRev.70.572.2.

R. A. Alpher, H. Bethe, and G. Gamow. The Origin of Chemical Elements. *Physical Review*, 73(7):803–804, April 1948. doi: 10.1103/PhysRev.73.803.

Ralph A. Alpher and Robert C. Herman. On the Relative Abundance of the Elements. *Physical Review*, 74(12):1737–1742, December 1948. doi: 10.1103/PhysRev.74.1737.

Ralph A. Alpher and Robert C. Herman. Remarks on the Evolution of the Expanding Universe. *Physical Review*, 75(7):1089–1095, April 1949. doi: 10.1103/PhysRev.75.1089.

A. A. Penzias and R. W. Wilson. A Measurement of Excess Antenna Temperature at 4080 Mc/s. *ApJ*, 142:419–421, July 1965. doi: 10.1086/148307.

Alan H. Guth. Inflationary universe: A possible solution to the horizon and flatness problems. *PRD*, 23(2):347–356, jan 1981. ISSN 0556-2821. doi: 10.1103/PhysRevD.23.347.

A. D. Linde. Fate of the false vacuum at finite temperature: Theory and applications. *Physics Letters B*, 100(1):37–40, March 1981. doi: 10.1016/0370-2693(81)90281-1.

Gravitation and the universe, January 1970.

Sébastien Renaux-Petel. Primordial non-Gaussianities after Planck 2015: An introductory review. *Comptes Rendus Physique*, 16(10):969–985, December 2015. doi: 10.1016/j.crhy.2015.08.003.

Masato Shirasaki, Naonori S. Sugiyama, Ryuichi Takahashi, and Francisco-Shu Kitaura. Constraining primordial non-gaussianity with postreconstructed galaxy bispectrum in redshift space. *Phys. Rev. D*, 103:023506, Jan 2021. doi: 10.1103/PhysRevD.103.023506.

Jan-Albert Viljoen, José Fonseca, and Roy Maartens. Multi-wavelength spectroscopic probes: prospects for primordial non-Gaussianity and relativistic effects. *arXiv e-prints*, art. arXiv:2107.14057, July 2021.

Planck Collaboration, N. Aghanim, Y. Akrami, M. Ashdown, J. Aumont, C. Baccigalupi, M. Ballardini, A. J. Banday, R. B. Barreiro, N. Bartolo, S. Basak, R. Battye, K. Benabed, J. P. Bernard, M. Bersanelli, P. Bielewicz, J. J. Bock, J. R. Bond, J. Borrill, F. R. Bouchet, F. Boulanger, M. Bucher, C. Burigana, R. C. Butler, E. Calabrese, J. F. Cardoso, J. Carron, A. Challinor, H. C. Chiang, J. Chluba, L. P. L. Colombo, C. Combet, D. Contreras, B. P. Crill, F. Cuttaia, P. de Bernardis, G. de Zotti, J. Delabrouille, J. M. Delouis, E. Di Valentino, J. M. Diego, O. Doré, M. Douspis, A. Ducout, X. Dupac, S. Dusini, G. Efstathiou, F. Elsner, T. A. Enßlin, H. K. Eriksen, Y. Fantaye, M. Farhang, J. Fergusson, R. Fernandez-Cobos, F. Finelli, F. Forastieri, M. Frailis, A. A. Fraisse, E. Franceschi, A. Frolov, S. Galeotta, S. Galli, K. Ganga, R. T. Génova-Santos, M. Gerbino, T. Ghosh, J. González-

Nuevo, K. M. Górski, S. Gratton, A. Gruppuso, J. E. Gudmundsson, J. Hamann, W. Handley, F. K. Hansen, D. Herranz, S. R. Hildebrandt, E. Hivon, Z. Huang, A. H. Jaffe, W. C. Jones, A. Karakci, E. Keihänen, R. Keskitalo, K. Kiiveri, J. Kim, T. S. Kisner, L. Knox, N. Krachmalnicoff, M. Kunz, H. Kurki-Suonio, G. Lagache, J. M. Lamarre, A. Lasenby, M. Lattanzi, C. R. Lawrence, M. Le Jeune, P. Lemos, J. Lesgourgues, F. Levrier, A. Lewis, M. Liguori, P. B. Lilje, M. Lilley, V. Lindholm, M. López-Caniego, P. M. Lubin, Y. Z. Ma, J. F. Macías-Pérez, G. Maggio, D. Maino, N. Mandolesi, A. Mangilli, A. Marcos-Caballero, M. Maris, P. G. Martin, M. Martinelli, E. Martínez-González, S. Matarrese, N. Mauri, J. D. McEwen, P. R. Meinhold, A. Melchiorri, A. Mennella, M. Migliaccio, M. Millea, S. Mitra, M. A. Miville-Deschênes, D. Molinari, L. Montier, G. Morgante, A. Moss, P. Natoli, H. U. Nørgaard-Nielsen, L. Pagano, D. Paoletti, B. Partridge, G. Patanchon, H. V. Peiris, F. Perrotta, V. Pettorino, F. Piacentini, L. Polastri, G. Polenta, J. L. Puget, J. P. Rachen, M. Reinecke, M. Remazeilles, A. Renzi, G. Rocha, C. Rosset, G. Roudier, J. A. Rubiño-Martín, B. Ruiz-Granados, L. Salvati, M. Sandri, M. Savelainen, D. Scott, E. P. S. Shellard, C. Sirignano, G. Sirri, L. D. Spencer, R. Sunyaev, A. S. Suur-Uski, J. A. Tauber, D. Tavagnacco, M. Tenti, L. Toffolatti, M. Tomasi, T. Trombetti, L. Valenziano, J. Valiviita, B. Van Tent, L. Vibert, P. Vielva, F. Villa, N. Vittorio, B. D. Wandelt, I. K. Wehus, M. White, S. D. M. White, A. Zacchei, and A. Zonca. Planck 2018 results. VI. Cosmological parameters. *A&A*, 641:A6, September 2020. doi: 10.1051/0004-6361/201833910.

F. Zwicky. Die Rotverschiebung von extragalaktischen Nebeln. *Helvetica Physica Acta*, 6:110–127, January 1933.

F. Zwicky. On the Masses of Nebulae and of Clusters of Nebulae. *ApJ*, 86:217, October 1937. doi: 10.1086/143864.

Horace W. Babcock. The rotation of the Andromeda Nebula. *Lick Observatory Bulletin*, 498:41–51, January 1939. doi: 10.5479/ADS/bib/1939LicOB.19.41B.

Vera C. Rubin and Jr. Ford, W. Kent. Rotation of the Andromeda Nebula from a

Spectroscopic Survey of Emission Regions. *ApJ*, 159:379, February 1970. doi: 10.1086/150317.

S. D. M. White, C. S. Frenk, and M. Davis. Clustering in a neutrino-dominated universe. *ApJl*, 274:L1–L5, November 1983. doi: 10.1086/184139.

Adam G. Riess, Alexei V. Filippenko, Peter Challis, Alejandro Clocchiatti, Alan Diercks, Peter M. Garnavich, Ron L. Gilliland, Craig J. Hogan, Saurabh Jha, Robert P. Kirshner, B. Leibundgut, M. M. Phillips, David Reiss, Brian P. Schmidt, Robert A. Schommer, R. Chris Smith, J. Spyromilio, Christopher Stubbs, Nicholas B. Suntzeff, and John Tonry. Observational Evidence from Supernovae for an Accelerating Universe and a Cosmological Constant. *AJ*, 116(3):1009–1038, September 1998. doi: 10.1086/300499.

S. Perlmutter, G. Aldering, G. Goldhaber, R. A. Knop, P. Nugent, P. G. Castro, S. Deustua, S. Fabbro, A. Goobar, D. E. Groom, I. M. Hook, A. G. Kim, M. Y. Kim, J. C. Lee, N. J. Nunes, R. Pain, C. R. Pennypacker, R. Quimby, C. Lidman, R. S. Ellis, M. Irwin, R. G. McMahon, P. Ruiz-Lapuente, N. Walton, B. Schaefer, B. J. Boyle, A. V. Filippenko, T. Matheson, A. S. Fruchter, N. Panagia, H. J. M. Newberg, W. J. Couch, and The Supernova Cosmology Project. Measurements of Ω and Λ from 42 High-Redshift Supernovae. *ApJ*, 517(2):565–586, June 1999. doi: 10.1086/307221.

J. M. Kovac, E. M. Leitch, C. Pryke, J. E. Carlstrom, N. W. Halverson, and W. L. Holzapfel. Detection of polarization in the cosmic microwave background using DASI. *Nature*, 420(6917):772–787, December 2002. doi: 10.1038/nature01269.

Daniel J. Eisenstein, Idit Zehavi, David W. Hogg, Roman Scoccimarro, Michael R. Blanton, Robert C. Nichol, Ryan Scranton, Hee-Jong Seo, Max Tegmark, Zheng Zheng, Scott F. Anderson, Jim Annis, Neta Bahcall, Jon Brinkmann, Scott Burles, Francisco J. Castander, Andrew Connolly, Istvan Csabai, Mamoru Doi, Masataka Fukugita, Joshua A. Frieman, Karl Glazebrook, James E. Gunn, John S. Hendry, Gregory Hennessy, Zeljko Ivezić, Stephen Kent, Gillian R. Knapp, Huan Lin, Yeong-Shang Loh, Robert H. Lupton, Bruce Margon, Timothy A. McKay, Avery

Meiksin, Jeffery A. Munn, Adrian Pope, Michael W. Richmond, David Schlegel, Donald P. Schneider, Kazuhiro Shimasaku, Christopher Stoughton, Michael A. Strauss, Mark SubbaRao, Alexander S. Szalay, István Szapudi, Douglas L. Tucker, Brian Yanny, and Donald G. York. Detection of the Baryon Acoustic Peak in the Large-Scale Correlation Function of SDSS Luminous Red Galaxies. *ApJ*, 633(2): 560–574, November 2005. doi: 10.1086/466512.

Shaun Cole, Will J. Percival, John A. Peacock, Peder Norberg, Carlton M. Baugh, Carlos S. Frenk, Ivan Baldry, Joss Bland-Hawthorn, Terry Bridges, Russell Cannon, Matthew Colless, Chris Collins, Warrick Couch, Nicholas J. G. Cross, Gavin Dalton, Vincent R. Eke, Roberto De Propris, Simon P. Driver, George Efstathiou, Richard S. Ellis, Karl Glazebrook, Carole Jackson, Adrian Jenkins, Ofer Lahav, Ian Lewis, Stuart Lumsden, Steve Maddox, Darren Madgwick, Bruce A. Peterson, Will Sutherland, and Keith Taylor. The 2dF Galaxy Redshift Survey: power-spectrum analysis of the final data set and cosmological implications. *MNRAS*, 362(2):505–534, September 2005. doi: 10.1111/j.1365-2966.2005.09318.x.

DES Collaboration, T. M. C. Abbott, M. Aguena, A. Alarcon, S. Allam, O. Alves, A. Amon, F. Andrade-Oliveira, J. Annis, S. Avila, D. Bacon, E. Baxter, K. Bechtol, M. R. Becker, G. M. Bernstein, S. Bhargava, S. Birrer, J. Blazek, A. Brandao-Souza, S. L. Bridle, D. Brooks, E. Buckley-Geer, D. L. Burke, H. Camacho, A. Campos, A. Carnero Rosell, M. Carrasco Kind, J. Carretero, F. J. Castander, R. Cawthon, C. Chang, A. Chen, R. Chen, A. Choi, C. Conselice, J. Cordero, M. Costanzi, M. Crocce, L. N. da Costa, M. E. da Silva Pereira, C. Davis, T. M. Davis, J. De Vicente, J. DeRose, S. Desai, E. Di Valentino, H. T. Diehl, J. P. Dietrich, S. Dodelson, P. Doel, C. Doux, A. Drlica-Wagner, K. Eckert, T. F. Eifler, F. Elsner, J. Elvin-Poole, S. Everett, A. E. Evrard, X. Fang, A. Farahi, E. Fernandez, I. Ferrero, A. Ferté, P. Fosalba, O. Friedrich, J. Frieman, J. García-Bellido, M. Gatti, E. Gaztanaga, D. W. Gerdes, T. Giannantonio, G. Giannini, D. Gruen, R. A. Gruendl, J. Gschwend, G. Gutierrez, I. Harrison, W. G. Hartley, K. Herner, S. R. Hinton, D. L. Hollowood, K. Honscheid, B. Hoyle, E. M. Huff, D. Huterer, B. Jain, D. J. James, M. Jarvis, N. Jeffrey, T. Jeltema, A. Kovacs, E. Krause, R. Kron, K. Kuehn,

N. Kuropatkin, O. Lahav, P. F. Leget, P. Lemos, A. R. Liddle, C. Lidman, M. Lima, H. Lin, N. MacCrann, M. A. G. Maia, J. L. Marshall, P. Martini, J. McCullough, P. Melchior, J. Mena-Fernández, F. Menanteau, R. Miquel, J. J. Mohr, R. Morgan, J. Muir, J. Myles, S. Nadathur, A. Navarro-Alsina, R. C. Nichol, R. L. C. Ogando, Y. Omori, A. Palmese, S. Pandey, Y. Park, F. Paz-Chinchón, D. Petravick, A. Pieres, A. A. Plazas Malagón, A. Porredon, J. Prat, M. Raveri, M. Rodriguez-Monroy, R. P. Rollins, A. K. Romer, A. Roodman, R. Rosenfeld, A. J. Ross, E. S. Rykoff, S. Samuroff, C. Sánchez, E. Sanchez, J. Sanchez, D. Sanchez Cid, V. Scarpine, M. Schubnell, D. Scolnic, L. F. Secco, S. Serrano, I. Sevilla-Noarbe, E. Sheldon, T. Shin, M. Smith, M. Soares-Santos, E. Suchyta, M. E. C. Swanson, M. Tabbutt, G. Tarle, D. Thomas, C. To, A. Troja, M. A. Troxel, D. L. Tucker, I. Tutusaus, T. N. Varga, A. R. Walker, N. Weaverdyck, J. Weller, B. Yanny, B. Yin, Y. Zhang, and J. Zuntz. Dark Energy Survey Year 3 Results: Cosmological Constraints from Galaxy Clustering and Weak Lensing. *arXiv e-prints*, art. arXiv:2105.13549, May 2021.

Rossana Ruggeri, Will J. Percival, Héctor Gil-Marín, Florian Beutler, Eva-Maria Mueller, Fangzhou Zhu, Nikhil Padmanabhan, Gong-Bo Zhao, Pauline Zarrouk, Ariel G. Sánchez, Julian Bautista, Jonathan Brinkmann, Joel R. Brownstein, Falk Baumgarten, Chia-Hsun Chuang, Kyle Dawson, Hee-Jong Seo, Rita Tojeiro, and Cheng Zhao. The clustering of the SDSS-IV extended Baryon Oscillation Spectroscopic Survey DR14 quasar sample: measuring the evolution of the growth rate using redshift-space distortions between redshift 0.8 and 2.2. *MNRAS*, 483(3):3878–3887, March 2019. doi: 10.1093/mnras/sty3395.

Shadab Alam, Metin Ata, Stephen Bailey, Florian Beutler, Dmitry Bizyaev, Jonathan A. Blazek, Adam S. Bolton, Joel R. Brownstein, Angela Burden, Chia-Hsun Chuang, Johan Comparat, Antonio J. Cuesta, Kyle S. Dawson, Daniel J. Eisenstein, Stephanie Escoffier, Héctor Gil-Marín, Jan Niklas Grieb, Nick Hand, Shirley Ho, Karen Kinemuchi, David Kirkby, Francisco Kitaura, Elena Malanushenko, Viktor Malanushenko, Claudia Maraston, Cameron K. McBride, Robert C. Nichol, Matthew D. Olmstead, Daniel Oravetz, Nikhil Padmanabhan, Nathalie Palanque-

Delabrouille, Kaike Pan, Marcos Pellejero-Ibanez, Will J. Percival, Patrick Petitjean, Francisco Prada, Adrian M. Price-Whelan, Beth A. Reid, Sergio A. Rodríguez-Torres, Natalie A. Roe, Ashley J. Ross, Nicholas P. Ross, Graziano Rossi, Jose Alberto Rubiño-Martín, Shun Saito, Salvador Salazar-Albornoz, Lado Samushia, Ariel G. Sánchez, Siddharth Satpathy, David J. Schlegel, Donald P. Schneider, Claudia G. Scóccola, Hee-Jong Seo, Erin S. Sheldon, Audrey Simmons, Anže Slosar, Michael A. Strauss, Molly E. C. Swanson, Daniel Thomas, Jeremy L. Tinker, Rita Tojeiro, Mariana Vargas Magaña, Jose Alberto Vazquez, Licia Verde, David A. Wake, Yuting Wang, David H. Weinberg, Martin White, W. Michael Wood-Vasey, Christophe Yèche, Idit Zehavi, Zhongxu Zhai, and Gong-Bo Zhao. The clustering of galaxies in the completed SDSS-III Baryon Oscillation Spectroscopic Survey: cosmological analysis of the DR12 galaxy sample. *MNRAS*, 470(3):2617–2652, September 2017. doi: 10.1093/mnras/stx721.

G. Hinshaw, D. Larson, E. Komatsu, D. N. Spergel, C. L. Bennett, J. Dunkley, M. R. Nolta, M. Halpern, R. S. Hill, N. Odegard, L. Page, K. M. Smith, J. L. Weiland, B. Gold, N. Jarosik, A. Kogut, M. Limon, S. S. Meyer, G. S. Tucker, E. Wollack, and E. L. Wright. NINE-YEAR WILKINSON MICROWAVE ANISOTROPY PROBE (WMAP) OBSERVATIONS: COSMOLOGICAL PARAMETER RESULTS. *ApJSupplement Series*, 208(2):19, sep 2013. ISSN 0067-0049. doi: 10.1088/0067-0049/208/2/19.

Simone Aiola, Erminia Calabrese, Loïc Maurin, Sigurd Naess, Benjamin L. Schmitt, Maximilian H. Abitbol, Graeme E. Addison, Peter A. R. Ade, David Alonso, Mandana Amiri, Stefania Amodeo, Elio Angile, Jason E. Austermann, Taylor Baildon, Nick Battaglia, James A. Beall, Rachel Bean, Daniel T. Becker, J. Richard Bond, Sarah Marie Bruno, Victoria Calafut, Luis E. Campusano, Felipe Carrero, Grace E. Chesmore, Hsiao-mei Cho, Steve K. Choi, Susan E. Clark, Nicholas F. Cothard, Devin Crichton, Kevin T. Crowley, Omar Darwish, Rahul Datta, Edward V. Denison, Mark J. Devlin, Cody J. Duell, Shannon M. Duff, Adriaan J. Duivenvoorden, Jo Dunkley, Rolando Dünner, Thomas Essinger-Hileman, Max Fankhanel, Simone Ferraro, Anna E. Fox, Brittany Fuzia, Patricio A. Gallardo,

Vera Gluscevic, Joseph E. Golec, Emily Grace, Megan Gralla, Yilun Guan, Kirsten Hall, Mark Halpern, Dongwon Han, Peter Hargrave, Matthew Hasselfield, Jakob M. Helton, Shawn Henderson, Brandon Hensley, J. Colin Hill, Gene C. Hilton, Matt Hilton, Adam D. Hincks, Renée Hložek, Shuay-Pwu Patty Ho, Johannes Hubmayr, Kevin M. Huffenberger, John P. Hughes, Leopoldo Infante, Kent Irwin, Rebecca Jackson, Jeff Klein, Kenda Knowles, Brian Koopman, Arthur Kosowsky, Vincent Lakey, Dale Li, Yaqiong Li, Zack Li, Martine Lokken, Thibaut Louis, Marius Lungu, Amanda MacInnis, Mathew Madhavacheril, Felipe Maldonado, Maya Mallaby-Kay, Danica Marsden, Jeff McMahon, Felipe Menanteau, Kavilan Moodley, Tim Morton, Toshiya Namikawa, Federico Nati, Laura Newburgh, John P. Nibarger, Andrina Nicola, Michael D. Niemack, Michael R. Nolta, John Orlowski-Sherer, Lyman A. Page, Christine G. Pappas, Bruce Partridge, Phumlani Phakathi, Giampaolo Pisano, Heather Prince, Roberto Puddu, Frank J. Qu, Jesus Rivera, Naomi Robertson, Felipe Rojas, Maria Salatino, Emmanuel Schaan, Alessandro Schillaci, Neelima Sehgal, Blake D. Sherwin, Carlos Sierra, Jon Sievers, Cristobal Sifon, Precious Sikhosana, Sara Simon, David N. Spergel, Suzanne T. Staggs, Jason Stevens, Emilie Storer, Dhaneshwar D. Sunder, Eric R. Switzer, Ben Thorne, Robert Thornton, Hy Trac, Jesse Treu, Carole Tucker, Leila R. Vale, Alexander Van Engelen, Jeff Van Lanen, Eve M. Vavagiakis, Kasey Wagoner, Yuhan Wang, Jonathan T. Ward, Edward J. Wollack, Zhilei Xu, Fernando Zago, and Ningfeng Zhu. The Atacama Cosmology Telescope: DR4 maps and cosmological parameters. *J. Cosmology Astropart. Phys.*, 2020(12):047, December 2020. doi: 10.1088/1475-7516/2020/12/047.

D. Dutcher, L. Balkenhol, P. A. R. Ade, Z. Ahmed, E. Anderes, A. J. Anderson, M. Archipley, J. S. Avva, K. Aylor, P. S. Barry, R. Basu Thakur, K. Benabed, A. N. Bender, B. A. Benson, F. Bianchini, L. E. Bleem, F. R. Bouchet, L. Bryant, K. Byrum, J. E. Carlstrom, F. W. Carter, T. W. Cecil, C. L. Chang, P. Chaubal, G. Chen, H. M. Cho, T. L. Chou, J. F. Cliche, T. M. Crawford, A. Cukierman, C. Daley, T. de Haan, E. V. Denison, K. Dibert, J. Ding, M. A. Dobbs, W. Everett, C. Feng, K. R. Ferguson, A. Foster, J. Fu, S. Galli, A. E. Gambrel, R. W. Gardner,

N. Goeckner-Wald, R. Gualtieri, S. Guns, N. Gupta, R. Guyser, N. W. Halverson, A. H. Harke-Hosemann, N. L. Harrington, J. W. Henning, G. C. Hilton, E. Hivon, G. P. Holder, W. L. Holzapfel, J. C. Hood, D. Howe, N. Huang, K. D. Irwin, O. B. Jeong, M. Jonas, A. Jones, T. S. Khaire, L. Knox, A. M. Kofman, M. Korman, D. L. Kubik, S. Kuhlmann, C. L. Kuo, A. T. Lee, E. M. Leitch, A. E. Lowitz, C. Lu, S. S. Meyer, D. Michalik, M. Millea, J. Montgomery, A. Nadolski, T. Natoli, H. Nguyen, G. I. Noble, V. Novosad, Y. Omori, S. Padin, Z. Pan, P. Paschos, J. Pearson, C. M. Posada, K. Prabhu, W. Quan, S. Raghunathan, A. Rahlin, C. L. Reichardt, D. Riebel, B. Riedel, M. Rouble, J. E. Ruhl, J. T. Sayre, E. Schiappucci, E. Shirokoff, G. Smecher, J. A. Sobrin, A. A. Stark, J. Stephen, K. T. Story, A. Suzuki, K. L. Thompson, B. Thorne, C. Tucker, C. Umilta, L. R. Vale, K. Vanderlinde, J. D. Vieira, G. Wang, N. Whitehorn, W. L. K. Wu, V. Yefremenko, K. W. Yoon, M. R. Young, and SPT-3G Collaboration. Measurements of the E -mode polarization and temperature-E -mode correlation of the CMB from SPT-3G 2018 data. *Phys. Rev. D*, 104(2):022003, July 2021. doi: 10.1103/PhysRevD.104.022003.

Adam G. Riess, Stefano Casertano, Wenlong Yuan, J. Bradley Bowers, Lucas Macri, Joel C. Zinn, and Dan Scolnic. Cosmic Distances Calibrated to 1% Precision with Gaia EDR3 Parallaxes and Hubble Space Telescope Photometry of 75 Milky Way Cepheids Confirm Tension with ΛCDM. *ApJl*, 908(1):L6, February 2021. doi: 10.3847/2041-8213/abdbaf.

Kenneth C. Wong, Sherry H. Suyu, Geoff C. F. Chen, Cristian E. Rusu, Martin Millon, Dominique Sluse, Vivien Bonvin, Christopher D. Fassnacht, Stefan Taubenberger, Matthew W. Auger, Simon Birrer, James H. H. Chan, Frederic Courbin, Stefan Hilbert, Olga Tihhonova, Tommaso Treu, Adriano Agnello, Xuheng Ding, Inh Jee, Eiichiro Komatsu, Anowar J. Shajib, Alessandro Sonnenfeld, Roger D. Blandford, Léon V. E. Koopmans, Philip J. Marshall, and Georges Meylan. H0LiCOW – XIII. A 2.4 per cent measurement of H_0 from lensed quasars: 5.3σ tension between early- and late-Universe probes. *MNRAS*, 498(1):1420–1439, October 2020. doi: 10.1093/mnras/stz3094.

Licia Verde, Tommaso Treu, and Adam G. Riess. Tensions between the early and

late Universe. *Nature Astronomy*, 3:891–895, September 2019. doi: 10.1038/s41550-019-0902-0.

Chiaki Hikage, Masamune Oguri, Takashi Hamana, Surhud More, Rachel Mandelbaum, Masahiro Takada, Fabian Köhlinger, Hironao Miyatake, Atsushi J. Nishizawa, Hiroaki Aihara, Robert Armstrong, James Bosch, Jean Coupon, Anne Ducout, Paul Ho, Bau-Ching Hsieh, Yutaka Komiyama, François Lanusse, Alexie Leauthaud, Robert H. Lupton, Elinor Medezinski, Sogo Mineo, Shoken Miyama, Satoshi Miyazaki, Ryoma Murata, Hitoshi Murayama, Masato Shirasaki, Cristóbal Sifón, Melanie Simet, Joshua Speagle, David N. Spergel, Michael A. Strauss, Naoshi Sugiyama, Masayuki Tanaka, Yousuke Utsumi, Shiang-Yu Wang, and Yoshihiko Yamada. Cosmology from cosmic shear power spectra with Subaru Hyper Suprime-Cam first-year data. *PASJ*, 71(2):43, April 2019. doi: 10.1093/pasj/psz010.

Catherine Heymans, Tilman Tröster, Marika Asgari, Chris Blake, Hendrik Hildebrandt, Benjamin Joachimi, Konrad Kuijken, Chieh-An Lin, Ariel G. Sánchez, Jan Luca van den Busch, Angus H. Wright, Alexandra Amon, Maciej Bilicki, Jelte de Jong, Martin Crocce, Andrej Dvornik, Thomas Erben, Maria Cristina Fortuna, Fedor Getman, Benjamin Giblin, Karl Glazebrook, Henk Hoekstra, Shahab Joudaki, Arun Kannawadi, Fabian Köhlinger, Chris Lidman, Lance Miller, Nicola R. Napolitano, David Parkinson, Peter Schneider, HuanYuan Shan, Edwin A. Valentijn, Gijs Verdoes Kleijn, and Christian Wolf. KiDS-1000 Cosmology: Multi-probe weak gravitational lensing and spectroscopic galaxy clustering constraints. *A&A*, 646: A140, February 2021. doi: 10.1051/0004-6361/202039063.

Arthur Kosowsky and Michael S. Turner. CBR anisotropy and the running of the scalar spectral index. *PRD*, 52(4):R1739–R1743, aug 1995. ISSN 05562821. doi: 10.1103/PhysRevD.52.R1739.

Nathalie Palanque-Delabrouille, Christophe Yèche, Nils Schöneberg, Julien Lesgourgues, Michael Walther, Solène Chabanier, and Eric Armengaud. Hints, neutrino bounds, and WDM constraints from SDSS DR14 Lyman-α and Planck full-

survey data. *J. Cosmology Astropart. Phys.*, 2020(4):038, April 2020. doi: 10.1088/1475-7516/2020/04/038.

James S. Bullock and Michael Boylan-Kolchin. Small-Scale Challenges to the Λ CDM Paradigm. *ARA&A*, 55(1):343–387, aug 2017. ISSN 0066-4146. doi: 10.1146/annurev-astro-091916-055313.

Anatoly Klypin, Andrey V Kravtsov, Octavio Valenzuela, and Francisco Prada. Where Are the Missing Galactic Satellites? *ApJ*, 522(1):82–92, 1999. ISSN 0004-637X. doi: 10.1086/307643.

Ben Moore, Sebastiano Ghigna, Fabio Governato, George Lake, Thomas Quinn, Joachim Stadel, and Paolo Tozzi. Dark Matter Substructure within Galactic Halos. *ApJ*, 524(1):L19–L22, 1999. ISSN 0004637X. doi: 10.1086/312287.

Ricardo A. Flores and Joel R. Primack. Observational and theoretical constraints on singular dark matter halos. *ApJ*, 427:L1, 1994. ISSN 0004-637X. doi: 10.1086/187350.

Julio F. Navarro, Carlos S. Frenk, and Simon D. M. White. The Structure of Cold Dark Matter Halos. *The Astrophysical Journal*, 462:563, may 1996. ISSN 0004-637X. doi: 10.1086/177173.

Michael Boylan-Kolchin, James S Bullock, and Manoj Kaplinghat. Too big to fail? The puzzling darkness of massive Milky Way subhaloes. *MNRAS*, 415(1):40–44, 2011. ISSN 17453933. doi: 10.1111/j.1745-3933.2011.01074.x.

James S Bullock, Andrey V Kravtsov, and David H Weinberg. Reionization and the Abundance of Galactic Satellites. *ApJ*, 539(2):517–521, 2000. ISSN 0004-637X. doi: 10.1086/309279.

A. J. Benson, C. G. Lacey, C. M. Baugh, S. Cole, and C. S. Frenk. The effects of photoionization on galaxy formation - I. Model and results at z=0. *MNRAS*, 333(1):156–176, June 2002. doi: 10.1046/j.1365-8711.2002.05387.x.

Julio F. Navarro, Vincent R. Eke, and Carlos S. Frenk. The cores of dwarf galaxy haloes. *MNRAS*, 283(3):L72–L78, December 1996. doi: 10.1093/mnras/283.3.L72.

Andrey V Kravtsov, Oleg Y Gnedin, and Anatoly A Klypin. The Tumultuous Lives of Galactic Dwarfs and the Missing Satellites Problem. *ApJ*, 609(2):482–497, 2004. ISSN 0004-637X. doi: 10.1086/421322.

Sergey Mashchenko, James Wadsley, and H. M.P. Couchman. Stellar feedback in dwarf galaxy formation. *Science*, 319(5860):174–177, jan 2008. ISSN 00368075. doi: 10.1126/science.1148666.

F Governato, A Zolotov, A Pontzen, C. Christensen, S. H. Oh, A M Brooks, T. Quinn, S Shen, and J Wadsley. Cuspy no more: how outflows affect the central dark matter and baryon distribution in Λ cold dark matter galaxies. *MNRAS*, 422(2):1231–1240, may 2012. ISSN 00358711. doi: 10.1111/j.1365-2966.2012.20696.x.

Alyson M Brooks and Adi Zolotov. Why baryons matter: The kinematics of dwarf spheroidal satellites. *ApJ*, 786(2):87, 2014. ISSN 15384357. doi: 10.1088/0004-637X/786/2/87.

Jose Oñorbe, Michael Boylan-Kolchin, James S Bullock, Philip F Hopkins, Dušan Kereš, Claude André Faucher-Giguère, Eliot Quataert, and Norman Murray. Forged in FIRE: Cusps, cores and baryons in low-mass dwarf galaxies. *MNRAS*, 454(2):2092–2106, 2015. ISSN 13652966. doi: 10.1093/mnras/stv2072.

Till Sawala, Carlos S. Frenk, Azadeh Fattahi, Julio F. Navarro, Richard G. Bower, Robert A. Crain, Claudio Dalla Vecchia, Michelle Furlong, John. C. Helly, Adrian Jenkins, Kyle A. Oman, Matthieu Schaller, Joop Schaye, Tom Theuns, James Trayford, and Simon D. M. White. The APOSTLE simulations: solutions to the Local Group's cosmic puzzles. *MNRAS*, 457(2):1931–1943, April 2016. doi: 10.1093/mnras/stw145.

Marco Velliscig, Marcel P. van Daalen, Joop Schaye, Ian G. McCarthy, Marcello Cacciato, Amand ine M. C. Le Brun, and Claudio Dalla Vecchia. The impact of galaxy

formation on the total mass, mass profile and abundance of haloes. *MNRAS*, 442(3): 2641–2658, August 2014. doi: 10.1093/mnras/stu1044.

Marcel P. van Daalen, Joop Schaye, Ian G. McCarthy, C. M. Booth, and Claudio Dalla Vecchia. The impact of baryonic processes on the two-point correlation functions of galaxies, subhaloes and matter. *MNRAS*, 440(4):2997–3010, June 2014. doi: 10.1093/mnras/stu482.

Marcel P. van Daalen, Joop Schaye, C. M. Booth, and Claudio Dalla Vecchia. The effects of galaxy formation on the matter power spectrum: a challenge for precision cosmology. *MNRAS*, 415(4):3649–3665, August 2011. doi: 10.1111/j.1365-2966.2011.18981.x.

Marcel P. van Daalen, Ian G. McCarthy, and Joop Schaye. Exploring the effects of galaxy formation on matter clustering through a library of simulation power spectra. *MNRAS*, 491(2):2424–2446, January 2020. doi: 10.1093/mnras/stz3199.

Euclid Collaboration, Mischa Knabenhans, Joachim Stadel, Stefano Marelli, Doug Potter, Romain Teyssier, Laurent Legrand, Aurel Schneider, Bruno Sudret, Linda Blot, Saeeda Awan, Carlo Burigana, Carla Sofia Carvalho, Hannu Kurki-Suonio, and Gabriele Sirri. Euclid preparation: II. The EUCLIDEMULATOR - a tool to compute the cosmology dependence of the nonlinear matter power spectrum. *MNRAS*, 484 (4):5509–5529, April 2019. doi: 10.1093/mnras/stz197.

Erik Holmberg. On the Clustering Tendencies among the Nebulae. II. a Study of Encounters Between Laboratory Models of Stellar Systems by a New Integration Procedure. *ApJ*, 94:385, November 1941. doi: 10.1086/144344.

S. von Hoerner. Die numerische Integration des n-Körper-Problemes für Sternhaufen. I. *ZAp*, 50:184–214, January 1960.

S. J. Aarseth. Dynamical evolution of clusters of galaxies, I. *MNRAS*, 126:223, January 1963. doi: 10.1093/mnras/126.3.223.

P. J. E. Peebles. Structure of the Coma Cluster of Galaxies. *AJ*, 75:13, February 1970. doi: 10.1086/110933.

Mark Vogelsberger, Federico Marinacci, Paul Torrey, and Ewald Puchwein. Cosmological simulations of galaxy formation. *Nature Reviews Physics*, 2(1):42–66, January 2020. doi: 10.1038/s42254-019-0127-2.

Y B Zel'dovich. Gravitational Instability: An approximate theory for large density perturbations. *Astron. and Astrophys.*, 5:84, 1970.

Volker Springel. The cosmological simulation code gadget-2. *MNRAS*, 364(4):1105–1134, dec 2005. ISSN 0035-8711. doi: 10.1111/j.1365-2966.2005.09655.x.

Ian G. McCarthy, Joop Schaye, Simeon Bird, and Amandine M. C. Le Brun. The BAHAMAS project: calibrated hydrodynamical simulations for large-scale structure cosmology. *MNRAS*, 465(3):2936–2965, March 2017. doi: 10.1093/mnras/stw2792.

Ian G. McCarthy, Simeon Bird, Joop Schaye, Joachim Harnois-Deraps, Andreea S. Font, and Ludovic van Waerbeke. The BAHAMAS project: the CMB-large-scale structure tension and the roles of massive neutrinos and galaxy formation. *MNRAS*, 476(3):2999–3030, May 2018. doi: 10.1093/mnras/sty377.

Joop Schaye, Robert A Crain, Richard G Bower, Michelle Furlong, Matthieu Schaller, Tom Theuns, Claudio Dalla Vecchia, Carlos S Frenk, I G Mccarthy, John C Helly, Adrian Jenkins, Y M Rosas-Guevara, Simon D.M. White, Maarten Baes, C M Booth, Peter Camps, Julio F Navarro, Yan Qu, Alireza Rahmati, Till Sawala, Peter A Thomas, and James Trayford. The EAGLE project: Simulating the evolution and assembly of galaxies and their environments. *MNRAS*, 446(1):521–554, 2015. doi: 10.1093/mnras/stu2058.

Robert A Crain, Joop Schaye, Richard G Bower, Michelle Furlong, Matthieu Schaller, Tom Theuns, Claudio Dalla Vecchia, Carlos S Frenk, Ian G. McCarthy, John C Helly, Adrian Jenkins, Yetli M Rosas-Guevara, Simon D.M. White, and James W Trayford. The EAGLE simulations of galaxy formation: Calibration of subgrid physics and model variations. *MNRAS*, 450(2):1937–1961, 2015. doi: 10.1093/mnras/stv725.

Andreea S. Font, Ian G. McCarthy, Robert Poole-Mckenzie, Sam G. Stafford, Shaun T. Brown, Joop Schaye, Robert A. Crain, Tom Theuns, and Matthieu Schaller. The ARTEMIS simulations: stellar haloes of Milky Way-mass galaxies. *arXiv e-prints*, art. arXiv:2004.01914, April 2020.

Sam G. Stafford, Ian G. McCarthy, Robert A. Crain, Jaime Salcido, Joop Schaye, Andreea S. Font, Juliana Kwan, and Simon Pfeifer. The BAHAMAS project: effects of a running scalar spectral index on large-scale structure. *MNRAS*, 493(1):676–697, March 2020a. doi: 10.1093/mnras/staa129.

. Planck Collaboration XIII. Planck 2015 results. *Astronomy & Astrophysics*, 594: A13, oct 2016. ISSN 0004-6361. doi: 10.1051/0004-6361/201525830.

V Bonvin, F Courbin, S H Suyu, P J Marshall, C E Rusu, D Sluse, M Tewes, K C Wong, T Collett, C D Fassnacht, T Treu, M W Auger, S Hilbert, L V E Koopmans, G Meylan, N Rumbaugh, A Sonnenfeld, and C Spiniello. H0LiCOW-V. New COSMOGRAIL time delays of HE 0435-1223: H0 to 3.8 per cent precision from strong lensing in a flat CDM model. *MNRAS*, 465:4914–4930, 2017. doi: 10.1093/mnras/stw3006.

Adam G Riess, Stefano Casertano, Wenlong Yuan, Lucas Macri, Jay Anderson, John W Mackenty, J Bradley Bowers, Kelsey I Clubb, Alexei V Filippenko, David O Jones, and Brad E Tucker. New Parallaxes of Galactic Cepheids from Spatially Scanning the Hubble Space Telescope: Implications for the Hubble Constant. *The Astrophysical Journal*, 855:136, 2018. doi: 10.3847/1538-4357/aaadb7.

Catherine Heymans, Emma Grocutt, Alan Heavens, Martin Kilbinger, Thomas D Kitching, Fergus Simpson, Jonathan Benjamin, Thomas Erben, Hendrik Hildebrandt, Henk Hoekstra, Yannick Mellier, Lance Miller, Ludovic Van Waerbeke, Michael L Brown, Jean Coupon, Liping Fu, Joachim Harnois-Déraps, Michael J Hudson, Konrad Kuijken, Barnaby Rowe, Tim Schrabback, Elisabetta Semboloni, Sanaz Vafaei, and Malin Velander. CFHTLenS tomographic weak lensing cosmological parameter constraints: Mitigating the impact of intrinsic galaxy alignments.

Monthly Notices of the Royal Astronomical Society, 432(3):2433–2453, jul 2013. ISSN 1365-2966. doi: 10.1093/mnras/stt601.

. Planck Collaboration. Planck 2015 results. *Astronomy & Astrophysics*, 594:A24, oct 2016. ISSN 0004-6361. doi: 10.1051/0004-6361/201525833.

H Hildebrandt, M Viola, C Heymans, S Joudaki, K Kuijken, C Blake, T Erben, B Joachimi, D Klaes, L Miller, C B Morrison, R Nakajima, G. Verdoes Kleijn, A Amon, A Choi, G Covone, J. T. A. de Jong, A Dvornik, I Fenech Conti, A Grado, J Harnois-Déraps, R Herbonnet, H Hoekstra, F Köhlinger, J. McFarland, A Mead, J Merten, N Napolitano, J A Peacock, M Radovich, P Schneider, P Simon, E A Valentijn, J. L. van den Busch, E. van Uitert, and L Van Waerbeke. KiDS-450: cosmological parameter constraints from tomographic weak gravitational lensing. *Monthly Notices of the Royal Astronomical Society*, 465(2):1454–1498, feb 2017. ISSN 0035-8711. doi: 10.1093/mnras/stw2805.

Shahab Joudaki, Chris Blake, Andrew Johnson, Alexandra Amon, Marika Asgari, Ami Choi, Thomas Erben, Karl Glazebrook, Joachim Harnois-Déraps, Catherine Heymans, Hendrik Hildebrandt, Henk Hoekstra, Dominik Klaes, Konrad Kuijken, Chris Lidman, Alexander Mead, Lance Miller, David Parkinson, Gregory B Poole, Peter Schneider, Massimo Viola, and Christian Wolf. KiDS-450 + 2dFLenS: Cosmological parameter constraints from weak gravitational lensing tomography and overlapping redshift-space galaxy clustering. *Monthly Notices of the Royal Astronomical Society*, 474(4):4894–4924, mar 2018. ISSN 0035-8711. doi: 10.1093/mnras/stx2820.

T M C Abbott, S Allam, P Andersen, C Angus, J Asorey, A Avelino, S Avila, B A Bassett, K Bechtol, G M Bernstein, E Bertin, D Brooks, D Brout, P Brown, D L Burke, J Calcino, A Carnero Rosell, D. Carollo, M. Carrasco Kind, J. Carretero, R. Casas, F. J. Castander, R. Cawthon, P. Challis, M. Childress, A. Clocchiatti, C. E. Cunha, C. B. D'Andrea, L. N. da Costa, C. Davis, T M Davis, J De Vicente, D. L. DePoy, S Desai, H T Diehl, P Doel, A Drlica-Wagner, T F Eifler, A E Evrard, E Fernandez, A V Filippenko, D A Finley, B Flaugher, R J Foley, P. Fosalba, J. Frie-

man, L. Galbany, J. García-Bellido, E. Gaztanaga, T. Giannantonio, K. Glazebrook, D. A. Goldstein, S. González-Gaitán, D. Gruen, R. A. Gruendl, J. Gschwend, R. R. Gupta, G. Gutierrez, W. G. Hartley, S. R. Hinton, D L Hollowood, K Honscheid, J K Hoormann, B Hoyle, D J James, T Jeltema, M. W. G. Johnson, M D Johnson, E Kasai, S Kent, R Kessler, A G Kim, R P Kirshner, E Kovacs, E Krause, R Kron, K Kuehn, S Kuhlmann, N Kuropatkin, O Lahav, J Lasker, G F Lewis, T S Li, C Lidman, M Lima, H Lin, E Macaulay, M A G Maia, K S Mandel, M March, J Marriner, J. L. Marshall, P. Martini, F. Menanteau, C. J. Miller, R. Miquel, V. Miranda, J. J. Mohr, E. Morganson, D. Muthukrishna, A. Möller, E Neilsen, R C Nichol, B Nord, P Nugent, R L C Ogando, A Palmese, Y.-C Pan, A A Plazas, M Pursiainen, A K Romer, A Roodman, E Rozo, E S Rykoff, M. Sako, E. Sanchez, V. Scarpine, R. Schindler, M. Schubnell, D. Scolnic, S. Serrano, I. Sevilla-Noarbe, R. Sharp, M. Smith, M. Soares-Santos, F. Sobreira, N. E. Sommer, H Spinka, E Suchyta, M Sullivan, E Swann, G Tarle, D. Thomas, R C Thomas, M A Troxel, B E Tucker, S A Uddin, A R Walker, W Wester, P Wiseman, R C Wolf, B Yanny, B. Zhang, and Y Zhang. First Cosmology Results using Type Ia Supernovae from the Dark Energy Survey: Constraints on Cosmological Parameters. *The Astrophysical Journal*, 872 (2):L30, feb 2019. ISSN 2041-8213. doi: 10.3847/2041-8213/ab04fa.

G. E. Addison, Y. Huang, D. J. Watts, C. L. Bennett, M. Halpern, G. Hinshaw, and J. L. Weiland. Quantifying Discordance in the 2015 Planck CMB Spectrum. *ApJ*, 818:132, February 2016. doi: 10.3847/0004-637X/818/2/132.

Planck Collaboration, N. Aghanim, Y. Akrami, M. Ashdown, J. Aumont, C. Baccigalupi, M. Ballardini, A. J. Banday, R. B. Barreiro, N. Bartolo, S. Basak, K. Benabed, M. Bersanelli, P. Bielewicz, A. Bonaldi, L. Bonavera, J. R. Bond, J. Borrill, F. R. Bouchet, C. Burigana, E. Calabrese, J.-F. Cardoso, A. Challinor, H. C. Chiang, L. P. L. Colombo, C. Combet, B. P. Crill, A. Curto, F. Cuttaia, P. de Bernardis, A. de Rosa, G. de Zotti, J. Delabrouille, E. Di Valentino, C. Dickinson, J. M. Diego, O. Doré, A. Ducout, X. Dupac, S. Dusini, G. Efstathiou, F. Elsner, T. A. Enßlin, H. K. Eriksen, Y. Fantaye, F. Finelli, F. Forastieri, M. Frailis, E. Franceschi, A. Frolov, S. Galeotta, S. Galli, K. Ganga, R. T. Génova-Santos, M. Gerbino,

J. González-Nuevo, K. M. Górski, S. Gratton, A. Gruppuso, J. E. Gudmundsson, D. Herranz, E. Hivon, Z. Huang, A. H. Jaffe, W. C. Jones, E. Keihänen, R. Keskitalo, K. Kiiveri, J. Kim, T. S. Kisner, L. Knox, N. Krachmalnicoff, M. Kunz, H. Kurki-Suonio, G. Lagache, J.-M. Lamarre, A. Lasenby, M. Lattanzi, C. R. Lawrence, M. Le Jeune, F. Levrier, A. Lewis, M. Liguori, P. B. Lilje, M. Lilley, V. Lindholm, M. López-Caniego, P. M. Lubin, Y.-Z. Ma, J. F. Macías-Pérez, G. Maggio, D. Maino, N. Mandolesi, A. Mangilli, M. Maris, P. G. Martin, E. Martínez-González, S. Matarrese, N. Mauri, J. D. McEwen, P. R. Meinhold, A. Mennella, M. Migliaccio, M. Millea, M.-A. Miville-Deschênes, D. Molinari, A. Moneti, L. Montier, G. Morgante, A. Moss, A. Narimani, P. Natoli, C. A. Oxborrow, L. Pagano, D. Paoletti, B. Partridge, G. Patanchon, L. Patrizii, V. Pettorino, F. Piacentini, L. Polastri, G. Polenta, J.-L. Puget, J. P. Rachen, B. Racine, M. Reinecke, M. Remazeilles, A. Renzi, G. Rocha, M. Rossetti, G. Roudier, J. A. Rubiño-Martín, B. Ruiz-Granados, L. Salvati, M. Sandri, M. Savelainen, D. Scott, C. Sirignano, G. Sirri, L. Stanco, A.-S. Suur-Uski, J. A. Tauber, D. Tavagnacco, M. Tenti, L. Toffolatti, M. Tomasi, M. Tristram, T. Trombetti, J. Valiviita, F. Van Tent, P. Vielva, F. Villa, N. Vittorio, B. D. Wandelt, I. K. Wehus, M. White, A. Zacchei, and A. Zonca. Planck intermediate results. LI. Features in the cosmic microwave background temperature power spectrum and shifts in cosmological parameters. *A&A*, 607:A95, November 2017. doi: 10.1051/0004-6361/201629504.

Richard A Battye and Adam Moss. Evidence for Massive Neutrinos from Cosmic Microwave Background and Lensing Observations. *Physical Review Letters*, 112 (5):051303, feb 2014. ISSN 0031-9007. doi: 10.1103/PhysRevLett.112.051303.

Florian Beutler, Shun Saito, Joel R Brownstein, Chia-Hsun Chuang, Antonio J Cuesta, Will J Percival, A. J. Ross, Nicholas P Ross, Donald P Schneider, Lado Samushia, A. G. Sanchez, H.-J. Seo, Jeremy L Tinker, Christian Wagner, and Benjamin A Weaver. The clustering of galaxies in the SDSS-III Baryon Oscillation Spectroscopic Survey: signs of neutrino mass in current cosmological data sets. *Monthly Notices of the Royal Astronomical Society*, 444(4):3501–3516, sep 2014. ISSN 0035-8711. doi: 10.1093/mnras/stu1702.

Mark Wyman, Douglas H Rudd, R Ali Vanderveld, and Wayne Hu. Neutrinos Help Reconcile Planck Measurements with the Local Universe. *Physical Review Letters*, 112(5):051302, feb 2014. ISSN 0031-9007. doi: 10.1103/PhysRevLett.112.051302.

Eleonora Di Valentino, Alessandro Melchiorri, Eric V Linder, and Joseph Silk. Constraining dark energy dynamics in extended parameter space. *Physical Review D*, 96(2):023523, jul 2017. ISSN 2470-0010. doi: 10.1103/PhysRevD.96.023523.

Weiqiang Yang, Supriya Pan, Eleonora Di Valentino, Emmanuel N Saridakis, and Subenoy Chakraborty. Observational constraints on one-parameter dynamical dark-energy parametrizations and the H_0 tension. *Physical Review D*, 99(4):043543, feb 2019. ISSN 2470-0010. doi: 10.1103/PhysRevD.99.043543.

Antonio De Felice and Shinji Tsujikawa. f(R) Theories. *Living Reviews in Relativity*, 13(1):3, dec 2010. ISSN 2367-3613. doi: 10.12942/lrr-2010-3.

Baojiu Li, Gong-Bo Zhao, Romain Teyssier, and Kazuya Koyama. ECOSMOG: an Efficient COde for Simulating MOdified Gravity. *J. Cosmology Astropart. Phys.*, 2012(1):051, Jan 2012. doi: 10.1088/1475-7516/2012/01/051.

Rafael C. Nunes. Structure formation in f (T) gravity and a solution for H 0 tension. *Journal of Cosmology and Astroparticle Physics*, 2018(05):052–052, may 2018. ISSN 1475-7516. doi: 10.1088/1475-7516/2018/05/052.

Nathalie Palanque-Delabrouille, Christophe Yèche, Julien Baur, Christophe Magneville, Graziano Rossi, Julien Lesgourgues, Arnaud Borde, Etienne Burtin, Jean-Marc LeGoff, James Rich, Matteo Viel, and David Weinberg. Neutrino masses and cosmology with Lyman-alpha forest power spectrum. *J. Cosmology Astropart. Phys.*, 2015(11):011, November 2015. doi: 10.1088/1475-7516/2015/11/011.

J Dunkley, R Hlozek, J Sievers, V Acquaviva, P. A. R. Ade, P Aguirre, M Amiri, J W Appel, L F Barrientos, E S Battistelli, J R Bond, B Brown, B Burger, J Chervenak, S Das, M J Devlin, S R Dicker, W. Bertrand Doriese, R. Dünner, T Essinger-Hileman, R P Fisher, J W Fowler, A Hajian, M Halpern, M Hasselfield,

C. Hernández-Monteagudo, G. C. Hilton, M Hilton, A D Hincks, K M Huffenberger, D. H. Hughes, J P Hughes, L Infante, K D Irwin, J B Juin, M Kaul, J Klein, A Kosowsky, J M Lau, M Limon, Y-t Lin, R H Lupton, T A Marriage, D Marsden, P Mauskopf, F Menanteau, K Moodley, H Moseley, C B Netterfield, M D Niemack, M R Nolta, L A Page, L Parker, B Partridge, B Reid, N Sehgal, B Sherwin, D N Spergel, S T Staggs, D S Swetz, E R Switzer, R Thornton, H Trac, C Tucker, R Warne, E Wollack, and Y Zhao. THE ATACAMA COSMOLOGY TELESCOPE: COSMOLOGICAL PARAMETERS FROM THE 2008 POWER SPECTRUM. *ApJ*, 739(1):52, sep 2011. ISSN 0004-637X. doi: 10.1088/0004-637X/739/1/52.

Gong-Bo Zhao, Shun Saito, Will J Percival, Ashley J. Ross, Francesco Montesano, Matteo Viel, Donald P Schneider, Marc Manera, Jordi Miralda-Escudé, Nathalie Palanque-Delabrouille, Nicholas P Ross, Lado Samushia, Ariel G Sánchez, Molly E. C. Swanson, Daniel Thomas, Rita Tojeiro, Christophe Yèche, and Donald G York. The clustering of galaxies in the SDSS-III Baryon Oscillation Spectroscopic Survey: weighing the neutrino mass using the galaxy power spectrum of the CMASS sample. *Monthly Notices of the Royal Astronomical Society*, 436(3):2038–2053, dec 2013. ISSN 1365-2966. doi: 10.1093/mnras/stt1710.

Z Hou, C L Reichardt, K T Story, B Follin, R Keisler, K A Aird, B A Benson, L E Bleem, J E Carlstrom, C L Chang, H.-M Cho, T M Crawford, A T Crites, T. de Haan, R. de Putter, M A Dobbs, S Dodelson, J Dudley, E M George, N W Halverson, G P Holder, W L Holzapfel, S Hoover, J D Hrubes, M Joy, L Knox, A T Lee, E M Leitch, M Lueker, D Luong-Van, J. J. McMahon, J. Mehl, S. S. Meyer, M. Millea, J. J. Mohr, T. E. Montroy, S. Padin, T Plagge, C Pryke, J E Ruhl, J T Sayre, K K Schaffer, L Shaw, E Shirokoff, H G Spieler, Z Staniszewski, A A Stark, A. van Engelen, K Vanderlinde, J D Vieira, R Williamson, and O Zahn. CONSTRAINTS ON COSMOLOGY FROM THE COSMIC MICROWAVE BACKGROUND POWER SPECTRUM OF THE 2500 deg 2 SPT-SZ SURVEY. *The Astrophysical Journal*, 782(2):74, jan 2014. ISSN 0004-637X. doi: 10.1088/0004-637X/782/2/74.

Miguel Escudero, Héctor Ramírez, Lotfi Boubekeur, Elena Giusarma, and Olga Mena. The present and future of the most favoured inflationary models after Planck 2015.

Journal of Cosmology and Astroparticle Physics, 2016(02):020–020, feb 2016. ISSN 1475-7516. doi: 10.1088/1475-7516/2016/02/020.

Antony Lewis, Anthony Challinor, and Anthony Lasenby. Efficient Computation of Cosmic Microwave Background Anisotropies in Closed Friedmann-Robertson-Walker Models. *ApJ*, 538(2):473–476, aug 2000. ISSN 0004-637X. doi: 10.1086/309179.

Joop Schaye, Claudio Dalla Vecchia, C M Booth, Robert P.C. Wiersma, Tom Theuns, Marcel R Haas, Serena Bertone, Alan R Duffy, I. G. McCarthy, and Freeke van de Voort. The physics driving the cosmic star formation history. *Monthly Notices of the Royal Astronomical Society*, 402(3):1536–1560, mar 2010. ISSN 00358711. doi: 10.1111/j.1365-2966.2009.16029.x.

J Lesgourges and S Pastor. Massive neutrinos and cosmology. *Physics Reports*, 429 (6):307–379, jul 2006. ISSN 03701573. doi: 10.1016/j.physrep.2006.04.001.

Yacine Ali-Haïmoud and Simeon Bird. An efficient implementation of massive neutrinos in non-linear structure formation simulations. *MNRAS*, 428(4):3375–3389, feb 2013. ISSN 0035-8711. doi: 10.1093/MNRAS/sts286.

J. R. Bond, G. Efstathiou, and J. Silk. Massive Neutrinos and the Large-Scale Structure of the Universe. *Physical Review Letters*, 45(24):1980–1984, dec 1980. ISSN 0031-9007. doi: 10.1103/PhysRevLett.45.1980.

Chung-Pei Ma and Edmund Bertschinger. Cosmological Perturbation Theory in the Synchronous and Conformal Newtonian Gauges. *ApJ*, 455:7, dec 1995. ISSN 0004-637X. doi: 10.1086/176550.

Jacob Brandbyge, Steen Hannestad, Troels Haugbølle, and Bjarne Thomsen. The effect of thermal neutrino motion on the non-linear cosmological matter power spectrum. *J. Cosmology Astropart. Phys.*, 2008(8):020, August 2008. doi: 10.1088/1475-7516/2008/08/020.

Jacob Brandbyge and Steen Hannestad. Grid based linear neutrino perturbations in cosmological N-body simulations. *J. Cosmology Astropart. Phys.*, 2009(5):002, May 2009. doi: 10.1088/1475-7516/2009/05/002.

Simeon Bird, Matteo Viel, and Martin G Haehnelt. Massive neutrinos and the non-linear matter power spectrum. *Mon. Not. R. Astron. Soc*, 420:2551–2561, 2012. doi: 10.1111/j.1365-2966.2011.20222.x.

Benjamin O. Mummery, Ian G. McCarthy, Simeon Bird, and Joop Schaye. The separate and combined effects of baryon physics and neutrino free streaming on large-scale structure. *Monthly Notices of the Royal Astronomical Society*, 471(1):227–242, 2017. ISSN 13652966. doi: 10.1093/MNRAS/stx1469.

Wessel Valkenburg and Francisco Villaescusa-Navarro. Accurate initial conditions in mixed dark matter-baryon simulations. *MNRAS*, 467(4):4401–4409, Jun 2017. doi: 10.1093/mnras/stx376.

Robert P C Wiersma, Joop Schaye, and Britton D Smith. The effect of photoionization on the cooling rates of enriched, astrophysical plasmas. *Monthly Notices of the Royal Astronomical Society*, 393(1):99–107, feb 2009a. ISSN 00358711. doi: 10.1111/j.1365-2966.2008.14191.x.

Joop Schaye and Claudio Dalla Vecchia. On the relation between the Schmidt and Kennicutt-Schmidt star formation laws and its implications for numerical simulations. *Monthly Notices of the Royal Astronomical Society*, 383(3):1210–1222, dec 2008. ISSN 00358711. doi: 10.1111/j.1365-2966.2007.12639.x.

Robert P C Wiersma, Joop Schaye, Tom Theuns, Claudio Dalla Vecchia, and Luca Tornatore. Chemical enrichment in cosmological, smoothed particle hydrodynamics simulations. *Monthly Notices of the Royal Astronomical Society*, 399(2):574–600, oct 2009b. ISSN 00358711. doi: 10.1111/j.1365-2966.2009.15331.x.

Claudio Dalla Vecchia and Joop Schaye. Simulating galactic outflows with kinetic supernova feedback. *Monthly Notices of the Royal Astronomical Society*, 387(4):1431–1444, jul 2008. ISSN 00358711. doi: 10.1111/j.1365-2966.2008.13322.x.

C M Booth and Joop Schaye. Cosmological simulations of the growth of supermassive black holes and feedback from active galactic nuclei: method and tests. *Monthly Notices of the Royal Astronomical Society*, 398(1):53–74, sep 2009. ISSN 00358711. doi: 10.1111/j.1365-2966.2009.15043.x.

Volker Springel, Tiziana Di Matteo, and Lars Hernquist. Modelling feedback from stars and black holes in galaxy mergers. *Monthly Notices of the Royal Astronomical Society*, 361(3):776–794, aug 2005. ISSN 00358711. doi: 10.1111/j.1365-2966.2005.09238.x.

. Planck Collaboration XX. Planck 2015 results - XX. Constraints on Inflation. *Astronomy & Astrophysics*, 594:A20, oct 2016. ISSN 0004-6361. doi: 10.1051/0004-6361/201525898.

Radford M Neal. Taking Bigger Metropolis Steps by Dragging Fast Variables. *arXiv:math/0502099 [math.ST]*, 2005.

Simon Pfeifer, Ian G. McCarthy, Sam G. Stafford, Shaun T. Brown, Andreea S. Font, Juliana Kwan, Jaime Salcido, and Joop Schaye. The BAHAMAS project: effects of dynamical dark energy on large-scale structure. *MNRAS*, 498(2):1576–1592, October 2020. doi: 10.1093/mnras/staa2240.

LSST Dark Energy Science Collaboration. Large Synoptic Survey Telescope: Dark Energy Science Collaboration. *arXiv e-prints*, art. arXiv:1211.0310, Nov 2012.

Luca Amendola, Stephen Appleby, David Bacon, Tessa Baker, Marco Baldi, Nicola Bartolo, Alain Blanchard, Camille Bonvin, Stefano Borgani, Enzo Branchini, Clare Burrage, Stefano Camera, Carmelita Carbone, Luciano Casarini, Mark Cropper, Claudia de Rham, Cinzia Di Porto, Anne Ealet, Pedro G. Ferreira, Fabio Finelli, Juan García-Bellido, Tommaso Giannantonio, Luigi Guzzo, Alan Heavens, Lavinia Heisenberg, Catherine Heymans, Henk Hoekstra, Lukas Hollenstein, Rory Holmes, Ole Horst, Knud Jahnke, Thomas D. Kitching, Tomi Koivisto, Martin Kunz, Giuseppe La Vacca, Marisa March, Elisabetta Majerotto, Katarina Markovic, David Marsh, Federico Marulli, Richard Massey, Yannick Mellier, David F. Mota, Nel-

son J. Nunes, Will Percival, Valeria Pettorino, Cristiano Porciani, Claudia Quercellini, Justin Read, Massimiliano Rinaldi, Domenico Sapone, Roberto Scaramella, Constantinos Skordis, Fergus Simpson, Andy Taylor, Shaun Thomas, Roberto Trotta, Licia Verde, Filippo Vernizzi, Adrian Vollmer, Yun Wang, Jochen Weller, and Tom Zlosnik. Cosmology and Fundamental Physics with the Euclid Satellite. *Living Reviews in Relativity*, 16(1):6, Sep 2013. doi: 10.12942/lrr-2013-6.

Dragan Huterer. Weak lensing and dark energy. *Phys. Rev. D*, 65(6):063001, Mar 2002. doi: 10.1103/PhysRevD.65.063001.

Dragan Huterer and Masahiro Takada. Calibrating the nonlinear matter power spectrum: Requirements for future weak lensing surveys. *Astroparticle Physics*, 23(4): 369–376, may 2005. ISSN 0927-6505. doi: 10.1016/J.ASTROPARTPHYS.2005.02.006.

Andrew P Hearin, Andrew R Zentner, and Zhaoming Ma. General requirements on matter power spectrum predictions for cosmology with weak lensing tomography. *Journal of Cosmology and Astroparticle Physics*, 2012(04):034–034, apr 2012. ISSN 1475-7516. doi: 10.1088/1475-7516/2012/04/034.

Marcel P. van Daalen and Joop Schaye. The contributions of matter inside and outside of haloes to the matter power spectrum. *Monthly Notices of the Royal Astronomical Society*, 452(3):2247–2257, sep 2015. ISSN 0035-8711. doi: 10.1093/mnras/stv1456.

R E Smith, J A Peacock, A Jenkins, S D M White, C S Frenk, F R Pearce, P A Thomas, G Efstathiou, and H M P Couchman. Stable clustering, the halo model and non-linear cosmological power spectra. *Monthly Notices of the Royal Astronomical Society*, 341(4):1311–1332, jun 2003. ISSN 0035-8711. doi: 10.1046/j.1365-8711.2003.06503.x.

Ryuichi Takahashi, Masanori Sato, Takahiro Nishimichi, Atsushi Taruya, and Masamune Oguri. REVISING THE HALOFIT MODEL FOR THE NONLINEAR

MATTER POWER SPECTRUM. *The Astrophysical Journal*, 761(2):152, dec 2012. ISSN 0004-637X. doi: 10.1088/0004-637X/761/2/152.

Robert E. Smith and Raul E. Angulo. Precision modelling of the matter power spectrum in a Planck-like Universe. *MNRAS*, 486(1):1448–1479, June 2019. doi: 10.1093/mnras/stz890.

Volker Springel, Simon D M White, Giuseppe Tormen, and Guinevere Kauffmann. Populating a cluster of galaxies - I. Results at \fontshape{it}{z}=0. *Monthly Notices of the Royal Astronomical Society*, 328(3):726–750, dec 2001. ISSN 00358711. doi: 10.1046/j.1365-8711.2001.04912.x.

K Dolag, S Borgani, G Murante, and V Springel. Substructures in hydrodynamical cluster simulations. *Mon. Not. R. Astron. Soc*, 399:497–514, 2009. doi: 10.1111/j.1365-2966.2009.15034.x.

M. Davis, G. Efstathiou, C. S. Frenk, and S. D. M. White. The evolution of large-scale structure in a universe dominated by cold dark matter. *ApJ*, 292:371–394, May 1985. doi: 10.1086/163168.

Shea Garrison-Kimmel, Shunsaku Horiuchi, Kevork N Abazajian, James S Bullock, and Manoj Kaplinghat. Running with BICEP2: implications for small-scale problems in CDM. *Monthly Notices of the Royal Astronomical Society*, 444(1):961–970, oct 2014. ISSN 0035-8711. doi: 10.1093/MNRAS/stu1479.

Marc Davis and P J E Peebles. A survey of galaxy redshifts. V - The two-point position and velocity correlations. *The Astrophysical Journal*, 267:465, apr 1983. ISSN 0004-637X. doi: 10.1086/160884.

Vincent Desjacques, Donghui Jeong, and Fabian Schmidt. Large-scale galaxy bias. *Physics Reports*, 733:1–193, feb 2018. ISSN 03701573. doi: 10.1016/j.physrep.2017.12.002.

C Fedeli, F Finelli, and L Moscardini. Primordial density perturbations with running spectral index: impact on non-linear cosmic structures. *Monthly Notices of the Royal*

Astronomical Society, 407(3):1842–1858, sep 2010. ISSN 00358711. doi: 10.1111/j.1365-2966.2010.17026.x.

Hillary L. Child, Salman Habib, Katrin Heitmann, Nicholas Frontiere, Hal Finkel, Adrian Pope, and Vitali Morozov. Halo Profiles and the Concentration–Mass Relation for a ΛCDM Universe. *ApJ*, 859(1):55, may 2018. ISSN 1538-4357. doi: 10.3847/1538-4357/aabf95.

D. H. Zhao, Y. P. Jing, H. J. Mo, and G. Brner. Mass and Redshift Dependence of Dark Halo Structure. *The Astrophysical Journal*, 597(1):L9–L12, nov 2003. ISSN 0004-637X. doi: 10.1086/379734.

Camila A Correa, J. Stuart B. Wyithe, Joop Schaye, and Alan R Duffy. The accretion history of dark matter haloes – III. A physical model for the concentration–mass relation. *Monthly Notices of the Royal Astronomical Society*, 452(2):1217–1232, sep 2015a. ISSN 0035-8711. doi: 10.1093/MNRAS/stv1363.

Aaron D Ludlow, Sownak Bose, Raúl E Angulo, Lan Wang, Wojciech A Hellwing, Julio F Navarro, Shaun Cole, and Carlos S Frenk. The mass–concentration–redshift relation of cold and warm dark matter haloes. *Monthly Notices of the Royal Astronomical Society*, 460(2):1214–1232, aug 2016. ISSN 0035-8711. doi: 10.1093/MNRAS/stw1046.

Giuseppe Tormen, F. R. Bouchet, and S. D. M. White. The structure and dynamical evolution of dark matter haloes. *Monthly Notices of the Royal Astronomical Society*, 286(4):865–884, apr 1997. ISSN 0035-8711. doi: 10.1093/MNRAS/286.4.865.

A. V. Macciò, Aaron A Dutton, Frank C Van Den Bosch, Ben Moore, Doug Potter, and Joachim Stadel. Concentration, spin and shape of dark matter haloes: scatter and the dependence on mass and environment. *Monthly Notices of the Royal Astronomical Society*, 378(1):55–71, jun 2007. ISSN 0035-8711. doi: 10.1111/j.1365-2966.2007.11720.x.

Emilio Romano-Díaz, Yehuda Hoffman, Clayton Heller, Andreas Faltenbacher, Daniel Jones, and Isaac Shlosman. Evolution of Characteristic Quantities for Dark Matter

Halo Density Profiles. *The Astrophysical Journal*, 657(1):56–70, mar 2007. ISSN 0004-637X. doi: 10.1086/509798.

Angelo F. Neto, Liang Gao, Philip Bett, Shaun Cole, Julio F. Navarro, Carlos S. Frenk, Simon D.M. M. White, Volker Springel, and Adrian Jenkins. The statistics of ΛCDM halo concentrations. *MNRAS*, 381(4):1450–1462, nov 2007. doi: 10.1111/j.1365-2966.2007.12381.x.

Alan R Duffy, Joop Schaye, Scott T Kay, and Claudio Dalla Vecchia. Dark matter halo concentrations in the Wilkinson Microwave Anisotropy Probe year 5 cosmology. *MNRAS*, 390(1):L64–L68, oct 2008. doi: 10.1111/j.1745-3933.2008.00537.x.

C Power, Julio F Navarro, A. Jenkins, Carlos S Frenk, Simon D M White, Volker Springel, Joachim Stadel, and T Quinn. The inner structure of CDM haloes – I. A numerical convergence study. *Monthly Notices of the Royal Astronomical Society*, 338(1):14–34, jan 2003. ISSN 0035-8711. doi: 10.1046/j.1365-8711.2003.05925.x.

Benedikt Diemer and Andrey V. Kravtsov. A universal model for halo concentrations. *Astrophysical Journal*, 799(1), 2015. ISSN 15384357. doi: 10.1088/0004-637X/799/1/108.

Anatoly Klypin, Andrey V. Kravtsov, James Bullock, and Joel Primack. Resolving the Structure of Cold Dark Matter Halos II. *The Astrophysical Journal*, 20, 2000. doi: 10.1086/321400.

Aaron D Ludlow, Joop Schaye, and Richard Bower. Numerical convergence of simulations of galaxy formation: the abundance and internal structure of cold dark matter haloes. *Monthly Notices of the Royal Astronomical Society*, jul 2019. ISSN 0035-8711. doi: 10.1093/mnras/stz1821.

William S. Cleveland. Robust locally weighted regression and smoothing scatterplots. *Journal of the American Statistical Association*, 74(368):829–836, 1979. doi: 10.1080/01621459.1979.10481038.

J S Bullock, T S Kolatt, Y Sigad, R S Somerville, A V Kravtsov, A A Klypin, J R Primack, and A Dekel. Profiles of dark haloes: evolution, scatter and environ-

ment. *Monthly Notices of the Royal Astronomical Society*, 321(3):559–575, mar 2001. ISSN 0035-8711. doi: 10.1046/j.1365-8711.2001.04068.x.

Aurel Schneider and Romain Teyssier. A new method to quantify the effects of baryons on the matter power spectrum. *Journal of Cosmology and Astroparticle Physics*, 2015(12):049–049, dec 2015. ISSN 1475-7516. doi: 10.1088/1475-7516/2015/12/049.

Till Sawala, Carlos S Frenk, Robert A Crain, Adrian Jenkins, Joop Schaye, Tom Theuns, and Jesus Zavala. The abundance of (not just) dark matter haloes. *MNRAS*, 431 (2):1366–1382, may 2013. ISSN 1365-2966. doi: 10.1093/mnras/stt259.

Weiguang Cui, Stefano Borgani, and Giuseppe Murante. The effect of active galactic nuclei feedback on the halo mass function. *Monthly Notices of the Royal Astronomical Society*, 441:1769–1782, 2014. doi: 10.1093/MNRAS/stu673.

Sam J Cusworth, Scott T Kay, Richard A Battye, and Peter A Thomas. Impact of baryons on the cluster mass function and cosmological parameter determination. *Monthly Notices of the Royal Astronomical Society*, 439:2485–2493, 2014. doi: 10.1093/MNRAS/stu105.

Matthieu Schaller, Carlos S Frenk, Richard G Bower, Tom Theuns, Adrian Jenkins, Joop Schaye, Robert A Crain, Michelle Furlong, Claudio Dalla Vecchia, and I G Mccarthy. Baryon effects on the internal structure of CDM haloes in the EAGLE simulations. *Monthly Notices of the Royal Astronomical Society*, 451:1247–1267, 2015. doi: 10.1093/MNRAS/stv1067.

Jonathan J Davies, Robert A Crain, Ian G McCarthy, Benjamin D Oppenheimer, Joop Schaye, Matthieu Schaller, and Stuart McAlpine. The gas fractions of dark matter haloes hosting simulated L * galaxies are governed by the feedback history of their black holes. *Monthly Notices of the Royal Astronomical Society*, 485:3783–3793, mar 2019. ISSN 0035-8711. doi: 10.1093/mnras/stz635.

Jeremy Tinker, Andrey V Kravtsov, Anatoly Klypin, Kevork Abazajian, Michael Warren, Gustavo Yepes, Stefan Gottlöber, and Daniel E Holz. Toward a Halo Mass

Function for Precision Cosmology: The Limits of Universality. *The Astrophysical Journal*, 688(2):709–728, dec 2008. ISSN 0004-637X. doi: 10.1086/591439.

Sam G. Stafford, Shaun T. Brown, Ian G. McCarthy, Andreea S. Font, Andrew Robertson, and Robert Poole-McKenzie. Exploring extensions to the standard cosmological model and the impact of baryons on small scales. *MNRAS*, 497(3):3809–3829, August 2020b. doi: 10.1093/mnras/staa2059.

Ben Moore. Evidence against dissipation-less dark matter from observations of galaxy haloes. *Nature*, 370(6491):629–631, 1994. ISSN 00280836. doi: 10.1038/370629a0.

David N. Spergel and Paul J. Steinhardt. Observational Evidence for Self-Interacting Cold Dark Matter. *PRL*, 84(17):3760–3763, apr 2000. ISSN 0031-9007. doi: 10.1103/PhysRevLett.84.3760.

Naoki Yoshida, Volker Springel, Simon D M White, and Giuseppe Tormen. Weakly Self-interacting Dark Matter and the Structure of Dark Halos. *ApJ*, 544(2):L87–L90, dec 2000. ISSN 0004637X. doi: 10.1086/317306.

Romeel Davé, David N. Spergel, Paul J. Steinhardt, and Benjamin D. Wandelt. Halo Properties in Cosmological Simulations of Self-interacting Cold Dark Matter. *ApJ*, 547(2):574–589, feb 2001. ISSN 0004-637X. doi: 10.1086/318417.

Pedro Colin, Vladimir Avila-Reese, Octavio Valenzuela, and Claudio Firmani. Structure and Subhalo Population of Halos in a Self-interacting Dark Matter Cosmology. *ApJ*, 581(2):777–793, dec 2002. ISSN 0004-637X. doi: 10.1086/344259.

Mark Vogelsberger, Jesus Zavala, and Abraham Loeb. Subhaloes in self-interacting galactic dark matter haloes. *MNRAS*, 423:3740–3752, 2012. doi: 10.1111/j.1365-2966.2012.21182.x.

Miguel Rocha, Annika H. G. Peter, James S. Bullock, Manoj Kaplinghat, Shea Garrison-Kimmel, Jose Oñorbe, and Leonidas A. Moustakas. Cosmological simulations with self-interacting dark matter - I. Constant-density cores and substructure. *MNRAS*, 430(1):81–104, March 2013. doi: 10.1093/mnras/sts514.

Oliver D Elbert, James S Bullock, Shea Garrison-Kimmel, Miguel Rocha, Jose Oñorbe, and Annika H G Peter. Core formation in dwarf haloes with self-interacting dark matter: no fine-tuning necessary. *MNRAS*, 453:29–37, 2015. doi: 10.1093/mnras/stv1470.

Manoj Kaplinghat, Sean Tulin, and Hai-Bo Yu. Dark Matter Halos as Particle Colliders: Unified Solution to Small-Scale Structure Puzzles from Dwarfs to Clusters. *PRL*, 116(4):041302, jan 2016. ISSN 0031-9007. doi: 10.1103/PhysRevLett.116.041302.

Jesús Zavala, Mark Vogelsberger, and Matthew G Walker. Constraining self-interacting dark matter with the Milky Way's dwarf spheroidals. *MNRAS*, 431:20–24, 2013. doi: 10.1093/mnrasl/sls053.

Ayuki Kamada, Manoj Kaplinghat, Andrew B. Pace, and Hai-Bo Yu. Self-Interacting Dark Matter Can Explain Diverse Galactic Rotation Curves. *PRL*, 119(11):111102, sep 2017. ISSN 0031-9007. doi: 10.1103/PhysRevLett.119.111102.

Peter Creasey, Omid Sameie, Laura V Sales, Hai-Bo Yu, Mark Vogelsberger, and Jesús Zavala. Spreading out and staying sharp-creating diverse rotation curves via baryonic and self-interaction effects. *MNRAS*, 468:2283–2295, 2017. doi: 10.1093/mnras/stx522.

Heinz Pagels and Joel R. Primack. Supersymmetry, Cosmology, and New Physics at Teraelectronvolt Energies. *PRL*, 48(4):223–226, jan 1982. ISSN 0031-9007. doi: 10.1103/PhysRevLett.48.223.

Scott Dodelson and Lawrence M Widrow. Sterile neutrinos as dark matter. *PRL*, 72 (1):17–20, jan 1994. ISSN 0031-9007. doi: 10.1103/PhysRevLett.72.17.

Craig J Hogan and Julianne J Dalcanton. New dark matter physics: Clues from halo structure. *PRD*, 62(6):063511, aug 2000. ISSN 0556-2821. doi: 10.1103/PhysRevD.62.063511.

Matteo Viel, Julien Lesgourgues, Martin G Haehnelt, Sabino Matarrese, and Antonio Riotto. Constraining warm dark matter candidates including sterile neutrinos and

light gravitinos with WMAP and the Lyman-α forest. *PRD*, 71(6):063534, mar 2005. ISSN 1550-7998. doi: 10.1103/PhysRevD.71.063534.

Kevork Abazajian. Production and evolution of perturbations of sterile neutrino dark matter. *PRD*, 73(6), 2006. ISSN 15507998. doi: 10.1103/PhysRevD.73.063506.

Pedro Colín, Vladimir Avila-Reese, and Octavio Valenzuela. Substructure and Halo Density Profiles in a Warm Dark Matter Cosmology. *ApJ*, 542(2):622–630, oct 2000. ISSN 0004-637X. doi: 10.1086/317057.

Paul Bode, Jeremiah P Ostriker, and Neil Turok. Halo Formation in Warm Dark Matter Models. *ApJ*, 556(1):93–107, jul 2001. ISSN 0004-637X. doi: 10.1086/321541.

Emil Polisensky and Massimo Ricotti. Constraints on the dark matter particle mass from the number of Milky Way satellites. *PRD*, 83(4), 2011. ISSN 15507998. doi: 10.1103/PhysRevD.83.043506.

Mark R. Lovell, Vincent Eke, Carlos S. Frenk, Liang Gao, Adrian Jenkins, Tom Theuns, Jie Wang, Simon D.M. M. White, Alexey Boyarsky, and Oleg Ruchayskiy. The haloes of bright satellite galaxies in a warm dark matter universe. *MNRAS*, 420(3): 2318–2324, mar 2012. ISSN 00358711. doi: 10.1111/j.1365-2966.2011.20200.x.

Donnino Anderhalden, Aurel Schneider, Andrea V. Macciò, Juerg Diemand, and Gianfranco Bertone. Hints on the nature of dark matter from the properties of Milky Way satellites. *JCAP*, 2013(3):014–014, mar 2013. ISSN 14757516. doi: 10.1088/1475-7516/2013/03/014.

Brandon Bozek, Michael Boylan-Kolchin, Shunsaku Horiuchi, Shea Garrison-Kimme, Kevork Abazajian, and James S. Bulloc. Resonant sterile neutrino dark matter in the local and high-z Universe. *MNRAS*, 459(2):1489–1504, 2016. ISSN 13652966. doi: 10.1093/mnras/stw688.

Shunsaku Horiuchi, Brandon Bozek, Kevork N Abazajian, Michael Boylan-Kolchin, James S Bullock, Shea Garrison-Kimmel, and Jose Oñorbe. Properties of resonantly produced sterile neutrino dark matter subhaloes. *MNRAS*, 456(4):4346–4353, 2016. ISSN 13652966. doi: 10.1093/mnras/stv2922.

Sownak Bose, Wojciech A. Hellwing, Carlos S. Frenk, Adrian Jenkins, Mark R. Lovell, John C. Helly, Baojiu Li, Violeta Gonzalez-Perez, and Liang Gao. Substructure and galaxy formation in the Copernicus Complexio warm dark matter simulations. *MNRAS*, 464(4):4520–4533, feb 2017. ISSN 0035-8711. doi: 10.1093/mnras/stw2686.

Mark R Lovell, Violeta Gonzalez-Perez, Sownak Bose, Alexey Boyarsky, Shaun Cole, Carlos S Frenk, and Oleg Ruchayskiy. Addressing the too big to fail problem with baryon physics and sterile neutrino dark matter. *MNRAS*, 468(3):2836–2849, 2017a. ISSN 0035-8711. doi: 10.1093/mnras/stx621.

Francisco Villaescusa-Navarro and Neal Dalal. Cores and cusps in warm dark matter halos. *JCAP*, 2011(3):24, 2011. ISSN 14757516. doi: 10.1088/1475-7516/2011/03/024.

Andrea V. Macciò, Sinziana Paduroiu, Donnino Anderhalden, Aurel Schneider, and Ben Moore. Cores in warm dark matter haloes: a Catch 22 problem. *MNRAS*, 424 (2):1105–1112, August 2012. doi: 10.1111/j.1365-2966.2012.21284.x.

Shi Shao, Liang Gao, Tom Theuns, and Carlos S Frenk. The phase-space density of fermionic dark matter haloes. *MNRAS*, 430(3):2346–2357, 2013. ISSN 00358711. doi: 10.1093/mnras/stt053.

Juan Garcia-Bellido and Diederik Roest. Large- N running of the spectral index of inflation. *PRD*, 89(10), 2014. ISSN 15502368. doi: 10.1103/PhysRevD.89.103527.

Nathalie Palanque-Delabrouille, Christophe Yèche, Nils Schöneberg, Julien Lesgourgues, Michael Walther, Solène Chabanier, and Eric Armengaud. Hints, neutrino bounds and wdm constraints from sdss dr14 lyman-α and planck full-survey data, 2019.

Andrew Pontzen and Fabio Governato. How supernova feedback turns dark matter cusps into cores. *MNRAS*, 421(4):3464–3471, 2012. ISSN 00358711. doi: 10.1111/j.1365-2966.2012.20571.x.

A. V. Macciò, G Stinson, C B Brook, J Wadsley, H. M.P. Couchman, S Shen, B K Gibson, and T Quinn. Halo expansion in cosmological hydro simulations: Toward a baryonic solution of the cusp/core problem in massive spirals. *ApJL*, 744(1):9, 2012. ISSN 20418205. doi: 10.1088/2041-8205/744/1/L9.

Piero Madau, Sijing Shen, and Fabio Governato. Dark matter heating and early core formation in dwarf galaxies. *ApJL*, 789(1):17, 2014. ISSN 20418213. doi: 10.1088/2041-8205/789/1/L17.

J I Read, O Agertz, and M. L.M. Collins. Dark matter cores all the way down. *MNRAS*, 459(3):2573–2590, 2016. ISSN 13652966. doi: 10.1093/mnras/stw713.

Edouard Tollet, Andrea V. Macciò, Aaron A Dutton, Greg S Stinson, Liang Wang, Camilla Penzo, Thales A Gutcke, Tobias Buck, Xi Kang, Chris Brook, Arianna Di Cintio, Ben W. Keller, and James Wadsley. NIHAO - IV: Core creation and destruction in dark matter density profiles across cosmic time. *MNRAS*, 456(4):3542–3552, 2016. ISSN 13652966. doi: 10.1093/mnras/stv2856.

Andrew R. Wetzel, Philip F. Hopkins, Ji-hoon Kim, Claude-André Faucher-Giguère, Dušan Kereš, and Eliot Quataert. Reconciling Dwarf Galaxies with ΛCDM Cosmology: Simulating a Realistic Population of Satellites around a Milky Way-mass Galaxy. *ApJl*, 827(2):L23, August 2016. doi: 10.3847/2041-8205/827/2/L23.

Alex Fitts, Michael Boylan-Kolchin, Oliver D Elbert, James S Bullock, Philip F Hopkins, Jose Oñorbe, Andrew Wetzel, Coral Wheeler, Claude André Faucher-Giguère, Dušan Kereš, Evan D Skillman, and Daniel R Weisz. FIRE in the field: Simulating the threshold of galaxy formation. *MNRAS*, 471(3):3547–3562, 2017. ISSN 13652966. doi: 10.1093/mnras/stx1757.

Rachel S Somerville. Can Photoionization Squelching Resolve the Substructure Crisis? *ApJ*, 572(1):L23–L26, 2002. ISSN 0004637X. doi: 10.1086/341444.

Elena D'Onghia, Volker Springel, Lars Hernquist, and Dusan Keres. Substructure depletion in the milky way halo by the disk. *ApJ*, 709(2):1138–1147, 2010. ISSN 15384357. doi: 10.1088/0004-637X/709/2/1138.

Shea Garrison-Kimmel, Andrew Wetzel, James S Bullock, Philip F Hopkins, Michael Boylan-Kolchin, Claude André Faucher-Giguère, Dušan Kereš, Eliot Quataert, Robyn E Sanderson, Andrew S Graus, and Tyler Kelley. Not so lumpy after all: Modelling the depletion of dark matter subhaloes by Milky Way-like galaxies. *MNRAS*, 471(2):1709–1727, 2017. ISSN 13652966. doi: 10.1093/MNRAS/STX1710.

Till Sawala, Pauli Pihajoki, Peter H Johansson, Carlos S Frenk, Julio F Navarro, Kyle A Oman, and Simon D.M. White. Shaken and stirred: The Milky Way's dark substructures. *MNRAS*, 467(4):4383–4400, 2017. ISSN 13652966. doi: 10.1093/mnras/stx360.

Adi Zolotov, Alyson M Brooks, Beth Willman, Fabio Governato, Andrew Pontzen, Charlotte Christensen, Avishai Dekel, Tom Quinn, Sijing Shen, and James Wadsley. Baryons matter: Why luminous satellite galaxies have reduced central masses. *ApJ*, 761(1):71, 2012. ISSN 15384357. doi: 10.1088/0004-637X/761/1/71.

Kenza S Arraki, Anatoly Klypin, Surhud More, and Sebastian Trujillo-Gomez. Effects of baryon removal on the structure of dwarf spheroidal galaxies. *MNRAS*, 438(2): 1466–1482, 2014. ISSN 00358711. doi: 10.1093/mnras/stt2279.

T K Chan, D Kereš, J Oñorbe, P F Hopkins, A L Muratov, C. A. Faucher-Giguère, and E Quataert. The impact of baryonic physics on the structure of dark matter haloes: The view from the FIRE cosmological simulations. *MNRAS*, 454(3):2981–3001, 2015. ISSN 13652966. doi: 10.1093/mnras/stv2165.

Mihai Tomozeiu, Lucio Mayer, and Thomas Quinn. TIDAL STIRRING OF SATELLITES WITH SHALLOW DENSITY PROFILES PREVENTS THEM FROM BEING TOO BIG TO FAIL. *ApJ*, 827(1):L15, 2016. ISSN 2041-8213. doi: 10.3847/2041-8205/827/1/l15.

Aaron A Dutton, Andrea V. Macciò, Jonas Frings, Liang Wang, Gregory S Stinson, Camilla Penzo, and Xi Kang. NIHAO V: Too big does not fail-reconciling the conflict between ΛCDM predictions and the circular velocities of nearby field galaxies. *MNRAS*, 457(1):L74–L78, 2016. ISSN 17453933. doi: 10.1093/mnrasl/slv193.

Alyson M Brooks, Emmanouil Papastergis, Charlotte R Christensen, Fabio Governato, Adrienne Stilp, Thomas R Quinn, and James Wadsley. How to Reconcile the Observed Velocity Function of Galaxies with Theory. *ApJ*, 850(1):97, 2017. ISSN 1538-4357. doi: 10.3847/1538-4357/aa9576.

J Lesgourgues and S Pastor. Massive neutrinos and cosmology. *Physics Reports*, 429 (6):307–379, jul 2006. ISSN 03701573. doi: 10.1016/j.physrep.2006.04.001.

J. R. Bond and A. S. Szalay. The collisionless damping of density fluctuations in an expanding universe. *ApJ*, 274:443, nov 1983. ISSN 0004-637X. doi: 10.1086/161460.

J. M. Bardeen, J. R. Bond, N. Kaiser, and A. S. Szalay. The statistics of peaks of Gaussian random fields. *ApJ*, 304:15, may 1986. ISSN 0004-637X. doi: 10.1086/164143.

Matteo Leo, Carlton M. Baugh, Baojiu Li, and Silvia Pascoli. The effect of thermal velocities on structure formation in N-body simulations of warm dark matter. *JCAP*, 2017(11):017, Nov 2017. doi: 10.1088/1475-7516/2017/11/017.

Matteo Viel, George D. Becker, James S. Bolton, and Martin G. Haehnelt. Warm dark matter as a solution to the small scale crisis: New constraints from high redshift Lyman-α forest data. *PRD*, 88(4):1–20, aug 2013. ISSN 15507998. doi: 10.1103/PhysRevD.88.043502.

Vid Iršič, Matteo Viel, Martin G. Haehnelt, James S. Bolton, Stefano Cristiani, George D. Becker, Valentina D'Odorico, Guido Cupani, Tae Sun Kim, Trystyn A.M. Berg, Sebastian López, Sara Ellison, Lise Christensen, Kelly D. Denney, and Gábor Worseck. New constraints on the free-streaming of warm dark matter from intermediate and small scale Lyman- α forest data. *PRD*, 96(2):023522, jul 2017. ISSN 24700029. doi: 10.1103/PhysRevD.96.023522.

Mark R Lovell, Carlos S Frenk, Vincent R Eke, Adrian Jenkins, Liang Gao, and Tom Theuns. The properties of warm dark matter haloes. *MNRAS*, 439(1):300–317, mar 2014. ISSN 1365-2966. doi: 10.1093/mnras/stt2431.

Rachel Kennedy, Carlos Frenk, Shaun Cole, and Andrew Benson. Constraining the warm dark matter particle mass with Milky Way satellites. *MNRAS*, 442(3):2487–2495, aug 2014. ISSN 1365-2966. doi: 10.1093/mnras/stu719.

P Jethwa, D. Erkal, and V Belokurov. The upper bound on the lowest mass halo. *MNRAS*, 473(2):2060–2083, 2018. doi: 10.1093/mnras/stx2330.

Ethan O Nadler, Vera Gluscevic, Kimberly K Boddy, and Risa H Wechsler. Constraints on Dark Matter Microphysics from the Milky Way Satellite Population. *ApJ*, 878 (2):L32, 2019. ISSN 2041-8213. doi: 10.3847/2041-8213/ab1eb2.

E. O. Nadler, R. H. Wechsler, K. Bechtol, Y. Y. Mao, G. Green, A. Drlica-Wagner, M. McNanna, S. Mau, A. B. Pace, J. D. Simon, A. Kravtsov, S. Dodelson, T. S. Li, A. H. Riley, M. Y. Wang, T. M. C. Abbott, M. Aguena, S. Allam, J. Annis, S. Avila, G. M. Bernstein, E. Bertin, D. Brooks, D. L. Burke, A. Carnero Rosell, M. Carrasco Kind, J. Carretero, M. Costanzi, L. N. da Costa, J. De Vicente, S. Desai, A. E. Evrard, B. Flaugher, P. Fosalba, J. Frieman, J. García-Bellido, E. Gaztanaga, D. W. Gerdes, D. Gruen, J. Gschwend, G. Gutierrez, W. G. Hartley, S. R. Hinton, K. Honscheid, E. Krause, K. Kuehn, N. Kuropatkin, O. Lahav, M. A. G. Maia, J. L. Marshall, F. Menanteau, R. Miquel, A. Palmese, F. Paz-Chinchón, A. A. Plazas, A. K. Romer, E. Sanchez, B. Santiago, V. Scarpine, S. Serrano, M. Smith, M. Soares-Santos, E. Suchyta, G. Tarle, D. Thomas, T. N. Varga, A. R. Walker, and DES Collaboration. Milky Way Satellite Census. II. Galaxy-Halo Connection Constraints Including the Impact of the Large Magellanic Cloud. *ApJ*, 893(1):48, April 2020a. doi: 10.3847/1538-4357/ab846a.

A. Garzilli, O. Ruchayskiy, A. Magalich, and A. Boyarsky. How warm is too warm? Towards robust Lyman-α forest bounds on warm dark matter. *arXiv e-prints*, art. arXiv:1912.09397, December 2019.

J-W Hsueh, W Enzi, S Vegetti, M W Auger, C D Fassnacht, G Despali, L V E Koopmans, and J P McKean. SHARP – VII. New constraints on the dark matter free-streaming properties and substructure abundance from gravitationally lensed

quasars. *MNRAS*, 3059:3047–3059, nov 2019. ISSN 0035-8711. doi: 10.1093/mnras/stz3177.

Jie Wang and Simon D.M. White. Discreteness effects in simulations of hot/warm dark matter. *MNRAS*, 380(1):93–103, 2007. ISSN 00358711. doi: 10.1111/j.1365-2966.2007.12053.x.

Andrew Robertson, David Harvey, Richard Massey, Vincent Eke, Ian G McCarthy, Mathilde Jauzac, Baojiu Li, and Joop Schaye. Observable tests of self-interacting dark matter in galaxy clusters: cosmological simulations with SIDM and baryons. *MNRAS*, 488(3):3646–3662, sep 2019. ISSN 0035-8711. doi: 10.1093/mnras/stz1815.

Andrew Robertson, Richard Massey, and Vincent Eke. What does the Bullet Cluster tell us about self-interacting dark matter? *MNRAS*, 465(1):569–587, feb 2017a. ISSN 0035-8711. doi: 10.1093/mnras/stw2670.

Andrew Robertson, Richard Massey, and Vincent Eke. Cosmic particle colliders: simulations of self-interacting dark matter with anisotropic scattering. *MNRAS*, 467(4):4719–4730, jun 2017b. ISSN 0035-8711. doi: 10.1093/mnras/stx463.

Massimo Meneghetti, Naoki Yoshida, Matthias Bartelmann, Lauro Moscardini, Volker Springel, Giuseppe Tormen, and Simon D.M. White. Giant cluster arcs as a constraint on the scattering cross-section of dark matter. *MNRAS*, 325(1):435–442, 2001. ISSN 00358711. doi: 10.1046/j.1365-8711.2001.04477.x.

Scott W Randall, Maxim Markevitch, Douglas Clowe, Anthony H Gonzalez, and Marusa Bradač. Constraints on the Self-Interaction Cross Section of Dark Matter from Numerical Simulations of the Merging Galaxy Cluster 1E 0657-56. *ApJ*, 679(2):1173–1180, jun 2008. ISSN 0004-637X. doi: 10.1086/587859.

Felix Kahlhoefer, Kai Schmidt-Hoberg, Janis Kummer, and Subir Sarkar. On the interpretation of dark matter self-interactions in Abell 3827. *MNRAS*, 452(1):L54–L58, 2015. ISSN 17453933. doi: 10.1093/mnrasl/slv088.

David Harvey, Richard Massey, Thomas Kitching, Andy Taylor, and Eric Tittley. The nongravitational interactions of dark matter in colliding galaxy clusters. *Science*, 347(6229):1462–1465, mar 2015. ISSN 10959203. doi: 10.1126/science.1261381.

Stacy Y Kim, Annika H.G. Peter, and David Wittman. In the wake of dark giants: New signatures of dark matter self-interactions in equal-mass mergers of galaxy clusters. *MNRAS*, 469(2):1414–1444, 2017. ISSN 13652966. doi: 10.1093/MNRAS/STX896.

David Wittman, Nathan Golovich, and William A Dawson. The Mismeasure of Mergers: Revised Limits on Self-interacting Dark Matter in Merging Galaxy Clusters. *ApJ*, 869(2):104, 2018. ISSN 1538-4357. doi: 10.3847/1538-4357/aaee77.

Jordi Miralda-Escude. A Test of the Collisional Dark Matter Hypothesis from Cluster Lensing. *ApJ*, 564(1):60–64, 2002a. ISSN 0004-637X. doi: 10.1086/324138.

Annika H G Peter, Miguel Rocha, James S Bullock, and Manoj Kaplinghat. Cosmological simulations with self-interacting dark matter – II. Halo shapes versus observations. *MNRAS*, 430(1):105–120, mar 2013. ISSN 1365-2966. doi: 10.1093/mnras/sts535.

Oleg Y Gnedin and Jeremiah P Ostriker. Limits on Collisional Dark Matter from Elliptical Galaxies in Clusters. *ApJ*, 561(1):61–68, nov 2001. ISSN 0004-637X. doi: 10.1086/323211.

S. McAlpine, J. C. Helly, M. Schaller, J. W. Trayford, Y. Qu, M. Furlong, R. G. Bower, R. A. Crain, J. Schaye, T. Theuns, C. Dalla Vecchia, C. S. Frenk, I. G. McCarthy, A. Jenkins, Y. Rosas-Guevara, S. D. M. White, M. Baes, P. Camps, and G. Lemson. The EAGLE simulations of galaxy formation: Public release of halo and galaxy catalogues. *Astronomy and Computing*, 15:72–89, April 2016. doi: 10.1016/j.ascom.2016.02.004.

. Planck Collaboration XVI. Planck 2013 results. XVI. Cosmological parameters. *A&A*, 571, 2014. ISSN 14320746. doi: 10.1051/0004-6361/201321591.

Robert P.C. Wiersma, Joop Schaye, Tom Theuns, Claudio Dalla Vecchia, and Luca Tornatore. Chemical enrichment in cosmological, smoothed particle hydrodynamics simulations. *MNRAS*, 399(2):574–600, oct 2009c. ISSN 00358711. doi: 10.1111/j.1365-2966.2009.15331.x.

Y M Rosas-Guevara, R G Bower, J Schaye, M Furlong, C S Frenk, C M Booth, R A Crain, C Dalla Vecchia, M Schaller, and T Theuns. The impact of angular momentum on black hole accretion rates in simulations of galaxy formation. *MNRAS*, 454 (1):1–22, 2015. ISSN 13652966. doi: 10.1093/mnras/stv2056.

Claudio Dalla Vecchia and Joop Schaye. Simulating galactic outflows with thermal supernova feedback. *MNRAS*, 426(1):140–158, 2012. ISSN 00358711. doi: 10.1111/j.1365-2966.2012.21704.x.

Edmund Bertschinger. Multiscale Gaussian Random Fields and Their Application to Cosmological Simulations. *ApJSupp. Ser.*, 137(1):1–20, 2001. doi: 10.1086/322526.

Oliver Hahn and Tom Abel. Multi-scale initial conditions for cosmological simulations. *MNRAS*, 415(3):2101–2121, aug 2011. ISSN 00358711. doi: 10.1111/j.1365-2966.2011.18820.x.

Jurg Diemand, Michael Kuhlen, and Piero Madau. Formation and Evolution of Galaxy Dark Matter Halos and Their Substructure. *ApJ*, 667(2):859–877, 2007. doi: 10.1086/520573.

V Springel, J Wang, M Vogelsberger, A Ludlow, A Jenkins, A Helmi, J F Navarro, C S Frenk, and S. D.M. White. The Aquarius Project: The subhaloes of galactic haloes. *MNRAS*, 391(4):1685–1711, 2008. doi: 10.1111/j.1365-2966.2008.14066.x.

Robert E. Smith and Katarina Markovic. Testing the warm dark matter paradigm with large-scale structures. *PRD*, 84(6):1–18, 2011. doi: 10.1103/PhysRevD.84.063507.

Raul E Angulo, Oliver Hahn, and Tom Abel. The warm dark matter halo mass function below the cut-off scale. *MNRAS*, 434(4):3337–3347, 2013. ISSN 00358711. doi: 10.1093/mnras/stt1246.

Sownak Bose, Wojciech A. Hellwing, Carlos S. Frenk, Adrian Jenkins, Mark R. Lovell, John C. Helly, and Baojiu Li. The Copernicus Complexio: statistical properties of warm dark matter haloes. *MNRAS*, 455(1):318–333, jan 2016. ISSN 0035-8711. doi: 10.1093/mnras/stv2294.

Riccardo Giovanelli, Martha P Haynes, Brian R Kent, Philip Perillat, Amelie Saintonge, Noah Brosch, Barbara Catinella, G Lyle Hoffman, Sabrina Stierwalt, Kristine Spekkens, Mikael S Lerner, Karen L Masters, Emmanuel Momjian, Jessica L Rosenberg, Christopher M Springob, Alessandro Boselli, Vassilis Charmandaris, Jeremy K Darling, Jonathan Davies, Diego Garcia Lambas, Giuseppe Gavazzi, Carlo Giovanardi, Eduardo Hardy, Leslie K Hunt, Angela Iovino, Igor D Karachentsev, Valentina E Karachentseva, Rebecca A Koopmann, Christian Marinoni, Robert Minchin, Erik Muller, Mary Putman, Carmen Pantoja, John J Salzer, Marco Scodeggio, Evan Skillman, Jose M Solanes, Carlos Valotto, Wim van Driel, and Liese van Zee. The Arecibo Legacy Fast ALFA Survey. I. Science Goals, Survey Design, and Strategy. *AJ*, 130(6):2598–2612, 2005. doi: 10.1086/497431.

Toby Brown, Barbara Catinella, Luca Cortese, Claudia Del P Lagos, Romeel Davé, Virginia Kilborn, Martha P Haynes, Riccardo Giovanelli, and Mika Rafieferantsoa. Cold gas stripping in satellite galaxies: from pairs to clusters. *MNRAS*, 466(2): 1275–1289, 2017. doi: 10.1093/mnras/stw2991.

Martha P Haynes, Riccardo Giovanelli, Brian R Kent, Elizabeth A K Adams, Thomas J Balonek, David W Craig, Derek Fertig, Rose Finn, Carlo Giovanardi, Gregory Hallenbeck, Kelley M Hess, G Lyle Hoffman, Shan Huang, Michael G Jones, Rebecca A Koopmann, David A Kornreich, Lukas Leisman, Jeffrey Miller, Crystal Moorman, Jessica O'Connor, Aileen O'Donoghue, Emmanouil Papastergis, Parker Troischt, David Stark, and Li Xiao. The Arecibo Legacy Fast ALFA Survey: The ALFALFA Extragalactic H i Source Catalog. *ApJ*, 861(1):49, 2018. doi: 10.3847/1538-4357/aac956.

Jonathan J Davies, Robert A Crain, Benjamin D Oppenheimer, and Joop Schaye. The quenching and morphological evolution of central galaxies is facilitated by

the feedback-driven expulsion of circumgalactic gas. *MNRAS*, 491(3):4462–4480, 2020. doi: 10.1093/mnras/stz3201.

Dylan Nelson, Annalisa Pillepich, Volker Springel, Rainer Weinberger, Lars Hernquist, Rüdiger Pakmor, Shy Genel, Paul Torrey, Mark Vogelsberger, Guinevere Kauffmann, Federico Marinacci, and Jill Naiman. First results from the IllustrisTNG simulations: The galaxy colour bimodality. *MNRAS*, 475(1):624–647, 2018. ISSN 13652966. doi: 10.1093/mnras/stx3040.

Volker Springel, Rüdiger Pakmor, Annalisa Pillepich, Rainer Weinberger, Dylan Nelson, Lars Hernquist, Mark Vogelsberger, Shy Genel, Paul Torrey, Federico Marinacci, and Jill Naiman. First results from the IllustrisTNG simulations: matter and galaxy clustering. *MNRAS*, 475(1):676–698, March 2018. doi: 10.1093/mnras/stx3304.

Annalisa Pillepich, Volker Springel, Dylan Nelson, Shy Genel, Jill Naiman, Rüdiger Pakmor, Lars Hernquist, Paul Torrey, Mark Vogelsberger, Rainer Weinberger, and Federico Marinacci. Simulating galaxy formation with the IllustrisTNG model. *MNRAS*, 473(3):4077–4106, 2018a. doi: 10.1093/mnras/stx2656.

Annalisa Pillepich, Dylan Nelson, Lars Hernquist, Volker Springe, Rüdiger Pakmor, Paul Torrey, Rainer Weinberger, Shy Gene, Jill P Naiman, Federico Marinacci, and Mark Vogelsberger. First results from the illustristng simulations: The stellar mass content of groups and clusters of galaxies. *MNRAS*, 475(1):648–675, 2018b. ISSN 13652966. doi: 10.1093/mnras/stx3112.

Robert A Crain, Yannick M Bahé, Claudia Del P Lagos, Alireza Rahmati, Joop Schaye, Ian G. McCarthy, Antonino Marasco, Richard G Bower, Matthieu Schaller, Tom Theuns, and Thijs van der Hulst. The EAGLE simulations: Atomic hydrogen associated with galaxies. *MNRAS*, 464(4):4204–4226, 2017. ISSN 13652966. doi: 10.1093/mnras/stw2586.

Adam R.H. Stevens, Benedikt Diemer, Claudia Del P Lagos, Dylan Nelson, Annalisa Pillepich, Toby Brown, Barbara Catinella, Lars Hernquist, Rainer Weinberger, Mark

Vogelsberger, and Federico Marinacci. Atomic hydrogen in IllustrisTNG galaxies: The impact of environment parallelled with local 21-cm surveys. *MNRAS*, 483(4): 5334–5354, 2019. ISSN 13652966. doi: 10.1093/mnras/sty3451.

Jorge Peñarrubia, Andrew J Benson, Matthew G Walker, Gerard Gilmore, Alan W. McConnachie, and Lucio Mayer. The impact of dark matter cusps and cores on the satellite galaxy population around spiral galaxies. *MNRAS*, 406(2):1290–1305, 2010. doi: 10.1111/j.1365-2966.2010.16762.x.

Gregory A Dooley, Annika H.G. Peter, Mark Vogelsberger, Jesús Zavala, and Anna Frebel. Enhanced tidal stripping of satellites in the galactic halo from dark matter self-interactions. *MNRAS*, 461(1):710–727, 2016. doi: 10.1093/mnras/stw1309.

Peter S. Behroozi, Risa H. Wechsler, and Charlie Conroy. The Average Star Formation Histories of Galaxies in Dark Matter Halos from z = 0-8. *ApJ*, 770(1):57, June 2013. doi: 10.1088/0004-637X/770/1/57.

Mark Vogelsberger, Jesús Zavala, Katelin Schutz, and Tracy R Slatyer. Evaporating the Milky Way halo and its satellites with inelastic self-interacting dark matter. *MNRAS*, 484(4):5437–5452, apr 2019. ISSN 0035-8711. doi: 10.1093/mnras/stz340.

Alejandro Benítez-Llambay, Carlos S. Frenk, Aaron D. Ludlow, and Julio F. Navarro. Baryon-induced dark matter cores in the EAGLE simulations. *MNRAS*, 488(2): 2387–2404, September 2019. doi: 10.1093/mnras/stz1890.

Aaron A. Dutton, Charlie Conroy, Frank C. van den Bosch, Luc Simard, J. Trevor Mendel, Stéphane Courteau, Avishai Dekel, Surhud More, and Francisco Prada. Dark halo response and the stellar initial mass function in early-type and late-type galaxies. *MNRAS*, 416(1):322–345, September 2011. doi: 10.1111/j.1365-2966.2011.19038.x.

Giulia Despali, Martin Sparre, Simona Vegetti, Mark Vogelsberger, Jesús Zavala, and Federico Marinacci. The interplay of self-interacting dark matter and baryons in shaping the halo evolution. *MNRAS*, 484(4):4563–4573, apr 2019. ISSN 13652966. doi: 10.1093/mnras/stz273.

Andrew Robertson, Richard Massey, Vincent Eke, Sean Tulin, Hai-Bo Yu, Yannick Bahé, David J. Barnes, Richard G. Bower, Robert A. Crain, Claudio Dalla Vecchia, Scott T. Kay, Matthieu Schaller, and Joop Schaye. The diverse density profiles of galaxy clusters with self-interacting dark matter plus baryons. *MNRAS*, 476(1): L20–L24, May 2018. doi: 10.1093/mnrasl/sly024.

Jürg Diemand, Ben Moore, and Joachim Stadel. Convergence and scatter of cluster density profiles. *MNRAS*, 353(2):624–632, 2004. doi: 10.1111/j.1365-2966.2004.08094.x.

Julio F Navarro, Aaron Ludlow, Volker Springel, Jie Wang, Mark Vogelsberger, Simon D.M. White, Adrian Jenkins, Carlos S Frenk, and Amina Helmi. The diversity and similarity of simulated cold dark matter haloes. *MNRAS*, 402(1):21–34, 2010. doi: 10.1111/j.1365-2966.2009.15878.x.

Mark R. Lovell, Sownak Bose, Alexey Boyarsky, Robert A. Crain, Carlos S. Frenk, Wojciech A. Hellwing, Aaron D. Ludlow, Julio F. Navarro, Oleg Ruchayskiy, Till Sawala, Matthieu Schaller, Joop Schaye, and Tom Theuns. Properties of Local Group galaxies in hydrodynamical simulations of sterile neutrino dark matter cosmologies. *Monthly Notices of the Royal Astronomical Society*, 468(4):4285–4298, jul 2017b. doi: 10.1093/mnras/stx654.

Ethan O. Nadler, Arka Banerjee, Susmita Adhikari, Yao-Yuan Mao, and Risa H. Wechsler. Signatures of Velocity-Dependent Dark Matter Self-Interactions in Milky Way-mass Halos. *arXiv e-prints*, art. arXiv:2001.08754, January 2020b.

Arka Banerjee, Susmita Adhikari, Neal Dalal, Surhud More, and Andrey Kravtsov. Signatures of self-interacting dark matter on cluster density profile and subhalo distributions. *J. Cosmology Astropart. Phys.*, 2020(2):024, February 2020. doi: 10.1088/1475-7516/2020/02/024.

Jack Richings, Carlos Frenk, Adrian Jenkins, Andrew Robertson, Azadeh Fattahi, Robert J J Grand, Julio Navarro, Rüdiger Pakmor, Facundo A Gomez, Federico

Marinacci, and Kyle A Oman. Subhalo destruction in the Apostle and Auriga simulations. *MNRAS*, 492(4):5780–5793, mar 2020. doi: 10.1093/mnras/stz3448.

Jenna Samuel, Andrew Wetzel, Erik Tollerud, Shea Garrison-Kimmel, Sarah Loebman, Kareem El-Badry, Philip F Hopkins, Michael Boylan-Kolchin, Claude-André Faucher-Giguère, James S Bullock, Samantha Benincasa, and Jeremy Bailin. A profile in FIRE: resolving the radial distributions of satellite galaxies in the Local Group with simulations. *MNRAS*, 491(1):1471–1490, 2020. ISSN 0035-8711. doi: 10.1093/mnras/stz3054.

Aaron A. Dutton and Andrea V. Macciò. Cold dark matter haloes in the Planck era: Evolution of structural parameters for Einasto and NFW profiles. *MNRAS*, 441(4): 3359–3374, 2014. doi: 10.1093/mnras/stu742.

Vincent R Eke, Julio F Navarro, and Matthias Steinmetz. The Power Spectrum Dependence of Dark Matter Halo Concentrations. *The Astrophysical Journal*, 554(1): 114–125, jun 2001. ISSN 0004-637X. doi: 10.1086/321345.

Vladimir Avila-Reese, Pedro Colín, Octavio Valenzuela, Elena D'Onghia, and Claudio Firmani. Formation and Structure of Halos in a Warm Dark Matter Cosmology. *ApJ*, 559(2):516–530, oct 2001. ISSN 0004-637X. doi: 10.1086/322411.

Aurel Schneider. Structure formation with suppressed small-scale perturbations. *MNRAS*, 451(3):3117–3130, aug 2015. ISSN 1365-2966. doi: 10.1093/mnras/stv1169.

Sam G Stafford, Ian G. McCarthy, Robert A Crain, Jaime Salcido, Joop Schaye, Andreea S Font, Juliana Kwan, and Simon Pfeifer. The bahamas project: effects of a running scalar spectral index on large-scale structure. *MNRAS*, 493(1):676–697, mar 2020. doi: 10.1093/mnras/staa129.

J. Einasto. On the Construction of a Composite Model for the Galaxy and on the Determination of the System of Galactic Parameters. *Trudy Astrofizicheskogo Instituta Alma-Ata*, 5:87–100, 1965.

A Burkert. The Structure of Dark Matter Halos in Dwarf Galaxies. *ApJ*, 447(1):L25–L28, 1995. ISSN 0004637X. doi: 10.1086/309560.

Abraham. Savitzky and M. J. E. Golay. Smoothing and Differentiation of Data by Simplified Least Squares Procedures. *Analytical Chemistry*, 36(8):1627–1639, jul 1964. ISSN 0003-2700. doi: 10.1021/ac60214a047.

Vladimir Avila-Reese, Claudio Firmani, Anatoly Klypin, and Andrey V Kravtsov. Density profiles of dark matter haloes: diversity and dependence on environment. *MNRAS*, 310(2):527–539, dec 1999. doi: 10.1046/j.1365-8711.1999.02968.x.

Sam G. Stafford, Ian G. McCarthy, Juliana Kwan, Shaun T. Brown, Andreea S. Font, and Andrew Robertson. Testing extensions to LCDM on small scales with forthcoming cosmic shear surveys. *arXiv e-prints*, art. arXiv:2109.11956, September 2021.

G. Efstathiou. Suppressing the formation of dwarf galaxies via photoionization. *MNRAS*, 256(2):43P–47P, May 1992. doi: 10.1093/mnras/256.1.43P.

Takashi Hamana, Masato Shirasaki, Satoshi Miyazaki, Chiaki Hikage, Masamune Oguri, Surhud More, Robert Armstrong, Alexie Leauthaud, Rachel Mandelbaum, Hironao Miyatake, Atsushi J. Nishizawa, Melanie Simet, Masahiro Takada, Hiroaki Aihara, James Bosch, Yutaka Komiyama, Robert Lupton, Hitoshi Murayama, Michael A. Strauss, and Masayuki Tanaka. Cosmological constraints from cosmic shear two-point correlation functions with HSC survey first-year data. *PASJ*, 72(1): 16, February 2020. doi: 10.1093/pasj/psz138.

Marika Asgari, Chieh-An Lin, Benjamin Joachimi, Benjamin Giblin, Catherine Heymans, Hendrik Hildebrandt, Arun Kannawadi, Benjamin Stölzner, Tilman Tröster, Jan Luca van den Busch, Angus H. Wright, Maciej Bilicki, Chris Blake, Jelte de Jong, Andrej Dvornik, Thomas Erben, Fedor Getman, Henk Hoekstra, Fabian Köhlinger, Konrad Kuijken, Lance Miller, Mario Radovich, Peter Schneider, HuanYuan Shan, and Edwin Valentijn. KiDS-1000 cosmology: Cosmic shear constraints and comparison between two point statistics. *A&A*, 645:A104, January 2021. doi: 10.1051/0004-6361/202039070.

Euclid Collaboration, A. Blanchard, S. Camera, C. Carbone, V. F. Cardone, S. Casas,

S. Clesse, S. Ilić, M. Kilbinger, T. Kitching, M. Kunz, F. Lacasa, E. Linder, E. Majerotto, K. Markovič, M. Martinelli, V. Pettorino, A. Pourtsidou, Z. Sakr, A. G. Sánchez, D. Sapone, I. Tutusaus, S. Yahia-Cherif, V. Yankelevich, S. Andreon, H. Aussel, A. Balaguera-Antolínez, M. Baldi, S. Bardelli, R. Bender, A. Biviano, D. Bonino, A. Boucaud, E. Bozzo, E. Branchini, S. Brau-Nogue, M. Brescia, J. Brinchmann, C. Burigana, R. Cabanac, V. Capobianco, A. Cappi, J. Carretero, C. S. Carvalho, R. Casas, F. J. Castander, M. Castellano, S. Cavuoti, A. Cimatti, R. Cledassou, C. Colodro-Conde, G. Congedo, C. J. Conselice, L. Conversi, Y. Copin, L. Corcione, J. Coupon, H. M. Courtois, M. Cropper, A. Da Silva, S. de la Torre, D. Di Ferdinando, F. Dubath, F. Ducret, C. A. J. Duncan, X. Dupac, S. Dusini, G. Fabbian, M. Fabricius, S. Farrens, P. Fosalba, S. Fotopoulou, N. Fourmanoit, M. Frailis, E. Franceschi, P. Franzetti, M. Fumana, S. Galeotta, W. Gillard, B. Gillis, C. Giocoli, P. Gómez-Alvarez, J. Graciá-Carpio, F. Grupp, L. Guzzo, H. Hoekstra, F. Hormuth, H. Israel, K. Jahnke, E. Keihanen, S. Kermiche, C. C. Kirkpatrick, R. Kohley, B. Kubik, H. Kurki-Suonio, S. Ligori, P. B. Lilje, I. Lloro, D. Maino, E. Maiorano, O. Marggraf, N. Martinet, F. Marulli, R. Massey, E. Medinaceli, S. Mei, Y. Mellier, B. Metcalf, J. J. Metge, G. Meylan, M. Moresco, L. Moscardini, E. Munari, R. C. Nichol, S. Niemi, A. A. Nucita, C. Padilla, S. Paltani, F. Pasian, W. J. Percival, S. Pires, G. Polenta, M. Poncet, L. Pozzetti, G. D. Racca, F. Raison, A. Renzi, J. Rhodes, E. Romelli, M. Roncarelli, E. Rossetti, R. Saglia, P. Schneider, V. Scottez, A. Secroun, G. Sirri, L. Stanco, J. L. Starck, F. Sureau, P. Tallada-Crespí, D. Tavagnacco, A. N. Taylor, M. Tenti, I. Tereno, R. Toledo-Moreo, F. Torradeflot, L. Valenziano, T. Vassallo, G. A. Verdoes Kleijn, M. Viel, Y. Wang, A. Zacchei, J. Zoubian, and E. Zucca. Euclid preparation. VII. Forecast validation for Euclid cosmological probes. *A&A*, 642:A191, October 2020a. doi: 10.1051/0004-6361/202038071.

Hu Zhan and J. Anthony Tyson. Cosmology with the Large Synoptic Survey Telescope: an overview. *Reports on Progress in Physics*, 81(6):066901, June 2018. doi: 10.1088/1361-6633/aab1bd.

D. Spergel, N. Gehrels, C. Baltay, D. Bennett, J. Breckinridge, M. Donahue,

A. Dressler, B. S. Gaudi, T. Greene, O. Guyon, C. Hirata, J. Kalirai, N. J. Kasdin, B. Macintosh, W. Moos, S. Perlmutter, M. Postman, B. Rauscher, J. Rhodes, Y. Wang, D. Weinberg, D. Benford, M. Hudson, W. S. Jeong, Y. Mellier, W. Traub, T. Yamada, P. Capak, J. Colbert, D. Masters, M. Penny, D. Savransky, D. Stern, N. Zimmerman, R. Barry, L. Bartusek, K. Carpenter, E. Cheng, D. Content, F. Dekens, R. Demers, K. Grady, C. Jackson, G. Kuan, J. Kruk, M. Melton, B. Nemati, B. Parvin, I. Poberezhskiy, C. Peddie, J. Ruffa, J. K. Wallace, A. Whipple, E. Wollack, and F. Zhao. Wide-Field InfrarRed Survey Telescope-Astrophysics Focused Telescope Assets WFIRST-AFTA 2015 Report. *arXiv e-prints*, art. arXiv:1503.03757, March 2015.

Katarina Markovic, Sarah Bridle, Anže Slosar, and Jochen Weller. Constraining warm dark matter with cosmic shear power spectra. *J. Cosmology Astropart. Phys.*, 2011 (1):022, January 2011. doi: 10.1088/1475-7516/2011/01/022.

Jonathan Hubert, Aurel Schneider, Doug Potter, and Joachim Stadel. Decaying Dark Matter: Simulations and Weak-Lensing Forecast. *arXiv e-prints*, art. arXiv:2104.07675, April 2021.

Planck Collaboration, P. A. R. Ade, N. Aghanim, C. Armitage-Caplan, M. Arnaud, M. Ashdown, F. Atrio-Barandela, J. Aumont, C. Baccigalupi, A. J. Banday, R. B. Barreiro, J. G. Bartlett, E. Battaner, K. Benabed, A. Benoît, A. Benoit-Lévy, J. P. Bernard, M. Bersanelli, P. Bielewicz, J. Bobin, J. J. Bock, A. Bonaldi, J. R. Bond, J. Borrill, F. R. Bouchet, M. Bridges, M. Bucher, C. Burigana, R. C. Butler, E. Calabrese, B. Cappellini, J. F. Cardoso, A. Catalano, A. Challinor, A. Chamballu, R. R. Chary, X. Chen, H. C. Chiang, L. Y. Chiang, P. R. Christensen, S. Church, D. L. Clements, S. Colombi, L. P. L. Colombo, F. Couchot, A. Coulais, B. P. Crill, A. Curto, F. Cuttaia, L. Danese, R. D. Davies, R. J. Davis, P. de Bernardis, A. de Rosa, G. de Zotti, J. Delabrouille, J. M. Delouis, F. X. Désert, C. Dickinson, J. M. Diego, K. Dolag, H. Dole, S. Donzelli, O. Doré, M. Douspis, J. Dunkley, X. Dupac, G. Efstathiou, F. Elsner, T. A. Enßlin, H. K. Eriksen, F. Finelli, O. Forni, M. Frailis, A. A. Fraisse, E. Franceschi, T. C. Gaier, S. Galeotta, S. Galli, K. Ganga, M. Giard, G. Giardino, Y. Giraud-Héraud, E. Gjerløw, J. González-

Nuevo, K. M. Górski, S. Gratton, A. Gregorio, A. Gruppuso, J. E. Gudmundsson, J. Haissinski, J. Hamann, F. K. Hansen, D. Hanson, D. Harrison, S. Henrot-Versillé, C. Hernández-Monteagudo, D. Herranz, S. R. Hildebrandt, E. Hivon, M. Hobson, W. A. Holmes, A. Hornstrup, Z. Hou, W. Hovest, K. M. Huffenberger, A. H. Jaffe, T. R. Jaffe, J. Jewell, W. C. Jones, M. Juvela, E. Keihänen, R. Keskitalo, T. S. Kisner, R. Kneissl, J. Knoche, L. Knox, M. Kunz, H. Kurki-Suonio, G. Lagache, A. Lähteenmäki, J. M. Lamarre, A. Lasenby, M. Lattanzi, R. J. Laureijs, C. R. Lawrence, S. Leach, J. P. Leahy, R. Leonardi, J. León-Tavares, J. Lesgourgues, A. Lewis, M. Liguori, P. B. Lilje, M. Linden-Vørnle, M. López-Caniego, P. M. Lubin, J. F. Macías-Pérez, B. Maffei, D. Maino, N. Mandolesi, M. Maris, D. J. Marshall, P. G. Martin, E. Martínez-González, S. Masi, M. Massardi, S. Matarrese, F. Matthai, P. Mazzotta, P. R. Meinhold, A. Melchiorri, J. B. Melin, L. Mendes, E. Menegoni, A. Mennella, M. Migliaccio, M. Millea, S. Mitra, M. A. Miville-Deschênes, A. Moneti, L. Montier, G. Morgante, D. Mortlock, A. Moss, D. Munshi, J. A. Murphy, P. Naselsky, F. Nati, P. Natoli, C. B. Netterfield, H. U. Nørgaard-Nielsen, F. Noviello, D. Novikov, I. Novikov, I. J. O'Dwyer, S. Osborne, C. A. Oxborrow, F. Paci, L. Pagano, F. Pajot, R. Paladini, D. Paoletti, B. Partridge, F. Pasian, G. Patanchon, D. Pearson, T. J. Pearson, H. V. Peiris, O. Perdereau, L. Perotto, F. Perrotta, V. Pettorino, F. Piacentini, M. Piat, E. Pierpaoli, D. Pietrobon, S. Plaszczynski, P. Platania, E. Pointecouteau, G. Polenta, N. Ponthieu, L. Popa, T. Poutanen, G. W. Pratt, G. Prézeau, S. Prunet, J. L. Puget, J. P. Rachen, W. T. Reach, R. Rebolo, M. Reinecke, M. Remazeilles, C. Renault, S. Ricciardi, T. Riller, I. Ristorcelli, G. Rocha, C. Rosset, G. Roudier, M. Rowan-Robinson, J. A. Rubiño-Martín, B. Rusholme, M. Sandri, D. Santos, M. Savelainen, G. Savini, D. Scott, M. D. Seiffert, E. P. S. Shellard, L. D. Spencer, J. L. Starck, V. Stolyarov, R. Stompor, R. Sudiwala, R. Sunyaev, F. Sureau, D. Sutton, A. S. Suur-Uski, J. F. Sygnet, J. A. Tauber, D. Tavagnacco, L. Terenzi, L. Toffolatti, M. Tomasi, M. Tristram, M. Tucci, J. Tuovinen, M. Türler, G. Umana, L. Valenziano, J. Valiviita, B. Van Tent, P. Vielva, F. Villa, N. Vittorio, L. A. Wade, B. D. Wandelt, I. K. Wehus, M. White, S. D. M. White, A. Wilkinson, D. Yvon, A. Zacchei, and A. Zonca. Planck 2013 results. XVI. Cosmological parameters. *A&A*, 571:A16, November

2014. doi: 10.1051/0004-6361/201321591.

E. O. Nadler, R. H. Wechsler, K. Bechtol, Y. Y. Mao, G. Green, A. Drlica-Wagner, M. McNanna, S. Mau, A. B. Pace, J. D. Simon, A. Kravtsov, S. Dodelson, T. S. Li, A. H. Riley, M. Y. Wang, T. M. C. Abbott, M. Aguena, S. Allam, J. Annis, S. Avila, G. M. Bernstein, E. Bertin, D. Brooks, D. L. Burke, A. Carnero Rosell, M. Carrasco Kind, J. Carretero, M. Costanzi, L. N. da Costa, J. De Vicente, S. Desai, A. E. Evrard, B. Flaugher, P. Fosalba, J. Frieman, J. García-Bellido, E. Gaztanaga, D. W. Gerdes, D. Gruen, J. Gschwend, G. Gutierrez, W. G. Hartley, S. R. Hinton, K. Honscheid, E. Krause, K. Kuehn, N. Kuropatkin, O. Lahav, M. A. G. Maia, J. L. Marshall, F. Menanteau, R. Miquel, A. Palmese, F. Paz-Chinchón, A. A. Plazas, A. K. Romer, E. Sanchez, B. Santiago, V. Scarpine, S. Serrano, M. Smith, M. Soares-Santos, E. Suchyta, G. Tarle, D. Thomas, T. N. Varga, A. R. Walker, and DES Collaboration. Milky Way Satellite Census. II. Galaxy-Halo Connection Constraints Including the Impact of the Large Magellanic Cloud. *ApJ*, 893(1):48, April 2020c. doi: 10.3847/1538-4357/ab846a.

Daniel Gilman, Simon Birrer, Tommaso Treu, Anna Nierenberg, and Andrew Benson. Probing dark matter structure down to 10^7 solar masses: flux ratio statistics in gravitational lenses with line-of-sight haloes. *MNRAS*, 487(4):5721–5738, August 2019. doi: 10.1093/mnras/stz1593.

Andrew Robertson, Richard Massey, and Vincent Eke. What does the Bullet Cluster tell us about self-interacting dark matter? *MNRAS*, 465(1):569–587, feb 2017c. ISSN 0035-8711. doi: 10.1093/mnras/stw2670.

Jordi Miralda-Escude. A Test of the Collisional Dark Matter Hypothesis from Cluster Lensing. *ApJ*, 564(1):60–64, 2002b. ISSN 0004-637X. doi: 10.1086/324138.

Laura Sagunski, Sophia Gad-Nasr, Brian Colquhoun, Andrew Robertson, and Sean Tulin. Velocity-dependent self-interacting dark matter from groups and clusters of galaxies. *J. Cosmology Astropart. Phys.*, 2021(1):024, January 2021. doi: 10.1088/1475-7516/2021/01/024.

Camila A. Correa. Constraining velocity-dependent self-interacting dark matter with the Milky Way's dwarf spheroidal galaxies. *MNRAS*, 503(1):920–937, May 2021. doi: 10.1093/mnras/stab506.

Volker Springel, Simon D. M. White, Adrian Jenkins, Carlos S. Frenk, Naoki Yoshida, Liang Gao, Julio Navarro, Robert Thacker, Darren Croton, John Helly, John A. Peacock, Shaun Cole, Peter Thomas, Hugh Couchman, August Evrard, Jörg Colberg, and Frazer Pearce. Simulations of the formation, evolution and clustering of galaxies and quasars. *Nature*, 435(7042):629–636, June 2005. doi: 10.1038/nature03597.

Chris Power and Alexander Knebe. The impact of box size on the properties of dark matter haloes in cosmological simulations. *MNRAS*, 370:691–701, 2006. doi: 10.1111/j.1365-2966.2006.10562.x.

Katrin Heitmann, Martin White, Christian Wagner, Salman Habib, and David Higdon. The Coyote Universe. I. Precision Determination of the Nonlinear Matter Power Spectrum. *ApJ*, 715(1):104–121, May 2010. doi: 10.1088/0004-637X/715/1/104.

Anatoly Klypin and Francisco Prada. Dark matter statistics for large galaxy catalogues: power spectra and covariance matrices. *MNRAS*, 478(4):4602–4621, August 2018. doi: 10.1093/mnras/sty1340.

Simeon Bird. GenPK: Power spectrum generator, June 2017.

M. Viel, K. Markovič, M. Baldi, and J. Weller. The non-linear matter power spectrum in warm dark matter cosmologies. *MNRAS*, 421(1):50–62, 2012. doi: 10.1111/j.1365-2966.2011.19910.x.

R. D. Blandford, A. B. Saust, T. G. Brainerd, and J. V. Villumsen. The distortion of distant galaxy images by large-scale structure. *MNRAS*, 251:600, August 1991. doi: 10.1093/mnras/251.4.600.

Jordi Miralda-Escude. The Correlation Function of Galaxy Ellipticities Produced by Gravitational Lensing. *ApJ*, 380:1, October 1991. doi: 10.1086/170555.

Nick Kaiser. Weak Gravitational Lensing of Distant Galaxies. *ApJ*, 388:272, April 1992. doi: 10.1086/171151.

Martin Kilbinger. Cosmology with cosmic shear observations: a review. *Reports on Progress in Physics*, 78(8):086901, July 2015. doi: 10.1088/0034-4885/78/8/086901.

D. Nelson Limber. The Analysis of Counts of the Extragalactic Nebulae in Terms of a Fluctuating Density Field. *ApJ*, 117:134, January 1953. doi: 10.1086/145672.

Wayne Hu. Power Spectrum Tomography with Weak Lensing. *ApJl*, 522(1):L21–L24, September 1999. doi: 10.1086/312210.

P. Schneider, L. van Waerbeke, and Y. Mellier. B-modes in cosmic shear from source redshift clustering. *A&A*, 389:729–741, July 2002. doi: 10.1051/0004-6361:20020626.

F. Bernardeau. The effects of source clustering on weak lensing statistics. *A&A*, 338:375–382, October 1998.

Takashi Hamana, Stéphane T. Colombi, Aurélien Thion, Julien E. G. T. Devriendt, Yannick Mellier, and Francis Bernardeau. Source-lens clustering effects on the skewness of the lensing convergence. *MNRAS*, 330(2):365–377, February 2002. doi: 10.1046/j.1365-8711.2002.05103.x.

Fabian Schmidt. Weak lensing probes of modified gravity. *Phys. Rev. D*, 78(4):043002, August 2008. doi: 10.1103/PhysRevD.78.043002.

Tommaso Giannantonio, Cristiano Porciani, Julien Carron, Adam Amara, and Annalisa Pillepich. Constraining primordial non-Gaussianity with future galaxy surveys. *MNRAS*, 422(4):2854–2877, June 2012. doi: 10.1111/j.1365-2966.2012.20604.x.

Martin Kilbinger, Catherine Heymans, Marika Asgari, Shahab Joudaki, Peter Schneider, Patrick Simon, Ludovic Van Waerbeke, Joachim Harnois-Déraps, Hendrik Hildebrandt, Fabian Köhlinger, Konrad Kuijken, and Massimo Viola. Precision

calculations of the cosmic shear power spectrum projection. *MNRAS*, 472(2):2126–2141, December 2017. doi: 10.1093/mnras/stx2082.

Nick Kaiser. Weak Lensing and Cosmology. *ApJ*, 498(1):26–42, May 1998. doi: 10.1086/305515.

M. Gatti, E. Sheldon, A. Amon, M. Becker, M. Troxel, A. Choi, C. Doux, N. MacCrann, A. Navarro-Alsina, I. Harrison, D. Gruen, G. Bernstein, M. Jarvis, L. F. Secco, A. Ferté, T. Shin, J. McCullough, R. P. Rollins, R. Chen, C. Chang, S. Pandey, I. Tutusaus, J. Prat, J. Elvin-Poole, C. Sanchez, A. A. Plazas, A. Roodman, J. Zuntz, T. M. C. Abbott, M. Aguena, S. Allam, J. Annis, S. Avila, D. Bacon, E. Bertin, S. Bhargava, D. Brooks, D. L. Burke, A. Carnero Rosell, M. Carrasco Kind, J. Carretero, F. J. Castander, C. Conselice, M. Costanzi, M. Crocce, L. N. da Costa, T. M. Davis, J. De Vicente, S. Desai, H. T. Diehl, J. P. Dietrich, P. Doel, A. Drlica-Wagner, K. Eckert, S. Everett, I. Ferrero, J. Frieman, J. García-Bellido, D. W. Gerdes, T. Giannantonio, R. A. Gruendl, J. Gschwend, G. Gutierrez, W. G. Hartley, S. R. Hinton, D. L. Hollowood, K. Honscheid, B. Hoyle, E. M. Huff, D. Huterer, B. Jain, D. J. James, T. Jeltema, E. Krause, R. Kron, N. Kuropatkin, M. Lima, M. A. G. Maia, J. L. Marshall, R. Miquel, R. Morgan, J. Myles, A. Palmese, F. Paz-Chinchón, E. S. Rykoff, S. Samuroff, E. Sanchez, V. Scarpine, M. Schubnell, S. Serrano, I. Sevilla-Noarbe, M. Smith, M. Soares-Santos, E. Suchyta, M. E. C. Swanson, G. Tarle, D. Thomas, C. To, D. L. Tucker, T. N. Varga, R. H. Wechsler, J. Weller, W. Wester, and R. D. Wilkinson. Dark energy survey year 3 results: weak lensing shape catalogue. *MNRAS*, 504(3):4312–4336, July 2021. doi: 10.1093/mnras/stab918.

Benjamin Joachimi, Marcello Cacciato, Thomas D. Kitching, Adrienne Leonard, Rachel Mandelbaum, Björn Malte Schäfer, Cristóbal Sifón, Henk Hoekstra, Alina Kiessling, Donnacha Kirk, and Anais Rassat. Galaxy Alignments: An Overview. *Space Sci. Rev.*, 193(1-4):1–65, November 2015. doi: 10.1007/s11214-015-0177-4.

Alina Kiessling, Marcello Cacciato, Benjamin Joachimi, Donnacha Kirk, Thomas D. Kitching, Adrienne Leonard, Rachel Mandelbaum, Björn Malte Schäfer, Cristóbal

Sifón, Michael L. Brown, and Anais Rassat. Galaxy Alignments: Theory, Modelling & Simulations. *Space Sci. Rev.*, 193(1-4):67–136, November 2015. doi: 10.1007/s11214-015-0203-6.

Donnacha Kirk, Michael L. Brown, Henk Hoekstra, Benjamin Joachimi, Thomas D. Kitching, Rachel Mandelbaum, Cristóbal Sifón, Marcello Cacciato, Ami Choi, Alina Kiessling, Adrienne Leonard, Anais Rassat, and Björn Malte Schäfer. Galaxy Alignments: Observations and Impact on Cosmology. *Space Sci. Rev.*, 193(1-4): 139–211, November 2015. doi: 10.1007/s11214-015-0213-4.

Rachel Mandelbaum. Weak Lensing for Precision Cosmology. *ARA&A*, 56:393–433, September 2018. doi: 10.1146/annurev-astro-081817-051928.

Euclid Collaboration, G. Desprez, S. Paltani, J. Coupon, I. Almosallam, A. Alvarez-Ayllon, V. Amaro, M. Brescia, M. Brodwin, S. Cavuoti, J. De Vicente-Albendea, S. Fotopoulou, P. W. Hatfield, W. G. Hartley, O. Ilbert, M. J. Jarvis, G. Longo, M. M. Rau, R. Saha, J. S. Speagle, A. Tramacere, M. Castellano, F. Dubath, A. Galametz, M. Kuemmel, C. Laigle, E. Merlin, J. J. Mohr, S. Pilo, M. Salvato, S. Andreon, N. Auricchio, C. Baccigalupi, A. Balaguera-Antolínez, M. Baldi, S. Bardelli, R. Bender, A. Biviano, C. Bodendorf, D. Bonino, E. Bozzo, E. Branchini, J. Brinchmann, C. Burigana, R. Cabanac, S. Camera, V. Capobianco, A. Cappi, C. Carbone, J. Carretero, C. S. Carvalho, R. Casas, S. Casas, F. J. Castander, G. Castignani, A. Cimatti, R. Cledassou, C. Colodro-Conde, G. Congedo, C. J. Conselice, L. Conversi, Y. Copin, L. Corcione, H. M. Courtois, J. G. Cuby, A. Da Silva, S. de la Torre, H. Degaudenzi, D. Di Ferdinando, M. Douspis, C. A. J. Duncan, X. Dupac, A. Ealet, G. Fabbian, M. Fabricius, S. Farrens, P. G. Ferreira, F. Finelli, P. Fosalba, N. Fourmanoit, M. Frailis, E. Franceschi, M. Fumana, S. Galeotta, B. Garilli, W. Gillard, B. Gillis, C. Giocoli, G. Gozaliasl, J. Graciá-Carpio, F. Grupp, L. Guzzo, M. Hailey, S. V. H. Haugan, W. Holmes, F. Hormuth, A. Humphrey, K. Jahnke, E. Keihanen, S. Kermiche, M. Kilbinger, C. C. Kirkpatrick, T. D. Kitching, R. Kohley, B. Kubik, M. Kunz, H. Kurki-Suonio, S. Ligori, P. B. Lilje, I. Lloro, D. Maino, E. Maiorano, O. Marggraf, K. Markovic, N. Martinet, F. Marulli, R. Massey, M. Maturi, N. Mauri, S. Maurogordato, E. Medinaceli, S. Mei, M. Meneghetti, R. Benton

Metcalf, G. Meylan, M. Moresco, L. Moscardini, E. Munari, S. Niemi, C. Padilla, F. Pasian, L. Patrizii, V. Pettorino, S. Pires, G. Polenta, M. Poncet, L. Popa, D. Potter, L. Pozzetti, F. Raison, A. Renzi, J. Rhodes, G. Riccio, E. Rossetti, R. Saglia, D. Sapone, P. Schneider, V. Scottez, A. Secroun, S. Serrano, C. Sirignano, G. Sirri, L. Stanco, D. Stern, F. Sureau, P. Tallada Crespí, D. Tavagnacco, A. N. Taylor, M. Tenti, I. Tereno, R. Toledo-Moreo, F. Torradeflot, L. Valenziano, J. Valiviita, T. Vassallo, M. Viel, Y. Wang, N. Welikala, L. Whittaker, A. Zacchei, G. Zamorani, J. Zoubian, and E. Zucca. Euclid preparation. X. The Euclid photometric-redshift challenge. *A&A*, 644:A31, December 2020b. doi: 10.1051/0004-6361/202039403.

Henrique S. Xavier, Filipe B. Abdalla, and Benjamin Joachimi. Improving lognormal models for cosmological fields. *MNRAS*, 459(4):3693–3710, July 2016. doi: 10.1093/mnras/stw874.

Wayne Hu. Weak lensing of the CMB: A harmonic approach. *Phys. Rev. D*, 62(4): 043007, August 2000. doi: 10.1103/PhysRevD.62.043007.

M. Bartelmann and P. Schneider. Weak gravitational lensing. *Phys. Rep.*, 340(4-5): 291–472, January 2001. doi: 10.1016/S0370-1573(00)00082-X.

S. Hilbert, J. Hartlap, and P. Schneider. Cosmic shear covariance: the log-normal approximation. *A&A*, 536:A85, December 2011. doi: 10.1051/0004-6361/201117294.

Tim Eifler, Melanie Simet, Elisabeth Krause, Christopher Hirata, Hung-Jin Huang, Xiao Fang, Vivian Miranda, Rachel Mandelbaum, Cyrille Doux, Chen Heinrich, Eric Huff, Hironao Miyatake, Shoubaneh Hemmati, Jiachuan Xu, Paul Rogozenski, Peter Capak, Ami Choi, Olivier Dore, Bhuvnesh Jain, Mike Jarvis, Niall MacCrann, Dan Masters, Eduardo Rozo, David N. Spergel, Michael Troxel, Anja von der Linden, Yun Wang, David H. Weinberg, Lukas Wenzl, and Hao-Yi Wu. Cosmology with the Wide-Field Infrared Survey Telescope – Synergies with the Rubin Observatory Legacy Survey of Space and Time. *arXiv e-prints*, art. arXiv:2004.04702, April 2020.

J. Hartlap, S. Hilbert, P. Schneider, and H. Hildebrandt. A bias in cosmic shear from

galaxy selection: results from ray-tracing simulations. *A&A*, 528:A51, April 2011. doi: 10.1051/0004-6361/201015850.

N. MacCrann, J. Aleksić, A. Amara, S. L. Bridle, C. Bruderer, C. Chang, S. Dodelson, T. F. Eifler, E. M. Huff, D. Huterer, T. Kacprzak, A. Refregier, E. Suchyta, R. H. Wechsler, J. Zuntz, T. M. C. Abbott, S. Allam, J. Annis, R. Armstrong, A. Benoit-Lévy, D. Brooks, D. L. Burke, A. Carnero Rosell, M. Carrasco Kind, J. Carretero, F. J. Castander, M. Crocce, C. E. Cunha, L. N. da Costa, S. Desai, H. T. Diehl, J. P. Dietrich, P. Doel, A. E. Evrard, B. Flaugher, P. Fosalba, D. W. Gerdes, D. A. Goldstein, D. Gruen, R. A. Gruendl, G. Gutierrez, K. Honscheid, D. J. James, M. Jarvis, E. Krause, K. Kuehn, N. Kuropatkin, M. Lima, J. L. Marshall, P. Melchior, F. Menanteau, R. Miquel, A. A. Plazas, A. K. Romer, E. S. Rykoff, E. Sanchez, V. Scarpine, I. Sevilla-Noarbe, E. Sheldon, M. Soares-Santos, M. E. C. Swanson, G. Tarle, D. Thomas, V. Vikram, and DES Collaboration. Inference from the small scales of cosmic shear with current and future Dark Energy Survey data. *MNRAS*, 465(3):2567–2583, March 2017. doi: 10.1093/mnras/stw2849.

Henk Hoekstra, Arun Kannawadi, and Thomas D. Kitching. Accounting for object detection bias in weak gravitational lensing studies. *A&A*, 646:A124, February 2021. doi: 10.1051/0004-6361/202038998.

Erin S. Sheldon, Matthew R. Becker, Niall MacCrann, and Michael Jarvis. Mitigating Shear-dependent Object Detection Biases with Metacalibration. *ApJ*, 902(2):138, October 2020. doi: 10.3847/1538-4357/abb595.

N. E. Chisari, M. L. A. Richardson, J. Devriendt, Y. Dubois, A. Schneider, A. M. C. Le Brun, R. S. Beckmann, S. Peirani, A. Slyz, and C. Pichon. The impact of baryons on the matter power spectrum from the Horizon-AGN cosmological hydrodynamical simulation. *MNRAS*, 480(3):3962–3977, November 2018. doi: 10.1093/mnras/sty2093.

Elisabetta Semboloni, Henk Hoekstra, Joop Schaye, Marcel P. van Daalen, and Ian G. McCarthy. Quantifying the effect of baryon physics on weak lensing tomogra-

phy. *MNRAS*, 417(3):2020–2035, November 2011. doi: 10.1111/j.1365-2966.2011.19385.x.

Wolfgang Enzi, Riccardo Murgia, Oliver Newton, Simona Vegetti, Carlos Frenk, Matteo Viel, Marius Cautun, Christopher D. Fassnacht, Matt Auger, Giulia Despali, John McKean, Léon V. E. Koopmans, and Mark Lovell. Joint constraints on thermal relic dark matter from a selection of astrophysical probes. *arXiv e-prints*, art. arXiv:2010.13802, October 2020.

Ethan O. Nadler, Simon Birrer, Daniel Gilman, Risa H. Wechsler, Xiaolong Du, Andrew Benson, Anna M. Nierenberg, and Tommaso Treu. Dark Matter Constraints from a Unified Analysis of Strong Gravitational Lenses and Milky Way Satellite Galaxies. *arXiv e-prints*, art. arXiv:2101.07810, January 2021.

Andrea V. Macciò, Jonas Frings, Tobias Buck, Aaron A. Dutton, Marvin Blank, Aura Obreja, and Keri L. Dixon. The edge of galaxy formation III: the effects of warm dark matter on Milky Way satellites and field dwarfs. *MNRAS*, 484(4):5400–5408, April 2019. doi: 10.1093/mnras/stz327.

Omid Sameie, Michael Boylan-Kolchin, Robyn Sanderson, Drona Vargya, Philip F. Hopkins, Andrew Wetzel, James Bullock, Andrew Graus, and Victor H. Robles. The central densities of Milky Way-mass galaxies in cold and self-interacting dark matter models. *MNRAS*, 507(1):720–729, October 2021. doi: 10.1093/mnras/stab2173.

Alex Fitts, Michael Boylan-Kolchin, Brandon Bozek, James S. Bullock, Andrew Graus, Victor Robles, Philip F. Hopkins, Kareem El-Badry, Shea Garrison-Kimmel, Claude-André Faucher-Giguère, Andrew Wetzel, and Dušan Kereš. Dwarf galaxies in CDM, WDM, and SIDM: disentangling baryons and dark matter physics. *MNRAS*, 490(1):962–977, November 2019. doi: 10.1093/mnras/stz2613.

Steen Hannestad and Robert J. Scherrer. Self-interacting warm dark matter. *Phys. Rev. D*, 62(4):043522, August 2000. doi: 10.1103/PhysRevD.62.043522.

Katrin Heitmann, Earl Lawrence, Juliana Kwan, Salman Habib, and David Higdon.

The Coyote Universe Extended: Precision Emulation of the Matter Power Spectrum. *ApJ*, 780(1):111, January 2014. doi: 10.1088/0004-637X/780/1/111.

Earl Lawrence, Katrin Heitmann, Juliana Kwan, Amol Upadhye, Derek Bingham, Salman Habib, David Higdon, Adrian Pope, Hal Finkel, and Nicholas Frontiere. The Mira-Titan Universe. II. Matter Power Spectrum Emulation. *ApJ*, 847(1):50, September 2017. doi: 10.3847/1538-4357/aa86a9.

Mark R. Lovell, Wojciech Hellwing, Aaron Ludlow, Jesús Zavala, Andrew Robertson, Azadeh Fattahi, Carlos S. Frenk, and Jennifer Hardwick. Local group star formation in warm and self-interacting dark matter cosmologies. *MNRAS*, 498(1):702–717, October 2020. doi: 10.1093/mnras/staa2525.

Camila A Correa, J. Stuart B. Wyithe, Joop Schaye, and Alan R Duffy. The accretion history of dark matter haloes – I. The physical origin of the universal function. *Monthly Notices of the Royal Astronomical Society*, 450(2):1514–1520, jun 2015b. ISSN 1365-2966. doi: 10.1093/mnras/stv689.

Camila A Correa, J. Stuart B. Wyithe, Joop Schaye, and Alan R Duffy. The accretion history of dark matter haloes – II. The connections with the mass power spectrum and the density profile. *Monthly Notices of the Royal Astronomical Society*, 450(2): 1521–1537, jun 2015c. ISSN 1365-2966. doi: 10.1093/mnras/stv697.

Michael Boylan-Kolchin, Volker Springel, Simon D.M. White, and Adrian Jenkins. There's no place like home? Statistics of Milky Way-mass dark matter haloes. *MNRAS*, 406(2):896–912, 2010. ISSN 00358711. doi: 10.1111/j.1365-2966.2010.16774.x.